On the metastable pitting of aluminium alloys

Submitted in partial fulfilment of the requirements

for the degree of

Doctor of Philosophy

of the

Indian Institute of Technology Bombay, India

and

Monash University, Australia

By

Gayathri Sridhar

Supervisors:

Prof V. S. Raja (IIT Bombay)

Prof Nick Birbilis (Monash University)

The course of study for this award was developed jointly by

the Indian Institute of Technology, Bombay and Monash University, Australia

and given academic recognition by each of them.

The programme was administered by the IITB-Monash Research Academy

(April 2021)

Dedicated to

The Almighty,

my dear son Achyuth Adithya, my husband Karthick Sudhan,

my parents S. Jeya Mithra, R. Sridhar

and

all my wonderful teachers

Declaration

I declare that this written submission represents my ideas in my own words and where other's ideas or words have been included, I have adequately cited and referenced the original sources.

I also declare that I have adhered to all principles of academic honesty and integrity and have not misrepresented or fabricated or falsified any idea/data/fact/source in my submission. I understand that any violation of the above will be cause for disciplinary action by the Institute and can also evoke penal action from the sources which have thus not been properly cited or from whom proper permission has not been taken when needed.

Notice 1

Under the Copyright Act 1968, this thesis must be used only under the normal conditions of scholarly fair dealing. In particular, no results or conclusions should be extracted from it, nor should it be copied or closely paraphrased in whole or in part without the written consent of the author. Proper written acknowledgement should be made for any assistance obtained from this thesis.

Notice 2

I certify that I have made all reasonable efforts to secure copyright permissions from third-party content included in this thesis and have not knowingly added copyright content to my work without the owner's permission.

Gayathri Sridhar

Abstract

Aluminium and its alloys suffer from localised corrosion that typically initiates as corrosion pits and eventually leads to the structural failure of the material, limiting their engineering life. Investigation of metastable pitting characteristics from the measurable current transients recorded at anodic potentials below the pitting potential (E_{pit}), is recognised as an efficient method in determining the stable pitting susceptibility of alloy systems. Notably, the metastable pit sizes (r_{pit}) estimated from the charge of the individual current transients ($C_{transient}$) is employed in determining the nature of pit stability which is crucial in predicting the pit-to-crack transition behaviour. In aluminium alloys, the distribution of r_{pit} estimated in this manner is reported to be an underestimate of the actual distribution of r_{pit} witnessed on the pitted surface. While this discrepancy is often attributed to the copious hydrogen evolution (HE) occurring within the pits, the influence of other predominant factors such as the spatiotemporal evolution of pit events and pit geometry has remained unexplored. The challenge herein resides in establishing a direct correlation between the current transients and their associated metastable pit events. Such investigations require in situ mapping of the pit locations, which is curbed by the stochastic nature of metastable pitting and the presence of reflective pit covers. With the insights derived using a novel approach to map the metastable pit locations in situ, this dissertation evaluates how the actual and estimated metastable pit volumes (V_{pit}) compare and the factors that affect the reliability of estimating the r_{pit} and V_{pit} from $C_{transient}$.

The phenomenon termed Negative Difference Effect (NDE), which favours hydrogen evolution within the pits in aluminium at anodic potentials, was employed to map the real-time evolution of the metastable pit locations associated with the current transients. By optimising the parameters, namely, (a) signal-to-noise ratio, (b) surface area of the electrode, (c) concentration of the electrolyte and (d) polarisation potential, a successful correlation of the current transients to their associated metastable pit events was possible. The metastable pit sites (identified from the evolution of hydrogen bubbles) located with in situ optical time-lapse imaging were validated post electrochemical testing using an optical microscope and Scanning Electron Microscope (SEM). During metastable pitting, the hydrogen bubbles remained adsorbed to the pit surface and underwent an increase or decrease in their diameter (d_{bubble})

following a corresponding change in I_{pit}. The feasibility and limitations of this novel approach for the in situ mapping of the metastable pit locations based on HE were evaluated.

With the d_{bubble} determined using in situ imaging, the fraction of pit dissolution charge lost to HE, i.e., C_{HE}/C_{pit} was determined for the current transients recorded during the potentiostatic testing of aged Al-Mg binary alloy at anodic potentials below E_{pit}. The results were validated by comparing the estimated and actual V_{pit} measured using a 3D optical profilometer. The findings indicate that the ratio C_{HE}/C_{pit} varied from 0.019 to 0.052 depending on the $C_{transient}$ and did not introduce an error greater than 2% in the estimated r_{pit}.

The conventional notion of treating each current transient as a signal arising from single discrete pit events and the error it introduces in the r_{pit} estimated from $C_{transient}$ were investigated from the spatiotemporal evolution of metastable pit events. The studies were performed on an aged Al-Mg binary alloy and commercially pure aluminium to derive a comparative understanding of the influence of electrochemically distinct second phase particles on the inconsistencies witnessed in the estimated r_{pit}. The findings suggest that the overestimation and underestimation of r_{pit} due to the co-occurring and recurring pit events, respectively, introduced significant error in the estimated r_{pit} which was greater than the HE-induced error. Further, the study revealed that the assumption of hemispherical pit geometry during the calculation of r_{pit} for irregular pits introduced significant ambiguity. With the insights derived, a critical $C_{transient}$ and V_{pit} were proposed to be associated with the transients that resulted in multiple pit recurrences and subsequent stabilisation of the metastable pit location.

Key words: *aluminium, metastable pitting, hydrogen, in situ investigation.*

CONTENTS

Chapter 6

The role of the spatiotemporal evolution of pit events on the estimated metastable pit sizes

Chapter 7

Conclusion

List of Figures

List of Tables

Abbreviations

AESEC	Atomic emission spectroelectrochemistry
AFM	Atomic force microscopy
Al-Mg	Aluminium-magnesium binary alloy
Al-5Mg	Aged Al – 5 wt.% Mg binary alloy
Soln. Al-5Mg	Solutionised Al – 5 wt.% Mg binary alloy
BIW	Body-in-weight
BSE	Backscattered electron
CP-Al	Commercially pure aluminium
CPT	Critical pitting temperature
EAC	Environmentally assisted cracking
ECN	Electrochemical noise
EDAX	Energy dispersive X-ray analyser
EIS	Electrochemical impedance spectroscopy
ESEM	Environmental scanning electron microscopy
FEG-SEM	Field emission gun – scanning electron microscopy
fps	Frames per second
GB	Grain boundary
HE	Hydrogen evolution
ICP-AES	Inductively coupled plasma - atomic emission spectroscopy
ICP-OES	Inductively coupled plasma – optical emission spectrometry
IGC	Intergranular corrosion
LED	Light-emitting diode
L-EIS	Local – Electrochemical impedance spectroscopy
M/O	Metal-Oxide
MPR	Metastable pitting rate
NDE	Negative difference effect
OCP	Open circuit potential
OM	Optical microscope
PDM	Point defect model
SECM	Scanning electrochemical microscopy
SEM	Scanning electron microscope

SCE	Saturated calomel electrode
SE	Secondary electron
SHE	Standard hydrogen electrode
SiC	Silicon carbide
SKP	Scanning kelvin probe
SS	Stainless steel
STP	Standard temperature and pressure
SVET	Scanning vibrating electrode technique
TRV	Time-resolved volumetry
Wire-EDM	Wire-Electrical discharge machining

Symbols

α	Bunsen coefficient for the dissolution of H_2 in water
β	Mg_2Al_3 phase-precipitate
δ	Diffusion layer thickness
δ_{crit}	Critical film thickness
ΔC	Difference in the concentration between the pit anolyte and bulk
ΔK_p	Critical stress intensity factor
Λ	Rate of stable pitting
λ	Frequency of metastable pitting
ϕ	Potential drop
ρ	Density
τ_c	Critical age required for the metastable pits to transition to stability
μ	Probability that the metastable pits would repassivate
µA	Microampere
µC	Microcoulomb
µM	Micromolar
µm	Micron
A_{bubble}	Radial surface area of the bubble
A_{pit}	Hemispherical pit area
b	Slope of the plot of d_{bubble} vs t
b_a	Anodic Tafel slope
$C_{bulk,HE}$	Bulk concentration of hydrogen
C_{crit}	Critical concentration of the pit anolyte
C_{HE}	Charge of hydrogen evolution
C_{pit}	Pit dissolution charge
$C_{s,HE}$	Saturation concentration of hydrogen
$C_{transient}$	Charge of the current transient
$[Cl^-]$	Chloride concentration
D_{H_2}	Diffusion coefficient of hydrogen
D_{met}	Diffusivity of the metal cation
d_{bubble}	Diameter of the hydrogen bubble
E	Potential

E_{bottom}	Pit bottom potential
E_{corr}	Corrosion potential
E_m	Metastable pitting potential
E_{pit}	Pitting potential
E_{prot}	Protection potential
E_r	Repassivation potential
E_T	Transition potential
F	Faraday's constant
f	Frequency
I	Current
$I-t$	Current-time trace / Current transient
$I_{passive}$	Background passive current
$I_{passive,begin}$	Passive current at the beginning of the transient
$I_{passive,end}$	Passive current at the end of the transient
I_{peak}	Peak current
I_{pit}	Instantaneous pit current
I_x	Current at any instant $t = x$
i	Current density
$i_{0,HE}$	Exchange current density for hydrogen evolution
i_Ω	Ohmically-controlled current density
i_{anodic}	Anodic current density
i_{corr}	Corrosion current density
i_{H_2}	Instantaneous hydrogen evolution current density
i_{lim}	Limiting current density
$i_{passive}$	Passive current density
i_{pit}	Instantaneous pit current density
J_{H_2}	Flux of hydrogen
j	Interval of time
M	Molar mass
m	Slope of the plot of d_{bubble}^2 vs t
nA	Nanoampere
nC	Nanocoulomb
n_{H_2}	Number of moles of hydrogen

nm	Nanometer
pA	Picoampere
pC	Picocoulomb
pH_{zc}	pH of zero charge
$R_{dissolved}$	Bubble dissolution rate
R_{int}	Solution resistance
R_p	Polarisation potential
r_{bubble}	Radius of the bubble
r_{pit}	Hemispherical pit radius
$r_{pit,\beta}$	Hemispherical pit radius for the complete dissolution of β phase-precipitate
$r_{pit,corrected}$	Corrected pit radius
$r_{pit,peak}$	Pit radius at I_{peak}
t	Time
t_{bubble}	Duration of the bubble
t_g	Pit growth time
t_i	Induction time
t_{pit}	Pit lifetime
$t_{pit\ dissolution}$	Time required for pit dissolution, i.e., the time required for r_{pit} to reach a constant value
t_r	Pit repassivation time
t_{salt}	Time required for the precipitation of salt film
t_w	Waiting time for the appearance of hydrogen bubble
$V_{chemical\ dissolution}$	Total volume of hydrogen chemically dissolving at the bubble interface
$V_{dissolved}$	Volume of hydrogen dissolving from the bubble
$V_{diffused}$	Volume of hydrogen diffusing away from the bubble
V_{HE}	Total volume of hydrogen generated at the pit site
$V_{HE,bubble}$	Volume of hydrogen in the bubble measured from d_{bubble}
V_{pit}	Pit volume
$V_{pit,\beta}$	Pit volume for the complete dissolution of β phase-precipitates
$V_{pit,actual}$	Actual pit volume
$V_{pit,corrected}$	Corrected pit volume
$V_{pit,matrix}$	Pit volume for the dissolution of the matrix

x	Any instant of time
y	β phase or Al-rich matrix
Z	Impedance
z_{β}	No. of electrons involved in the complete dissolution of β phase-precipitate
z_{HE}	No. of electrons involved in the hydrogen evolution reaction
z_{matrix}	No. of electrons involved in the dissolution of Al-rich matrix
z_y	No. of electrons involved in the reaction concerning y

Acknowledgements

My deepest gratitude, praises and thanks to the Almighty for giving me the strength, wisdom and blessings that guided me through my PhD research.

I would like to express my sincere gratitude to my supervisors, Prof. V. S. Raja (IIT Bombay) and Prof. Nick Birbilis (Monash University), for their mentoring, guidance, understanding and support through my research journey. I also thank them for their patience as I took my time to understand the research methods. They gave me the liberty to think independently, inspired me and, most importantly, shaped me as a strategic thinker.

Special thanks to IITB Monash Research Academy for providing me with this excellent opportunity to collaborate and research across two premier universities.

I would like to thank Prof. Smrutiranjan Parida (IIT Bombay) and Dr. Sebastian Thomas (Monash University) for being my Research Progress Committee (RPC) members and contributing their valuable time in reviewing and providing constructive feedback for my work. I would like to thank Prof. J. Rangarajan (IIT Bombay) for his casual and informal technical discussions that gave me new perspectives.

I acknowledge Dr. Ruifeng Zhang (Monash University) for casting the alloys, Dr. Oumaima Gharbi (Monash University) for 3D printing the electrochemical cell, Dr. Shravan Kairy for providing the automated macro to analyse metastable pitting and Mr. Anirudh B Salian (Machine Tools Lab, IIT Bombay) for the careful fabrication of the microelectrodes used in this research work. I also acknowledge Ms. Mayura Sule (SAIF, IIT Bombay) and Ms. Pritee Navgharee (MEMS, IIT Bombay) for analysing the so-called ‘unconventional’ microelectrode surfaces using SEM. I am grateful to Mr. Sachin Alya and Mr. Alwin Varghese (Machine Tools Lab, IIT Bombay) for helping me with the 3D optical profilometer studies, especially during the Covid-19 lockdown.

Special thanks to Prof. K. Narasimhan (HOD – MEMS, IIT Bombay), Prof. Ashutosh S Gandhi (IIT Bombay), Prof. Ramesh Singh (Machine Tools Lab, IIT Bombay) for permitting me and providing me with the facilities for undertaking research during the unprecedented Covid-19

lockdown. I also take this opportunity to appreciate and thank Prof. George Mathew (Associate Dean SA, IIT Bombay) for extending my stay on campus to carry out my research work during the Covid-19 lockdown.

I thank my colleagues Dr. Ajay Krishnan (IIT Bombay), Dr. Poorwa Gore (IIT Bombay), Dr. Shravan Kairy (Monash University), Dr. Trina Majumdar (Monash University), Dr. Kate Nairn (Monash University), Mr. Rahul Agarwal (IIT Bombay) and other present and ex-lab mates of ACL-IIT Bombay and Monash University for the valuable technical discussions and constant support.

I would like to thank IIT Bombay, Monash University, IITB Monash Research Academy and NACE International - Gateway India Section for providing me with the fund to take part in the conference GRS and GRC – Aqueous Corrosion 2018, wherein fruitful discussions with the leading corrosion researchers across the world helped me shape my work. I also express my sincere gratitude to NACE International and CORCON Institute of Corrosion for granting me the prestigious NACE Foundation India Scholarship 2021.

I owe a huge thanks to Dr. Maria Gardiner (ThinkWell) for her insightful cum exhaustive sessions on the psychology of PhD at Monash University and the book ‘Get smart’ by Brian Tracy. They served as the polestar and guided me through the completion of my PhD.

My special and dearest thanks to my son Achyuth Adithya for his understanding, broad smiles, comfort hugs and timely wisdom that helped me overcome my failed experiments and motivated me to try one more time. I am thankful to my husband, Mr. Karthick Sudhan, for encouraging me and supporting me while also managing to file 4 different patents during my PhD tenure. Warm hugs to my mother, Mrs. Jeya Mithra and father, Mr. R. Sridhar, who morally supported me through my entire career. Special mention to the dedicated and devoted nuns of St. Elizabeth Creche’ - Powai, for nurturing, imparting the sense of love and humanity and caring for my son on the days when I was busy with my research work.

Last but not least, I owe a huge thanks to my outstanding and excellent teachers. My undergraduate research mentor, Dr. N. Kalaiselvi (CSIR-CECRI), inculcated the art of research methods in me, motivated me. It was those three years of research in her lab, working on Lithium batteries, that kindled my passion for research in electrochemistry. I thank my other

professors from CSIR-CECRI, Dr. V Yegnaraman, Dr. Sheela Berchmans, Dr. S Sathyanarayanan, Dr. S Syed Azim, Dr. J Mathiyarasu, Dr. G T Parthiban and Dr. N Lakshminarasimhan, who introduced electrochemistry, electrodics, electrocatalysis, materials science, energy devices and corrosion to me. With much gratitude, I also take this opportunity to appreciate the passion of my school teachers, who were more than happy to teach me after class hours, be it a one-on-one session or a quick visit to my home.

Gayathri Sridhar

Chapter 1
Introduction

1.1. Background

The engineering life of aluminium and its alloys is limited by their corrosion performance which causes premature failure by the loss of structural integrity. The nature of corrosion upon aluminium is predominantly localised. It often initiates as humble microscopic corrosion pits that subsequently grow into various types of macroscopic corrosion failures. Of the various forms of corrosion that develop from pits, environmentally assisted cracking (EAC) is more detrimental, resulting in the mechanical breakdown and fatigue failure of the material [Kondo 1989; Connolly et al. 2006]. Therefore, a critical understanding of the pitting susceptibility of aluminium alloys plays a vital role in material selection for various engineering applications and alloy development.

The parameter pitting potential (E_{pit}) is traditionally employed in determining the stable pitting susceptibility of alloy systems. However, over the past few decades, E_{pit} per se has been criticised as an inadequate parameter since it fails to determine the pitting kinetics and the pitting propensity of certain alloys [Cavanaugh et al. 2009; Gupta et al. 2012]. On the contrary, the investigation of metastable pitting characteristics from the measurable current transients recorded at anodic potentials below E_{pit}, has gained significance [Williams et al. 1994; Gupta et al. 2012] since the metastable and stable pit events follow the same growth law [Isaacs 1989; Pistorius et al. 1992]. The metastable pitting characteristics, viz., frequency, shape and charge accumulation of the current transients, have considerably advanced the knowledge on the mechanistic and kinetic aspects of stable pitting in addition to providing a quantitative assessment of the stable pitting susceptibility of alloy systems [Sato et al. 1998; Kim et al. 2007; Gupta et al. 2014].

The critical metastable pitting parameter that aids in estimating the pit size (r_{pit}) and thereby determining its stability [Buzza et al. 1995] from the so-called 'pit stability criterion' [Pride et al. 1994] is the charge accumulated by the current transients ($C_{transient}$). In a current transient trace (I vs t), $C_{transient}$ is determined by integrating the area under the I-t curve [Williams et al. 1994; Pride et al. 1994]. The distribution of r_{pit} grossly estimated using this method was found to be consistent with the distribution of the actual r_{pit} witnessed on a pitted stainless steel (SS) [Williams et al. 1994] and aluminium surface [Pride et al. 1994]; a fact which further promoted the relevance of $C_{transient}$.

1.2. Motivation:

Pistorius et al. [Pistorius et al. 1992] reported that the distribution of r_{pit} calculated from the $C_{transient}$ in SS was either underestimated or overestimated as compared to the distribution of the actual r_{pit} measured on the pitted surface. In aluminium and its alloys, the r_{pit} estimated from $C_{transient}$ is considered to be severely underestimated owing to the charge consumed by the copious hydrogen evolution (HE) occurring within the pits [Frankel 1998]. In pure aluminium, the ratio of HE current density (i_{H_2}) to the total anodic current density (i_{anodic}), i.e., i_{H_2}/i_{anodic} was reported to be 0.16 in $AlCl_3$ solutions using one-dimensional (1D) pits [Beck 1984]. This ratio for two-dimensional (2D) pits on aluminium tested in de-aerated 0.1 M NaCl was reported to range between 0.05 and 0.09 [Frankel 1990]. Pride et al. [Pride et al. 1994], through derivative approaches, showed that the HE within the pits in aluminium does not impart a significant error in the estimated metastable r_{pit}. However, several other works reported that such a discrepancy exists in aluminium alloys [Guan et al. 2014; Guan et al. 2015]. Considering the significant fraction of pit dissolution current lost to HE during stable pit propagation, incorporation of an excess charge (~16%) to that determined from $C_{transient}$ became a practice [Kim et al. 2007; Guan et al. 2016b].

The foregoing discussions do not provide an adequate understanding of the discrepancies (if any) between the actual and estimated metastable r_{pit} and V_{pit}. The primary issue therein is the basis of comparing the distribution of metastable r_{pit} rather than associating a current transient to its respective metastable pit event. Such investigations do not provide a precise understanding of the actual error in the estimated r_{pit} and V_{pit} associated with a single

current transient/metastable pit event. Besides, the incorporation of an additional 16% $C_{transient}$ to the measured $C_{transient}$ to account for the charge lost to HE (C_{HE}) during metastable pit growth based on the results derived from stable pit propagation studies is speculative. Cook et al. [Cook et al. 2012] showed that the HE induced noise in the current decreased progressively for the same anodic current density when the potential was progressively stepped down to the repassivation potential (E_r). This study validates that the rate of HE within the pits in aluminium is strongly dependent on the potential than on i_{anodic}. Therefore, incorporating the same value of i_{H_2}/i_{anodic} from the stable pit propagation studies conducted at potentials above E_{pit} to the metastable pit growth (performed at potentials below E_{pit}) could be erroneous. Further, other factors, apart from HE, could result in the inconsistencies witnessed between the estimated and actual metastable r_{pit}, of which the spatiotemporal evolution of pit events and pit geometry are a few to mention. These factors are commonly overlooked during the evaluation of the inconsistencies witnessed in the r_{pit} estimated from $C_{transient}$ and warrant meticulous investigation.

The question: "what is the reliability of the pit sizes analysed from the metastable pitting data in relevance to predicting the stable pitting susceptibility of alloy systems?" therefore remains unresolved. A deterministic conclusion in this regard requires the association of the current transients to their respective metastable pit events, which has remained elusive due to the dynamic nature of pitting that hampers its visualisation and subsequent mapping of its locations. Recently Sander et al. [Sander et al. 2020] performed an in situ investigation of metastable pitting in SS and reported that the actual metastable r_{pit} was smaller than that determined from the $C_{transient}$. They attributed the excess charge in $C_{transient}$ to the capacitive effect resulting from what they called 'the switching' of the surface condition related to local rupture of the passive film.

To date, no study has successfully addressed the issue concerning the discrepancy between the estimated and measured metastable r_{pit} by correlating the current transients to their respective metastable pit events in aluminium and its alloys.

1.3. Objective

The objective of this dissertation is to evaluate the error introduced by various factors on the estimation of metastable r_{pit} and V_{pit} from $C_{transient}$ by employing an in situ imaging technique to map the real-time evolution of metastable pit events.

1.4. Scope of the work

The scope of this work is to address the following objectives/questions to evaluate the reliability of estimating metastable r_{pit} and V_{pit} from $C_{transient}$.

(a) Develop an in situ investigation method to facilitate the correlation of the metastable pit events to their associated current transients.
(b) What is the fraction of pit dissolution charge lost to hydrogen evolution, i.e., C_{HE}/C_{pit}?
(c) Does the area under the $I-t$ curve, i.e., current transient, correlate with the actual mass loss at the pit site?
(d) Is a single current transient associated with a single discrete pit event or multiple co-occurring pit events?
(e) Does a subsequent current transient evolve from a pit event recurring at the same location or a discrete pit event evolving at a different location?
(f) Do the findings derived for questions (d) and (e) vary depending on the electrochemical (anodic/cathodic) nature of the second phase particles?

1.5. Thesis outline

This dissertation has seven chapters, including this chapter (Introduction).

- ***Chapter 1. Introduction:*** This chapter begins with a brief overview explaining the significance of the charge of the transient ($C_{transient}$) and the ambiguities related to estimating the metastable r_{pit} from $C_{transient}$. The motivation, objective and scope of the work are defined.

- ***Chapter 2. Literature review:*** This chapter provides a detailed review of the literature concerning the various stages of pitting corrosion witnessed in aluminium, followed by the different methods employed in investigating the same. Later, the merits of

metastable pitting studies are discussed with an emphasis on the importance of $C_{transient}$ in determining the stable pitting susceptibility of alloy systems. The contents of the chapter are finally summarised to identify the gaps in the existing literature. In this context, the problem statement is introduced.

- ***Chapter 3: Experimental methods:*** A detailed account of the materials, heat treatment procedures, electrode fabrication, electrochemical testing methods, in situ imaging setup and other experimental methods employed in performing the research described in this dissertation has been presented.

- ***Chapter 4: A novel approach for the in situ visualisation of metastable pitting events from hydrogen evolution:*** This chapter addresses the question (a) presented in the scope of this dissertation (Section 1.4). After a brief description of the background, this chapter presents the requirements, feasibility and limitations of the in situ investigation method adopted to map the metastable pit locations in situ.

- ***Chapter 5: In situ investigation on the role of hydrogen evolution on the estimated metastable pit sizes:*** This chapter addresses questions (b) and (c) presented in the scope of this dissertation (Section 1.4). After a brief introduction of the context of the problem, an extensive discussion on the calculation and implications of the fraction of pit dissolution charge consumed by HE, i.e., C_{HE}/C_{pit} is presented. The results are later validated by comparing the actual and estimated values of V_{pit} for a single discrete metastable pit event associated with a current transient.

- ***Chapter 6. The role of the spatiotemporal evolution of pit events on the estimated metastable pit sizes:*** This chapter addresses questions (d), (e) and (f) presented in the scope of this dissertation (Section 1.4). After a brief introduction of the background, an extensive evaluation of the error introduced by the spatiotemporal evolution of metastable pit events on the estimated r_{pit} is presented.

- ***Chapter 7. Summary and scope for future work:*** This chapter summarises the findings of the present work, presents a broader perspective and the challenges in this research work that allow for improved scope for future work.

Chapter 2

Literature Review

2.1. Aluminium and its alloys

Aluminium is the most widely used alloy system among the non-ferrous and light-metal alloy community. It is also the second most widely used alloy system after steel. According to the 2017 Niti Aayog document on 'Need for an Aluminum Policy in India', the annual consumption of aluminium (including scrap) in the world was 80 million tonnes with a global average of 11 kg per capita. Today, some of the leading manufacturers of aluminium, namely Hindalco (India), BALCO (India) and Alcoa (Australia), supply aluminium to cater to the various global engineering requirements. Aluminium finds application in industries ranging from large-scale sectors such as automobile, aircraft and defence to small-scale sectors related to manufacturing appliances and packaging. The pie chart in Figure 2.1 provides an understanding of the percentage consumption of aluminium across the various industrial sectors in India.

Aluminium exhibits a unique combination of properties that favour its utilisation in a wide range of engineering applications. Some of its remarkable properties are discussed below.

- ***High strength to weight ratio:*** Aluminium has a density of 2.7 $g.cm^{-3}$, which is three times lower than steel [Vargel 2004]. Pure aluminium is soft and ductile; commercially pure aluminium (AA1100) has a tensile strength of 90 MPa [Scamans et al. 2010]. However, when suitably alloyed and tempered, their mechanical properties can be augmented to meet specific engineering requirements. For instance, the tensile strength of fully work-hardened AA5456 is 385 MPa [Scamans et al. 2010], and age-hardened AA7068-T6511 alloy is 683 MPa [United et al. 2008]. Depending on the temper, aluminium is also ductile and

malleable such that it can be welded, bolted, riveted and brazed. The high strength to weight ratio of aluminium compared to steel provides economic benefits in reducing fuel consumption, handling, and shipment, making them suitable for automotive and aerospace applications. Up to 50% weight savings have been reported when steel is substituted with aluminium for Body-In-Weight (BIW) applications which amounts to a 20% to 30% reduction in the total vehicle weight along with other reduction opportunities [Cole et al. 1995]. In the present day, almost 80% of the commercial aircraft structures, such as the fuselage, engine turbines, wing panels, and cockpit instrumentation, are made from aluminium and its alloys.

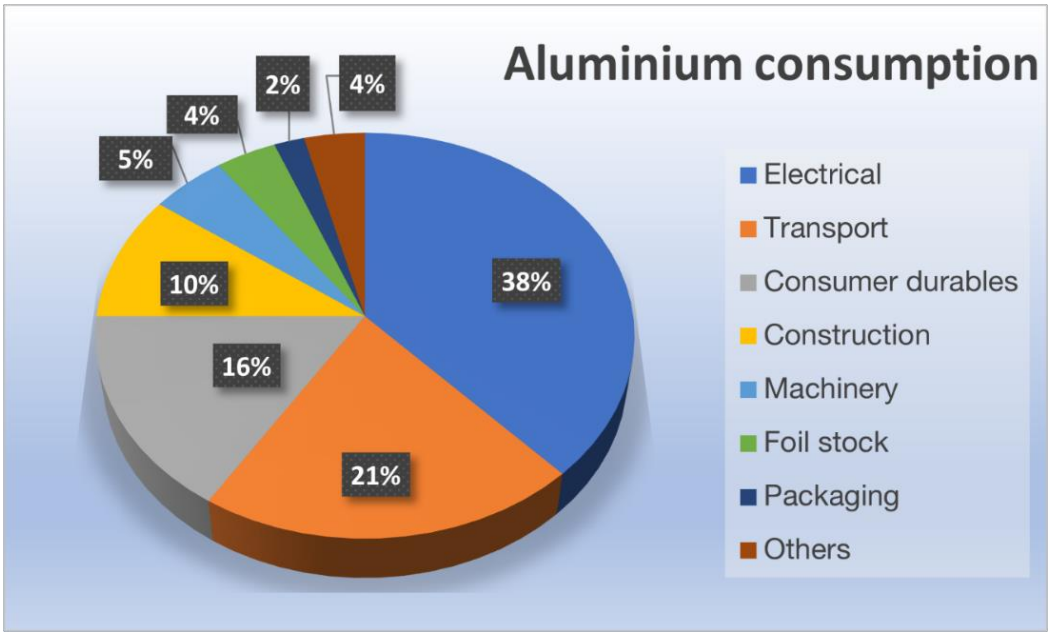

Figure 2.1. Pie chart describing the consumption of aluminium across various industrial sectors in India [Mishra et al. 2020].

- ***Corrosion resistance***: Aluminium tends to form a protective oxide film on its surface by a phenomenon termed passivity that prevents the dissolution of the underlying metal surface and provides excellent atmospheric and aqueous corrosion resistance. In the shipbuilding sectors, Al-Mg alloys (5XXX series) have efficiently replaced carbon steel due to their excellent corrosion resistance (corrodes over 100 times slower) coupled with the high strength to weight benefits (~ 60% weight reduction) [Romhanji et al. 2006]. However, the protectiveness or stability of the passive film on aluminium alloys varies depending on the environmental (concentration of aggressive species, temperature, pH) [Pride et al. 1994; Birbilis et al. 2008], metallurgical (alloying addition, precipitate size) [Birbilis et al. 2005;

Ralston et al. 2010] and mechanical factors. As discussed later in Section 2.2, the formation of such localised flaws in the passive film results in localised corrosion of aluminium alloys.

- ***Electrical and thermal conductivity:*** The high electrical conductivity of aluminium (63 – 57% IACS at 293 K [Scamans et al. 2010]) makes them suitable for application in power transmission cables as a substitute for copper. Aluminium also exhibits high thermal conductivity (214 $Wm^{-1}K^{-1}$ at 293 K [Scamans et al. 2010]), making them suitable for manufacturing cookware and other household appliances.
- ***Recycling:*** Aluminium can be efficiently recycled, with its percentage recycling ranging from 80% in the transportation sector to 65% in household applications, making them cost-effective [Vargel 2004].

With the recent advancements in additively manufacturing corrosion-resistant high strength aluminium alloys [Gharbi et al. 2018], the relevance of aluminium and its alloys will scale to embark on a new era of serving intricate and advanced engineering requirements.

2.2. Corrosion induced failure of aluminium – an overview

The failure of aluminium as an engineering material due to corrosion can be catastrophic. The numerous aircraft failures witnessed [Czaban 2018] signify the concern of aluminium corrosion as a potential threat to human safety. The estimated total annual cost of corrosion in the U.S. aircraft industry was reported as $2.2 billion, wherein the cost of corrosion maintenance alone was audited to be $1.7 billion [Koch et al. 2002]. The insidious nature of aluminium corrosion arises from its inherent tendency to undergo localised dissolution. The minuscule corrosion pits that form during the preliminary stage of corrosion are often covered with reflective pit covers [Frankel 1998] and corrosion products akin to the metal surface, leaving them visually undetected for maintenance. Figure 2.2 illustrates an overview of the corrosion-induced failure of aluminium as an engineering structure.

Localised corrosion upon aluminium initiates when the naturally protective passive film suffers local damages and exposes the underlying metal surface to the environment. The localised failure of the passive film occurs due to several factors such as the presence of inherent defects in the passive film, its exposure to aggressive species, mechanical rupture of the film or underlying microstructural heterogeneity that can locally alter the passive film

characteristics and induce depassivation [Szklarska-Smialowska 1999; Soltis 2015]. The time taken by an alloy to undergo passivity breakdown and commence localised nano-scale/micro-scale metal dissolution is termed the incubation period.

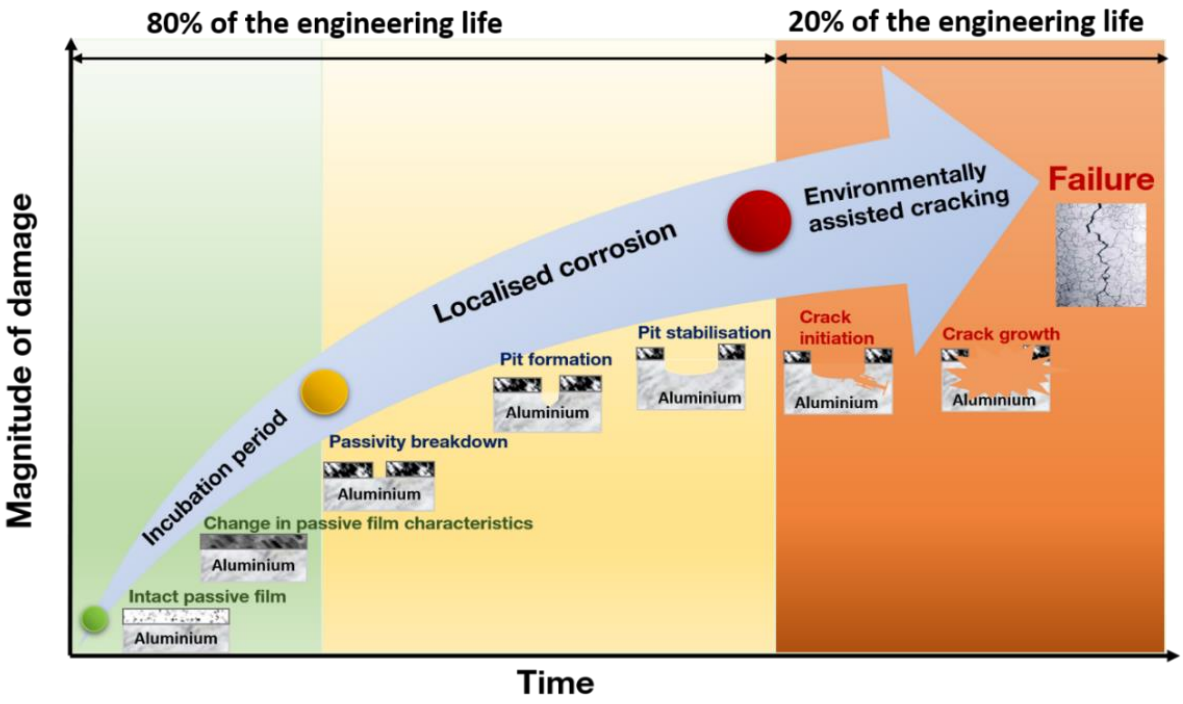

Figure 2.2. Overview of the corrosion-induced failure of aluminium as an engineering material [McCafferty 2003; Soltis 2015; Bobby Kannan et al. 2011].

In lieu of the protective passive film at localised locations, the underlying metal surface undergoes rapid dissolution owing to the high electronegativity of film-free aluminium (standard electrode potential = - 1.66 V_{SHE}) [Vargel 2004]. Such localised dissolution results in different forms of localised corrosion such as pitting corrosion when the occluded site forms on an open surface, crevice corrosion when such sites develop within a crevice and intergranular corrosion (IGC) when the dissolution occurs preferentially at the grain boundaries (GBs). The nano- or microscale localised dissolution may cease if the conducive chemistry, typically acidic pH, in the occluded site is lost and the passive film reforms, resulting in metastability [Siitari et al. 1982; Pride et al. 1994; Lim et al. 2016]. However, if the passive film fails to reform and the dissolving front propagates, developing the critical conditions (viz., critical pit depth and critical acidification [Pistorius et al. 1992; Pride et al. 1994]) necessary to facilitate the conservation of aggressive pit chemistry, the occlusion becomes a stable corrosion site. Subsequently, further dissolution becomes autocatalytic in nature [Baumgärtner et al.

1988; Frankel 1998; Lim et al. 2016]. The period ranging from the incubation of an occluded corrosion site until this stage associated with microscale dissolution is termed the period of localised corrosion.

Upon reaching a critical size such that a critical stress intensity factor (ΔK_p) is overcome [Kondo 1989], the micro-scale occluded corrosion sites transition to macro-scale cracks [Connolly et al. 2006], termed environmentally assisted cracking (EAC). Thereupon, depending on the crack growth kinetics, the structural failure of the material is imminent.

Typically, the period comprising pit incubation through localised corrosion accounts for ~ 80% of the engineering life expectancy of the material, while that related to crack growth and subsequent failure of the alloy forms only the remaining ~ 20%. Hence, to improve the engineering life expectancy of materials from a corrosion perspective, the factors relevant to maximising the period before crack initiation need to be understood. Efforts in this direction can be directed to investigating the pitting performance of alloy systems, as pitting corrosion bears a direct relationship with EAC [Kondo 1989]. Further, since corrosion pits and other forms of localised corrosion (crevice corrosion and IGC [Baumgärtner et al. 1988; Lim et al. 2016]) develop similar occluded chemistry, their investigation can provide critical mechanistic insights regarding the overall localised corrosion performance of the alloy system. The primary interest of this thesis is to understand the reliability of metastable pitting studies, which is a promising method employed to quantitatively determine the stable pitting susceptibility of alloy systems [Gupta et al. 2012] and understand the associated mechanistic and kinetic aspects thereof [Pride et al. 1994; Kim et al. 2007; Gupta et al. 2014].

2.3. Passivity

The phenomenon by which a specific class of metals develop protective surface film upon their interaction with the environment rather than undergoing dissolution is termed passivity. The protective film, typically nanometer-sized and predominantly comprised of oxides and hydroxides, confer immunity by stifling the dissolution of the underlying metal surface by acting as a kinetic barrier. Some of the spontaneously passivating alloy systems of engineering significance, apart from aluminium, include stainless steel (SS), titanium and nickel.

The phenomenon of passivity has been scientifically recognised since the 18th century. Lomonosov, Russia (1738), Wenzel, Germany (1782) and Keir, England (1790) documented the non-reactive nature of an iron surface when it was exposed to concentrated HNO_3 [Uhlig 1979]. Schonbein [Schönbein 1836] became the first person to term this phenomenon as "passivity". Nevertheless, the knowledge of the concept of passivity dates back to ancient civilisations. The Iron Pillar in New Delhi, India (Figure 2.3 (a)) is one of the oldest architectural marvels that serves as a classic testimony to this knowledge. Built by the blacksmiths of the imperial Gupta monarch, this structure has remained corrosion-resistant for over 1600 years. The superior corrosion performance of this structure is conferred by the multiple layers of protective iron oxide films that have formed upon its surface (Figure 2.3 (b)) [Balasubramaniam 2000].

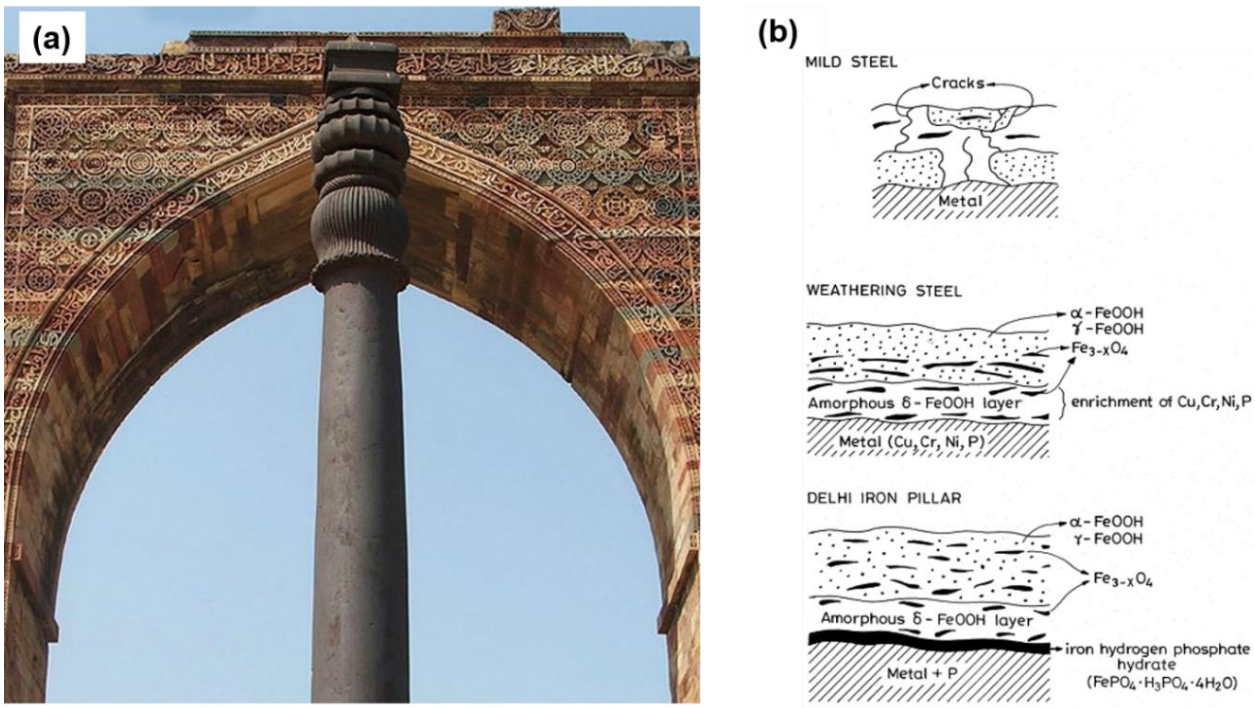

Figure 2.3. (a) A photograph of the Iron Pillar in New Delhi, India, (b) comparative study of the various passive layers formed upon mild steel, weathering steel and the Delhi Iron Pillar steel [Balasubramaniam 2000].

Passive films form natively on the metal surface and confer corrosion resistance. However, not all films that form on a metal surface are passivating. For instance, the metal ions dissolving away during active corrosion may deposit back on the surface as a salt film when the electrolyte is supersaturated or the salt formed is sparingly soluble. These salt films are

non-passivating as they are non-continuous, crystalline and weakly adhered to the metal surface [Burstein 1994]. A typical example of this case is the formation of a bluish-green patina on the corroded copper pipes. The spontaneously passivating aluminium also precipitates non-passivating salt films during their active dissolution [Beck 1984]. These salt films promote and regulate active corrosion within the occluded pit cavities, while passive films offer barrier-like corrosion protection by preventing the dissolution of the underlying metal surface [Alkire et al. 1988].

2.3.1. Pourbaix diagram

The thermodynamic conditions that favour the stability of passive films can be investigated from the Pourbaix diagram, which is a plot of the potential versus pH constructed using the thermodynamic laws of the Nernst equation and solubility products [Pourbaix 1966]. It is employed in determining the chemical and electrochemical equilibria between the metals and their oxides when in contact with water and thereby defines the zones of corrosion, passivity and immunity.

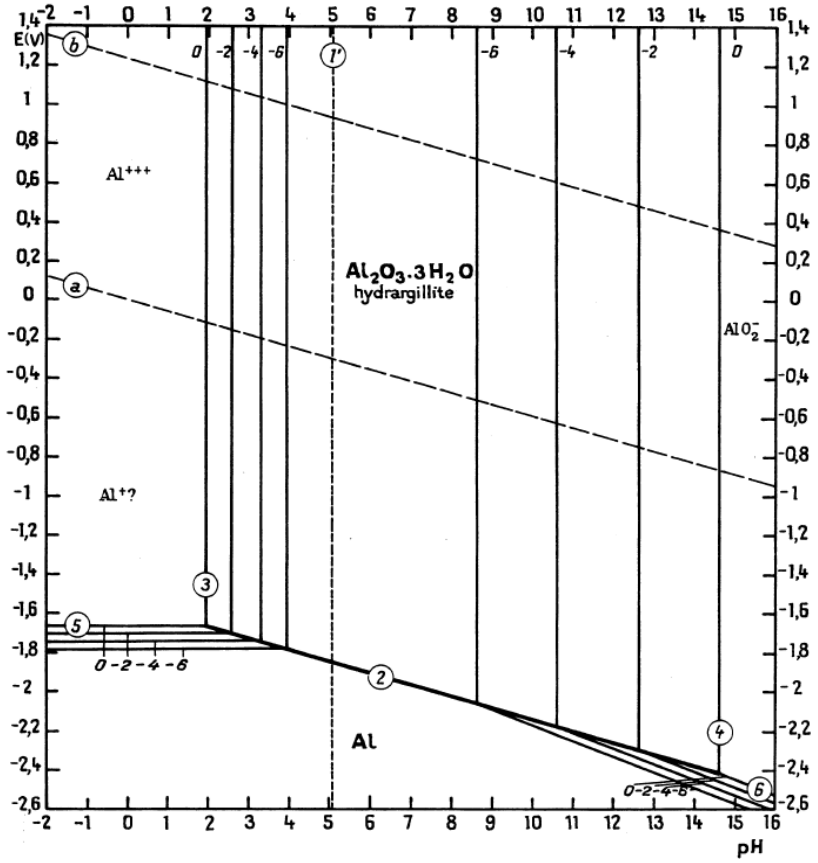

Figure 2.4. The Pourbaix (E-pH) diagram of aluminium [Pourbaix 1966].

The E-pH diagram of aluminium (Figure 2.4) [Pourbaix 1966] reveals the following facts:

- Passivity in aluminium is conferred by the formation of hydrargillite ($Al_2O_3.3H_2O$).
- The passive films that form upon aluminium are amphoteric in nature; i.e., they are unstable in acidic and alkaline solutions.
- In acidic pH, Al dissolves as Al^{3+} and evolves hydrogen, while in alkaline pH, Al dissolves as AlO^{2-}.
- Within the pH range 4 – 9, aluminium is covered with a passivating oxide film, wherein its composition, structure, porosity, thickness and extent of hydration depends on the combination of potential and pH.

2.3.2. Characteristics of the passive film

Aluminium undergoes spontaneous passivation and forms a hydrous oxide film upon its exposure to aqueous solutions. A direct investigation of the precise characteristics of the passive film has remained elusive owing to its small thickness that intercepts with the interphase (metal and electrolyte) and the presence of high electric fields across this thickness [Burstein 1994].

The typical composition of the initial oxide film that forms on aluminium upon its exposure to water has been reported as pseudo-boehmite (AlOOH) [Vedder et al. 1969], which has a lamellar structure [Boer et al. 1970] with its lamella oriented perpendicular to the metal surface [Hart 1957]. This layer is highly porous on the surface exposed to the electrolyte and dense near the metal-oxide interface [Alwitt 1974]. Upon prolonged exposure to water, a bayerite ($Al(OH)_3$) film forms on the pseudo-boehmite film [Hart 1957].

The structure, thickness and physicochemical properties of the passive film can vary depending on the electrolyte and exposure temperature [Smialowska 1999]. For instance, the anodic films formed upon exposing aluminium to borate and tartaric acid were thin, dense, coherent, and amorphous, while those formed in sulfuric and phosphoric acids were thick, porous, and crystalline [Szklarska-Smialowska 1999]. The passive film characteristics also vary depending on the microstructural heterogeneity introduced by alloying additions, micro-

defects (vacancies, voids) and macro-defects (shape of the intermetallics, inclusions) [Szklarska-Smialowska 1999].

The passive film upon aluminium is known to exhibit very low electronic conductivity, limiting the occurrence of redox reactions on its surface [Szklarska-Smialowska 1999]. However, Sato [Sato 1978] reported that the redox reactions could occur on sufficiently thin passive films by electronic tunnelling. The passive film on aluminium has a bandgap of ~ 3 eV [Menezes et al. 1989] and exhibits semiconductive properties depending on the alloy composition and environment [Szklarska-Smialowska 1999]. The passive films with n-type semiconductive properties promote pitting corrosion [Bianchi et al. 1970].

The pH of zero charge (pH_{zc}) or the iso-electric point, which is the pH at which the charge on the passive film is zero, is an important parameter that determines the susceptibility of a passive metal surface to localised corrosion. The pH_{zc} of the air-formed passive film on aluminium upon its exposure to aqueous solutions is 9.5 [McCafferty et al. 1997]. Therefore, in neutral pH solutions, the passive film upon aluminium bears a positive charge that enhances its affinity to aggressive anions such as halides. This phenomenon forms the basis behind the breakdown of passivity and subsequent localised corrosion in aluminium [McCafferty 2003].

2.4. Breakdown of passivity

The failure of passive film at localised locations exposes the underlying aluminium surface to the environment resulting in its rapid dissolution and generation of acidity that curbs the passive film reformation and promotes sustained dissolution [McCafferty 2003]. Following is a brief overview of the various theories concerning the localised breakdown of passivity in aluminium (Figure 2.5).

2.4.1. Penetration mechanism

The positive charge bestowed by the pH_{zc} of the passive film upon aluminium facilitates the adsorption of aggressive anionic species (such as Cl^-, Br^- and I^-) to its surface. Upon adsorption, these anions penetrate the film at the film imperfections under the influence of a high electric field (~ 10^6 $V.cm^{-1}$) [Evans 1927; Hoar et al. 1965] and reach the metal-oxide (M/O) interface, inducing aluminium dissolution. The incorporation of such anions into the

passive film is regarded to facilitate higher ionic conductivities along the penetration paths and result in an autocatalytic process. Recently, Natishan et al. [Natishan et al. 2014], in their review, validated this mechanism with their finding that the Cl^- ions can incorporate and remain mobile in the air-formed and anodically formed films of aluminium.

Though the penetration model could successfully explain the concept of E_{pit} and induction time (t_i), it does not address the dynamic electrochemical noise generated during metastable pitting and the explosive growth of pits above E_{pit} [Soltis 2015].

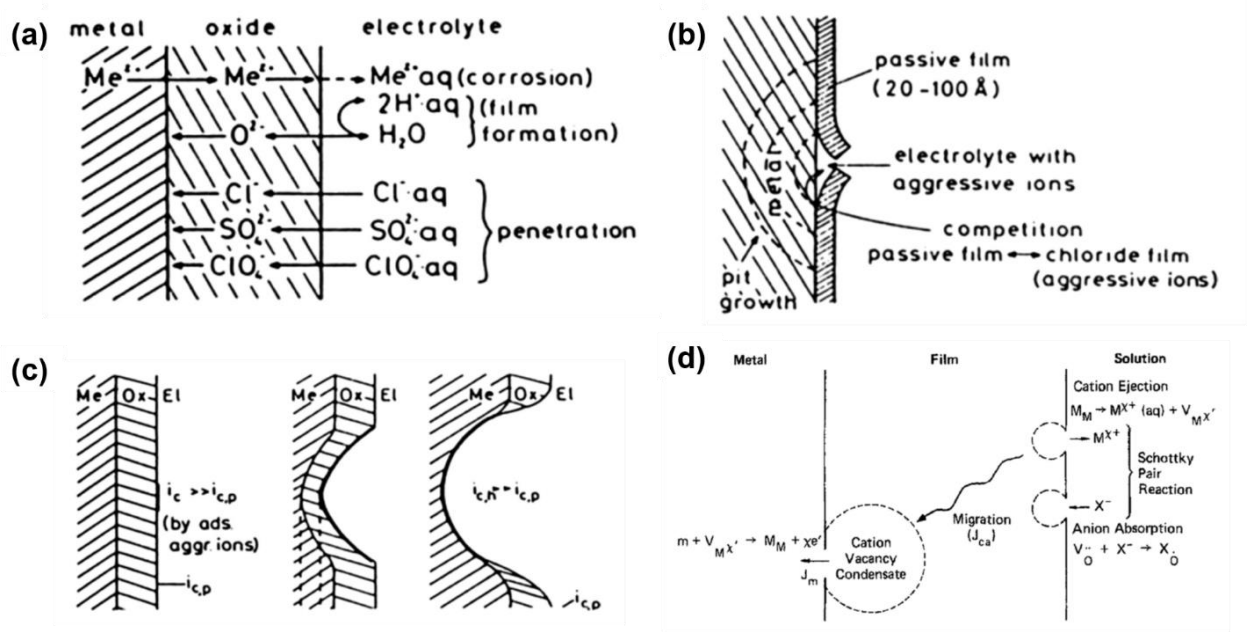

Figure 2.5. Schematic illustration of the various models for passivity breakdown (a) penetration mechanism [Bohni 1987], (b) film breakdown mechanism [Bohni 1987] (c) adsorption mechanism [Bohni 1987] and (d) point defect model (PDM) [Urquidi et al. 1985].

2.4.2. Point defect model (PDM):

The point defect model (PDM) intends to explain the mechanism of passive film growth by the mobility of vacancies within the passive film, particularly at the sites of film imperfections induced by GBs, dislocations or inclusions [Soltis 2015]. The model assumes that the metal cations migrate from the M/O interface to the film-solution interface while the oxide vacancies incorporated with Cl^- ions move in the opposite direction under the influence of a potential drop (ϕ). The sluggish mobility of the vacancies into the metal phase results in their accumulation at the M/O interface, inducing stresses and the subsequent breakdown of

the passive film. An extension of this model results in the well-known semi-logarithmic relationship between E_{pit} and $[Cl^-]$ (shown in Equation 2.1, wherein A and B are constants).

$$E_{pit} = A - Blog[Cl^-] \qquad \textit{Equation 2.1}$$

The limitation of this model resides in the utilisation of linear transport equations for the migration of species under high electric fields (10^6 V.cm^{-1}) instead of the characteristic exponential dependence [Strehblow 1984, 2002]. Further, since PDM was a deterministic model, it could not explain the current fluctuations associated with metastable pitting.

2.4.3. Film breakdown mechanism

The film breakdown mechanism assumes that the internal stresses prevalent within the passive film [Evans 1960] induce cracks or physical discontinuities (blisters) that allow direct access of the anions to the underlying metal surface. In the absence of aggressive species, these damages are considered to self-heal. Sato showed that at a critical film thickness (δ_{crit}), the film pressure induced by the electric field across the film (electrostriction) and surface tension would exceed the mechanical breakdown stress of the film, resulting in its rupture and pit initiation [Sato 1971]. The δ_{crit} was shown to decrease either with increasing field strength or decreasing surface tension which was facilitated by the adsorbed Cl^-, resulting in pitting [Sato 1982]. In aluminium, blistering due to hydrogen evolution occurring beneath the passive film was reported to induce mechanical rupture of the film, resulting in pit nucleation [Bargeron et al. 1980a; Natishan et al. 1989].

2.4.4. Adsorption mechanism

The adsorption mechanism [Kolotyrkin 1963; Hoar et al. 1967] postulates that the adsorbed Cl^- ions catalyse the dissolution of metal cations from the oxide film by forming transient complexes, leading to localised thinning and breakdown of the passive film. Such passivity breakdown in aluminium is considered to occur by forming soluble metal chloride salts upon the adsorption of Cl^- to the hydrated oxide surface [Foroulis et al. 1975].

Though the adsorption mechanism successfully explained the increase in t_i with the film thickness, it fails to explain the dynamic electrochemical noise generated during metastable pitting.

2.4.5. Localised acidification theory

Localised acidification theory, based on the pit stability work of Galvele [Galvele 1976; Galvele 1981], assumes that a combination of electrolyte penetration through the passive film and the rate at which the metals can dissolve play a critical role in the pit nucleation. This model successfully explained the phenomenon of metastable pitting wherein the metal at the locations of the cracks in the passive film is considered to undergo repassivation if critical acidification is not established. The model also explained the dependence of E_{pit} on $[Cl^-]$ and indirectly the dependence of E_{pit} on film thickness by the concept of critical pit depth. However, the model fails to explain the concept of t_i.

2.4.5. Voids at the M/O interface

This model explains that the pit nucleation in aluminium is assisted by the formation of physically or chemically distinct precursor structures such as voids or pores upon the adsorption of Cl^- to the passive film [Zavadil et al. 2003, 2006; Huang et al. 2004a; Huang et al. 2004b]. The formation of nanoscopic voids is assisted by the cation and anion vacancy saturation depending on the ionic transport properties of the oxide film when it is polarised below E_{pit}. Such nanoscopic void formation was reported to be independent of the underlying metal microstructure [Zavadil et al. 2003, 2006]. A faster transport of the dissolved cations in the intergranular boundary resulted in the formation of voids at the M/O interface, which upon growth, induced stresses and induced localised depassivation [Marcus et al. 2008]. This model, however, does not explain the passivity breakdown in alloys with an amorphous passive film [Di Quarto et al. 2004].

2.5. Pitting corrosion

Pitting corrosion is the accelerated localised dissolution of metals within occluded sites where the passive film had undergone local failure. Pitting corrosion progresses sequentially

by three stages, namely: pit nucleation, metastable pitting and stable pitting. Figure 2.6 provides a schematic illustration of the various stages of pitting corrosion in aluminium and its alloys.

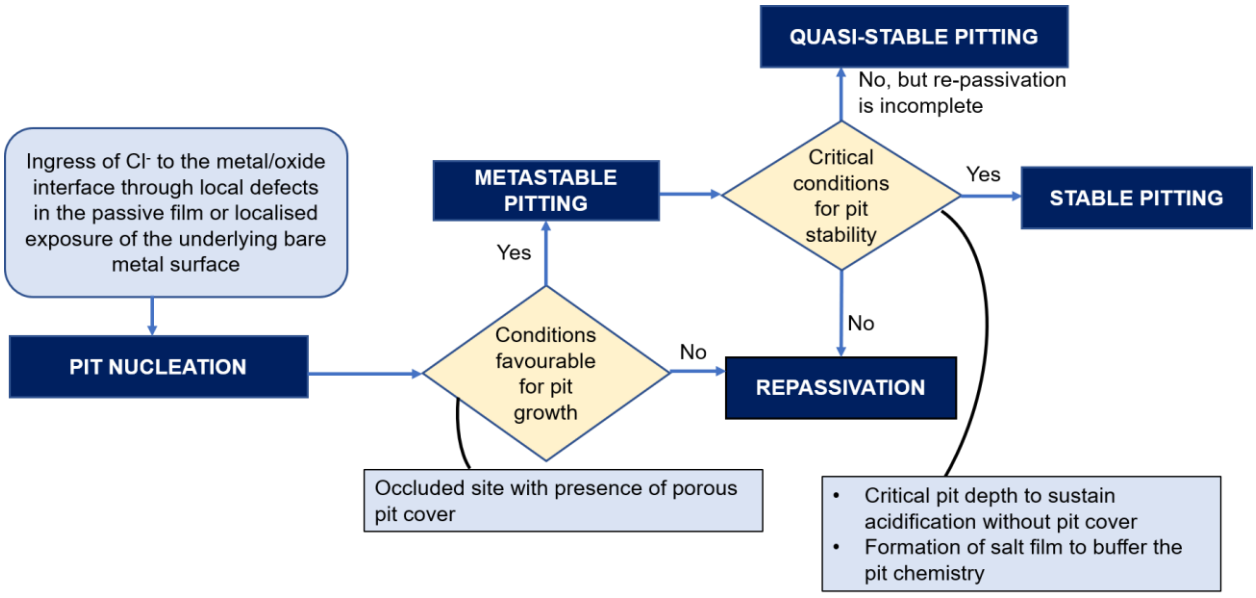

Figure 2.6. The various stages of pitting corrosion in aluminium and its alloys [Soltis 2015].

2.5.1. Pit nucleation

Passivity breakdown in aluminium occurs either by the mechanical breakdown of the passive film or chloride assisted penetrative depassivation at localised locations [Soltis 2015], as discussed in Section 2.4. Localised depassivation exposes the underlying aluminium to the environment. Bare aluminium, being highly electronegative, undergoes rapid dissolution resulting in trenches termed corrosion pits. Water that ingresses at the M/O interface acts as the electrolyte to support this dissolution [Szklarska-Smialowska 1999]. The Cl^- assisted reactions at the M/O interface result in the hydrolysis of Al^{3+} ions, resulting in the generation of acidic pH within the pit, inducing blisters. [Bargeron et al. 1977; Bargeron et al. 1980b; Natishan et al. 1989]. Beck et al. reported that the current densities at a latent pit nucleus of 10 A° could be as high as 10^3 to 10^6 $A.cm^{-2}$ [Beck et al. 1979], a value that can result in rapid acidification within the nascent pits. The hydrogen pressure in the blister induces its rupture resulting in the formation of a corrosion pit. The internal hydrogen pressure required to rupture an oxide film thickness of 100 A° was reported as 1.58 atm [Natishan et al. 1988]. McCafferty calculated that the acidic pH within the corrosion pit associated with this pressure ranged between 0.85 to 2.28 [McCafferty 2003].

2.5.2. Metastable pitting

Metastable pitting is the second stage of pitting corrosion wherein the nucleated corrosion pits that grow may fail to attain stability and undergo repassivation. Every nucleated pit grows through a metastable pitting stage despite becoming metastable or stable. This fact is evident from the same growth laws they follow during the initial stages of pit growth [Isaacs 1989; Pistorius et al. 1992]. As discussed in Section 2.5.1, the high dissolution rates, homogeneous chemical reactions and restricted mass transfer within the pit anolyte result in an acidic pH within the nucleated pit. The driving force critical to sustaining any further pit dissolution resides in the combined action of a large potential difference (ϕ) across the pit and conservation of acidity within the pit to prevent its repassivation. The pit covers and salt films assist in establishing these conditions by providing the necessary ϕ and constricting the migration of the aggressive chemistry out of the pit. Upon failing to maintain such critical pit growth conditions, the pits undergo repassivation and the phenomenon is termed metastable pitting.

Metastable pitting characteristics are investigated in the passive regime of an alloy system at anodic potentials below E_{pit}. Metastable pitting is characterised by the appearance of current transients during potentiostatic testing [Pride et al. 1994; Gupta et al. 2012] and potential transients in the active direction during freely corroding conditions [Frankel 1998]. Burstein et al. described such fluctuations as the major source of true passivity breakdown [Burstein et al. 1996a]. The frequency, shape, lifetime and charge accumulation of such current transients have been employed in evaluating the mechanistic, kinetic [Pride et al. 1994; Kim et al. 2007; Sato et al. 1998; Gupta et al. 2014] and quantitative aspects of the stable pitting susceptibility of alloy systems [Gupta et al. 2012].

Mechanisms of pit repassivation

Pit covers are the remnants of the undermined passive film present over the pit mouth [Burstein 1994; Frankel et al. 1987; Isaacs 1989; Isaacs et al. 1972]. The layer that precipitates above the pit when the concentrated acidic pit anolyte meets the relatively dilute bulk solution can also act as a pit cover [Frankel 1998]. The pores in the pit covers provide the ohmic resistance necessary to furnish the potential difference (ϕ) across the pit and stabilise its dissolution [Vetter et al. 1974]. Pit covers also act as diffusion barriers for the transport of

aggressive pit anolyte out of the pit and thereby aids in conserving the aggressive pit chemistry. The rupture of the pit covers may be driven either by the osmotic pressure [Natishan et al. 1989] or the hydrogen pressure within the pit that causes blisters in the case of aluminium (Figure 2.7). The rupture of pit covers results in pit repassivation due to the loss of the diffusion barrier to conserve the aggressive pit chemistry [Frankel et al. 1987].

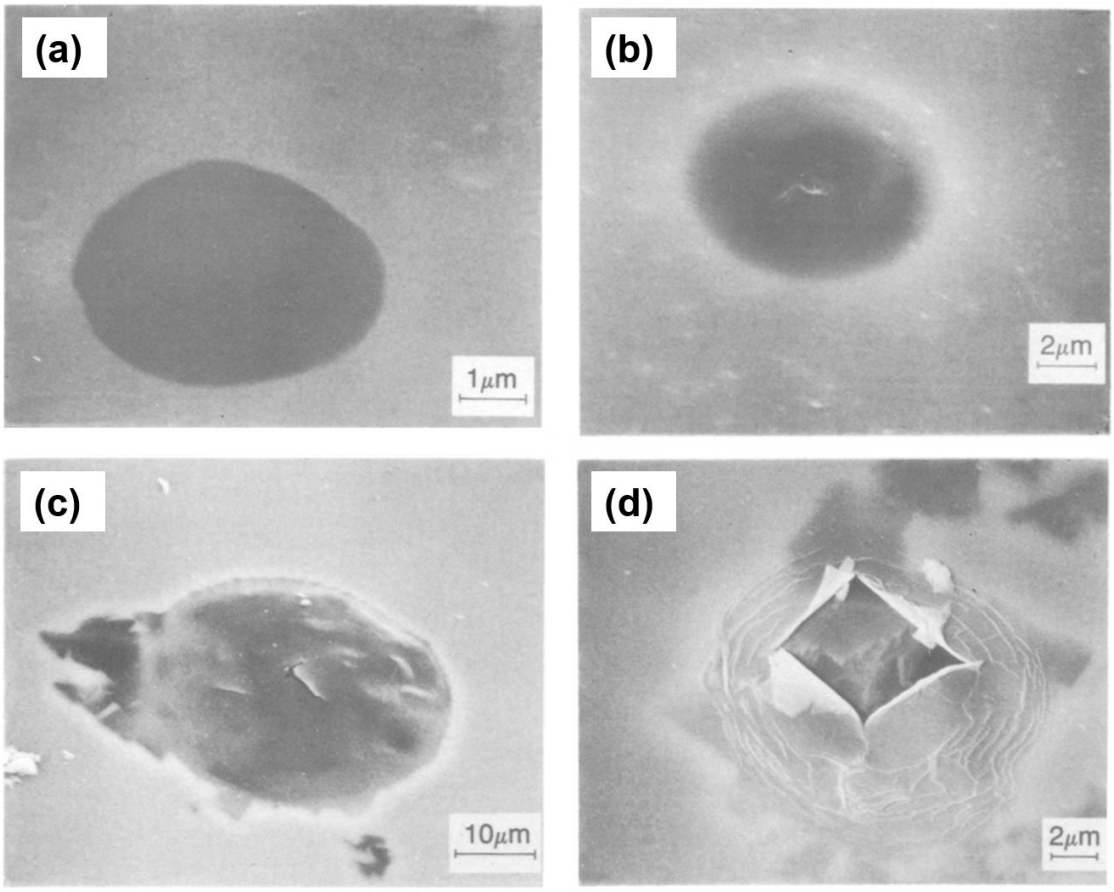

Figure 2.7. The various stages of blistering in aluminium [a] stage 1, [b] stage 2, [c] stage 3 and [d] stage 4 [Natishan et al. 1989].

Salt films are the thin layers of corrosion products that precipitate within the pit interior when the concentration of the dissolved metal cations in the pit anolyte exceeds supersaturation, especially at high anodic potentials [Isaacs 1973; Beck 1990]. The formation of such quasi-thermodynamic salt films has been associated with a characteristic potential such that metastable pitting does not take place below this potential [Frankel et al. 1987; Hunkeler et al. 1987; Beck 1990]. Beck reported that the salt film precipitation occurred when the limiting current density (i_{lim}) was lesser than the ohmically-controlled current density (i_{Ω}), i.e., $i_{lim} < i_{\Omega}$ and repassivation occurred when $i_{lim} \geq i_{\Omega}$ due to the salt film dissolution [Beck

1990]. The time required for the precipitation of the salt film (t_{salt}) can be calculated using Sand's equation, as shown in Equation 2.2.

$$I\sqrt{t_{salt}} = zF\sqrt{\pi D_{met}\frac{\Delta C}{2}} \qquad \textit{Equation 2.2}$$

wherein ΔC is the difference in the concentration between the supersaturated pit anolyte and the bulk electrolyte and D_{met} is the diffusivity of the metal cation. Salt films support the diffusion-controlled propagation of pits [Frankel et al. 1987; Pistorius et al. 1992]. Some researchers consider salt films as a necessary aspect for the transition of pits from metastability to stability [Vetter et al. 1974; Beck 1990]. Vetter et al. reported that the ϕ lost during the rupture of pit cover is recovered by the salt film precipitated within the pit resulting in its stabilisation [Vetter et al. 1974]. Cook et al. showed that even a slight drop in the salt concentration below its saturation level could result in the repassivation of the crystallographic tunnels that form within the pits in aluminium [Cook et al. 2012]. The threshold concentration for the transition of pit growth from ohmically-controlled crystallographic morphology to diffusion-controlled electropolished morphology was reported as 90% saturation concentration [Cook et al. 2002].

While the loss of pit covers and salt films are regarded as the primary factors that govern repassivation, other factors such as the metallurgical aspects and pit geometry also play a vital role in inducing pit repassivation. Corrosion pits in alloys often initiate at the second phase particles due to micro-galvanic coupling with the matrix [Birbilis et al. 2005]. The second phase particles that are anodic to the matrix undergo dissolution and result in deep pits, while the cathodic entities promote matrix dissolution and result in circumferential pits. Ralston et al. reported that the second phase particles stop acting as distinct electrochemical entities below a critical precipitate size [Ralston et al. 2010], signifying the vital role of the metallurgical factors in pitting corrosion. Repassivation also occurs when the second phase particles undergo annihilation before generating the critical pit chemistry [Burstein et al. 2001]. The pit geometry is another factor that plays a critical role in pit repassivation. Laycock et al. demonstrated that the repassivation of metastable pits in SS depended on the structural development of the pits rather than the collapse of the pit cover [Laycock et al. 2001b].

Pit stability criterion

Based on the concept of Galvele's localised acidification theory [Galvele 1976; Galvele 1981], the pit stability criterion was proposed. According to the pit stability criterion, a critical combination of pit depth (r_{pit}) and pit current (I_{pit}) is necessary for a pit to develop the acidic pH required to attain stability. In SS, Williams et al. proposed that for a pit to transition from metastability to stability, the condition I_{pit}/r_{pit} > 40 mA.cm^{-1} should be satisfied [Williams et al. 1994]. Pistorius et al. showed that the metastable pits that exceeded the product $i_{pit}.\, r_{pit}$ > 3 mA.cm were capable of attaining stability by withstanding the loss of pit cover in SS [Pistorius et al. 1992]. Their work also showed that the transition of pits from metastability to stability was marked by a change in the linear dependence of $i_{pit}.\, r_{pit}$ to a constant value. The pit stability criterion proposed for SS was later extended to aluminium by Pride et al. [Pride et al. 1994], who suggested that the transition of pits from metastability to stability occurred upon the satisfaction of the criterion $I_{pit}.\, r_{pit}$ > 10^{-2} A.cm^{-1}.

2.5.3. Stable pit propagation

The pits that sustain the critical conditions necessary for their propagation during the metastable pitting stage reach a critical depth sufficient to conserve the aggressive pit chemistry even in the absence of pit covers. At this stage, the pit is "autocatalytic" in nature [Hoar 1937]. A brief overview of the various models for stable pit propagation is presented below.

Ohmically controlled pit growth

Pickering et al. [Pickering et al. 1972] and Frankenthal et al. [Frankenthal et al. 1972] speculated that stable pit propagation occurs under ohmic control. They reported that the pit bottom potential (E_{bottom}) of an actively corroding pit would be relatively electronegative even at high anodic potentials and thereby promote stable pitting. However, from their calculations of ϕ and ionic concentrations as a function of pit depth, they found that the calculated ϕ was insufficient to drive pitting and concluded that the hydrogen bubble provided the necessary ϕ. The model was considered flawed as it predicted an increase in pH within the pit anolyte, which is contradictory to the conventional wisdom that the pH within the pit is acidic [Soltis 2015].

Diffusion controlled pit growth

It is widely accepted that stable pit propagation occurs under diffusion control [Tester et al. 1975; Isaacs 1973; Novakovski et al. 1966] due to high rates of anodic dissolution. Using modelling, the evolution of pit depth and width, studied by Scheiner et al., showed that stable pit propagation is governed by a diffusion-controlled mechanism [Scheiner et al. 2007, 2009].

Mixed ohmic and diffusion-controlled growth

Some researchers consider that the stable pit growth transitioned from ohmic control to diffusion-control [Frankel 1990; Beck 1984]. The potential at which this transition occurs is termed the transition potential [Laycock et al. 1997, 1998b]. Laycock et al. determined the transition potential from the polarisation curve and later using Equation 2.3 with artificial pit electrodes of SS [Laycock et al. 1997, 1998b].

$$E_T = E_{corr} + b_a \, log \frac{i_{lim}}{i_{corr}} + i_{lim} R_{int} \qquad \textit{Equation 2.3}$$

wherein E_T is the transition potential, E_{corr} is the corrosion potential, b_a is the anodic Tafel slope, i_{lim} is the limiting current density, i_{corr} is the corrosion current density and R_{int} is the solution resistance within the pit. The transition potential was independent of the passive film characteristics indicating that it is a strong function of pit propagation than pit nucleation [Laycock et al. 1998b, 2001a; Burstein et al. 2009].

Localised acidification

Galvele suggested that the stable pit propagation is driven by localised acidification and calculated the minimum degree of acidification required to attain and sustain stable pit growth [Galvele 1976]. The model adopted a uni-directional pit geometry and assumed that the metal dissolution was followed by hydrolysis, and the transport of species was governed by Fick's first law. Their model presented a simplified version wherein complexing reactions and further degrees of hydrolysis were ignored. The bulk solution was treated as a supporting electrolyte. Their study revealed a critical value of $r_{pit}.i$ (wherein r_{pit} is the pit depth and i is the current density at the pit bottom) to achieve the critical pH necessary to sustain the pit dissolution. Galvele further improved this model by including the reactions pertaining to hydrolysis and the precipitation of corrosion products [Galvele 1981].

Crystallographic tunnelling

Pitting corrosion in aluminium is known to propagate by the accumulation of local tunnelling events termed crystallographic tunnelling (Figure 2.8) [Edeleanu 1960; Nisancioglu et al. 1978; Kaesche 1990], which occurs when the current available for dissolution becomes insufficient to grow a conventional hemispherical pit [Newman 1995].

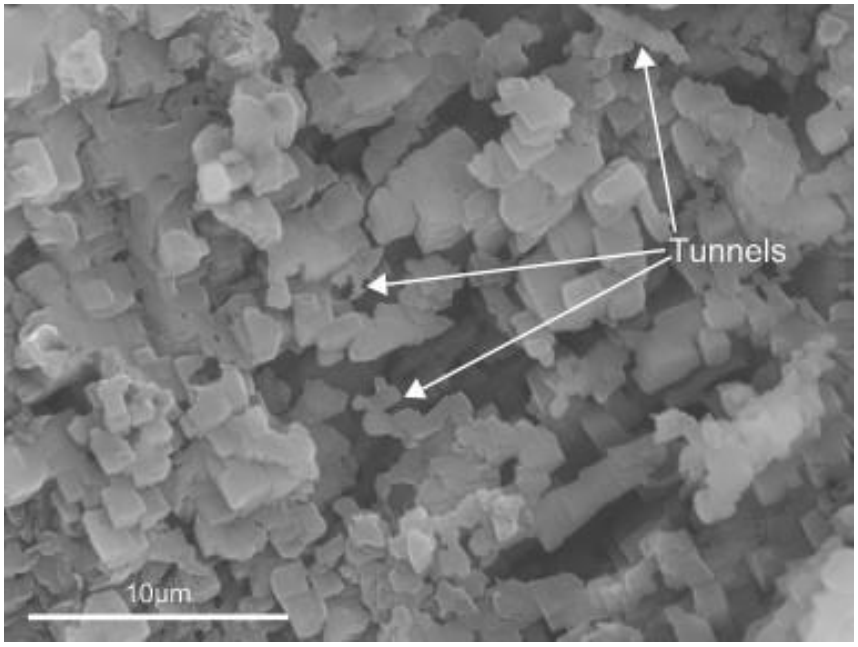

Figure 2.8. A resin replica demonstrates the evidence of crystallographic tunnelling in AA5083 [Moore et al. 2008].

During tunnelling, the chemistry within the individual tunnels could be more aggressive than the average chemistry present within the entire hemispherical envelope of the pit. The active tunnel tips may develop current densities as high as 30 $A.cm^{-2}$, while their walls may remain passive due to the reformation of passive film or precipitation of a salt film [Soltis 2015]. The tunnels also respond to the reduction in currents by narrowing their propagation front [Hebert et al. 1988; Alwitt et al. 1990]. Kaesche described that a passivated tunnel would dissolve again when the electrolyte retained within the tunnels gets enriched with aluminium halide [Kaesche 1990]. Many such tunnels may later coalesce to form larger tunnels.

The pit dissolution at the propagating front is driven by mass transport through a thin salt film which provides the ϕ and conserves the critical chemistry necessary for the tunnel dissolution just above the salt film. Some researchers argue that the tunnel tip grows under ohmic control [Hebert et al. 1988], while others consider the growth to be under diffusion control [Goad 1996]. Burstein et al. reported that the individual crystallographic tunnels grow

under diffusion control, though the entire hemispherical pit in which the crystallographic tunnelling occurs would follow an ohmic pit growth law [Burstein et al. 1996b].

2.6. Role of alloying additions

Alloying followed by ageing and/or work hardening treatments and the incorporation of impurities during the manufacturing processes impart heterogeneous microstructures comprising precipitates, constituent particles and dispersoids in aluminium alloys [Scamans et al. 2010]. These second phase particles exhibit electrochemical properties significantly different from the matrix [Buccheit 1995], rendering them either anodic or cathodic to the matrix, resulting in micro-galvanic coupling and subsequent localised corrosion [Birbilis et al. 2005]. Unlike pure aluminium, wherein pitting is primarily governed by the passive film characteristics [McCafferty 2003], pitting in aluminium alloys is driven by the type of alloying addition [Szklarska-Smialowska 1998] or impurity and the (electrochemical and metallurgical) characteristics of the second phase particles they engender [Birbilis et al. 2005].

In their review, Smialowska suggested that based on the investigation of homogeneous binary metastable aluminium alloys, the mechanism of inhibition of pit growth due to the alloying additions could be classified as follows: (a) solubility of passive film in acidic solutions, (b) enrichment of solute in the passive film and (c) retarding of pit dissolution kinetics [Szlarska-Smialowska 1998]. Smialowska discussed the first mechanism by demonstrating the correlation between the solubility of oxidised species of the alloying element at acidic pH and the pitting potential [Szklarska-Smialowska 1992]. Many researchers discussed the mechanism of passive film enrichment by the alloying elements [Frankel et al. 1990; Davis et al. 1990; Inturi et al. 1993]. The addition of Ta, Mo and Cr were considered to enrich the passive film resulting in the ennoblement of E_{pit} [Szklarska-Smialowska 1998]. However, subsequent works using thin films [Frankel et al. 1993] showed that the alloying additions influenced the pit dissolution kinetics more than the passive film characteristics. Several studies focused on understanding the mechanism of how the alloying additions drive pit dissolution kinetics. Sato et al. 1998 (a) suggested that Zn in the solid solution activated aluminium for pit propagation but did not influence pit nucleation. In another study, they suggested that the presence of Mg in solid solution did not activate aluminium but enhanced its repassivation by preferential dissolving resulting in aluminium enrichment [Sato et al. 1998 (b)]. The presence of Cu in the solid solution increases E_{pit} and E_r [Yasuda et al. 1990]. Kim

et al. using metastable pitting studies, attributed the better pitting performance of Al-Cu homogenised alloy to the two stages of repassivation [Kim et al. 2007].

Detail investigation of the electrochemical characteristics of the various second phase particles present in commercial aluminium alloys by Birbilis et al. 2005, emphasises that a first-order classification of the second phase particles as anodic and cathodic is insufficient. In fact, several second phase particles, including Al_3Fe [Nisancioglu 1990], Mg_2Al_3 [Liu et al. 2010] and Al_2CuMg (S phase) [Hashimoto et al. 2016] are known to undergo incongruent dissolution and therefore alter the pitting characteristics. The electrochemical nature of the second phase particles also influences the pit morphologies. The presence of noble second phase particles results in circumferential pits due to the undermined matrix surrounding them, whereas the selective dissolution of anodic entities results in deep pits [Buchler et al. 2000; Ilevbare et al. 2004; Schneider et al. 2004]. Ralston et al. 2010 showed that the precipitate in Al-Cu-Mg alloy ceased to act as a distinct electrochemical entity below a critical precipitate size. A similar conclusion and the role of Cu in promoting grain refinement in Al-Mg-Si alloy was discussed by Kairy et al. 2016.

2.7. Investigation of pitting corrosion

The pitting susceptibility of alloy systems may be investigated using electrochemical, chemical or natural exposure methods. The choice of the technique depends on the objective of testing, which could range from quantitatively evaluating the pitting performance of alloy systems to deriving a mechanistic understanding of the kinetics involved in the pitting process. Techniques such as potentiodynamic polarisation and Electrochemical Impedance Spectroscopy (EIS) furnish insights into the bulk pitting performance of the alloy systems. In contrast, techniques such as the scanning or micro-electrochemical methods assist in deriving a mechanistic understanding of the localised pitting behaviour. Pit investigation tests are invariably followed by post-mortem studies using (optical/electron) microscopy, profilometry or Atomic Force Microscopy (AFM) for failure analysis to examine the morphology, dimensions, location and distribution of the pits.

2.7.1. Potentiodynamic polarisation

Potentiodynamic polarisation is the traditional method for investigating the pitting performance of alloy systems. The test procedure involves scanning the potential at a fixed scan rate from cathodic to anodic potentials and simultaneously recording the current response of the specimen, as described in ASTM G61-86. Though this standard is conventionally adopted for the pitting assessment of Fe, Ni and Co-based alloys, a similar procedure is adopted for testing the pitting susceptibility of aluminium alloys [Pride et al. 1994]. The typical cyclic potentiodynamic polarisation response of pure aluminium recorded at a scan rate of 0.5 mV.s^{-1} (both forward and backward) in aerated 0.01 M NaCl is shown in Figure 2.9.

Analysis of the potentiodynamic polarisation plots yields the characteristic potentials, namely corrosion potential (E_{corr}), pitting potential (E_{pit}), transition potential (E_T), protection potential (E_{prot}), metastable pitting potential (E_m) and other parameters such as the corrosion current density (i_{corr}) and passive current density ($i_{passive}$). These parameters aid in determining the pitting susceptibility of alloy systems. The significance of these parameters is discussed below.

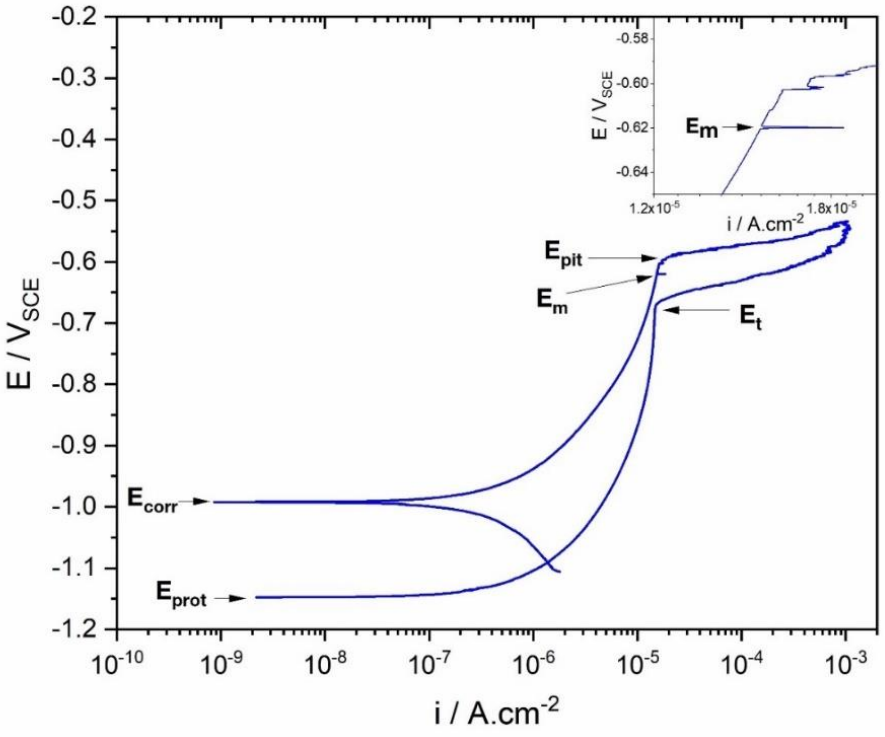

Figure 2.9. The cyclic potentiodynamic polarisation response of pure aluminium at a (forward & reverse) scan rate of 0.5 mV.s^{-1}, reversed at 1 mA.cm^{-2} in aerated 0.01 M NaCl.

Pitting potential (E_{pit})

In a potentiodynamic polarisation plot of a passivating metal-alloy system, E_{pit} is the anodic potential above which the current transitions from an almost constant $i_{passive}$ to a sharp, sudden and rapid increase. In their review [Soltis 2015], Soltis reported that the concept of pitting was introduced by Brennert in 1936 [Brennert 1936]. Conventionally E_{pit} is considered as the potential above which the stable pits propagate and below which metastable pitting is possible [Sasaki et al. 1996]. E_{pit} is also considered as the potential above which co-operative interaction among the pits occur [Scully et al. 2008]. Mechanistically, E_{pit} is also described as the potential required for the maintenance of a salt film inside the pit [Laycock et al. 1997, 1998b] since the dissolving pit can generate chemistry that is aggressive enough to prevent repassivation [Inturi et al. 1993]. At E_{pit}, the pit geometry transitions from crystallographic to polished hemispherical due to the change in kinetics from ohmic-controlled pit propagation to diffusion-controlled propagation [Beck 1984; Frankel 1998].

E_{pit} can also be determined using potentiostatic methods by the so-called 'point to point' measurement. This test method involves determining the extent of pit damage after exposing the alloy at a constant potential for a specific period [Schwenk 1964, 1965]. Galvanostatic methods employed to determine E_{pit} [Schwenk 1964] were later proven ambiguous owing to the periodic oscillations of E_{pit} that occur over several orders of magnitude [Rosenfeld et al. 1967].

Repassivation potential (E_r)/Transition potential (E_T)

Pourbaix et al. introduced the concept of repassivation potential (E_r) [Pourbaix et al. 1963]. In the reverse scan of a cyclic potentiodynamic polarisation curve, E_r is the potential below which the current decreases proportionally with potential. The classic E_r witnessed in SS, i.e., the potential at the intersection of the reverse scan with the forward scan does not occur in aluminium and its alloys [Yasuda et al. 1990; Comotti et al. 2013]. Hence, the potential at which the curve transitions from diffusion-limited propagation (i.e., i varies independent of E) to ohmic-limited propagation (i.e., i varies as a function of potential) is termed the pit transition potential (E_T) in aluminium. The proper repassivation potential (E_r) for aluminium can be determined from ASTM D6208-07.

Mechanistically, E_r is defined as the minimum potential required to conserve critical pit chemistry and, therefore, the potential below which metastable pitting is not possible [Frankel et al. 1993]. The factors influencing pit growth can be studied from the difference of E_r and E_{pit}, i.e., when $E_{pit} - E_r$ is small, the influence of the passive film is minimal such that pitting is dominated by pit growth kinetics [Li et al. 2018]. On the contrary, when $E_{pit} - E_r$ is large, pitting is dominated by both the passive film characteristics and pit growth kinetics [Li et al. 2018].

Though E_r furnishes insights regarding the repassivation kinetics, the pitting susceptibility of alloy systems is not primarily investigated from E_r as it varies significantly depending on the scan rate, pit depth and current density at the instant of current reversal [Wilde et al. 1971].

Protection potential (E_{prot})

Protection potential (E_{prot}) is the potential at which the current reaches its lowest anodic current density during the reverse scan [Comotti et al. 2013], as shown in Figure 2.9. The difference in the potentials $E_{pit} - E_{prot}$, i.e., the width of the hysteresis aids in understanding the localised corrosion susceptibility of aluminium alloys.

Metastable pitting potential (E_m)

Using slow scan-rate potentiodynamic polarisation studies, Tang et al. introduced a parameter called the metastable pitting potential (E_m) which is defined as the potential at which the first current transient appears in a potentiodynamic polarisation plot [Tang et al. 2014]. E_m and E_{pit} exhibit a linear relationship signifying the relevance of E_m in determining the stable pitting susceptibility of alloy systems.

Passive current density ($i_{passive}$)

Passive current density ($i_{passive}$) is the current density exhibited by passive metals in their passive region. It results from the constant rate of metal dissolution into the environment and film thickening processes. The $i_{passive}$ is also considered to arise from the summation of numerous breakdown and repair events occurring on the passive film surface [Frankel 1998;

Burstein et al. 2009]. A higher $i_{passive}$ is attributed to a higher pit nucleation frequency in SS [Williams et al. 1994]. In fact, a higher local $i_{passive}$ recorded at localised locations at lower anodic potentials were the locations that eventually developed into pits at higher anodic potentials in SS when tested in chloride solutions [Zhu et al. 1997]. Such observations emphasise that the $i_{passive}$ is a measure of the pitting susceptibility of passivating alloy systems.

2.7.2. Critical pitting temperature (CPT)

Critical pitting temperature (CPT), a concept proposed by Brigham et al. [Brigham et al. 1973], is the temperature above which stable pitting occurs. At CPT, the condition $i_{lim} \geq i_{passive}$ promotes stable pitting [Laycock et al. 1998a; Moayed et al. 2006] while below this temperature the condition $i_{lim} < i_{passive}$ causes repassivation of the metastable pits. CPT is considered to exhibit a sharp transition with an accuracy of ~ 1°C. It is also independent of [Cl^-] in the range of 1 – 5 M Cl^- [Brigham et al. 1973; Ovarfort 1989] and pH in the range of 1 – 7 [Soltis 2015] for SS.

CPT can be investigated by scanning the potential at a constant temperature or scanning the temperature at a constant potential. CPT can also be determined from the electrochemical noise measurements (ECN) [Zhang et al. 2012] and EIS [Ebrahimi et al. 2012]. The CPT of aluminium in HNO_3 was first reported by Burstein et al. using thermammetry as 38.6°C [Burstein et al. 2004]. Their results suggested that metastable pitting was possible below CPT. Recently, Li et al. suggested that the CPT is a statistically distributed parameter and not a deterministic parameter [Li et al. 2018].

2.7.3. Induction time (t_i)

Induction time (t_i) is the time required by a metal surface to develop pits upon its exposure to the environment. Induction time is dependent on the parameters that affect the breakdown of passivity, such as the concentration of aggressive species, potential, passive film thickness and temperature. In aluminium, the increase in t_i with anodic potential is attributed to the increase in the oxide film thickness [Nguyen et al. 1979; Foroulis et al. 1975]. The relationship between t_i and [Cl^-] is shown in Equation 2.4. The parameters k and n are constants.

$$\frac{1}{t_i} = k[Cl^{-1}]^n \qquad \textit{Equation 2.4}$$

2.7.4. Electrochemical Impedance Spectroscopy (EIS)

Pitting corrosion in aluminium can be investigated from the characteristic parameters of an EIS spectrum. The model developed by Mansfeld et al. aids in investigating pitting corrosion of aluminium using area fraction values, capacitance and polarisation resistance from an EIS spectrum recorded at E_{corr} [Mansfeld et al. 1988; Mansfeld et al. 1992]. For freely corroding samples, the initiation of a visual pit is accompanied by an increase in the polarisation resistance (R_p), constant capacitance and a sharp decrease in impedance in the capacitive region of the spectra, i.e., a slope of -1 in the $log|Z| - \log f$ plot wherein f is the frequency [Mansfeld et al. 1992]. The passivation behaviour of aluminium can also be investigated from the variation of time constants [de Wit et al. 1996]. An increase in the anodic potential decreases the capacitance and increases the time-constants from two to three, signifying an increase in the ionic transport within the passive film [Martin et al. 2005].

2.7.5. Scanning and micro-electrochemical methods:

Scanning electrochemical methods viz. scanning electrochemical microscopy (SECM) [Niu et al. 2009], scanning vibrating electrode technique (SVET) [Lin et al. 2000], scanning kelvin probe (SKP) [Muster et al. 2006], local-EIS (LEIS) [Niu et al. 2009] and other micro-electrochemical methods [Birbilis et al. 2005; Birbilis et al. 2009] are employed in understanding the localised pitting mechanism. These techniques permit electrochemical mapping of the local current, potential and pH distribution on a corroding surface. They have been successfully employed in understanding the physicochemical nature of the electroactive defective sites on a passive film surface [Serebrennikova et al. 2001; Casillas et al. 1993], dynamic electrochemical nature of the second phase particles [Birbilis et al. 2005; Birbilis et al. 2009] and chemistry within the dissolving pits including pH [Ding et al. 2009; Oltra et al. 2010; Paik et al. 2000]. Figure 2.10 illustrates the local ionic current densities measured using SVET over Mg_2Al_3, Al and their junction as a function of various pH.

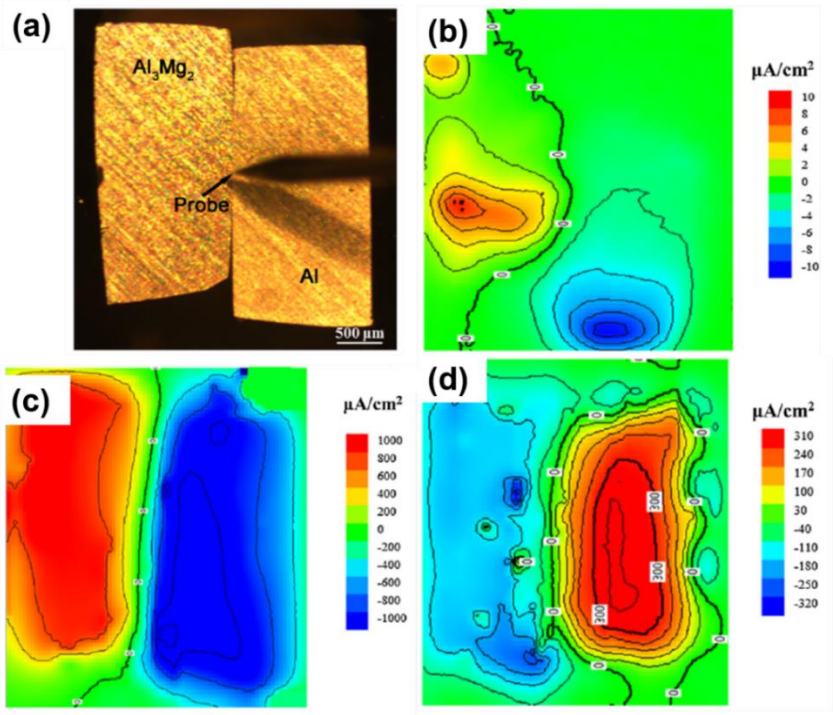

Figure 2.10. The SVET ionic current density maps of (a) a junction between Al and Mg_2Al_3 (β) phase recorded at (b) pH = 2, (c) pH = 7 and (d) pH = 12 [Li et al. 2019].

Scanning electrochemical studies have shown that the dynamic electrochemical activity of the second phase particles requires meticulous consideration instead of a first-order classification based on their nobility [Birbilis et al. 2005; Birbilis et al. 2009]. They have also enabled an understanding of the precursor events that trigger localised corrosion [Williams et al. 1998]. SECM studies have also helped to successfully demonstrate the relationship between the electron transfer rates, oxide conductivity and localised corrosion [Serebrennikova et al. 2001; Serebrennikova et al. 2002]. By inducing pitting at selected locations with the chloride generated at the probe tip, SECM has also been used to map the corrosion initiation as a function of potential [Still et al. 1997].

2.7.6. In situ visualisation of pit events

In situ/real-time visualisation of pit evolution is one of the most powerful techniques to understand and evaluate the pitting susceptibility of alloy systems. However, the dynamic nature of pitting corrosion complicates such visualisation and hampers mechanistic investigation of pitting corrosion. For instance, it is difficult to determine when and where a pit event would occur. In aluminium and its alloys, this complexity is further augmented by the corrosion products and pit covers at the pit sites that are reflective akin to the metal surface,

making the pit locations visually unresolvable [Frankel 1998]. Hence indirect investigation routes are adopted to visualise the pit events in situ.

Newton and Holroyd discussed a simple time-lapse video technique for investigating pitting corrosion in aluminium and its alloys [Newton et al. 1992]. Isaacs et al. used pH-sensitive agar gels to determine the pit locations in several aluminium alloys based on the pH changes during pit dissolution (Figure 2.11) [Isaacs et al. 2000]. Buchler et al. used fluorescent dyes to locate the pit dissolution sites, which allowed them to study the inhibitor efficiency [Büchler et al. 2000]. Ellipsometry has been used by several researchers for the visualisation of pitting [NASA-CR-132301]. In-situ confocal laser scanning microscopy was used to visualise the selective dissolution of second phase particles in AA2024-T3 [Ilevbare et al. 2004]. In situ synchrotron X-ray microtomography has remained another promising method for the in situ investigation of pit growth [Ghahari et al. 2011].

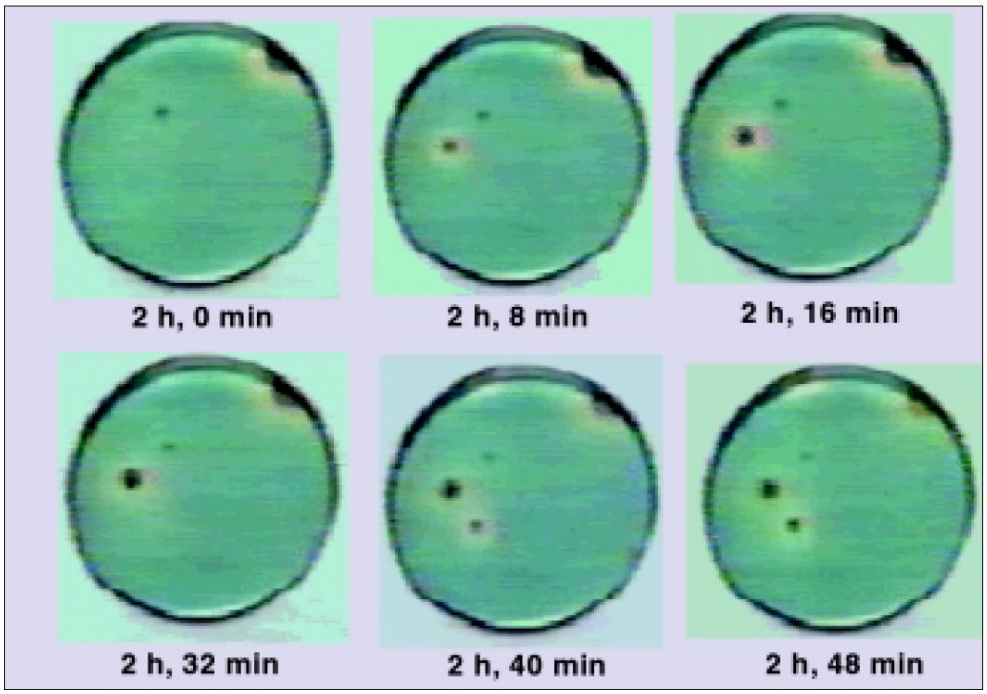

Figure 2.11. The temporal evolution of pitting on AA1100 studied in situ using pH-sensitive agar gels containing 1 M NaCl [Isaacs et al. 2000].

2.7.7. Atomic emission spectroelectrochemistry (AESEC)

Introduced to the field of corrosion by Ogle, Atomic emission spectroelectrochemistry (AESEC) is a promising technique that allows an in situ determination of the kinetics of

corrosion from the dissolution rates of various elements [Ogle 2019]. A method termed time-resolved volumetry (TRV) coupled with AESEC was developed to determine the moles of hydrogen evolving during NDE. [Lebouil et al. 2014]. Gharbi et al. demonstrated incongruent dissolution of the intermetallic phases in AA2024-T3 using AESEC [Gharbi et al. 2016]. Recently, an in situ ICP-OES study was performed to understand hydrogen evolution upon aluminium [Yu et al. 2020].

2.7.8. Artificial pits

Artificial one-dimensional (1D) and two-dimensional (2D) pits provide a simplified version of the natural three-dimensional (3D) pits and are employed in understanding the mechanism and kinetics of stable pit growth [Beck 1984; Frankel 1990]. The characteristics of the salt films that precipitate in the pit interior and assist in the pit stability were investigated using 1D pits of aluminium [Beck 1984]. The transition of pit growth from diffusion-control to ohmic-control was also demonstrated using 1D pits of aluminium [Cook et al. 2012]. The study of 2D pits using thin films of aluminium enable a precise determination of the pit dissolution area while also generating results proximate to the 3D pits [Frankel 1990]. Frankel showed that the 2D pits grew under ohmic control at low potentials and transitioned to diffusion control at higher potentials [Frankel 1990]. The pit depth was found to vary with $t^{1/2}$ when the pits grew under ohmic control [Hunkeler et al. 1981, 1984].

2.7.9. Exposure tests

Exposure tests are employed in understanding the pitting characteristics from the density, geometry and dimension of the pits formed after exposing the samples to the desired environment for a specific duration. Exposure tests are often carried out to validate the results from other pitting tests and are rarely used as a solitary test for determining the pitting susceptibility since the duration required for deriving a deterministic conclusion could be significantly high. The examination and evaluation of pitting corrosion after exposure tests are carried out according to ASTM G46 – 94.

2.7.10. Chemical methods

As early as 1960, Smialowska, in their review [Szklarska-Smialowska 1971], reported that a group of researchers relied on investigating pitting corrosion by chemical methods

instead of electrochemical techniques. They believed that the simultaneous occurrence of anodic and cathodic reactions on the sample surface during chemical test methods closely represented the natural corroding conditions as opposed to electrochemical techniques that studied only the anodic reactions during polarisation. The chemical methods used electrolyte solutions containing chloride with substances that had a higher redox potential than E_{pit}. In their review, Smialowska described that the results derived from the chemical methods were not significantly different from the electrochemical methods [Szklarska-Smialowska 1971]. In modern days, many researchers adopt electrochemical routes instead of chemical routes to investigate pitting corrosion.

2.8. Metastable pitting investigation

Metastable pitting events are characterised by the appearance of potential perturbations during open circuit potential (OCP) or current transients in the so-called anodic direction (more positive current) during potentiostatic testing of passive metals at anodic potentials below (less positive than) the potentiodynamically determined E_{pit} [Frankel 1998]. The basis of treating each current transient as a signal arising from individual metastable pitting events [Pistorius et al. 1992; Frankel 1998] forms the unique feature of the metastable pitting studies over other techniques discussed in Section 2.6. Analysis of the various features of the current transients, namely their shape, duration and charge accumulation, provide substantial knowledge on the kinetics and mechanism involved in the evolution of metastable pit events, without the need for sophisticated testing [Pistorius et al. 1992; Pride et al. 1994]. Further, since metastable and stable pits follow the same growth law during the initial stages of pit growth [Isaacs 1989; Pistorius et al. 1992], the investigation of the stable pitting susceptibility from metastable pitting characteristics becomes more relevant. Therefore, metastable pitting studies have gained considerable significance over the conventional E_{pit} in unambiguously predicting the stable pitting propensity of alloy systems [Cavanaugh et al. 2009; Gupta et al. 2012].

2.8.1. Metastable pitting rate (MPR)

Metastable pitting rate (MPR) is determined from the number of current transients recorded per unit time and surface area of the sample. Williams et al. defined a relationship between MPR and the probability of stable pit formation in SS through stochastic modelling [Williams et al. 1985a, 1985b] as shown in Equation 2.5.

$$\Lambda = A\lambda \exp(-\mu\tau_c) \qquad \textit{Equation 2.5}$$

wherein Λ is the rate of stable pitting, λ is the frequency of metastable pitting, A is the surface area of the specimen, μ is the probability that the metastable pits would repassivate and τ_c is the critical age required for the metastable pits to transition to stability. This relationship was later experimentally verified by Balkwill et al. [Balkwill et al. 1991]. Recently, Gupta et al. showed that the pitting susceptibility of several aluminium alloys determined from MPR was consistent with the density of pits recorded at freely corroding conditions [Gupta et al. 2012](Figure 2.12). Such studies demonstrate the efficiency of MPR in the quantitative evaluation of the stable pitting susceptibility of alloy systems.

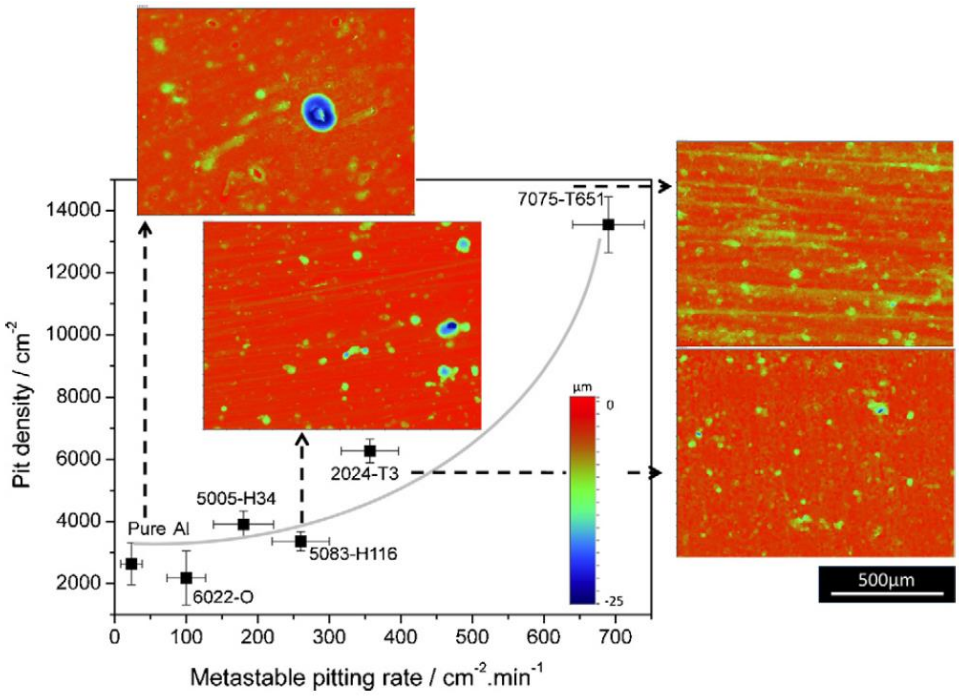

Figure 2.12. A comparative study of the pit density measured using profilometry after exposure of various aluminium alloys for 14 days versus the metastable pitting rate measured at E_{pit} – 25 mV [Gupta et al. 2012].

2.8.2. Parameters of current transients

Critical insights regarding the mechanistic and kinetic aspects of pitting can be derived from the various parameters of the current transients (Figure 2.13), namely: peak current (I_{peak}), pit growth time (t_g), pit repassivation time (t_r) and shape of the current transients (i.e., the variation of I_{pit} with t).

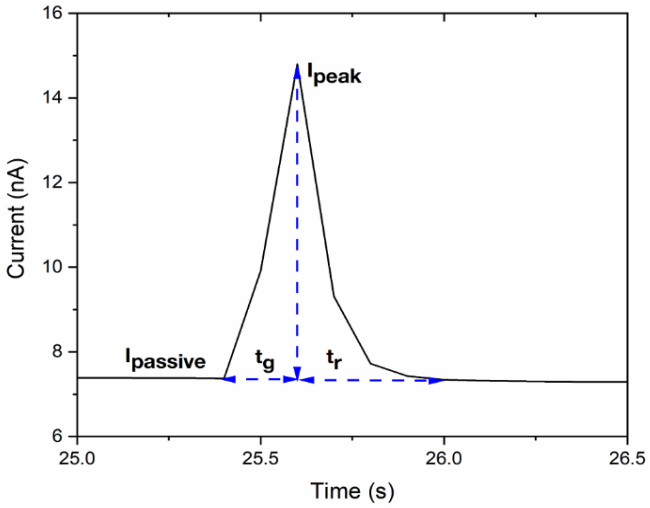

Figure 2.13. A typical current transient with its metastable pitting parameters recorded during the potentiostatic testing of Al – 5 wt.% Mg aged at 100°C for 40h at E_{pit} – 25 mV in 0.01 M NaCl.

Kim et al. showed that the presence of Cu in the solid solution of aluminium decreased the pitting propensity of Al-Cu alloys by reducing I_{peak} and resulting in two stages of repassivation [Kim et al. 2007]. Sato and Newman observed that the presence of Zn as an alloying element in aluminium increased I_{peak}, t_g and pit growth rate (I_{peak}/t_g) with little effect on pit nucleation [Sato et al. 1998]. The shape of the current transients is also employed in understanding the pit growth kinetics as inferred from the relationship of current (I) vs time (t). The initial growth rate of both the metastable and stable pits in SS follow the same relationship of $I \sim t^2$ which is attributed to the propagation of pits under a pit cover [Frankel 1998]. Upon the precipitation of a salt film and reaching the critical depth necessary for sustained pit propagation, stable pits were observed to propagate at a rate of $I \sim t^{1/2}$ [Pistorius et al. 1992; Frankel 1998].

2.8.3. Charge accumulated by the current transients ($C_{transient}$)

The charge accumulated by the current transients, determined by integrating the area under the I - t curve, is employed in determining the mass loss at the pit site. This prospect of determining the mass loss at an individual pit site directly from the electrochemical signal is one of the unique advantages of metastable pitting studies. When the exact fraction of the dissolving species and area of the pit are known (or by assuming a hemispherical pit geometry), the volume of the pit (V_{pit}) and pit radius (r_{pit}) can be estimated from $C_{transient}$ [Frankel et al. 1987; Williams et al. 1994; Pistorius et al. 1992; Pride et al. 1994]. The V_{pit} and r_{pit} estimated

in this manner has a wide range of implications in determining the stable pitting susceptibility of alloy systems, as discussed in Section 2.8.

2.9. Pit radius (r_{pit}) estimated from $C_{transient}$ – significance and limitations

The pit radius (r_{pit}) estimated from $C_{transient}$ provides a quantitative assessment of the mass loss at the pitted site. The distribution of the metastable r_{pit} estimated from $C_{transient}$ was reported to be comparable with the distribution of the actual r_{pit} that was recorded on the corroded surface [Pride et al. 1994, Williams et al. 1994] (Figure 2.14). Similar inferences were derived from the ex-situ AFM investigations of single metastable pit events in 304 SS [Guan et al. 2016a]. Such prospects make $C_{transient}$ a remarkable feature of the metastable pitting data. Further, since the stable pits are autocatalytic in nature and may eventually transition to EAC [Kondo 1989], determining the number of stable pits from metastable pitting studies furnishes the critical information necessary for predicting the engineering life of alloy systems.

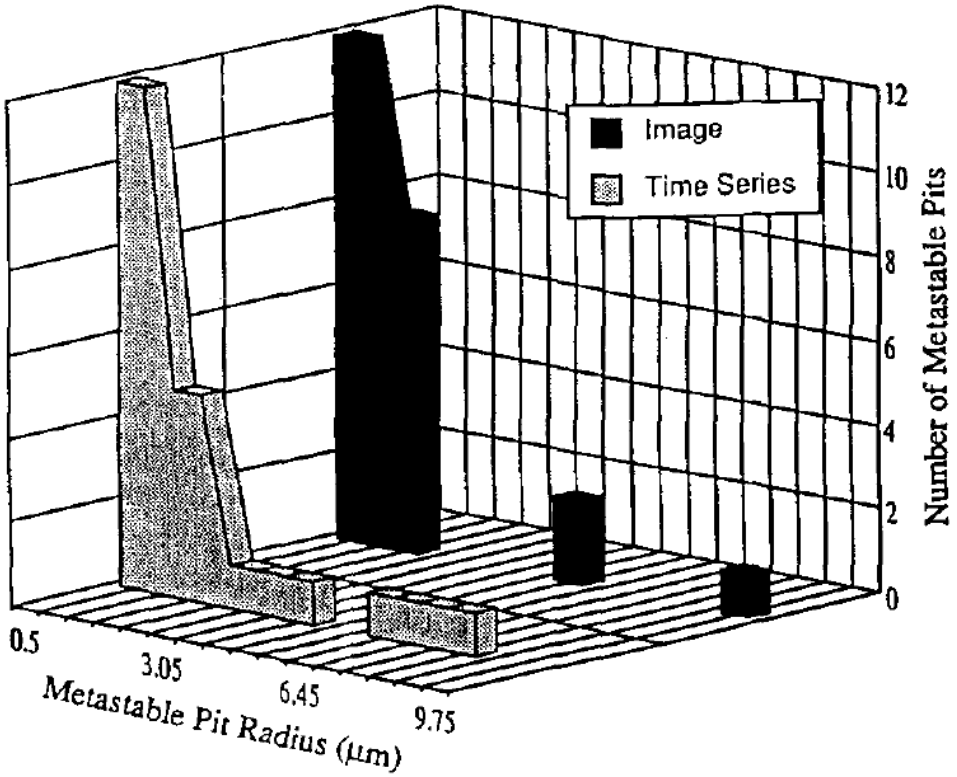

Figure 2.14. The comparison of the distribution of the actual vs estimated metastable pit sizes in pure aluminium [Pride et al. 1994].

The r_{pit} determined from current transients has direct relevance in understanding the stable pitting susceptibility of alloy systems. The transition of pits from metastability to stability is dependent on the size of the pits [Buzza et al. 1995]. In an independent study, Trueman concluded that a critical $C_{transient}$ equivalent to a hemispherical r_{pit} of 6.75 μm was necessary for the transition of pits from metastability to stability in AA2024-T3 [Trueman 2005]. Such transition in the stability of pits at a critical r_{pit} agrees with the critical acidification theory proposed by Galvele [Galvele 1981; Galvele 1976]. With this theory as a basis, the pit stability criterion ($I_{peak}/r_{pit} > 10^{-2}$ A.cm^{-1}) developed by Williams et al. in SS [Williams et al. 1994] and Pride et al. in pure aluminium [Pride et al. 1994] could successfully determine the transition of pits from metastability to stability using the current transient data. Thus, the r_{pit} and V_{pit} determined from $C_{transient}$ is a promising candidate for determining the pit stability and the engineering life of aluminium alloys.

Limitations of $C_{transient}$

While certain studies report that the distribution of r_{pit} estimated from $C_{transient}$ agrees with the actual distribution of r_{pit} witnessed on a pitted surface [Pistorius et al. 1992; Pride et al. 1994], several studies have reported that the estimated and actual r_{pit} values do not agree [Guan et al. 2015; Guan et al. 2014]. Pistorius et al. reported that the size of the larger pits was underestimated while that of the smaller pits was overestimated in SS [Pistorius et al. 1992]. Recently, using in situ optical monitoring of metastable pit evolution, Sander et al. reported that the mass loss determined at the pit site using a profilometer in SS was smaller than its associated $C_{transient}$ [Sander et al. 2020]. They attributed this discrepancy to the capacitive charging of the surface. In an Al – 5 wt. % Mg alloy, the distribution of the metastable r_{pit} determined from $C_{transient}$ was found to be significantly smaller than that determined using ex-situ SEM and TEM investigations [Guan et al. 2020; Guan et al. 2015]. This discrepancy was attributed to the multiple pit reactivations occurring from the same location since the number of actual pits witnessed was smaller than the total number of current transients recorded. In an Al-Mg-Si alloy with cathodic second phase particles, the MPR was reported to be significantly smaller than the actual number of pits due to the dominance of negative current from the localised reduction reactions that resulted in depreciated current transients [Guan et al. 2014].

In aluminium and its alloys, the severely underestimated r_{pit} is attributed to the occurrence of hydrogen evolution within the pit that is considered to consume a significant fraction of the actual pit dissolution charge (C_{pit}) [Frankel 1998]. Beck reported that the i_{H_2}/i_{anodic} was 0.16 during stable pit propagation of pure Al in $AlCl_3$ solution [Beck 1984]. Recently, this ratio was deduced as 10% in AA2024 using 1D pits in aerated 0.1 M NaCl [Bonzom et al. 2016]. Frankel using two-dimensional (2D) pits in thin films of pure aluminium, reported that the i_{H_2} remained constant at 1.6 A.cm^{-2} when i_{anodic} ranged between 18 to 30 A.cm^{-2} in de-aerated 0.1 M NaCl [Frankel 1990]. Boag et al. stated that the HE consumed ~ 40% of the total anodic current during the stable pit formation in AA2024-T3 when tested in aerated 0.1 M NaCl [Boag et al. 2010]. Other values reported for this ratio include 6% in 0.5 M NaCl [Dražić et al. 1999] and 20% in 12 M HCl [Frankel et al. 2015] during the investigation of NDE in aluminium. Based on such works, the $C_{transient}$ recorded from the current transients is considered to be depreciated. To account for this error, the incorporation of an additional ~ 16 % charge to $C_{transient}$ became a practice [Kim et al. 2007; Guan et al. 2016b] though Pride et al. using derivative methods showed that this discrepancy would be minimal [Pride et al. 1994].

Another important assumption adopted in the estimation of r_{pit} from $C_{transient}$ is the consideration of hemispherical pit geometry. The geometry of pits that form upon aluminium is complex. Stable pits that propagate under mass transport control are etched and hemispherical, while metastable pits that propagate under mixed ohmic and mass transport control are crystallographic in nature [Frankel 1998]. The crystallographic pits tend to propagate as tunnels (shown in Figure 2.8), depending on the pit chemistry in the tunnels resulting in irregular pit geometries. Yasuda et al. 1990 reported that the pits in single crystals of pure aluminium were faceted while those in Al-Cu alloys were irregular. Therefore, assumption of hemispherical pit geometry to estimate r_{pit} from $C_{transient}$ [Pride et al. 1994] could be erroneous without the knowledge of the actual pit geometry.

2.10. The reliability of r_{pit} and V_{pit} estimated from $C_{transient}$

The foregoing discussions in Section 2.8 indicate that the reliability of r_{pit} and V_{pit} determined from $C_{transient}$ in determining the actual r_{pit} and V_{pit} has not been investigated systematically in aluminium. Hitherto, the investigations that focus on comparing the estimated

versus actual r_{pit} were performed on the distribution of pits rather than associating the current transients to their respective metastable pit events [Williams et al. 1994; Pride et al. 1994; Guan et al. 2015]. Such correlations preclude a deterministic understanding of which metastable pit on the electrode surface is associated with a particular current transient. Further, adopting the same i_{H_2}/i_{anodic} = 16% from stable pit propagation [Beck 1984] to metastable pit growth [Kim et al. 2007] needs to be validated as the rate of HE decreases with potential for the same current density [Cook et al. 2012]. Pride et al. showed through derivative approaches that the fraction of $C_{transient}$ lost to HE was minimal [Pride et al. 1994]. In such a case, it becomes crucial to understand what other factors depreciate the reliability of the r_{pit} estimated from $C_{transient}$. The works of Guan et al. showcase the possibility of multiple co-occurring pit events resulting in overlapped current transients [Guan et al. 2014] and pit recurrences resulting in a smaller number of current transients as compared to the actual number of pits witnessed on the corroded surface [Guan et al. 2015]. Though the occurrence of such multiple overlapping current transients and pit reactivations is widely acknowledged, the error they introduce in the context of metastable r_{pit} estimations from $C_{transient}$ has often been overlooked. More specifically, a comparison between the magnitude of error introduced by the spatiotemporal evolution of pit events and the conventionally held HE has remained unexplored. Such insights being critical to understanding the factors that limit the reliable assessment of metastable r_{pit} from current transients, forms the motive of the present dissertation. Briefly, the work herein is an attempt to investigate if the conventional notion of treating each current transient as a signal arising from single discrete pit events is valid in the context of metastable r_{pit} estimations from $C_{transient}$.

The challenge in establishing a correlation between the metastable pit event and its relevant current transient resides in the elusiveness of locating the metastable pit events due to their dynamic nature and reflective pit covers that impede their visualisation. This dissertation attempts to develop an in-situ imaging technique that can directly correlate the current transients to their associated metastable pit events and thereafter probe the causes for the inconsistencies (if any) witnessed between the actual and estimated r_{pit} or V_{pit}.

2.11. Summary

An extensive literature review concerning pitting corrosion in aluminium and its alloys, focusing on the significance and limitations of $C_{transient}$ in determining the actual r_{pit} or V_{pit} has been presented. In summary, the failure of aluminium as an engineering structure (Section 2.2) by pitting corrosion results from passivity breakdown (Section 2.3 and 2.4) and progresses sequentially via three stages: pit nucleation, metastable and stable pitting. The various models in the literature concerning the different stages of pitting is discussed (Section 2.5). The techniques employed in the investigation of pitting corrosion (Section 2.6) focus either on the quantitative assessment of the bulk pitting characteristics or understanding the local mechanistic and kinetic aspects of pitting. On the contrary, metastable pitting studies provide a comprehensive assessment of pitting that includes a combination of quantitative, mechanistic and kinetic assessment of pitting (Section 2.7). Notably, the r_{pit} determined from the $C_{transient}$ plays a crucial role in assessing the stable pitting susceptibility of alloy systems and, therefore, the engineering life of aluminium alloys (Section 2.8). In this context, the discrepancies witnessed between the r_{pit} estimated from current transients and measured from the pit surface, reported in the literature, are introduced (Section 2.9) as an issue that has remained topical. This issue limits the utilisation of metastable pitting studies as a deterministic tool for investigating pitting corrosion to make engineering decisions for material selection and alloy development.

This dissertation attempts to develop an in-situ imaging method for mapping the metastable pitting locations using a novel approach. Subsequently, the role of various factors, namely, hydrogen evolution within the pits, spatiotemporal evolution of pit events, pit geometry and the electrochemical nature of second phase particles, on the reliability of r_{pit} estimated from $C_{transient}$ has been investigated.

Chapter 3

Experimental methods

The materials, experimental methods, characterisation techniques and data analysis employed in the investigation of the objective of this dissertation have been presented.

3.1. Materials selection

Pure aluminium, commercially pure aluminium (referred to as CP-Al hereinafter) and model binary Al – 5 wt. % Mg alloy were chosen for the present study. Pure aluminium is devoid of second phase particle. Hence the electrochemical data generated from pure aluminium was used as a baseline for preliminary feasibility studies. Commercially pure aluminium comprises Al_3Fe constituent particles. These particles are cathodic to the Al-rich matrix and induce matrix dissolution [Park et al. 1999]. The Al – 5 wt.% Mg alloy, on the other hand, generates Mg_2Al_3 (β) phase-precipitates upon aging, which are anodic to the matrix and undergo selective dissolution [Lyndon et al. 2013]. The motive for selecting these materials was to investigate the inconsistencies witnessed in the r_{pit} estimated from $C_{transient}$ as a function of the electrochemically distinct second phase particles.

Pure aluminium and commercially pure aluminium were supplied by Alfa-Aesar. Al – 5 wt.% Mg was cast in-house at Monash University by melting pure Al (99.9%) and pure Mg (99.9%) in a muffle furnace. After melting Al at ~ 720°C, Mg was added and subjected to constant stirring for 1 h in the molten state. The mixture was later cast into a graphite crucible preheated to 300°C. The chemical composition of the selected alloys analysed using Inductively Coupled Plasma – Atomic Emission Spectroscopy (ICP-AES) is presented in Table 3.1.

Table 3.1. The chemical composition analysis of the materials used in the present study.

Element	Al	Mg	Fe	Cu	Cr	Ni	Zn
Pure aluminium	Rest	0.026	0.006	0.003	0.002	ND	0.005
Commercially pure aluminium	Rest	0.037	0.361	ND	0.046	ND	0.102
Al – 5 wt. % Mg	Rest	4.887	0.028	ND	ND	ND	0.007

3.2. Materials processing

The cast blocks of the Al – 5 wt.% Mg alloy specimens were cold-rolled (thickness reduction of 5%) using a Buhler roller mill to fabricate thin plates with a thickness of ~ 1 mm. The thin plates were subjected to solutionising heat treatment. Al – 5 wt.% Mg binary alloy plates were homogenised at 430°C for 17h, water quenched, solutionised (referred to as soln. Al-5Mg hereinafter) and aged in a silicone oil bath at 100°C for 40h (referred to as Al-5Mg hereinafter) to facilitate the precipitation of β phase-precipitates. The selected ageing temperature curbed excessive sensitisation and promoted generation of an optimum number of time-resolved metastable current transients during potentiostatic testing, permitting analysis of the different stages of pitting. The Al-5Mg specimens were stored under refrigeration after artificial ageing to stifle natural ageing at room temperature. These thin plates were later machined to fabricate electrodes with a small surface area, as described in Section 3.4.

3.3. Microstructural characterisation

The specimens for microstructural characterisation were prepared by grinding the samples to a 5000 grit SiC paper finish, followed by ultrasonically cleaning them in ethanol for 300 s. The samples were transferred to a Chennai Metco polishing wheel and polished until 0.25 μm diamond finish at 300 rpm. The samples were later ultrasonically cleaned in ethanol for 600 s and wiped with soft tissue paper to remove any residues of the polishing suspension adhered to the surface. The Al-5Mg specimens do not reveal Mg_2Al_3 (β) phase-precipitates by phase contrast in the Back Scattered Electron (BSE) mode of imaging using Scanning Electron Microscope (SEM) without etching. Therefore, it was etched using ammonium persulfate ($((NH_4)_2S_2O_8$) for 140 min (optimised based on preliminary experiments) at room temperature, as discussed elsewhere [Yang et al. 2013].

The microstructure of CP-Al was investigated using Environmental Scanning Electron Microscope (ESEM) (Model: FEI Quanta 200), which was attached with an Energy Dispersive X-Ray Analyser (EDAX). The microstructure of Al-5Mg was investigated using a Field Emission Gun-Scanning Electron Microscope (FEG-SEM) (Model: JEOL JSM-7600F) fitted with an EDAX (Model: Oxford Instruments 80 mm^2). All the microstructures were investigated in BSE mode to enable phase contrast-enhanced imaging of the second phase particles.

The microstructures of pure aluminium. CP-Al and Al-5Mg are shown in Figure 3.1, Figure 3.2 and Figure 3.4, respectively. The microstructure of CP-Al exhibited second phase particles with two different morphologies, namely clusters of irregularly shaped particles and others with round morphologies, as indicated with arrows. Both these particles were confirmed to be Al_3Fe constituent particles using EDAX, as shown in Figure 3.3. The microstructure of aged Al-5Mg, shown in Figure 3.4, revealed discontinuous β phase-precipitates along the grain boundaries (GBs) with their dimensions in the order of 1012 ± 87 nm lengthwise and 310 ± 36 nm breadthwise. The presence of Mg_2Al_3 precipitates in the etched microstructures of Al-5Mg was confirmed based on the ICP-AES data that demonstrated the formation of a binary Al-Mg alloy and comparison of the precipitate geometry and its dimensions with the literature [Guan et al. 2016].

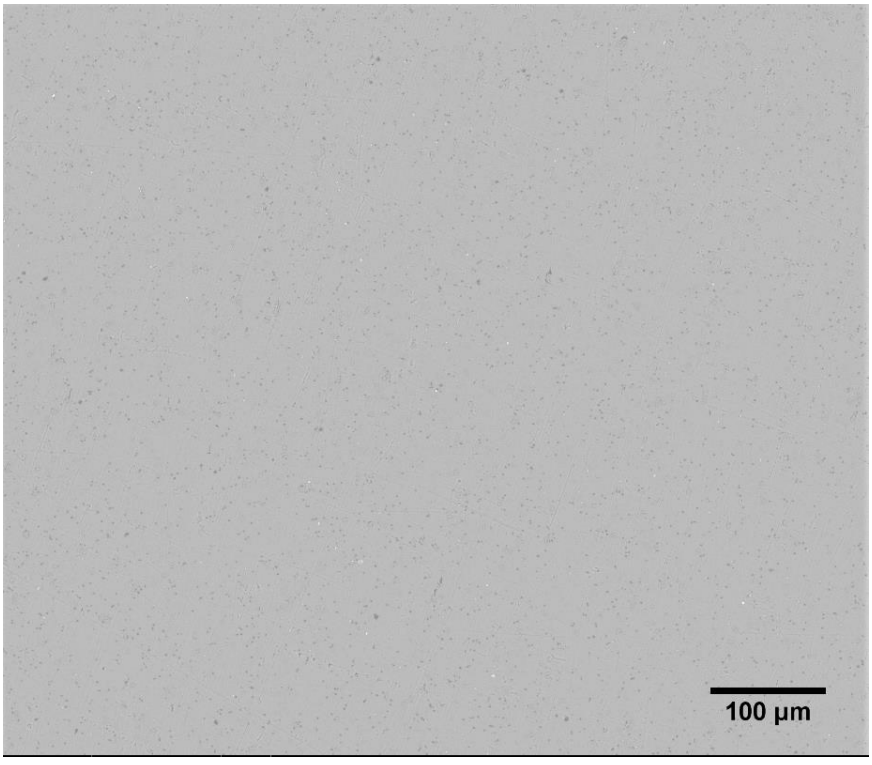

Figure 3.1. The BSE image of the microstructure of pure aluminium.

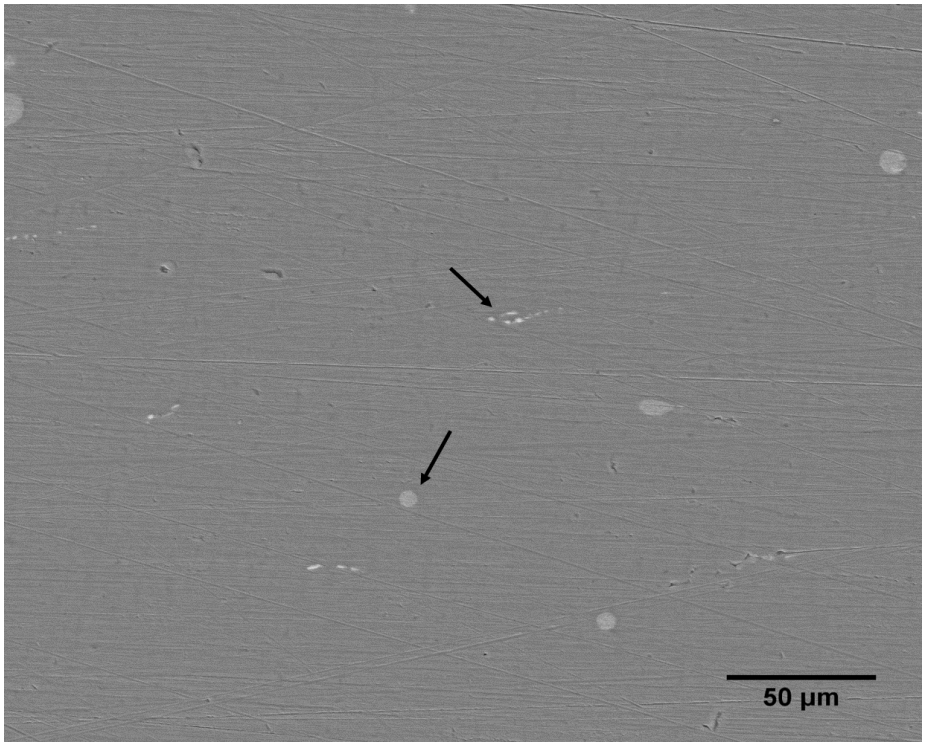

Figure 3.2. The BSE image of the microstructure of commercially pure aluminium.

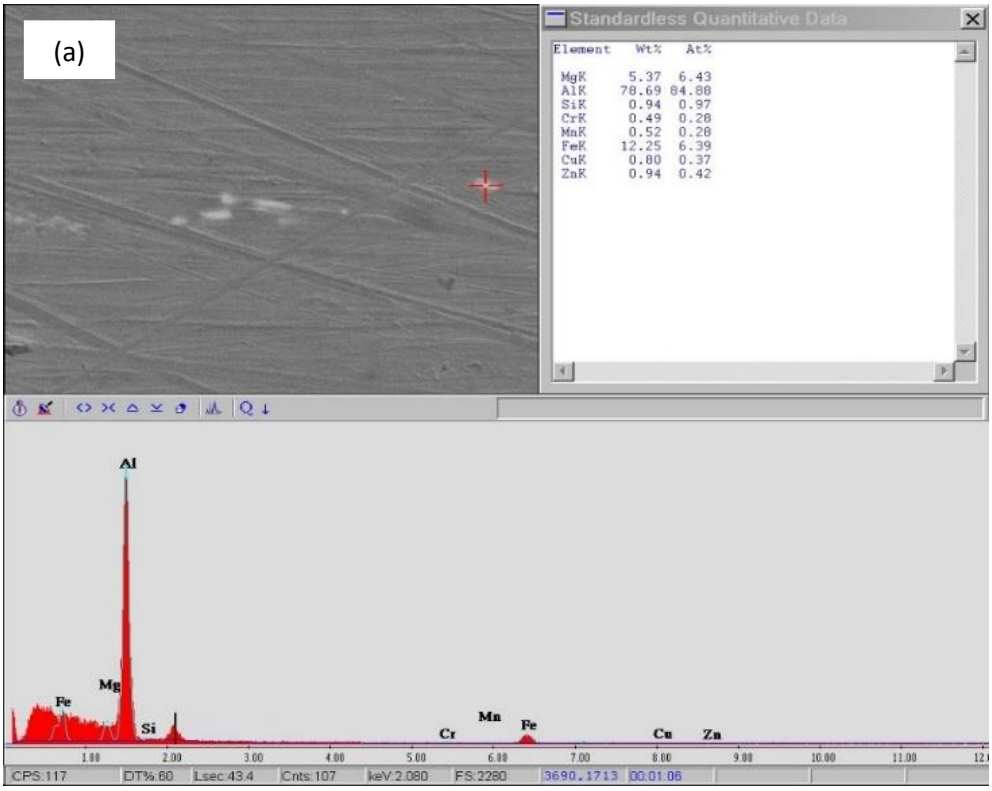

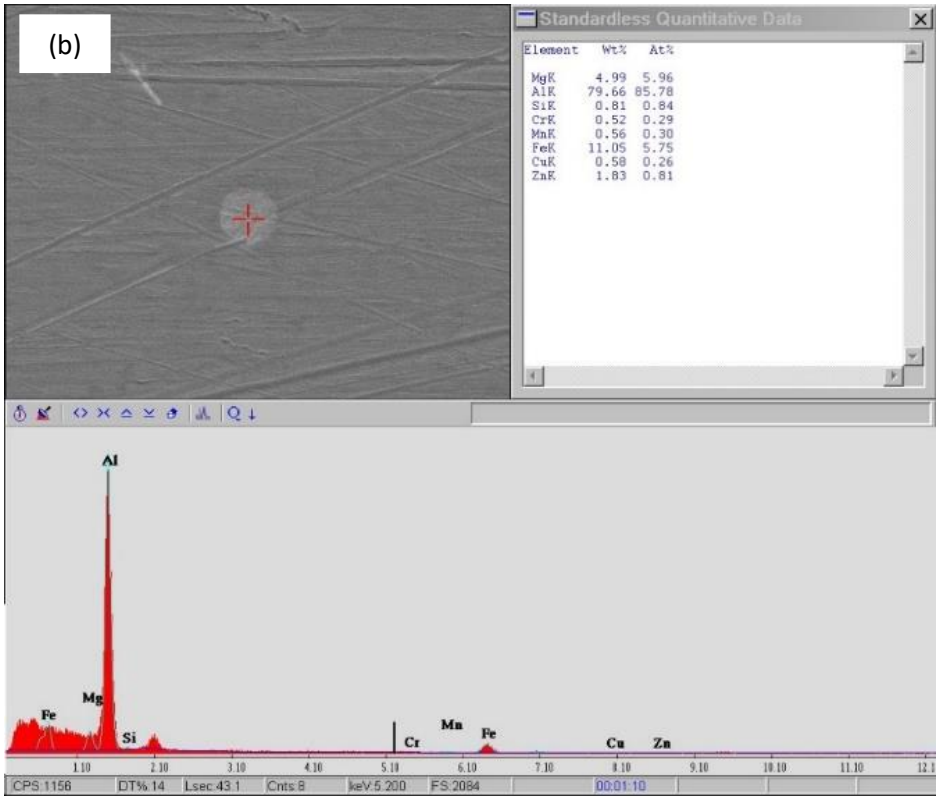

Figure 3.3. The elemental composition studies of the second phase particles present in commercially pure aluminium demonstrating the presence of Al_3Fe IMPs for (a) pit clusters and (b) round shape particles.

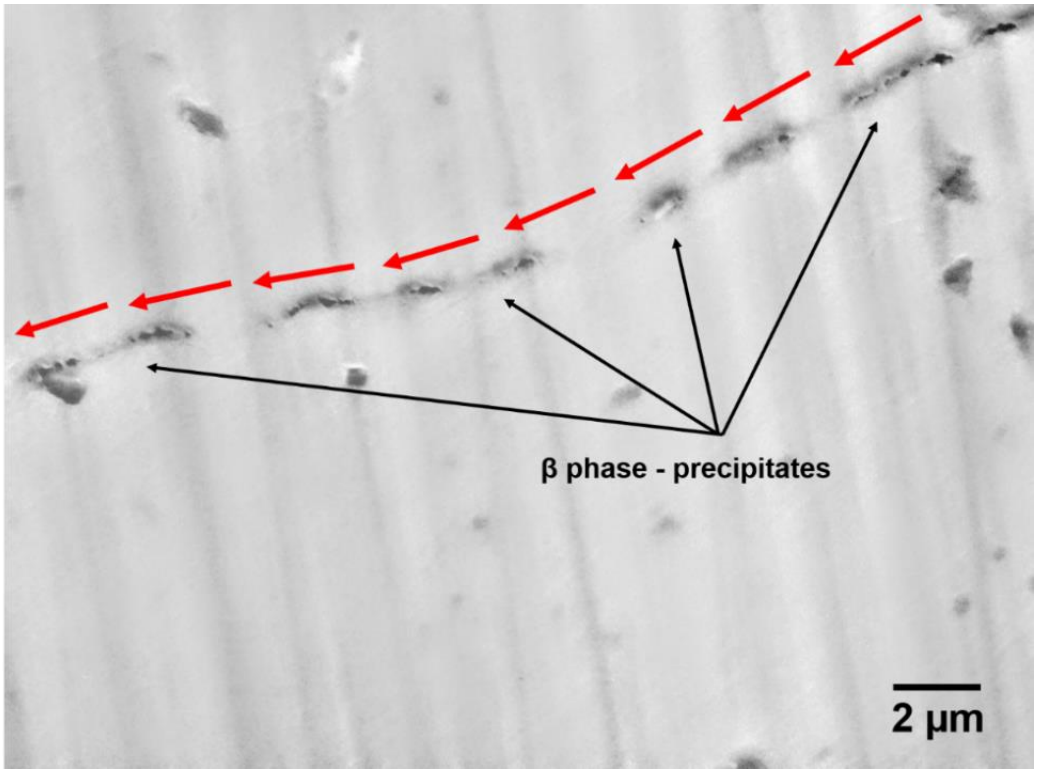

Figure 3.4. The BSE image of the microstructure of aged Al-5Mg (etched in $(NH_4)_2S_2O_8$ for 140 min).

3.4. Electrode fabrication

Metastable pitting potentiostatic studies require the electrode specimens to be fabricated with a small surface area to enable better resolution of the nA to pA sized current transients for the following reasons:

(a) The small surface area of the electrode results in a corresponding decrease in the background passive current density ($i_{passive}$).
(b) The small surface area also scales down the number of prospective pit sites, permitting the generation of a manageable number of metastable pit events that enables the separation and detailed analysis of a single current transient-pit event pair.
(c) The interfacial capacitance on a small electrode specimen is negligible [Riley et al. 1991], which allows the measurement of rapid metastable transients associated with pit nucleation events characterised by the breakdown and repassivation of the passive film.

To prepare the 'small surface area' electrodes (i.e., the so-called microelectrodes), the thin rolled plates of the alloy specimens subjected to heat treatment (as detailed in Section 3.2.) were machined using Wire Electrical Discharge Machining (Wire-EDM) (Accutex AU-300i). The rolled plates could not be sliced using a slow-speed saw as the plates were soft, resulting in severe deformation of the resulting electrodes. The fabricated electrodes were abraded on all sides to remove the deformation layer introduced by Wire-EDM machining. The final surface area of the electrodes used in the present study ranged between 1.75 mm^2 to 0.5 mm^2.

3.5. Specimen preparation for electrochemical testing

The electrode specimens for electrochemical testing were prepared by winding an insulated copper wire to one of the ends of the electrode to provide an electrical connection. The electrodes were then placed carefully on a double-sided tape within the Teflon mount with the aid of tweezers. A quick-setting adhesive was not used to fix the electrode on the double-sided tape as it could generate high local temperatures during the setting process. Though this temperature should not significantly alter the microstructure, the process was avoided to minimise the ambiguities related to the modification of surface characteristics, considering the high sensitivity of the 'small surface area' electrodes. The electrical continuity between the electrode and the copper wire was constantly verified during the entire specimen preparation

process. The specimens were later mounted using a slow-setting araldite resin which prevented the formation of crevices along the edges of the microelectrode and porosity within the resin mount. The mounted electrode specimens were finally checked for electrical continuity, labelled and stored. The image of a mounted 'small surface area' electrode specimen is shown in Figure 3.5.

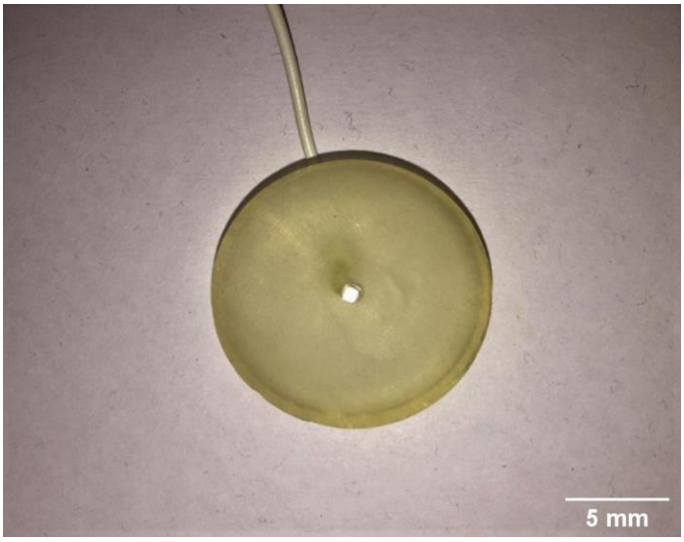

Figure 3.5. Photograph of an Al-5Mg electrode with a surface area of 1.5 mm^2.

The metastable pitting parameters, such as pitting rate, peak current and pit lifetime, determined from the current transients tend to increase with increasing surface roughness in aluminium [Tian et al. 2018]. Therefore, the surface of the specimens for electrochemical testing was carefully prepared by grinding it until 2500 or 5000 grit SiC paper finish under ethanol. During the final stages of grinding, the sample was constantly checked under an inverted microscope for the presence of crevices and scratches. The specimens were then ultrasonically cleaned in ethanol for 300 s before electrochemical testing. The specimens were not polished further using diamond suspensions as surface contamination induced by these suspensions could not be removed successfully using ultrasonication which resulted in significantly altered electrochemical data.

Some efforts were directed to further reducing the surface area of the electrodes to improve the resolution of the potentiostatic data. For this purpose, two different methods were adopted: (a) application of nail polish as a lacquer (Figure 3.6) and (b) the application of an adhesive electrical insulation tape [Chiba et al. 2012]. The application of nail polish as a lacquer altered the electrochemical response of the sample and resulted in under-film corrosion, as shown in Figure 3.6. On the contrary, the utilisation of electrical insulation tapes successfully

helped in reducing the surface area without compromising the electrochemical response. However, with a significant reduction in the surface area, metastable pitting became a rare event that compromised the objective of the study. Hence the surface area of the electrode specimens was not modified using lacquers or insulation tapes. Instead, the whole surface area of the electrode specimen was investigated.

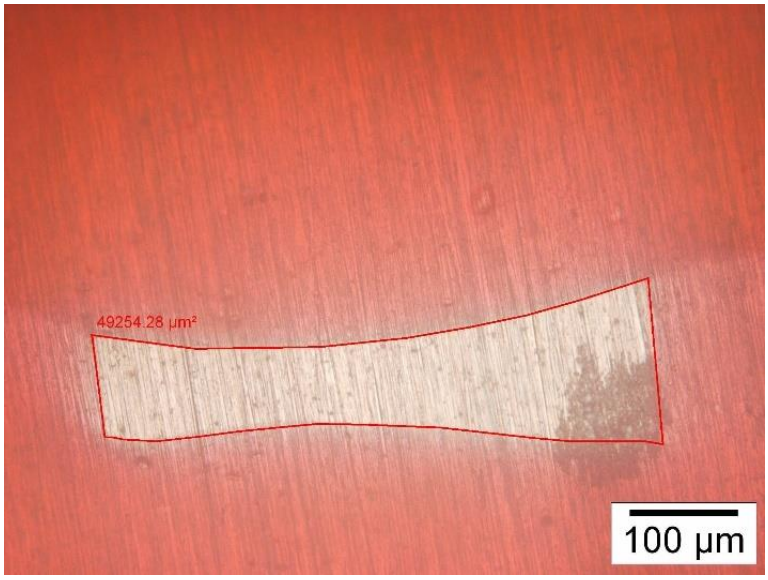

Figure 3.6. Optical image of an Al-5Mg electrode surface subjected to area reduction using nail polish as a lacquer.

3.6. Small electrode specific requirements for electrochemical testing

Metastable pitting corrosion generates current transients with current amplitudes in the range of nA to pA. Such electrochemical signals are prone to be lost within the stray electrical noise arising from gadgets (e.g., plugged in laptops) and other electrical devices (e.g., fluorescent lamps) surrounding the setup. The magnitude of this interference could be imagined to be as bad as that witnessed during the frequency modulation in a radio. A sample potentiodynamic polarisation response of aluminium in the presence of stray electrical interference, recorded during our preliminary studies, is shown in Figure 3.7 (a).

For this purpose, the electrochemical setup requires shielding with a properly grounded Faraday cage so that the stray electrical noise is filtered from interfering with the charge within the cage, i.e., the electrochemical cell. A faraday cage is a container made of a conductive material such as a metallic mesh or metallic plates or a box covered with metallic foils such as

aluminium. An essential requirement in the faraday cage design is that the opening in the faraday cage should be minimal as the wavelength of the noise entering through the opening is twice that of the opening, including the noises with smaller wavelengths. Figure 3.7 (b) shows the improvement in the electrochemical data quality with proper shielding using a grounded Faraday cage.

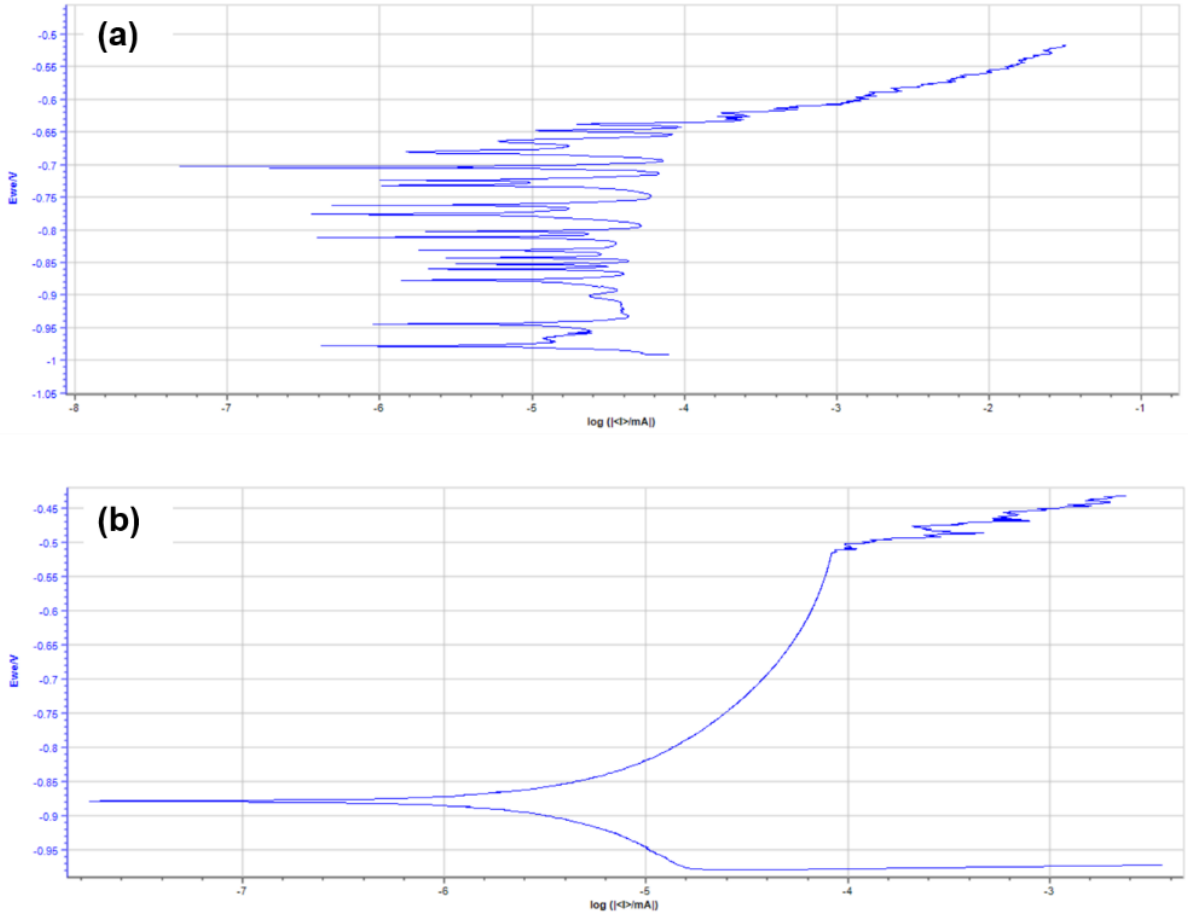

Figure 3.7. Comparison of the potentiodynamic polarisation data generated (a) in the absence of and (b) in the presence of proper grounding and Faraday cage shielding.

In order to sense the small current, with amplitudes as low as nA to pA at the small surface area of the electrodes, the Saturated Calomel Electrode (SCE) was placed in a luggin (luggin gel made from agar-agar and KCl) with the luggin tip placed in the best proximity to the electrode surface. This setup also helped to overcome any possible ohmic drop during the electrochemical measurements. The Pt-mesh used as the counter electrode was also placed closer to the working electrode surface.

3.7. Setup for electrochemical testing and in situ optical imaging

The electrochemical cell for in the situ optical timelapse imaging during potentiostatic testing was 3D printed using Created Pro Flashforge (Monash University, Australia). The photograph of the cell used in the present study is shown in Figure 3.8.

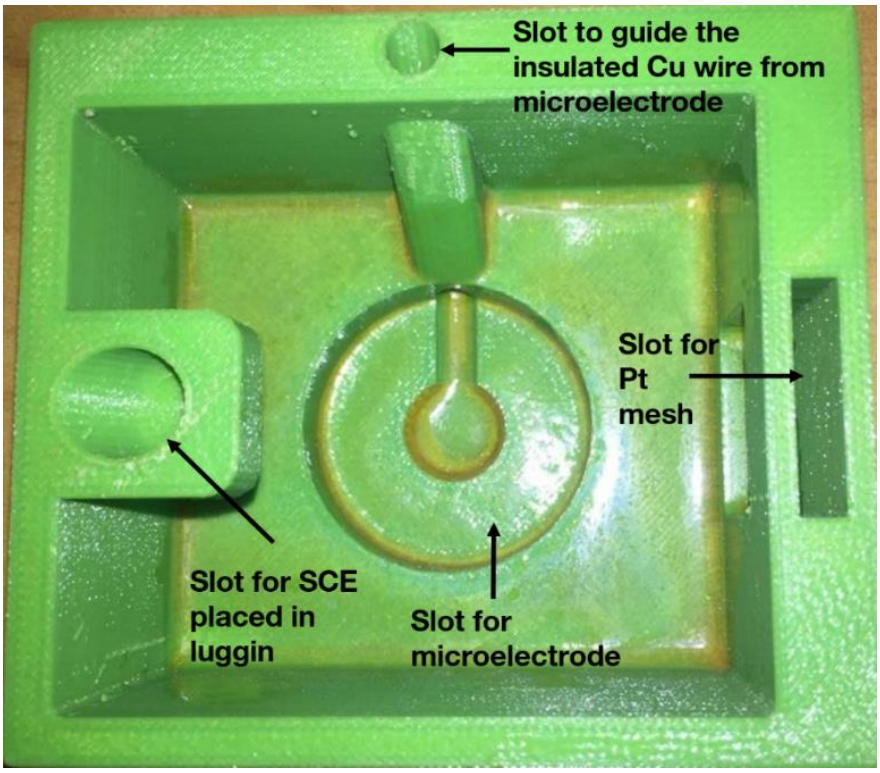

Figure 3.8. Top view of the 3D printed electrochemical cell.

The mounted microelectrode specimen was placed in an up-facing position with its insulated copper wire guided through the socket at the edge of the cell. The SCE placed in a luggin was used as the reference electrode. The platinum mesh used as the counter electrode was extended through its slot shown in Figure 3.8 to the proximity of the working electrode. The electrolyte for all the studies was chosen as 50 ml of 0.01 M NaCl (prepared with millipore water) exposed to ambient conditions. The fill height of the electrolyte over the electrode surface was optimised to 8 mm ± 1 mm. Below this fill height or solution thickness (i.e., the thickness of the electrolyte above the specimen surface), the electrochemical data was not repeatable due to the effect of the thin electrolyte layer. The whole electrochemical setup was placed inside a grounded Faraday cage during electrochemical experimentation. The SCE placed in the luggin was calibrated against the mother/master SCE reference electrode regularly to ensure its reliable operation.

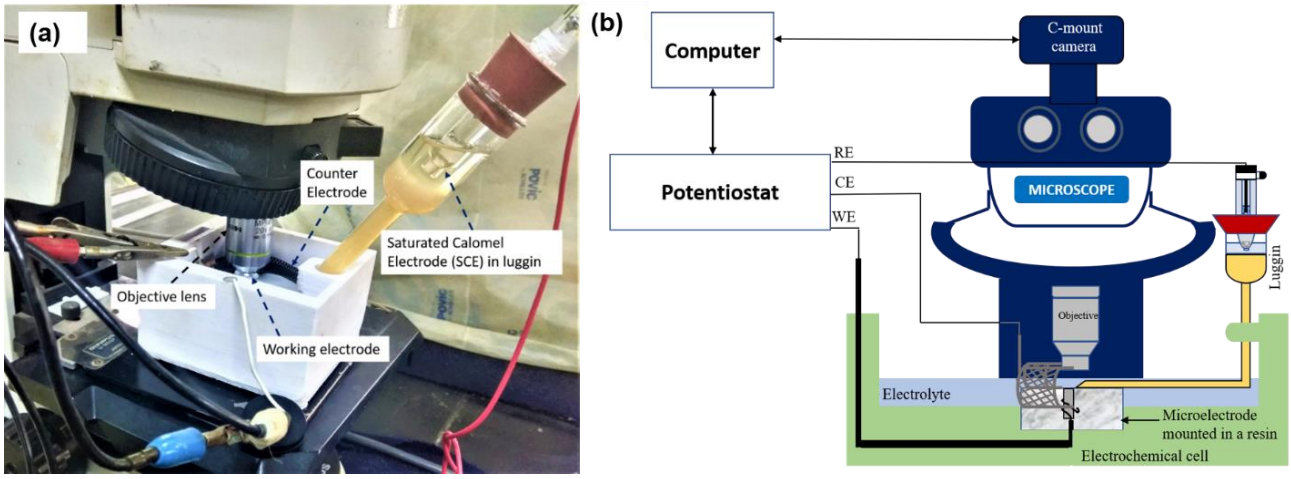

Figure 3.9. (a) The photograph and (b) schematic illustration of the electrochemical cell setup used for potentiostatic polarisation and in situ imaging combination studies.

The photograph and schematic illustration of the experimental set-up used for performing in-situ optical imaging of the electrode surface during electrochemical testing is shown in Figure 3.9. Electrochemical studies were performed using Gamry® Reference 600 potentiostat, which was calibrated periodically. In situ optical 2D timelapse imaging of the entire electrode surface was carried out using an Olympus upright microscope (Model BX41M-LED) fitted with a Tucsen ISH 500 camera. The light source in the optical microscope was chosen as LED instead of a halogen lamp so that the temperature of the electrolyte is not affected and subsequently the electrolyte does not evaporate during the course of testing. The objective lens of type MPLN5X/0.1∞/-/FN22 or MPLN10X/0.25∞/-/FN22, which provided a magnification of 50X or 100X, respectively, was employed. The choice of the objective lens depended on the dimensions of the electrode used for the study. The video was recorded at a rate of ~ 3 frames per second (fps) with a resolution of 2584 x 1936 pixels. The video was compressed using Xvid 1.1.3 software and later sequentially decoded by frames at the required timescale for image analysis.

3.8. Potentiodynamic polarisation

The open circuit potential (OCP) was allowed to stabilise for 900 s before the initiation of polarisation. Potentiodynamic polarisation experiments were performed using the 'Gamry Framework' interface wherein the potential was scanned at a forward scan rate of 0.5 $mV.s^{-1}$ from – 100 mV vs OCP until a current density of 1 $mA.cm^{-2}$ was reached. The potentiodynamic

polarisation experiments allowed the determination of E_{pit} so that the test potential for subsequent potentiostatic experiments could be chosen. The minimum value (excluding outliers) of E_{pit} determined from a dataset of 15 experiments was chosen as the reference E_{pit} so that the probability of the onset of stable pitting during potentiostatic metastable testing can be reduced.

3.9. Potentiostatic polarisation

Potentiostatic polarisation experiments were carried out at E_{pit} – 25 mV with data points recorded at a frequency of 10 Hz. This test potential was chosen based on the preliminary experiments that revealed that this potential could generate current transients associated with the different pitting stages, i.e., pit nucleation, metastable and quasi-stable pit events (discussed further in Section 3.12). The selected potential also enabled the generation of visible hydrogen bubbles at the metastable pit locations, as discussed further in Chapter 4. At least 30 experiments were carried out on each alloy specimen.

3.10. In situ visualisation of pit events and their analysis

The pits in aluminium are known to evolve anomalous hydrogen at anodic potentials due to a mechanism termed the Negative Difference Effect (NDE) [Frankel et al. 2015]. This phenomenon was employed to visualise the metastable pit locations in situ based on the hydrogen bubbles evolving from their locations.

The timelapse video recorded by the camera was compressed using Xvid 1.1.3 software facilitated by the camera software TC Capture. The time lag between the electrochemical signal and imaging was calibrated at the beginning and during the experiment by comparing the timestamp of the data from the potentiostat and camera to ensure that it does not exceed 0.1 s. This video was later analysed using Movavi Video Suite 18 by sequentially decoding the video by frames. The critical parameters from the in situ timelapse images required for investigating metastable pitting, namely the diameter of the bubble (d_{bubble}) and the locations undergoing metastable pitting were analysed using the ImageJ image analysis software. The scale bar for analysing the video snapshots required calibration using a standard sample. For this purpose, the image of a steel ruler was recorded using a calibrated camera attached to a standard microscope. From the scale bar provided by this microscope and the dimensions in the ruler,

the scale bar for the snapshots in the video was calibrated. The d_{bubble} was calculated from the average of the values determined by three methods: (a) an average was calculated from the largest vertical and horizontal dimensions of the bubble, (b) the image was inverted to a gray-value image from which the average of the largest vertical and horizontal dimensions were calculated, (c) the circumference of the bubble was measured and the radius of the bubble (r_{bubble}) was calculated uring the formula: circumference of the bubble = $2\pi r_{bubble}$. The pit locations on the sample surface were mapped using the 'analysis using grids' option in the ImageJ software. For the dissertation, results from 15 repeatable experiments performed on each alloy specimen of interest have been reported.

3.11. Bubble dynamics and its analysis

The evolution of current transients was associated with the simultaneous growth and dissolution of adsorbed hydrogen bubbles at the respective metastable pit locations. Since the objective of this dissertation resides in understanding the metastable pitting characteristics from the HE occurring at the pit locations, the dynamics of bubble evolution requires critical consideration. The following text presents a brief overview of the dynamics of hydrogen bubble evolution at a pit location.

The faradaic current from the pit dissolution drives the electrogeneration of hydrogen by NDE [Frankel et al. 2015]. Within the V_{pit}, the electrogenerated hydrogen is initially present in its dissolved form, which later nucleates as a hydrogen bubble when its concentration exceeds supersaturation [Epstein et al. 1950]. Therefore, the formation of a hydrogen bubble within a pit is a combination of both the electrochemical and physicochemical factors. Therefore, the d_{bubble} at any instant varies as a function of the supersaturation concentration of hydrogen within the V_{pit}, rate of generation of hydrogen and the rate of its dissolution. Upon cessation of faradaic current from pit dissolution current, the electrogeneration of hydrogen and therefore its feed into the bubble are curbed. This phenomenon leads to the chemical dissolution of the bubble into the electrolyte resulting in its shrinkage and disappearance.

The parameters associated with HE were determined as follows. The cumulative d_{bubble} maybe calculated from the sum of the maximum d_{bubble} and the subsequent increments in d_{bubble}. The estimation of the volume of hydrogen ($V_{HE,bubble}$) from d_{bubble}

requires an assumption of the bubble shape as the contact angle of the bubbles with the pit surface was not measured due to experimental limitations. Since the hydrogen bubbles remained adsorbed to the surface, their three-dimensional shape would be a segmented sphere [Glas et al. 1964]. Yang et al. reported that the contact angle of electrogenerated hydrogen bubbles adsorbed to a Pt electrode surface for a maximum instantaneous d_{bubble} of 50 μm recorded in the present study, was ~ 100° through the liquid [Yang et al. 2015]. They also reported that this value would change dynamically depending on the electrode material, bubble growth rate, and radius. Herein, for the sake of simplification and to assume a worst-case scenario, the geometry of the adsorbed hydrogen bubbles was considered as a complete sphere so that an extreme case representing maximum $V_{HE,bubble}$ is accounted for. Accordingly, the volume of the hydrogen bubble ($V_{HE,bubble}$) may be calculated using Equation 3.1.

$$V_{HE,bubble} = \frac{4}{3} \times \pi \times \left(\frac{d_{bubble}}{2}\right)^3 \qquad \textit{Equation 3.1}$$

For the hydrogen evolution reaction as per Equation 3.2,

$$2H^+ + 2e^- \rightarrow H_2 \qquad \textit{Equation 3.2}$$

the charge consumed by hydrogen evolution (C_{HE}) may be calculated from Equation 3.3.

$$C_{HE} = \frac{z_{HE} F V_{HE}}{22.4 \times 10^3} \qquad \textit{Equation 3.3}$$

wherein z_{HE} = 2, F is the Faraday constant with a value of 96485.33 C.mol^{-1} and the value 22.4 × 10^3 cm^3 in the denominator represents the volume (in cm^3) occupied by 1 mol of H_2 at STP.

The instantaneous HE current density (i_{H_2}) was determined from the instantaneous area of the pit (A_{pit}) and instantaneous C_{HE} calculated from the instantaneous change in d_{bubble} (i.e., $d_{bubble,t=x+j} - d_{bubble,t=x}$; wherein j is the interval of time). Herein, the instantaneous A_{pit} represents the hemispherical surface area of the pit calculated from the C_{pit} accumulated by the transient until the specified instant, $t = x$ (as discussed further in Section 3.13).

3.12. Analysis of potentiostatic polarisation data

The schematic illustration of a typical current transient with its characteristic parameters is shown in Figure 3.10. The following parameters are described: $I_{passive}$ is the background passive current, I_x is the current at any instant $t = x$ along the transient, I_{pit} is the instantaneous pit current at any point along the current transient determined from the relation: $I_{pit} = I_x - I_{passive}$, I_{peak} is the peak current determined from the relation: $I_{peak} = I_{x,peak} - I_{passive}$, t_g is the pit growth time (i.e., the time required for I_{pit} to reach I_{peak}), t_r is the pit repassivation time (i.e., the time required for I_{pit} to reach $I_{passive}$ from I_{peak}), t_{pit} is the pit lifetime wherein $t_{pit} = t_g + t_r$. Segregation and counting of the individual current transients from the noise in the $i_{passive}$ was accomplished using an automated script based on the criteria developed by Cavanaugh et al. [Cavanaugh 2009b] and later described by Sander et al. [Sander et al. 2020]. According to these criteria, the current transients should satisfy the following conditions for it to be treated as a signal arising from metastable pits: (a) The current density increases by at least 1.5% from $I_{passive}$, (b) the t_{pit} > 1.5 s, (c) the current density decreased to 1.5% from $I_{passive}$ after reaching I_{peak}. The pitting rate was calculated from the number of current transients recorded per second per square centimetre of the electrode surface.

Current transients may be classified based on the nature of pit propagation and the recovery of I_{pit} to $I_{passive}$ at the end of the current transient as follows: (i) pit nucleation transients if $I_{passive,end} \leq I_{passive,begin}$ with no apparent propagation (Figure 3.10) (ii) metastable transients if $I_{passive,end} \leq I_{passive,begin}$ and exhibits propagation (Figure 3.11 (a)), (iii) quasi-stable transients if $I_{passive,end} > I_{passive,begin}$ (Figure 3.11 (b)) and (iv) stable pit events when there is no apparent current transient but an abrupt and drastic increase in the noise and absolute value of $I_{passive}$ (Figure 3.11 (c)). Quasi-stable transients have been deemed as stable transients in literature [Gupta et al. 2012]. However, in the present work, they have been explicitly termed as 'quasi-stable transients' (Figure 3.11 (b)) to unambiguously distinguish them from stable pitting (Figure 3.11 (c)).

The single peaked transients may also be classified depending on the relative durations of pit growth time (t_g) and pit repassivation time (t_r) as (i) Type I if $t_g > t_r$ (Figure 3.12 (a)), (ii) Type II if $t_g < t_r$ (Figure 3.12 (b)). The transients that exhibited multiple peaks, i.e., more

than one peak with a current amplitude ≥ 75% of I_{peak}, were not classified under the above-stated categories and may be designated as 'unclassified' (Figure 3.12 (c)). The classification of current transients based on the type of pit propagation (nucleation/metastability/quasi-stability) enables an understanding of the extent of repassivation. In contrast, the shape (Type I / II or unclassified) of the transients provides insights regarding the relevant pitting mechanism.

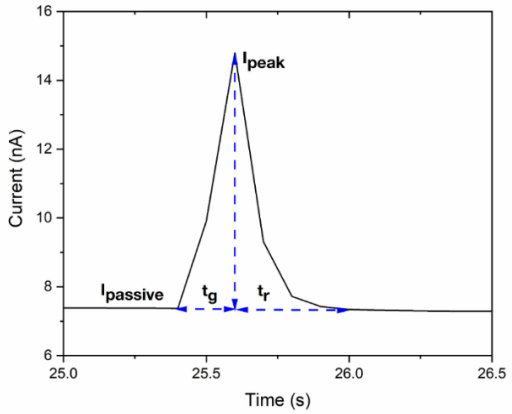

Figure 3.10. A typical (pit nucleation) current transient with its respective metastable pitting parameters.

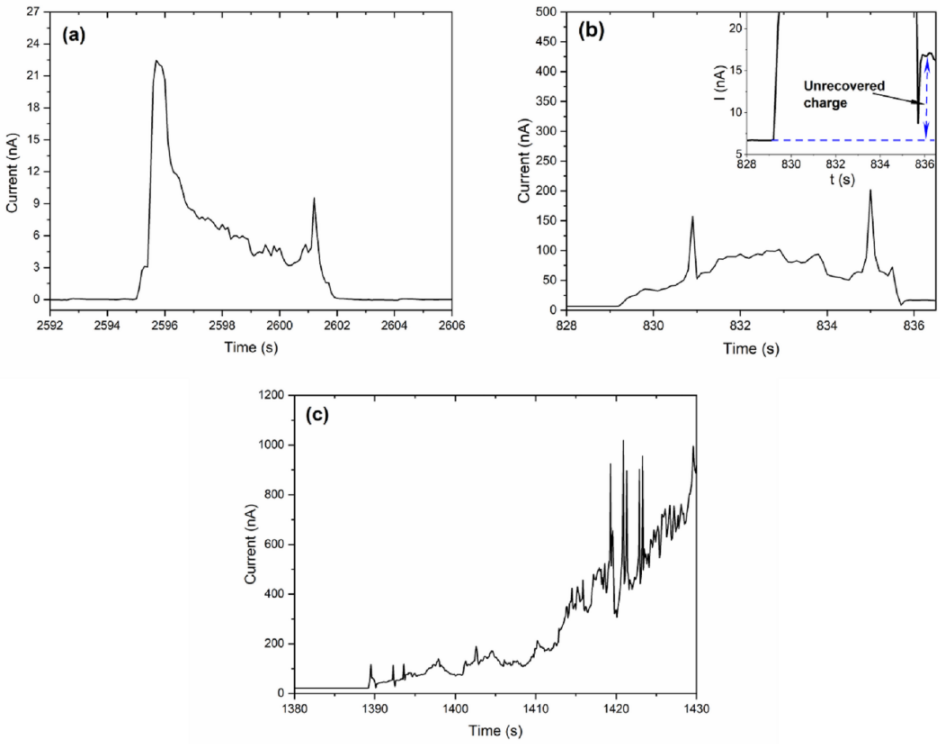

Figure 3.11. The different types of current transients depending on the recovery of $I_{passive}$ at the end of the current transient (a) metastable transient, (b) quasi-stable transient and (c) stable pitting.

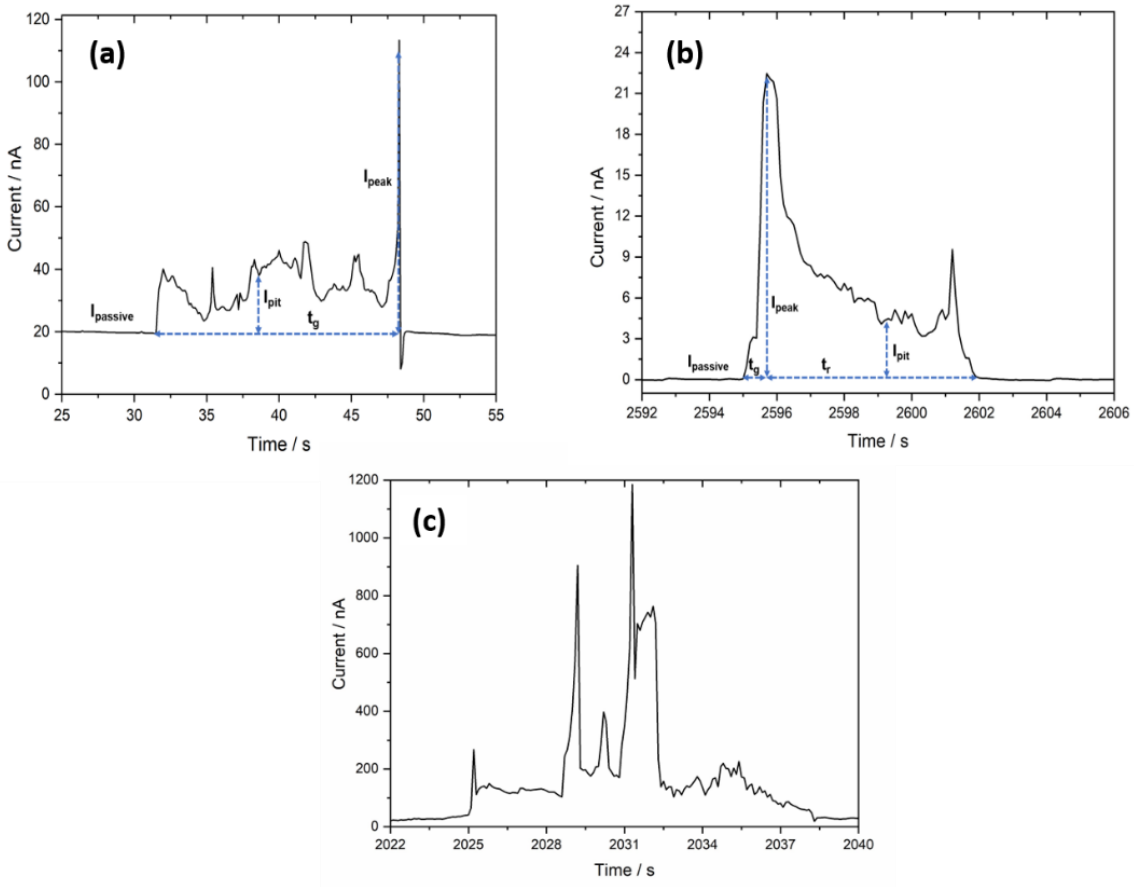

Figure 3.12. The different types of current transients depending on the relative values of t_g and t_r (a) Type I, (b) Type II and (c) Type unclassified.

3.13. Determination of the pit dissolution charge (C_{pit})

The charge accumulated by the current transient ($C_{transient}$), determined by integrating the area under the I-t curve, may be employed in the determination of pit volume (V_{pit}) and its equivalent hemispherical pit radius (r_{pit}). A detailed account of the various steps involved in this estimation is presented below.

Commercially pure aluminium undergoes pitting by the dissolution of Al-rich matrix as per Equation 3.4, under the influence of Al_3Fe constituent particles.

$$Al \rightarrow Al^{3+} + 3\,e^{-} \qquad \textit{Equation 3.4}$$

Binary Al-Mg alloys undergo pitting corrosion by the selective dissolution of Mg_2Al_3 (β) phase-precipitates as they are highly electronegative [Lyndon et al. 2013]. The β phase-precipitates may also undergo incongruent dissolution by the selective leaching of Mg [Liu et al. 2009; Liu et al. 2010]. In the present study, the pitted locations revealed trenches (upon microscopic investigation), indicating that the entity had undergone complete dissolution. Hence, the β phase-precipitates may be assumed to have undergone congruent dissolution as per Equation 3.5.

$$Mg_2Al_3 \rightarrow 2\,Mg^{2+} + 3\,Al^{3+} + 13\,e^- \qquad \textit{Equation 3.5}$$

In the binary Al-Mg alloy, though the pits may initiate preferentially at the β phase-precipitates, the surrounding Al-rich matrix (according to Equation 3.4) and the neighbouring β phase-precipitates may also undergo subsequent dissolution. This fact is evident from the magnitude of the $C_{transient}$, recorded in the present study, which is significantly larger than the minimum charge required for the dissolution of single β phase-precipitates (~2.8 pC [Guan et al. 2015]).

The total pit dissolution charge (C_{pit}) may be calculated from the sum of C_{HE} (from Equation 3.3) and $C_{transient}$ as per Equation 3.6.

$$C_{pit} = C_{transient} + C_{HE} \qquad \textit{Equation 3.6}$$

The pit volume ($V_{pit,y}$; wherein $y = \beta$ or the Al-rich matrix depending on the species undergoing dissolution) can be calculated using Faraday's law from C_{pit} using Equation (3.7).

$$V_{pit,y} = \frac{C_{pit}.\mathrm{M}}{z_y \rho \mathrm{F}} \qquad \textit{Equation 3.7}$$

wherein M and ρ are the molar mass and density of the dissolving entity, respectively and z_y (wherein $y = \beta$ or the Al-rich matrix depending on the species undergoing dissolution) is the no. of electrons generated during dissolution. The values associated with these parameters for an exclusive dissolution of the β phase-precipitate (according to Equation 3.5) are M = 129.55 $g.mol^{-1}$, ρ = 2.24 $g.cm^{-3}$ and z_β = 13 while that for an exclusive dissolution of the Al-rich matrix (according to Equation 3.4) are M = 26.98 $g.mol^{-1}$, ρ = 2.70 $g.cm^{-3}$ and z_{matrix} = 3. The corrected V_{pit} ($V_{pit,corrected}$) for the dissolution of the β phase-precipitates in Al – 5 Mg should lie between $V_{pit,\beta}$ and $V_{pit,matrix}$ depending on the percentage contribution of the β phase and the

Al-rich matrix to the C_{pit}. An exclusive dissolution of the Al-rich matrix in this case, i.e., $V_{pit,matrix}$ calculated from 100% C_{pit} would result in a negative difference of ~ 33.33% as compared to $V_{pit,\beta}$ determined from an exclusive dissolution of the β phase, such that $V_{pit,\beta} \geq V_{pit,corrected} \geq 0.67\ V_{pit,\beta}$.

The pit geometry was assumed to be a hemisphere with its entire surface area being active for dissolution. Therefore, the pit radius, $r_{pit,y}$ (wherein $y = \beta$ or the Al-rich matrix depending on the species undergoing dissolution) equivalent to $V_{pit,y}$ may be calculated using Equation 3.8. A change in the assumption from an exclusive dissolution of β phase-precipitate to an exclusive dissolution of the Al-rich matrix in the Al – 5 Mg alloy introduces a negative error of ~ 9.97% in the $r_{pit,\beta}$. Accordingly, the corrected r_{pit} ($r_{pit,corrected}$) depending on the percentage contribution of the β phase and the Al-rich matrix would be $r_{pit,\beta} \geq r_{pit,corrected} \geq 0.9\ r_{pit,\beta}$.

$$r_{pit,x} = \left(\frac{3}{2} \times \frac{1}{\pi} \times V_{pit}\right)^{1/3} \qquad \textit{Equation 3.8}$$

The active pit surface area (A_{pit}) of the hemispherical pit may be determined from $r_{pit,x}$ using Equation 3.9.

$$A_{pit} = 2 \times \pi \times r_{pit,x}^2 \qquad \textit{Equation 3.9}$$

The instantaneous pit current density (i_{pit}) was calculated from the instantaneous change in I_{pit} (i.e., $I_{pit,t=x+j} - I_{pit,t=x}$; wherein j is the interval of time) and instantaneous A_{pit}. Herein, the instantaneous A_{pit} represents the hemispherical surface area of the pit calculated from the C_{pit} accumulated by the transient until the specific instant, $t = x$.

The pit stability value can be determined from the ratio of I_{peak} and the pit radius at I_{peak} ($r_{pit,peak}$) as shown in Equation 3.10. The $r_{pit,peak}$ was estimated from the charge accumulated by the transient at I_{peak}.

$$\text{Pit stability value} = \frac{I_{peak}}{r_{pit,peak}} \qquad \textit{Equation 3.10}$$

The pit growth rate may be determined from the ratio of I_{peak} and t_g as shown in Equation 3.11.

$$\text{Pit growth rate} = \frac{I_{peak}}{t_g} \quad (3.10)$$

3.14. Post-mortem studies

After potentiostatic testing, the samples were ultrasonically cleaned for 300 s to remove any remnant corrosion products. The pits on the electrode surface associated with the current transients of interest were investigated ex-situ using SEM (Hitachi S3400 N). This investigation did not require applying a conductive coating to overcome charging arising from the surrounding resin, allowing a detailed investigation of the pit locations. In secondary electron (SE mode), the pit locations were analysed to gather information regarding the pit mouth dimension, geometry and pit location. In BSE mode, the area surrounding the pit location was analysed to investigate the presence of second phase particles that could have initiated the pit. In Al-5Mg, the BSE mode of investigation did not provide any critical insights as the precipitates did not provide a phase-contrast without etching.

The 3D optical profilometer (Alicona Infinitefocus) was used to determine the actual 3D pit volume ($V_{pit,actual}$) at the pit location of the metastable pit associated with its respective current transient. During analysis, the sample was first focused and the pit was located at low magnification. Subsequently, the analysis was carried out at higher magnification, i.e., at 1000X. The software was used to correct the surface tilt and then measure the depth after averaging the surface roughness to zero. The 3D images of the pits and their depth profiles were recorded. Later, the $V_{pit,actual}$ was measured and employed to compare it against the V_{pit} estimated the current transients using Faraday's law.

Chapter 4

A novel approach for the in situ visualisation of metastable pitting events from hydrogen evolution

4.1. Background

Pitting corrosion is a dynamic process governed by a favourable combination of thermodynamic and kinetic conditions. Several factors, such as the presence of locally distinct passive film characteristics [Szklarska-Smialowska 1999], heterogeneous microstructures [Birbilis et al. 2005] and surface roughness [Burstein et al. 1995a], influence the evolution of pit events, making the deterministic prediction of the pitting sites in real-time elusive. Recently, Sander et al. 2020 visualised the evolution of metastable pit events in-situ in stainless steel. In aluminium and its alloys, the optical visualisation of pit evolution is further obscured by the presence of reflective pit covers [Frankel 1998] over the pit mouth. These challenges are augmented during metastable pitting as the metastable pit events are short-lived (few seconds) and occur in small sizes (few micrometres).

Owing to the intricacies involved in the direct in situ visualisation of pit events in aluminium, researchers adopt an indirect approach wherein the pit locations are mapped based on the factors that change during pitting, such as the pH and current. Ellipsometry is the most widely adopted in situ visualisation technique (NASA-CR-132301) but is limited by the complexities involved in determining the ellipsometric parameters for pit propagation [Kruger et al. 1976]. Scanning electrochemical and micro-electrochemical methods enable mapping the local current densities or potential differences that evolve during pitting corrosion [Böhni et al. 1995]. Zhu et al. successfully demonstrated that the locations that exhibited higher local

‡*G. Sridhar, N. Birbilis and V.S. Raja, CORROSION (Revision).*

$i_{passive}$ values were the exact locations that eventually underwent pitting at higher anodic potentials [Zhu et al. 1997]. Despite the advantages, the utilisation of scanning and micro-electrochemical methods to investigate metastable pitting is limited by the excessive time required for scanning the surface that fails to capture the dynamic metastable pit events. Isaacs visualised the pit events in situ based on the pH changes that occur during pitting using pH-sensitive agar gels [Isaacs et al. 2000]. Büchler et al. used fluorescent dyes to study the evolution of pit events in situ [Büchler et al. 2000]. These methods may alter the natural corrosion response of the alloy due to the ambiguities introduced, such as crevice corrosion in the case of pH-sensitive gels and the interaction of dyes with the surface. Ilevbare et al. employed in-situ confocal laser scanning microscopy to study pitting corrosion in AA 2024-T3 from the in situ 3D surface profiles [Ilevbare et al. 2004].

As discussed in the preceding paragraph, the conventional techniques adopted for the in situ visualisation of pit events in aluminium alloys pose limitations for mapping the dynamic metastable pit events. Further, these techniques do not permit evaluation of the hydrogen evolving at the pit surface during active pitting. For this purpose, a simple methodology that can facilitate both the mapping of metastable pit events and an in situ evaluation of the hydrogen evolution at the metastable pit locations needs to be developed.

Hydrogen evolution during the pitting corrosion of aluminium and its alloys is a well-known phenomenon [Kaesche 1962; Bargeron et al. 1980a]. At anodic potentials, HE occurs from the active pit surface as a consequence of anodic dissolution [Frankel 1990] rather than on the passive film as a cathodic reaction. This phenomenon of an anomalous increase in HE rates with anodic potentials, counterintuitive to the Tafel rate equation, in aluminium and other metals such as magnesium is termed the Negative Difference Effect (NDE) [Frankel et al. 2015]. Recently, Frankel et al. suggested that the mechanism behind such superfluous HE during NDE was the enhanced catalytic nature of the pit surface for HE that develops as a consequence of anodic dissolution [Frankel et al. 2015]. The present study explores the utilisation of hydrogen bubbles evolving at the metastable pit locations to investigate their dynamic evolution and map their locations.

4.2. Objective

Develop an in situ visualisation method to map the dynamic metastable pit locations in situ to correlate them with their respective current transients. For this purpose, pure aluminium (referred to as pure Al), solutionised Al-5Mg (referred to as soln. Al-5Mg) and aged Al-5Mg (referred to as Al-5Mg) specimens were used.

4.3. Results and discussion

4.3.1. Preliminary electrochemical characterisation

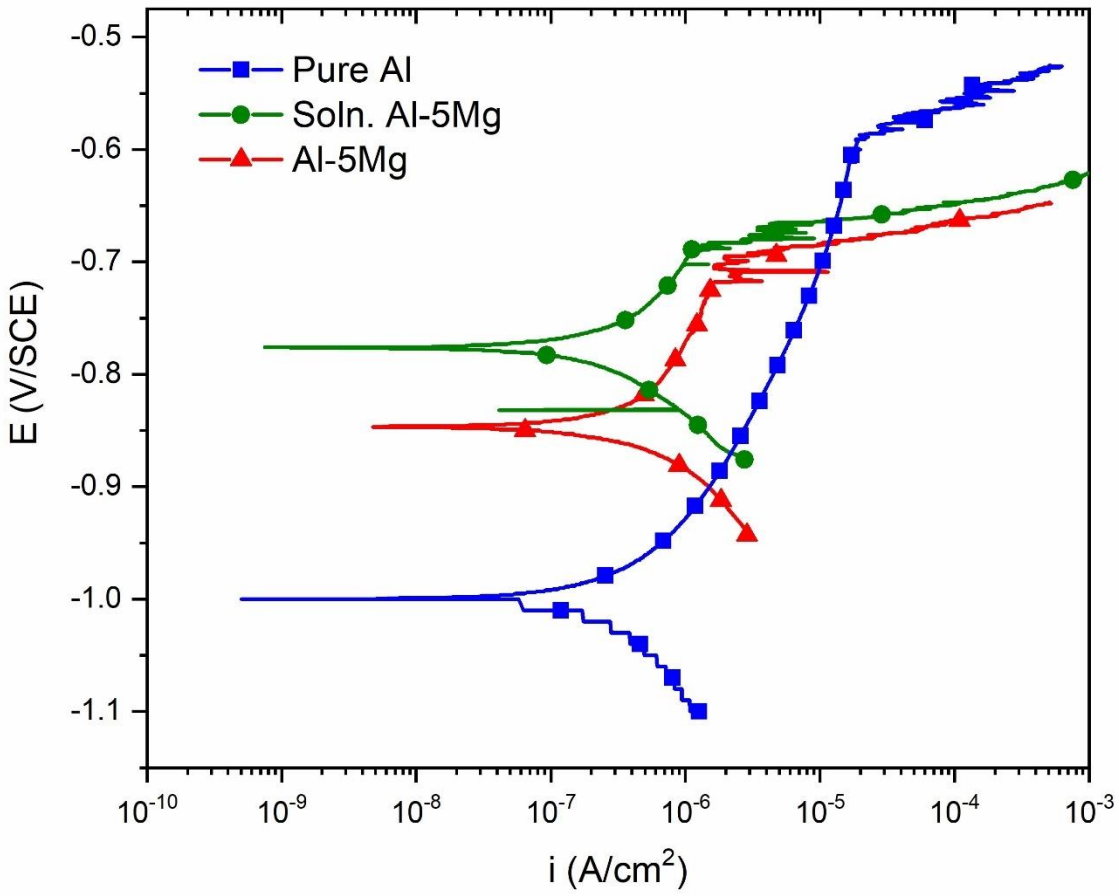

Figure 4.1. The potentiodynamic polarisation plot of pure Al, soln. Al-5Mg and Al-5Mg specimens used herein.

The potentiodynamic polarisation response of pure Al, soln. Al-5Mg and Al-5Mg alloy specimens used in this study are shown in Figure 4.1. The E_{pit} of these specimens is shown in Table 4.1.

Table 4.1. The pitting potential (E_{pit}) of pure Al, soln. Al-5Mg and Al-5Mg determined from the potentiodynamic polarisation plots shown in Figure 4.1.

Sl. No	Specimen	E_{pit} (mV) vs SCE
1	Pure aluminium	- 593 ± 13
2	Solutionised Al – 5 Mg	- 679 ± 37
3	Al – 5 Mg	- 710 ± 32

4.3.2. Requirements

Signal to noise ratio

The current transients of the metastable pitting events range in the order of pA to nA. These electrochemical signals are lost within the stray electrical noise (from gadgets) surrounding the electrochemical cell when the amplitude of the stray noise is greater than that of the current transients, as discussed in Chapter 3. For this purpose, a grounded Faraday cage was placed around a properly grounded electrochemical cell in the present study.

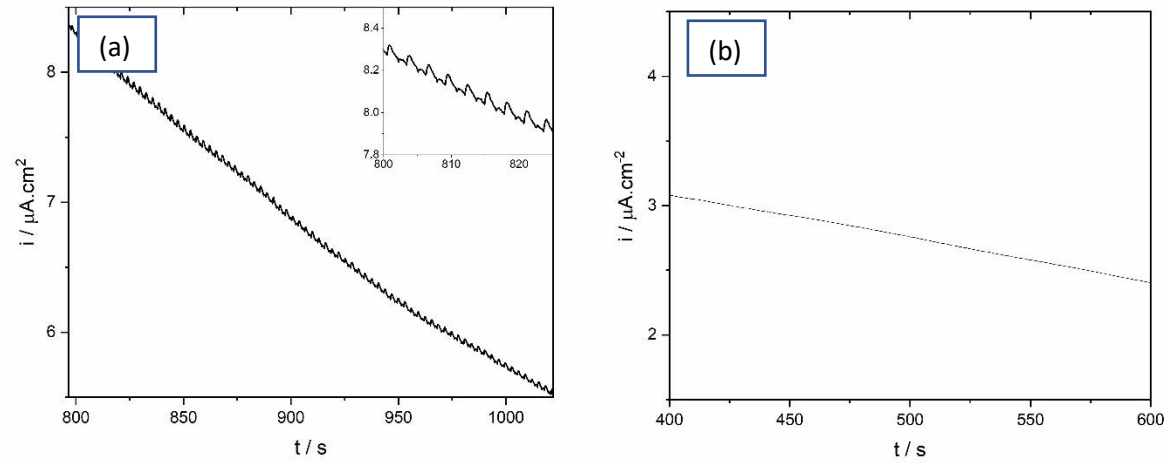

Figure 4.2. The potentiostatic polarisation data of pure aluminium recorded (a) without a Faraday cage and (b) with a Faraday cage at E_{pit} – 50 mV in 0.01 M NaCl.

Figure 4.2. shows the comparison of the potentiostatic polarisation data of pure aluminium recorded at E_{pit} – 50 mV in 0.01 M NaCl with and without proper grounding. The inset in Figure 4.2(a) shows periodic oscillations in the $i_{passive}$ associated with the stray electrical noise. With proper grounding, such oscillations disappeared in the potentiostatic trend, as witnessed from Figure 4.2 (b). Optimising the signal-to-noise ratio is, therefore, vital

during the investigation of metastable pitting so that the spikes arising from the stray electrical noise are not misinterpreted as metastable pits. The signal-to-noise ratio may also be enhanced by optimising the 'Bandwidth' option in the potentiostat.

Electrolyte selection

The aggressiveness and conductivity of the electrolyte are important factors to be considered during electrolyte selection. The aggressiveness of the electrolyte determines the MPR and extent of pit propagation, while the conductivity of the electrolyte plays a vital role in reducing the solution resistance and enabling reliable measurement of the electrochemical signals. Less aggressive solutions (such as 10 µM NaCl) significantly reduce the probability of metastable pitting events. Figure 4.3 and Table 4.2 present the potentiostatic polarisation data of soln. Al-5Mg recorded at E_{pit} – 25 mV in 0.05 M NaCl vs 0.01 M NaCl. The data demonstrate that reduction in the [Cl^-] reduced the MPR and resulted in spatially resolved transients.

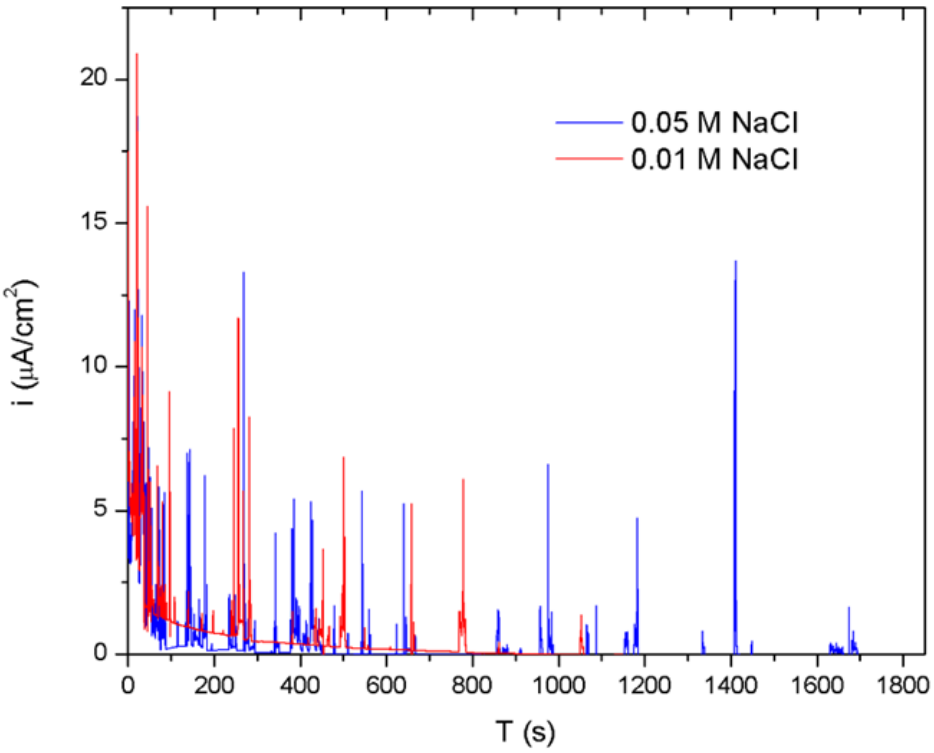

Figure 4.3. The potentiostatic polarisation data of soln. Al-5Mg recorded in 0.01 M NaCl vs 0.05 M NaCl at E_{pit} - 25 mV.

Table 4.2. The potentiostatic polarisation data of soln. Al-5Mg recorded in 0.01 M NaCl vs 0.05 M NaCl at E_{pit} - 25 mV.

NaCl concentration (M)	**0.05 M NaCl**	**0.01 M NaCl**
MPR ($cm^{-2}.s^{-1}$)	27 ± 5	14 ± 2

On the contrary, aggressive solutions such as (0.1 M NaCl) increase the probability of stable pitting during metastable pitting investigation. Figure 4.4 presents the potentiostatic polarisation response of pure aluminium at E_{pit} – 25 mV in 0.1 M NaCl. The figure illustrates that the electrochemical noise arising from the propagation of a stable pit event (I_{pit} ranging in the order of µA) masked the signals from metastable pitting events (I_{pit} ranging in the order of nA to pA) and thereby limits the effective investigation of metastable pitting events.

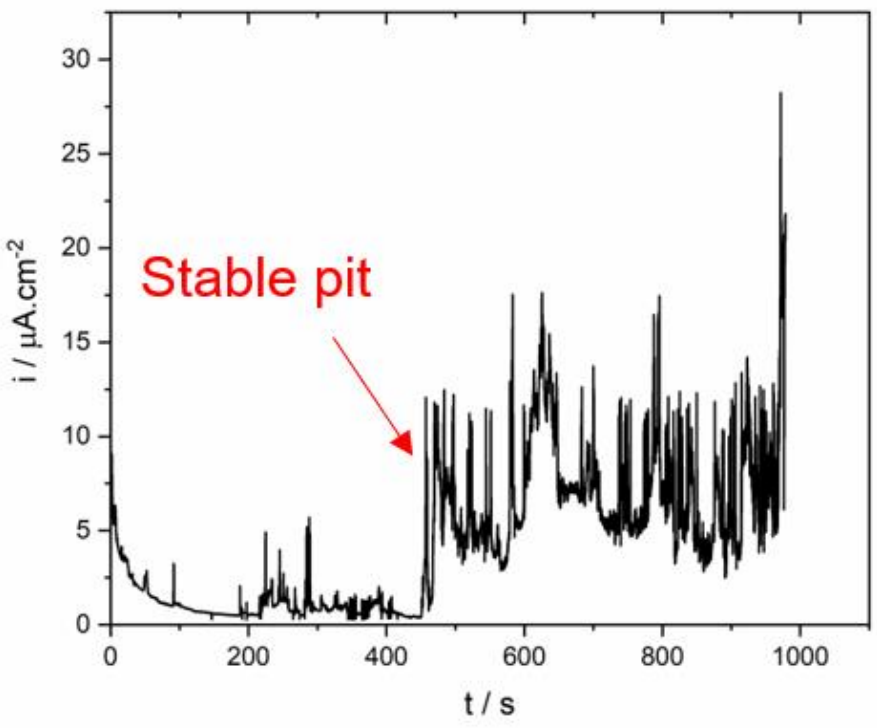

Figure 4.4. The potentiostatic polarisation data of pure aluminium recorded at E_{pit} - 25 mV in 0.1 M NaCl.

The foregoing discussions signify the need for trial-and-error experiments to optimise the electrolyte composition. With preliminary studies, the concentration of NaCl for the present study was optimised as 0.01 M.

Potential

The selection of an optimum polarisation potential is essential for the following reasons: (i) the MPR scales down with the applied polarisation potential [Pride et al. 1994] and (ii) the hydrogen evolution decreases as a function of applied potential [Cook et al. 2012]. At larger underpotentials to E_{pit}, metastable pitting becomes a rare event and at potentials closer to E_{pit}, the probability of stable pitting increases. Therefore, optimising the applied potential is essential for generating an optimum number of measurable and temporally resolved current transients. Figure 4.5 demonstrates this phenomenon with the potentiostatic polarisation data of pure aluminium recorded at E_{pit} - 100 mV and E_{pit} – 25 mV in 0.01 M NaCl. Figure 4.5 (a) recorded at E_{pit} – 100 mV demonstrates that the metastable pitting is a rare event whereas Figure 4.5 (b) recorded at E_{pit} - 25 mV exhibits an optimum number of both pit nucleation and pit propagation transients (as shown in Figure 3.12 (c)). Table 4.3 presents the comparison of the MPR for the potentiostatic polarisation data presented in Figure 4.5.

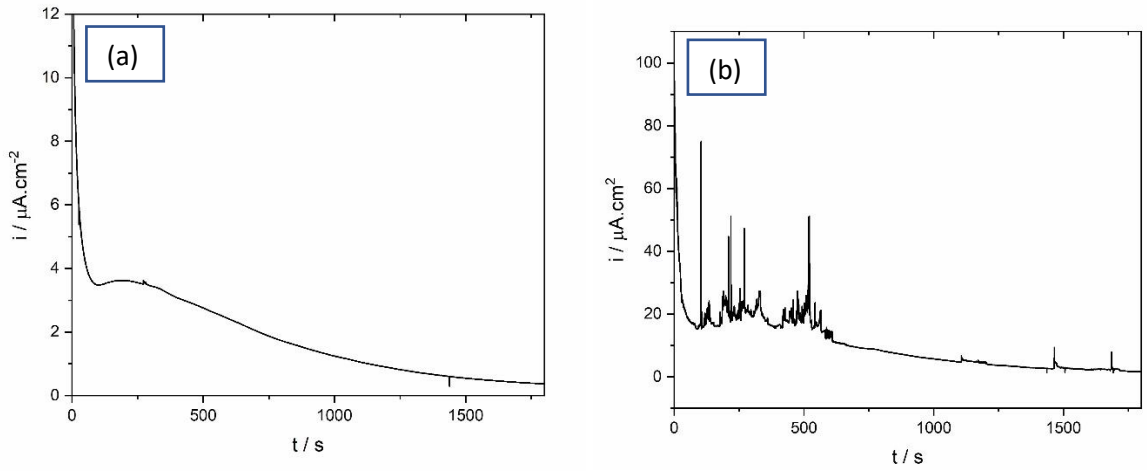

Figure 4.5. The potentiostatic polarisation data of pure aluminium recorded in 0.01 M NaCl at (a) E_{pit} - 100 mV and (b) E_{pit} - 25 mV

Table 4.3. The potentiostatic polarisation data of pure aluminium recorded at E_{pit} – 100 mV and E_{pit} – 25 mV in 0.01 M NaCl

Polarisation potential (V)	**E_{pit} – 100 mV**	**E_{pit} – 25 mV**
MPR ($cm^{-2}.s^{-1}$)	0.02 ± 0.001	8 ± 0.9

The hydrogen evolution decreases as a function of applied potential [Cook et al. 2012]. Therefore, to generate visually resolvable hydrogen bubbles at the metastable pit locations to enable their mapping, the applied polarisation potential should be above E_r. From preliminary experiments, a threshold potential was observed to be associated with the generation of pit propagation transients which was in agreement with the E_r reported in other studies [Pride et al. 1994].

Based on the preliminary experiments, E_{pit} - 25 mV was chosen as the optimised polarisation potential for the present work as it enabled the generation of both an optimum MPR and visually resolvable hydrogen bubbles at the metastable pit locations.

Electrode surface area

The surface area of the electrodes used in the present study ranged between 1.75 mm^2 and 0.5 mm^2. Further reduction in the electrode surface area was attempted to improve the resolution of the potentiostatic polarisation data by adopting two different methods: (a) application of nail polish as lacquer and (b) the application of an adhesive electrical insulation tape, as discussed in Chapter 3. However, with a substantial reduction in the surface area, the formation of a metastable pit became a rare event and compromised the objective of the study. Hence the surface area of the electrode specimens was not modified. Instead, the whole surface area of the electrodes was investigated for understanding the evolution of metastable pit events.

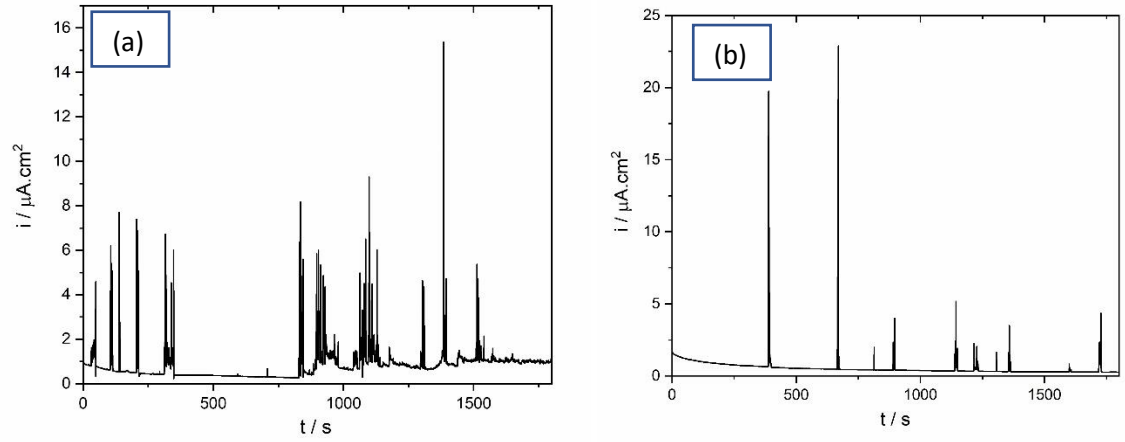

Figure 4.6. The potentiostatic polarisation data of Al-5Mg recorded in 0.01 M NaCl at E_{pit} - 25 mV using a working electrode with an area of (a) 2.1 mm^2 and (b) 0.8 mm^2.

Table 4.4. The potentiostatic polarisation data of Al-5Mg with a surface area of 2.1 mm^2 vs 0.8 mm^2 at E_{pit} - 25 mV in 0.01 M NaCl.

Surface area of the electrode (cm^2)	**2.1 mm^2**	**0.8 mm^2**
MPR (cm^{-2}.s^{-1})	30 ± 5	14 ± 2

Figure 4.6 and Table 4.4 present the comparison of the potentiostatic polarisation data of Al-5Mg with a surface area of 2.1 mm^2 vs 0.8 mm^2 in 0.01 M NaCl at E_{pit} – 25 mV. The data demonstrate that a decrease in the electrode surface area resulted in a decrease in the MPR and $i_{passive}$. The optimised electrode surface area for the present study ranged between 1.75 mm^2 and 0.5 mm^2.

4.3.3. Feasibility

Potentiostatic metastable pitting experiments performed with the optimised specifications discussed in the previous section (Section 4.3.2) resulted in the generation of visually resolvable hydrogen bubbles at the metastable pit locations during the simultaneous evolution of current transients. The formation, growth and dissolution of a hydrogen bubble at a metastable pit location during the simultaneous evolution of its corresponding current transient is shown in the timelapse images of Figure 4.7.

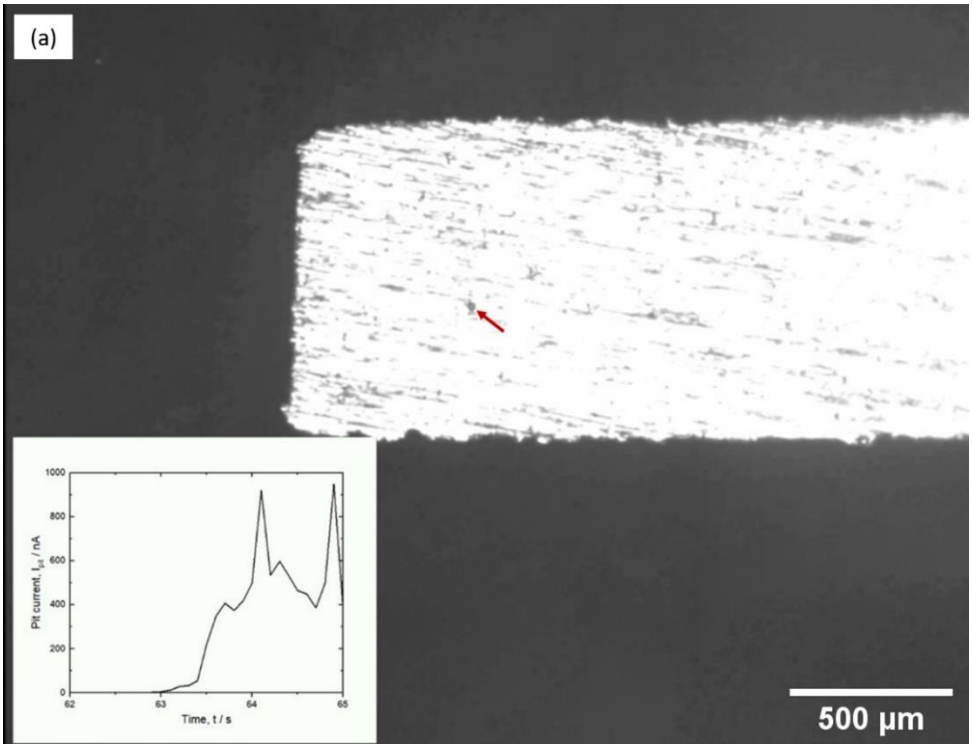

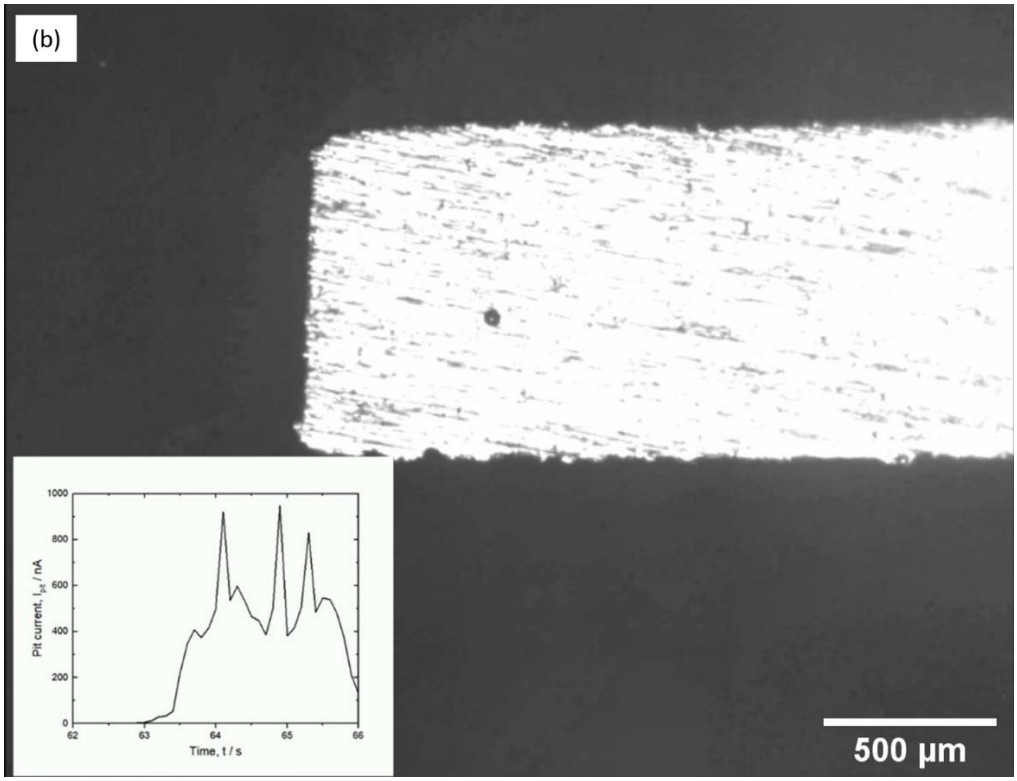
(b)
Pit current, I_{pit} / nA
Time, t / s
500 µm

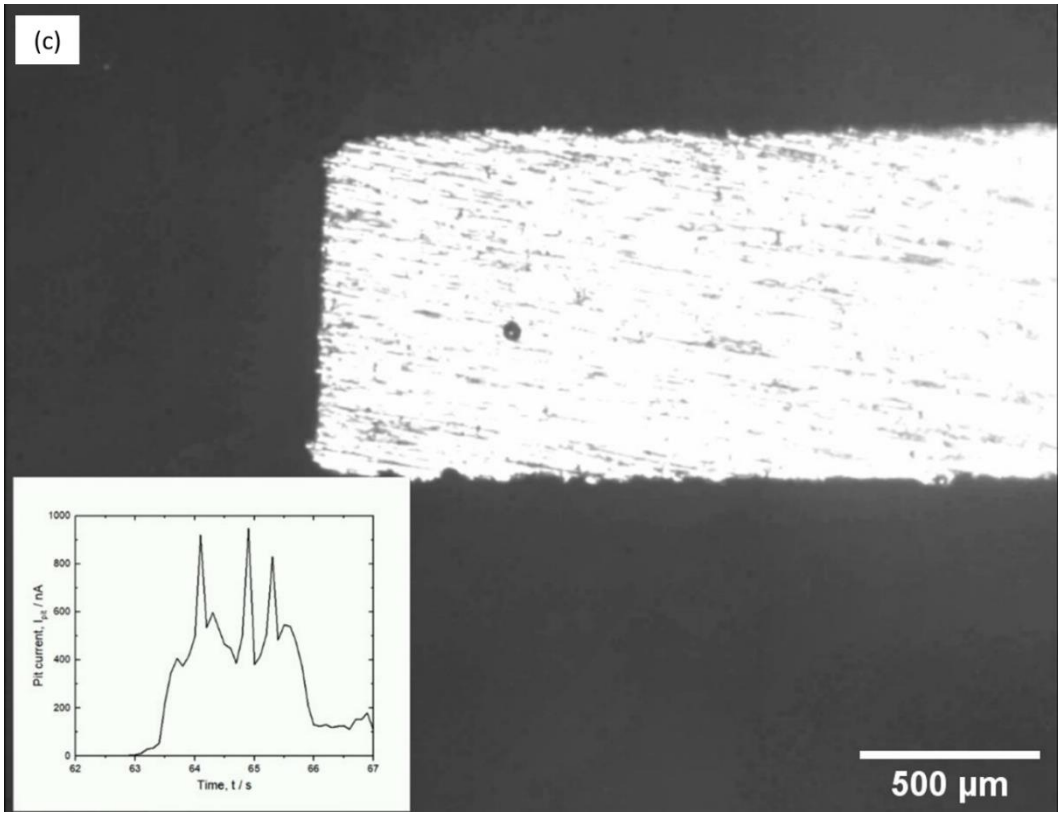
(c)
Pit current, I_{pit} / nA
Time, t / s
500 µm

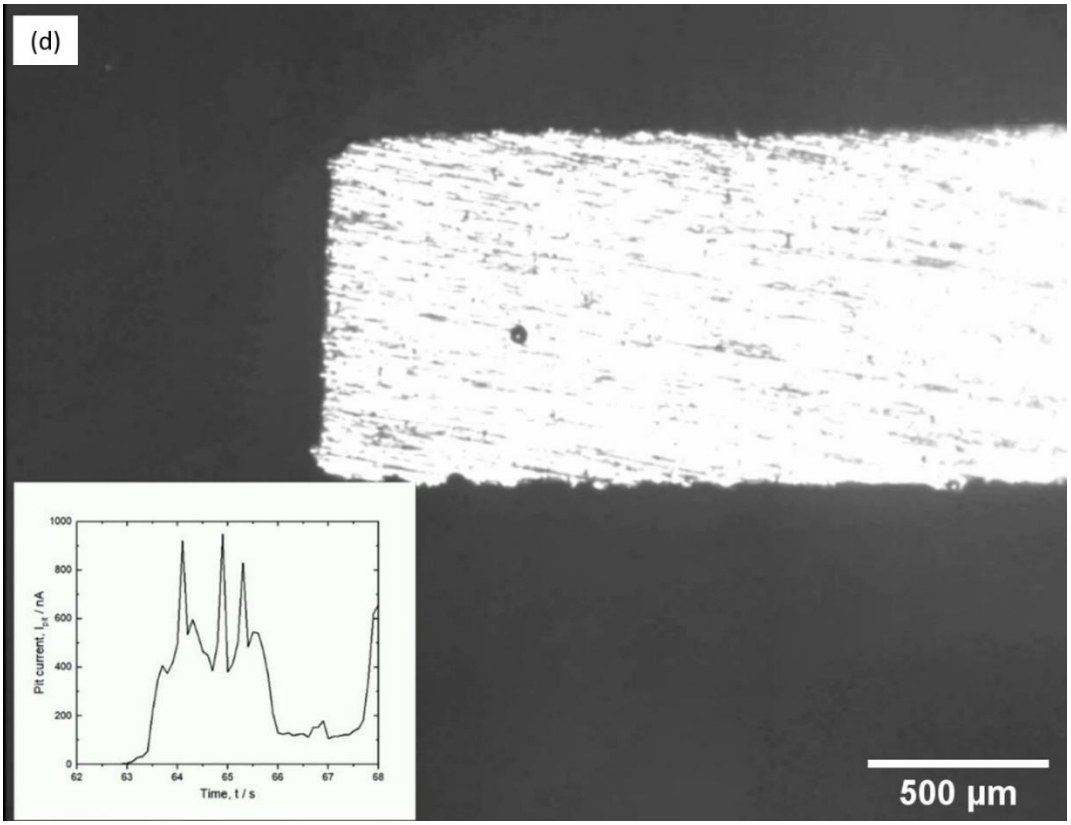
(d)
Pit current, I_{pit} / nA
Time, t / s
500 µm

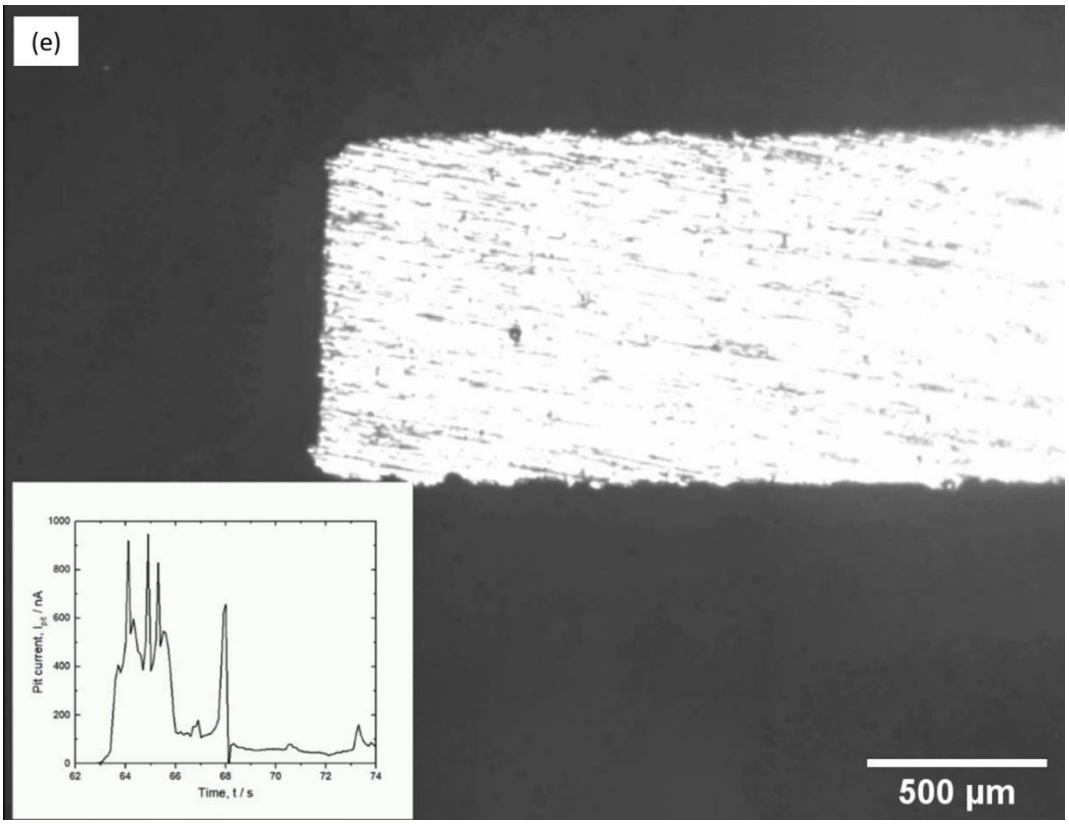
(e)
Pit current, I_{pit} / nA
Time, t / s
500 µm

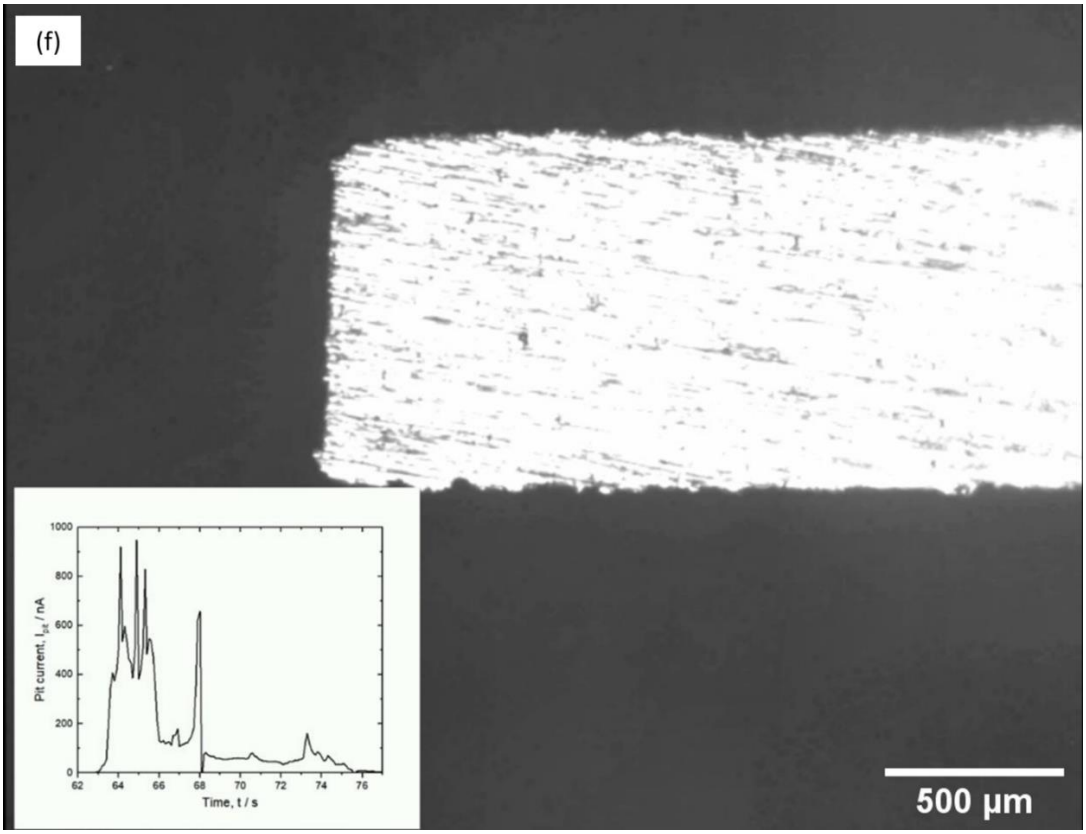

Figure 4.7. Timelapse video showing the simultaneous in situ evolution of a metastable pit event and its associated current transient during the potentiostatic testing of Al – 5 Mg alloy at E_{pit} - 25 mV in 0.01 M NaCl.

Figure 4.8 demonstrates that the location of hydrogen evolution during in situ imaging was the metastable pit location using SEM images captured post electrochemical experiments. Figure 4.9 presents the metastable pit location and its respective current transient associated with the metastable pit event presented in Figure 4.7.

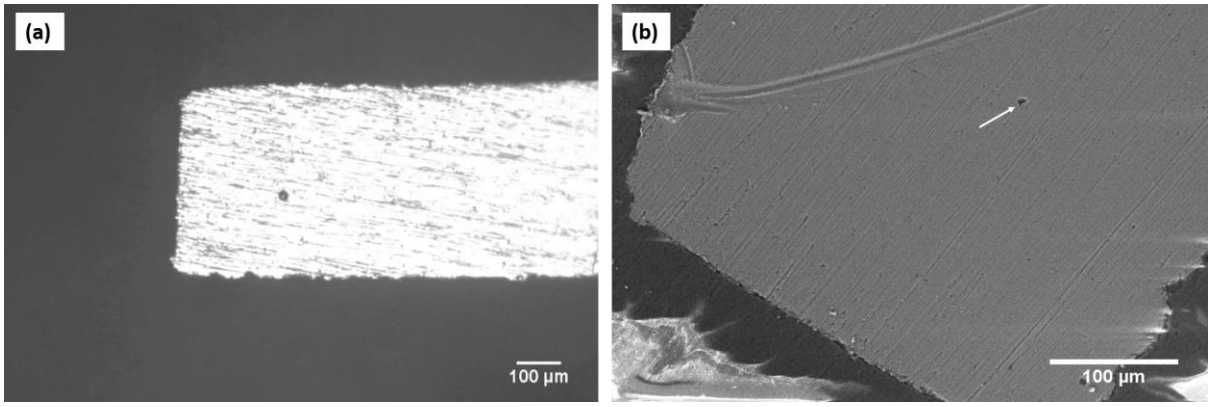

FIGURE 4.8. In situ image of the bubble at the metastable pit location (snapshot) associated with the transient in Figure 4.8 (b) ex-situ SEM image of the corresponding pit location after potentiostatic testing.

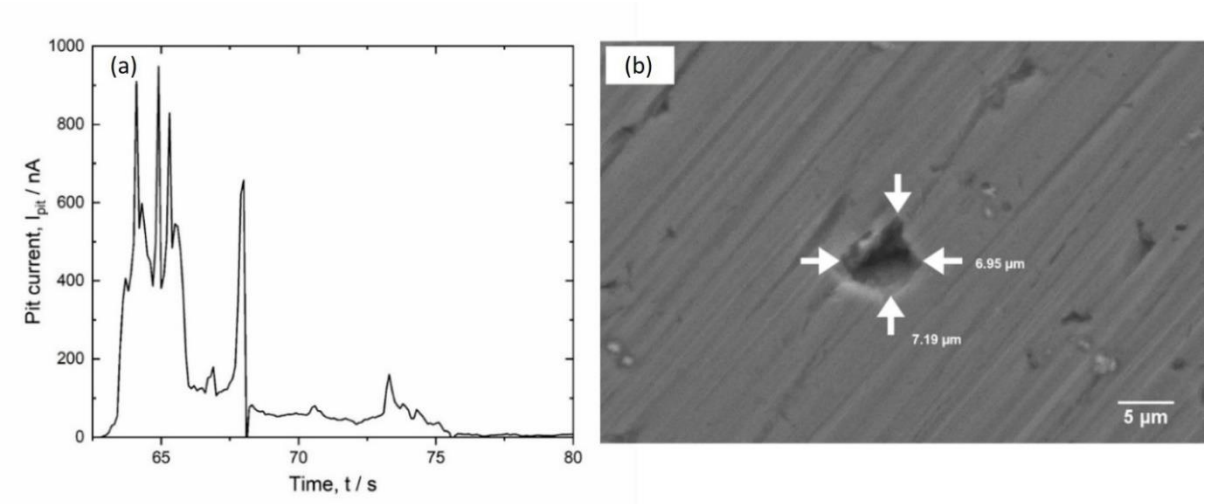

FIGURE 4.9. (a) The current transient and (b) an SEM image of its associated pit location with dimensions, recorded during the potentiostatic testing of Al – 5 Mg alloy at E_{pit} - 25 mV in 0.01 M NaCl.

The hydrogen bubble at the metastable pit location was visible after a waiting time (t_w) of 1 s post the commencement of its associated current transient [Glas et al. 1964]. The occurrence of such t_w before the visualisation of pH changes at the pit locations was reported in a related study using pH-sensitive agar gels in aluminium and its alloys [Sasaki et al. 2004]. In the present study, this duration may be attributed to the induction time necessary for the electrochemical processes to generate acidity and therefore dissolved hydrogen (the term dissolved hydrogen herein represents molecular hydrogen unless otherwise stated) [McCafferty 2003], followed by the physicochemical processes that govern its desorption into the gaseous phase (bubble) upon reaching supersaturation [Epstein et al. 1950; Glas et al. 1964; Vogt 2011]. As revealed by the timelapse images in Figure 4.7, the nucleated hydrogen bubble remained adsorbed to the metastable pit location and underwent growth and shrinkage in its size following a corresponding change in I_{pit}. Similar observations concerning the entrapment of hydrogen bubbles at the pit locations by columnar aluminium hydroxide corrosion products have been reported elsewhere during the pitting experiments conducted in neutral NaCl solutions [Rudd et al. 1980; Cook et al. 2002].

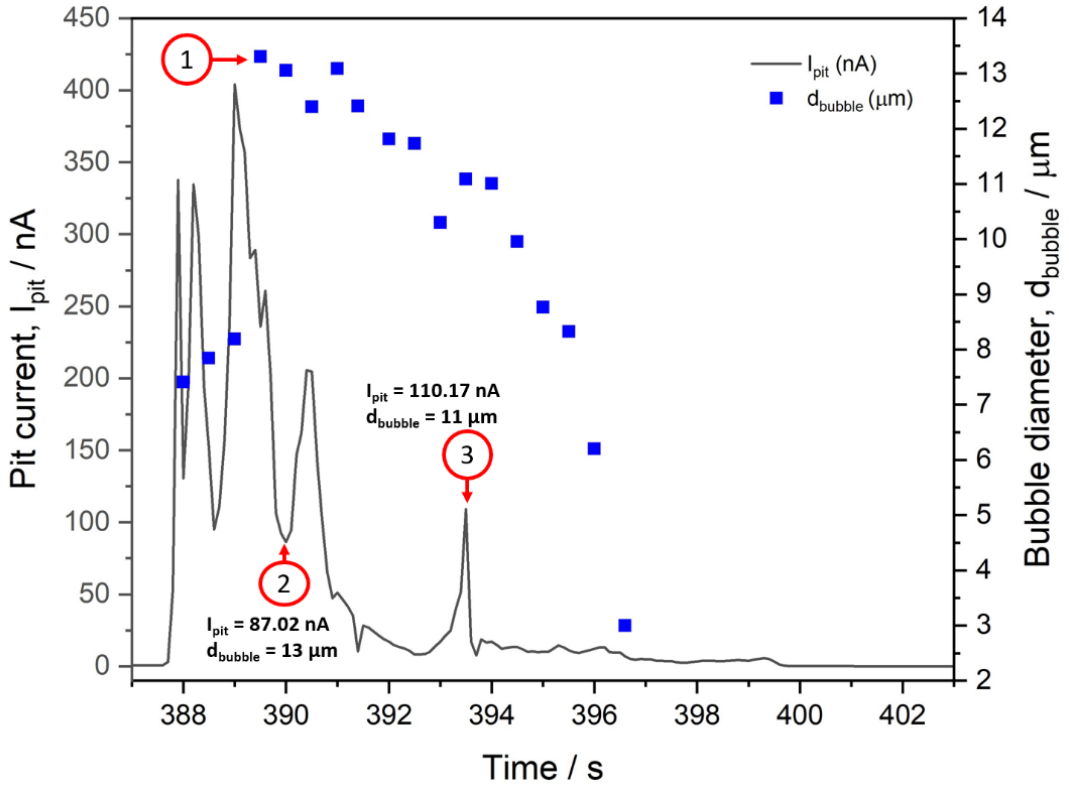

FIGURE 4.10. The variation of bubble diameter, d_{bubble} (µm) with pit current, I_{pit} (nA) of a metastable current transient recorded during the potentiostatic polarisation of Al – 5 Mg alloy at E_{pit} – 25 mV in 0.01 M NaCl.

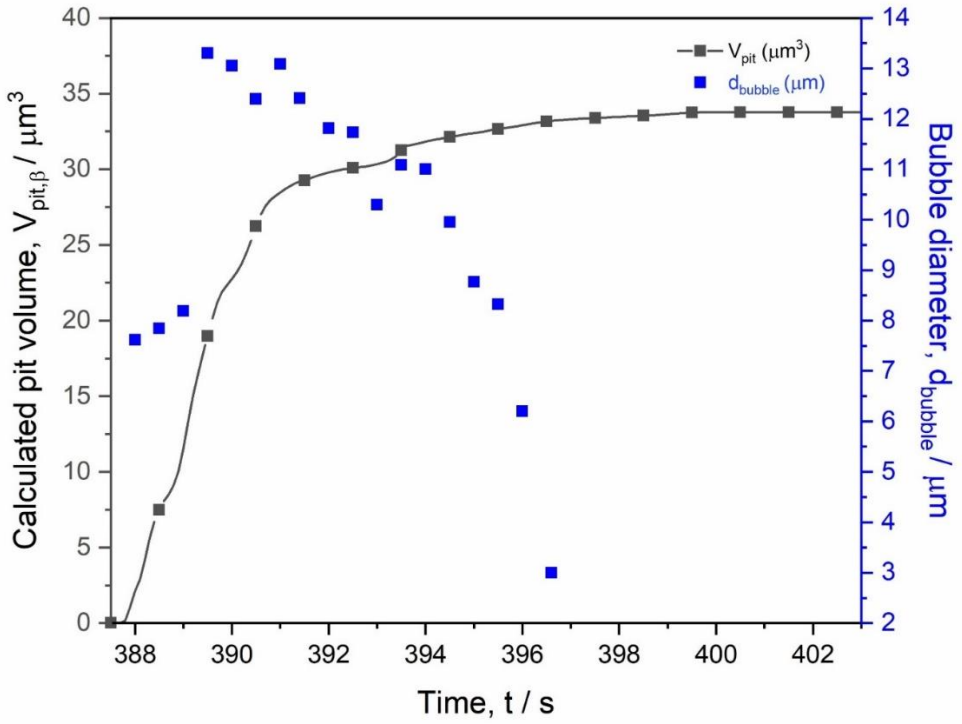

FIGURE 4.11. The variation of calculated pit volume, $V_{pit,\beta}$ (µm^3) with the diameter of the bubble, d_{bubble} (µm) for the metastable current transient presented in Figure 4.9.

The hydrogen bubbles remained adsorbed to the pit site and underwent growth and shrinkage (by dissolution) in their d_{bubble} following a corresponding change in I_{pit}, as shown in Figure 4.10. However, this variation did not follow a proportional relationship owing to the chemical aspects involved in the bubble dynamics, as discussed in Chapter 3. Upon cessation of anodic dissolution at the end of the current transient, hydrogen from the bubble adsorbed to the pit surface underwent dissolution into the electrolyte resulting in its shrinkage [Epstein et al. 1950]. This phenomenon can be witnessed from the decrease in d_{bubble} when $V_{pit,\beta}$ reached a constant value after the pit dissolution time ($t_{pit\ dissolution}$) of 6 s in Figure 4.11, which is a plot of the temporal variation of d_{bubble} and $V_{pit,\beta}$ for the metastable transient shown in Figure 4.10. Figure 4.12 illustrates the variation of d_{bubble} with I_{pit} during a quasi-stable current transient.

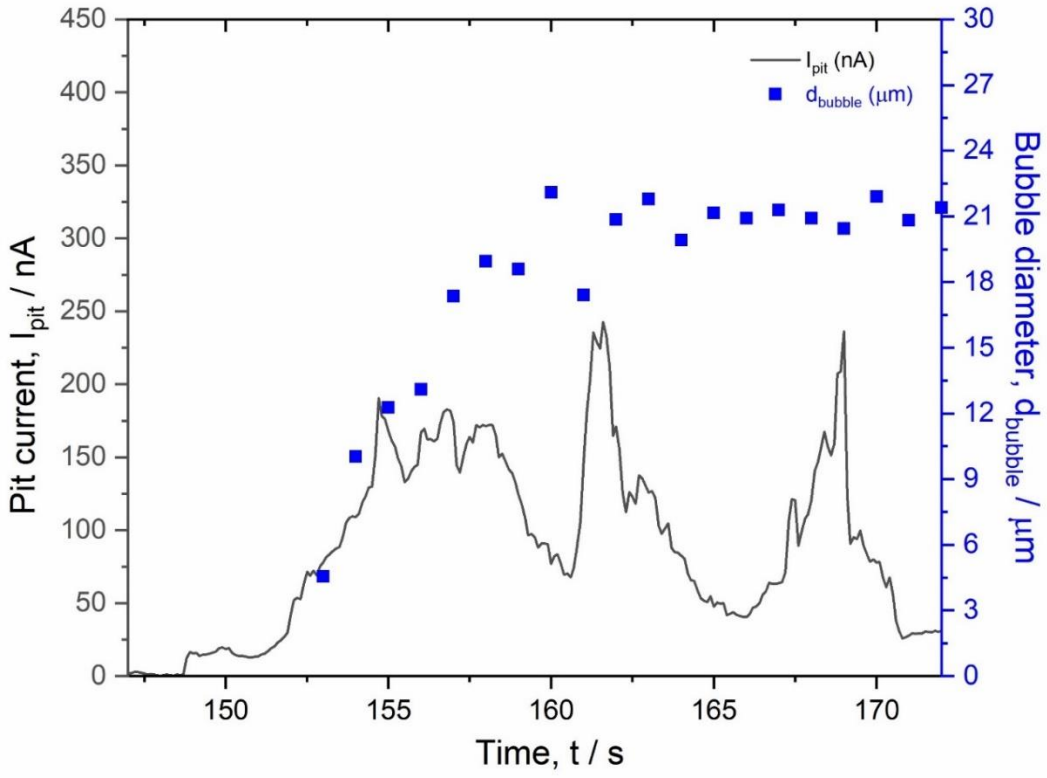

FIGURE 4.12. The variation of bubble diameter, d_{bubble} (µm) with pit current, I_{pit} (nA) of a quasi-stable current transient recorded during the potentiostatic polarisation of Al – 5 Mg alloy at E_{pit} – 25 mV in 0.01 M NaCl.

The duration of the hydrogen bubbles (t_{bubble}) varied depending on the pit stability. When the transients were metastable (Figure 4.10) in nature, the t_{bubble} was consistent with the t_{pit}. However, for quasi-stable transients (Figure 4.12), the t_{bubble} exceeded t_{pit} indicating

incomplete repassivation and ongoing dissolution at the pit site concomitant with the unrecovered charge (i.e., a difference in $I_{passive,begin}$ and $I_{passive,end}$, indicating incomplete repassivation of the pit event) witnessed at the end of the current transient. The hydrogen bubble that evolved during the transient in Figure 4.12 underwent gradual dissolution at 191 s, which was ~ 20 s post the end of the transient. This extended lifetime of the bubble, post the end of the current transient, was higher than the maximum duration of 2 s required for the chemical dissolution of bubbles during the metastable pitting events.

The discussions herein demonstrate that the in situ optical imaging method of mapping the metastable pitting locations based on hydrogen evolution at the pit sites enabled a successful correlation of the current transients to their respective metastable pit events. The method also offers a wide range of insights concerning the mechanism relevant to pitting corrosion and other localised corrosion phenomena. This technique may also be extended to investigating the localised corrosion phenomena of other alloy systems and notably in alloy systems where the direct visualisation of the corrosion propagation is obscured.

4.3.4. Limitations

In Figure 4.10, the increase in I_{pit} at 389 s was associated with a corresponding increase in d_{bubble} at 389.5 s, as indicated by annotation 1. The time-lag of ~ 0.5 s recorded between the I_{pit} and d_{bubble} may be attributed to the factors that govern the bubble dynamics akin to those that occur during t_w. This delay, combined with the competitive flux of hydrogen diffusing into and dissolving away at the bubble interface depending on the bubble growth rate, result in different values of d_{bubble} for similar values of I_{pit} (annotations 2 & 3 in Figure 4). For this reason, an instantaneous correlation of i_{H_2} to i_{pit} could be misleading; instead, a correlation of the total C_{HE} to C_{pit} is meaningful.

The generation of visible hydrogen bubbles at the metastable pit locations required the current transients to exceed a critical $C_{transient}$. Therefore, the pit events associated with the pit nucleation transients, that are short-lived and bear $C_{transient}$ below 100 nC, could not be visualised with the proposed in situ imaging method. Nevertheless, since the pit propagation events are more critical than the pit nucleation events in understanding the pitting susceptibility

of alloy systems [Laycock et al. 1997] (discussed further in Chapter 6), the inability to study pit nucleation events did not alter the inferences derived from the present study.

4.4. Conclusions

The major conclusions from work in this chapter are as follows:

- The novel approach adopted to image the metastable pit events based on the inherent tendency of aluminium to evolve hydrogen during active pit growth was successful in correlating the current transients to their respective metastable pit events. The method also allowed a direct evaluation of the hydrogen evolution occurring at the metastable pit site.
- An optimisation of the following parameters was required: (a) signal-to-noise ratio, (b) surface area of the electrode, (c) concentration of the electrolyte and (d) polarisation potential for the feasibility of the in situ imaging method proposed herein.
- During metastable pit growth, the hydrogen bubbles remained adsorbed to the pit location and underwent growth and shrinkage in d_{bubble} following a corresponding change in I_{pit}.
- The in situ visualisation method limited the imaging of pit nucleation events and an instantaneous correlation of i_{H_2} with i_{pit}.

Chapter 5

In situ investigation on the role of hydrogen evolution on the estimated metastable pit sizes

5.1. Background

The charge accumulated by the measurable current transients recorded during the potentiostatic testing of passive metals at anodic potentials below E_{pit} is regarded to represent the extent of anodic dissolution and mass loss within the respective metastable pit locations [Cavanaugh 2009a; Cavanaugh et al. 2009; Gupta et al. 2012]. However, in aluminium and its alloys, HE occurring within the pits is considered to consume a significant fraction of the anodic charge [Frankel 1998], resulting in depreciated current transients and therefore underestimated pit sizes. Using 1D pits, Beck reported that the ratio of HE current density to the total anodic current density (i_{H_2}/i_{anodic}) in pure aluminium was 0.16 in saturated $AlCl_3$ solution [Beck 1984]. Recently, this ratio was deduced as 10% in AA2024 using 1D pits in aerated 0.1 M NaCl [Bonzom et al. 2016]. Frankel, using 2D pits in the thin films of pure aluminium, reported that the i_{H_2} remained constant at 1.6 A.cm^{-2} when i_{anodic} ranged between 18 to 30 A.cm^{-2} in de-aerated 0.1 M NaCl [Frankel 1990]. Boag et al. stated that the HE consumed about 40% of the total anodic current during stable pit formation in AA2024-T3 when tested in aerated 0.1 M NaCl [Boag et al. 2010]. Other values reported for this ratio include 6% in 0.5 M NaCl [Dražić et al. 1999] and 20% in 12 M HCl during the investigation of NDE in aluminium [Frankel et al. 2015]. Considering the significant amount of charge lost to HE during pit propagation, incorporating an excess charge (~16%) to the charge determined from the current transients became a practice during the investigation of metastable pitting in aluminium and its alloys [Kim et al. 2007; Guan et al. 2015]. The notion of utilising the same

‡*G. Sridhar, N. Birbilis and V.S. Raja, CORROSION (Accepted).*

ratio of i_{H_2}/i_{anodic} from the stable pit propagation studies to the investigation of metastable pit propagation could have stemmed from the fact that both the metastable and stable pits follow the same growth law [Isaacs 1989].

In an extensive study of metastable pitting in aluminium, Pride et al. discussed that the distribution of the metastable r_{pit} estimated from the current transients was not significantly different from the actual values determined using ex-situ imaging of the potentiostatically tested specimens [Pride et al. 1994]. It was also shown through derivative approaches that the charge lost to HE within the metastable pits would not substantially alter the estimated metastable r_{pit}. The apparent contradiction of this conclusion with those deduced from the stable pit propagation studies may arise from the differences in the rates of HE depending on the pit stability. As discussed by Frankel et al., HE at anodic potentials is a catalytically enhanced process [Frankel et al. 2015] that requires a catalytically active pit surface. Though both the metastable and stable pits follow the same growth law, the catalytic nature of the pit surface could vary depending on factors such as the potential, pH and therefore lead to differences in the rates of HE. Using 25 µm artificial 1D pits in aluminium, Cook et al. showed that for the same anodic current density, the noise due to HE decreased as the potential was progressively stepped down to the repassivation potential [Cook et al. 2012]. They attributed this phenomenon to the gradual loss of salt films which was speculated to catalyse anodic dissolution and its concomitant HE. Therefore, understanding the rates of HE within metastable pits is essential to evaluate the error it introduces in the metastable r_{pit} calculated from current transients rather than adopting such values from the stable pit propagation studies. The present study is an attempt to investigate this aspect by determining the volume (V_{HE}) and, therefore, the charge of hydrogen (C_{HE}) evolving at the real-time metastable pit locations in an aged Al-Mg binary alloy.

In situ temporal evolution of hydrogen at the metastable pit locations on the electrode surface was optically recorded during their potentiostatic testing at 25 mV below E_{pit} to determine the charge consumed by HE (C_{HE}) from the 2D size of the bubbles. A study involving the utilization of the 2D bubble area to determine the moles of hydrogen generated upon Mg due to NDE was reported using a methodology termed time-resolved volumetry (TRV) [Lebouil et al. 2014]. In the present study, binary Al – 5 wt. % Mg alloy in aged condition was chosen such that the anodic dissolution of the Mg_2Al_3 (β) phase-precipitates [Liu

et al. 2010; Lyndon et al. 2013] during pitting could be investigated. Complete dissolution of this phase was expected to generate maximum hydrogen than what would be expected from the solitary dissolution of Al since the dissolution of both Mg and Al should evolve hydrogen due to NDE [Frankel et al. 2015].

5.2. Objective

The role of hydrogen evolution (HE) on the r_{pit} and V_{pit} estimated from $C_{transient}$ was investigated by (a) determining the ratio C_{HE}/C_{pit} during metastable pit growth and (b) comparing the actual V_{pit} with the V_{pit} estimated from $C_{transient}$.

5.3. Results and discussion

5.3.1. Estimation of V_{HE} from d_{bubble}

The quantum of charge lost to HE within the metastable (Figure 4.9) and quasi-stable (Figure 4.11) pits may be determined from the volume of hydrogen calculated from the cumulative d_{bubble}, i.e., $V_{HE,bubble}$. For this purpose, it is vital to evaluate if the fraction of hydrogen lost in its dissolved form and, therefore, unaccounted in the calculation of the hydrogen volume from d_{bubble} is negligible. The total volume of hydrogen (V_{HE}) dynamically generated within a pit is the sum of the volume of dissolved hydrogen in its supersaturated concentration within the pit (A), the measurable volume of hydrogen in the bubble as determined from d_{bubble} i.e., $V_{HE,bubble}$ (B) and the volume of hydrogen chemically dissolving away from the bubble (C), as indicated by Equation 5.1.

Total volume of hydrogen, V_{HE} = A + B + C *Equation 5.1*

Component A in Equation 5.1 may be considered negligible if the mass transfer rate of the dissolved hydrogen from the pit to the bubble is not the rate-controlling factor. Roušar and Cezner reported that the fraction of dissolved hydrogen in the vicinity of a growing bubble would be negligible when the current density for HE exceeded 1 mA.cm^{-2} [Rousar et al. 1975; Vogt 2011]. Therefore, to evaluate if the fraction of dissolved hydrogen within the pit is negligible, it is essential to estimate the instantaneous HE current density (i_{H_2}). Figure 5.1 and

Figure 5.2 present the temporal variation of the instantaneous i_{pit} and i_{H_2} associated with the metastable transient in Figure 4.9 and the quasi-stable transient in Figure 4.11, respectively.

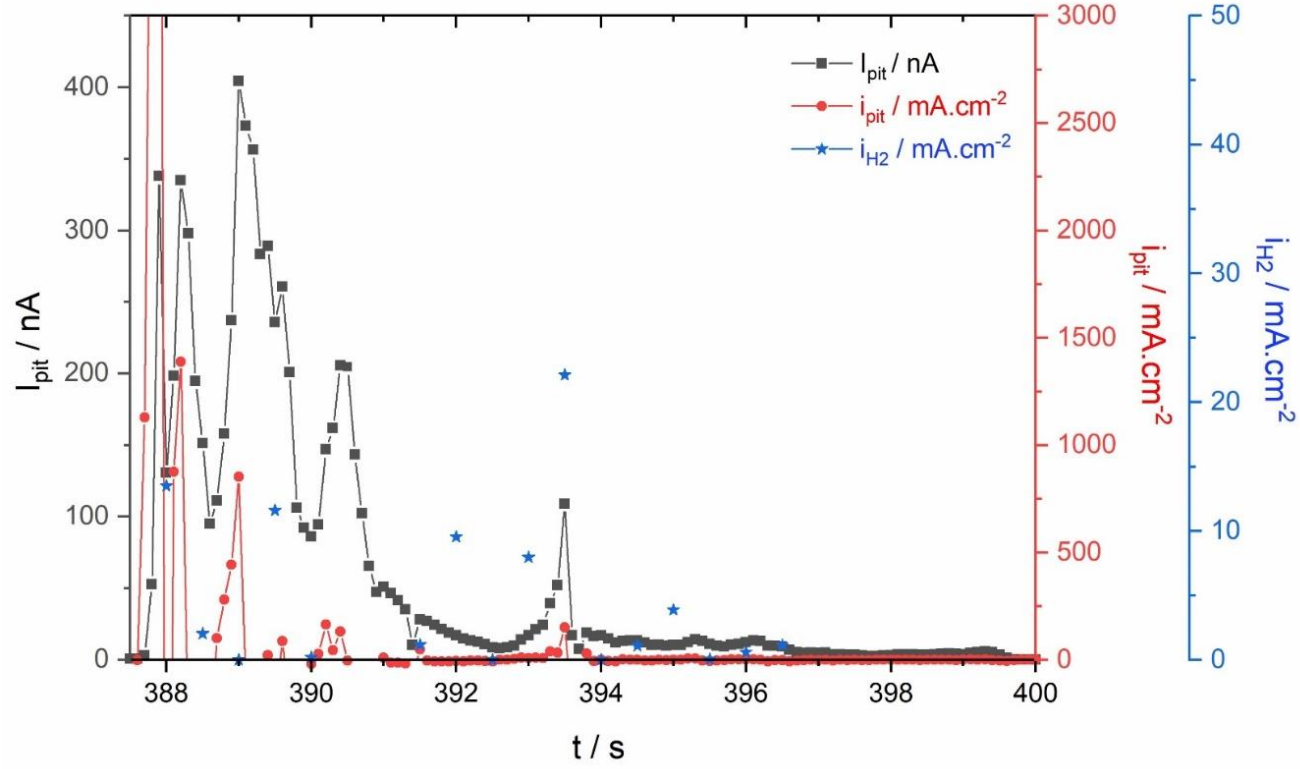

FIGURE 5.1. The instantaneous i_{H_2} and i_{pit} during the metastable current transient presented in Figure 4.10.

From the plots in Figure 5.1 and Figure 5.2, it is evident that the i_{H_2} during pit growth was greater than 1 mA.cm^{-2} demonstrating that the volume of dissolved hydrogen within the pit left unaccounted in the calculation of V_{HE} from d_{bubble} would be negligible. Nevertheless, considering the lag in the variation of I_{pit} with d_{bubble}, it may be argued that the mass transfer rate of dissolved hydrogen to the bubble could be a rate-determining step. For this purpose, the volume of dissolved hydrogen within the pit needs to be determined. The supersaturation concentration of dissolved hydrogen in the vicinity of a Pt electrode was reported to increase asymptotically as a function of current density and reach a constant value of 1.16×10^{-4} mol.cm^{-3} for current densities higher than 300 mA.cm^{-2} [Shibata 1963]. By incorporating this value considering a worst-case scenario, the volume of dissolved hydrogen within the $V_{pit,\beta}$ for the transient in Figure 4.9 would be 8.78×10^{-11} cm^3 and therefore correspond to a charge

consumption of 0.75 nC. Therefore, component A in Equation 5.1 may be considered negligible.

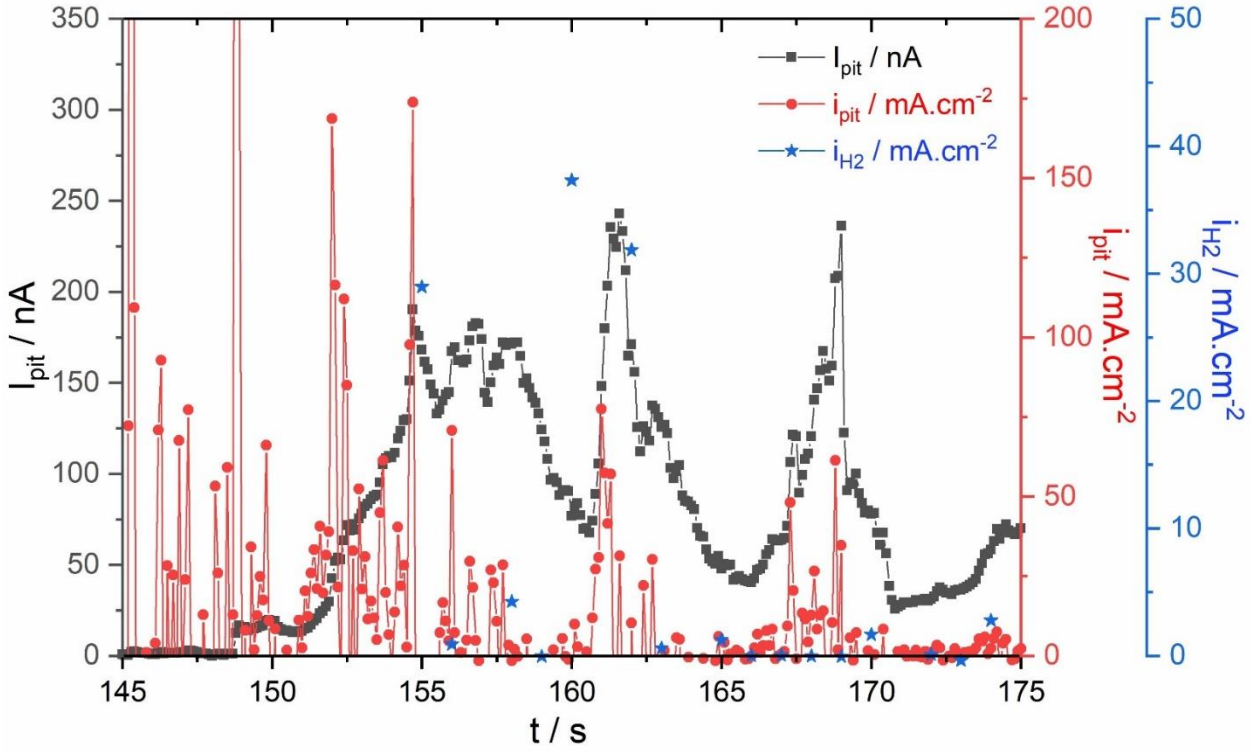

FIGURE 5.2. The instantaneous i_{H_2} and i_{pit} during the quasi-stable current transient presented in Figure 4.12.

Component C, which represents the volume of hydrogen dynamically dissolving away from the bubble, may also be considered negligible during bubble growth as the vicinity of the bubble remains supersaturated with dissolved hydrogen within the Nernst boundary layer. Also, at the bubble periphery, which is possibly exposed outside the boundary layer, hydrogen dissolution would still be minimum as the saturation concentration, or the solubility of hydrogen is 7.5×10^{-7} mol.cm^{-3} at 28 °C [Glas et al. 1964]. A critical consideration of the volume of hydrogen lost by chemical dissolution from the bubble is presented below.

The dynamic chemical dissolution of hydrogen occurring from the bubble into the solution is a diffusion-controlled dissolution process [Krieger et al. 1967], which may be determined from the sum of the volume of hydrogen that dissolves ($V_{dissolved}$) at the bubble-electrolyte interphase and that which diffuses away ($V_{diffused}$) from the bubble, as shown in Equation 5.2.

Equation 5.2

$$V_{chemical\ dissolution} = V_{dissolved} + V_{diffused}$$

The $V_{dissolved}$ maybe determined from the dissolution rate of the bubble after the pit stops growing. For this purpose, the slope (b) of the plot of d_{bubble} vs t after the pit dissolution time ($t_{pit\ dissolution}$) was determined from a dataset of 10 transients. The slope b was determined as 0.7 ± 0.15 µm.s$^{-1,}$ which results in a dissolution rate ($R_{dissolved}$) of ~ 1.8 × 10^{-13} cm^3.s^{-1}. The $V_{dissolved}$ during the pit dissolution time ($t_{pit\ dissolution}$) may be determined using Equation 5.3. The $t_{pit\ dissolution}$ herein is the time required for the estimated metastable pit size to reach a constant value.

Equation 5.3

$$V_{dissolved} = R_{dissolved} \times t_{pit\ dissolution}$$

The volume of hydrogen that diffuses away from the bubble ($V_{diffused}$) during bubble growth, may be calculated by determining the flux of hydrogen (J_{H_2} in mol. s^{-1}) using Fick's law of diffusion (Equation 5.4).

Equation 5.4

$$J_{H_2} = \frac{D_{H_2} A_{bubble}\left(C_{s,HE} - C_{bulk,HE}\right)}{\delta}$$

wherein, D_{H_2} is the diffusion coefficient of hydrogen in cm^2.s^{-1}, A_{bubble} is the radial surface area of the bubble in cm^2 (calculated using the equation $A_{bubble} = 4\pi r_{bubble}^2$), $C_{s,HE}$ and $C_{bulk,HE}$ are the saturation concentration and the bulk concentration of hydrogen respectively in mol.cm^{-3} and δ is the diffusion layer thickness in cm.

The parameter D_{H_2} (in cm^2.s^{-1}) maybe determined from the slope (m) of the plot of d_{bubble}^2 vs t using Equation 5.5, as discussed by Houghton et al. 1962 [Houghton et al. 1962].

Equation 5.5

$$D_{H_2} = 3.04 \frac{m}{\alpha}\left[\frac{273}{T}\right] \times 10^{-5}$$

wherein α = 0.0176 is the Bunsen coefficient for the dissolution of H_2 in water [Winkler 1891] and T is temperature in K which may be assumed as 273 K. The value of m determined from

a dataset of 10 current transients is 20.6 ± 4.1 μm^2.s^{-1}. The resulting D_{H_2} is ~ 3.46 × 10^{-10} cm^2.s^{-1}.

The value of J_{H_2} maybe calculated by incorporating the values of D_{H_2} = 3.46 × 10^{-10} cm^2.s^{-1}, $C_{s,HE}$ = 7.5 × 10^{-7} mol.cm^{-3} at STP [Glas et al. 1964], $C_{bulk,HE}$ = 0 mol.cm^{-3} in Equation 5.4. The diffusion layer thickness (δ) may be assumed as 6.8 × 10^{-4} cm [Frankel 1990]. The A_{bubble} may be calculated from the maximum d_{bubble}, to consider a worst-case scenario.

The number of moles of hydrogen (n_{H_2}) dissolved away during the $t_{pit\ dissolution}$ maybe calculated using Equation 5.6.

$$n_{H_2} = J_{H_2} \times t_{pit\ dissolution} \qquad \textit{Equation 5.6}$$

Therefore, the volume of hydrogen that has diffused away ($V_{diffused}$) may be calculated using Equation 5.7.

$$V_{diffused} = 22.4 \times 10^3 \times n_{H_2} \qquad \textit{Equation 5.7}$$

wherein 22.4 × 10^3 is the volume occupied by 1 mol of H_2 at STP.

The total volume of hydrogen lost by chemical dissolution ($V_{chemical\ dissolution}$) may be determined from Equation 5.2.

The calculation of $V_{chemical\ dissolution}$ for the metastable transient in Figure 4.9 is shown in Table 5.1. From the table, it is evident that the charge consumed by the volume of hydrogen lost to chemical dissolution during pit growth was only a few pC. A similar calculation for the quasi-stable transient in Figure 4.11 with a $t_{pit\ dissolution}$ of 22 s yields a $V_{chemical\ dissolution}$ of 6.92 × 10^{-12} cm^3 and a corresponding charge of 59.4 pC. Hence the volume of hydrogen lost dynamically by the chemical dissolution of molecular hydrogen from the bubble into the solution may be considered negligible.

Table 5.1. The calculation of $V_{chemical\ dissolution}$ and $C_{HE,dissolution}$ for the metastable transient in Figure 4.10.

Pit growth time, $t_{pit\ dissolution}$ (s)	Surface area of the bubble, A_{bubble} (cm^2)	Flux of diffusing hydrogen, J_{H_2} ($mol.s^{-1}$)	No. of moles of H_2, n_{H_2} (mol)	Volume of H_2 diffused, $V_{diffused}$ (cm^3)	Volume of H_2 dissolved, $V_{dissolved}$ (cm^3)	Volume of H_2 chemically dissolved, $V_{chemical\ dissolu}$ (cm^3)	Charge consumed by $V_{chemical\ dissolution}$, $C_{HE,dissolution}$ (pC)
6	5.55×10^{-6}	2.12×10^{-18}	1.27×10^{-17}	2.84×10^{-13}	1.08×10^{-12}	1.36×10^{-12}	11.68

The calculations herein indicate that the charge consumed by the volume of hydrogen dynamically dissolved away, i.e., Component C in Equation 5.2 was only a few pC for the metastable and quasi-stable transients in Figures 4.9 and 4.11, respectively. From the discussions, it may be concluded that the volume of hydrogen determined from d_{bubble} (component B in Equation 5.2) presents a proximate measure of the actual volume of hydrogen evolved within the pit.

5.3.2. The ratio C_{HE}/C_{pit} and its role on the r_{pit} estimated from $C_{transient}$

The estimated C_{HE}/C_{pit} for the metastable transient and quasi-stable transients presented in Figures 4.9 and 4.11 are 0.019 and 0.051, respectively, as shown in Table 5.2.

Table 5.2. The estimation of C_{HE}/C_{pit}, pit volume ($V_{pit,\beta}$) and hemispherical pit radius ($r_{pit,\beta}$) for the metastable and quasi-stable current transients presented in Figure 4.10 and Figure 4.12, respectively.

Transient/ pitting type	Cumulative bubble diameter, d_{bubble} (μm)	Volume of the bubble, V_{HE} (cm^3)	Charge of hydrogen evolution, C_{HE} (nC)	Charge of the transient, $C_{transient}$ (nC)	Charge of the pit, C_{pit} (nC)	Pit volume, $V_{pit,\beta}$ (cm^3)	Hemispherical pit radius, $r_{pit,\beta}$ (μm)	$\frac{C_{HE}}{C_{pit}}$
Metastable	14.78	1.68×10^{-9}	14.44	734.77	749.21	3.44×10^{-11}	2.54	0.019
Quasi-stable	30.47	14.8×10^{-9}	127.18	2369.91	2497.09	1.15×10^{-10}	3.80	0.051

The values of C_{HE}/C_{pit} varied, however, depending on the $C_{transient}$ as shown in Table 5.3. The resultant HE induced error in the $r_{pit,corrected}$ was found to be less than 2%. This

observation indicates that the fraction of the total pit dissolution charge lost to HE and, therefore, unavailable for the potentiostat to sense during the generation of current transients was minimal. This observation is in agreement with Pride et al., wherein, through derivative approaches, they showed that the influence of HE upon the underestimation of the calculated metastable pit sizes was less than 5% [Pride et al. 1994].

TABLE 5.3. The ratio C_{HE}/C_{pit} determined for different ranges of $C_{transient}$ for the transients recorded during the potentiostatic polarisation of aged Al – 5 Mg at E_{pit} – 25 mV in 0.01 M NaCl.

Sl. No	$C_{transient}$ **(nC)**	C_{HE}/C_{pit}
1	100 - 500	1.51 ± 0.04
2	500 - 1000	2.42 ± 0.26
3	1000 - 5000	5.16 ± 1.04

The ratio C_{HE}/C_{pit} (an analogous parameter to i_{H_2}/i_{anodic} for the same A_{pit} and t_{pit}) for the metastable/quasi-stable pit events recorded (at anodic potentials below E_{pit}) in the present study was smaller than the i_{H_2}/i_{anodic} values (at potentials above E_{pit}) witnessed during stable pit propagation [Beck 1984; Frankel 1990] in aluminium. This disparity may be explained as follows: In aluminium, HE within the pits at anodic potentials is catalyzed by the active pit surface [Frankel et al. 2015; Frankel et al. 2013], which ceases to evolve hydrogen when the pit stops growing. During active pit propagation, the critical concentration (C_{crit}) maintained within the pit, typically 48% [Frankel et al. 1996] to 80% [Beck 1984] saturation concentration of $AlCl_3$ in aluminium, engenders pH as low as 0.45 [Beck 1984] which promotes HE at to the negative pit bottom potentials. The higher exchange current densities for HE [Zheng et al. 2016; Sheng et al. 2015] ($i_{0,HE}$) at the low pH values within the pit anolyte may also support HE similar to NDE as discussed by Frankel et al.[Frankel et al. 2013] Therefore, HE from an active pit surface in aluminium bears a direct correlation to the factors that govern pit propagation, such as the potential and pH within the pits. From the work of Cook et al. [Cook et al. 2012], it is evident that at applied anodic potentials below E_{pit}, HE rate decreases with potential for a constant i_{anodic}. This observation may be attributed to the changes in the pit chemistry concomitant to the rate of pit propagation and stability of metastable pits that vary with applied potential [Laycock et al. 1997]. During metastable pit growth at applied anodic potentials below E_{pit}, the C_{crit} that gets lost due to the rupture of pit cover by hydrogen bubble [Natishan et al. 1989] is not replenished, resulting in pit

repassivation [Cook et al. 2002]. The multiple peaks within a metastable current transient validate that the concentration of the pit anolyte is not consistently above C_{crit} i.e., the pH dynamically varies, resulting in a dynamically changing $i_{0,HE}$ that results in reduced rates of HE. Besides, any further dissolution within the metastable pits after hydrogen blistering would occur by anisotropic dissolution, i.e., selective dissolution through local tunnelling events within the pit interior [Cook et al. 2002] and therefore reduced volume of HE. On the contrary, at potentials closer to or greater than E_{pit} , i.e., during stable pit propagation, the high rates of pit propagation assisted by the salt film or mixed ohmic-diffusion control buffer the C_{crit} in the event of pit anolyte dilution and thereby promote sustained HE [Beck 1984; Laycock et al. 1997]. Such differences in the pit chemistry changes that govern pit propagation explain why the C_{HE}/C_{pit} for metastable/quasi-stable pits in the present study was smaller than the i_{H_2}/i_{anodic} recorded at anodic potentials above E_{pit} for stable pits.

The discussions herein suggest that the occurrence of HE within the pits does not impart a percentage error greater than 2% in the metastable pit sizes estimated from the current transients. In aluminium [Pride et al. 1994] and its alloys [Guan et al. 2015], the non-faradaic current consumed during the discharging of the oxide film surrounding the active pits due to their capacitive behaviour was reported to be negligible. Such insights signify that the charge consumed by a single current transient should represent the pit size of an individual pit event. Therefore, it may be concluded that the underestimation of the metastable pit sizes in aluminium and its alloys reported in literature should arise from the association of such pit locations with multiple current transients depending on their spatiotemporal evolution. Re-activation of pit events due to the partial dissolution of second phase particles [Burstein et al. 2001] may lead to the charge accumulation at the pit location being associated with multiple current transients. Besides, the superposition of multiple transients may camouflage the signal arising from the re-activating pit events under a seemingly single current transient and make them unavailable for pit size calculations [Guan et al. 2016b]. The implications of such aspects would be magnified in microstructurally complex alloys wherein the kinetics of dissolution induced by metallurgically and chemically distinct second phase particles would present a complex case. This aspect is commonly overlooked when estimating pit sizes from current transients due to the inherent complications related to identifying the re-activating and simultaneously occurring pit events from the potentiostatic current transient data. A detailed

investigation of the error introduced by the spatiotemporal evolution of pit events towards the metastable pit size calculations has been discussed in Chapter 6 [Sridhar et al. 2021].

5.3.3. Comparison of actual vs estimated V_{pit}

A comparative study of the actual pit volume ($V_{pit,actual}$) measured using a 3D optical profilometer (Alicona Infinite Focus) at the metastable pit location versus the estimated pit volume ($V_{pit,corrected}$) determined from Faraday's laws (as discussed in Chapter 3) was carried out to validate if the fraction of C_{pit} lost to C_{HE} was negligible. Figure 4.8 shows the transient and its associated metastable pit location that was considered for this comparative study. The cumulative d_{bubble} and $C_{transient}$ during this event was 25.68 μm and 2382.37 nC, respectively. Accordingly, the C_{HE}/C_{pit} for this event was 0.035. From Figure 4.8 A-2, it is evident that the pit mouth was irregular in geometry. The largest vertical and horizontal dimensions through the centre of the pit were 7.19 μm and 6.95 μm, respectively. Hence, an assumption of hemispherical pit geometry and calculation of the corresponding hemispherical r_{pit} would not provide a deterministic conclusion. Therefore, the determination of pit volume is essential to derive a reasonable comparison. Figure 5.3 (a) and (b), which present the top and the side view of the pit, respectively, indicate that this pit had a maximum depth of 2.47 μm. The $V_{pit,actual}$ measured at this pit location using the 3D optical profilometer was 82.23 ± 6.4 μm^3. Table 5.4 presents the comparison of $V_{pit,actual}$ versus $V_{pit,corrected}$ for C_{HE}/C_{pit} of 0.035 determined during this transient and C_{HE}/C_{pit} of 0.16 reported by Beck [Beck 1984]. The data in Table 5.4 indicates that the values of $V_{pit,actual}$ were in the range of $V_{pit,corrected}$ for both C_{HE}/C_{pit} = 0.035 and C_{HE}/C_{pit} = 0.16. However, without an accurate knowledge of the percentage contribution of the β phase-precipitates and the Al-rich matrix to the C_{pit}, a deterministic conclusion could not be arrived for this study. In addition, the difference in $V_{pit,corrected}$ was not significantly different enough to overcome the measurement error of the 3D optical profilometer to derive a deterministic conclusion.

Table 5.4 Comparison of the actual and estimated V_{pit} for the transient/pit in Figure 4.9.

$V_{pit,corrected}$ at C_{HE}/C_{pit} = 0.035 (μm^3)	**$V_{pit,corrected}$ at C_{HE}/C_{pit} = 0.16 (μm^3)**	**Actual V_{pit} (μm^3)**
98.93 ($V_{pit,\beta}$) ≥ $V_{pit,corrected}$ ≥ 74.28 ($V_{pit,matrix}$)	110.69 ($V_{pit,\beta}$) ≥ $V_{pit,corrected}$ ≥ 83.12 ($V_{pit,matrix}$)	82.23 ± 6.4

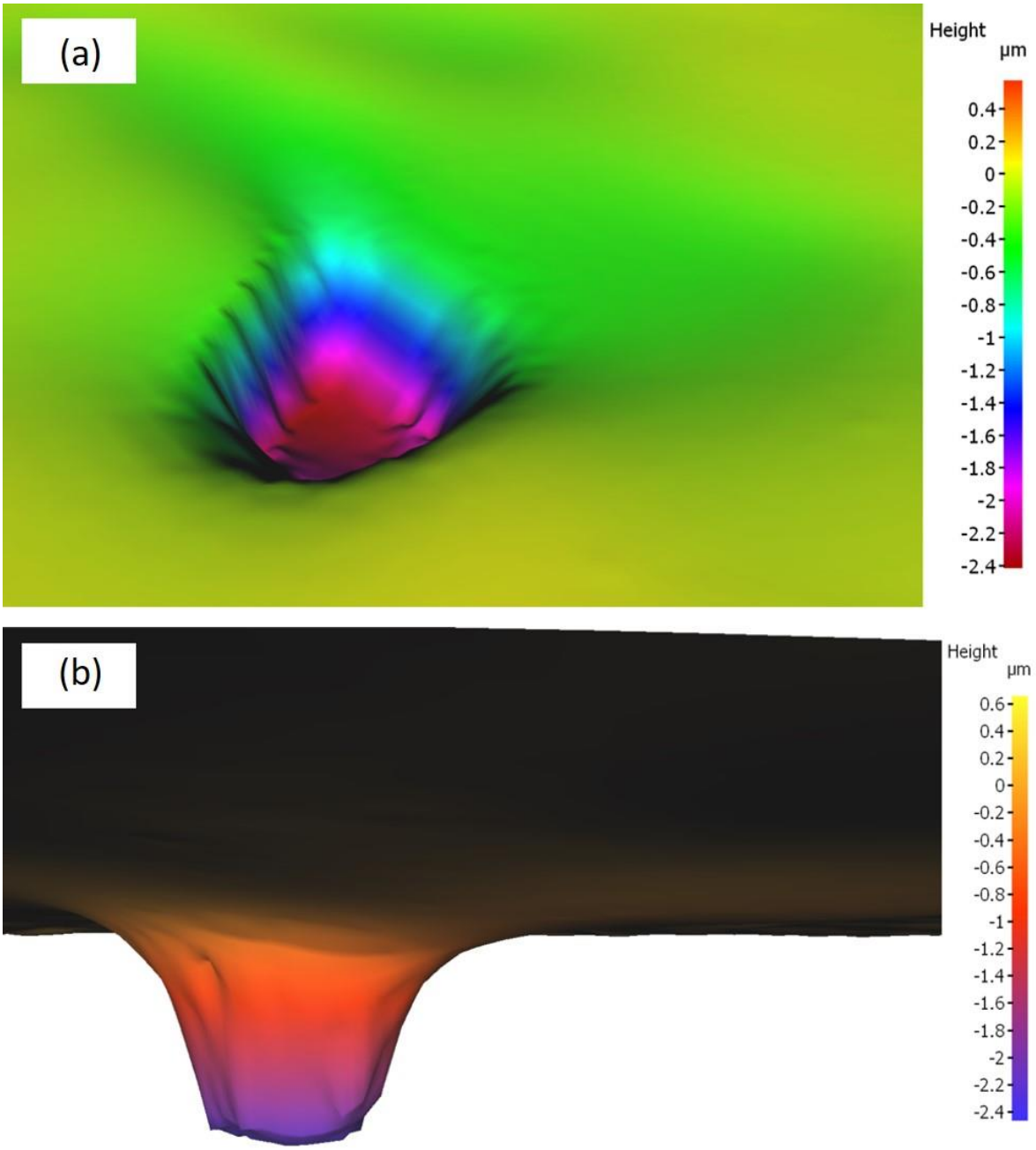

FIGURE 5.3. The 3D optical profilometric image: (a) top view and (b) side view of the metastable pit associated with the transient shown in Figure 4.9.

5.4. Conclusions

The present in situ study evaluates the error introduced by hydrogen evolution (HE) occurring within pits on the estimation of metastable r_{pit} from the $C_{transient}$. Following are the key conclusions:

- The HE current density (i_{H_2}) during metastable pitting studies was higher than 1 mA.cm$^{-2,}$ indicating that the bubble diameter (d_{bubble}) was a proximate measure of the volume of hydrogen generated within the pit. Therefore, the d_{bubble} was employed in understanding the fraction of the pit dissolution charge (C_{pit}) lost to hydrogen evolution (C_{HE}).
- The fraction of the net pit dissolution charge consumed by HE, C_{HE}/C_{pit} was observed to vary from 0.019 to 0.052 depending on the $C_{transient}$. By incorporating these values from the present study, the percentage error in the hemispherical metastable r_{pit} calculated from $C_{transient}$ was a maximum of 2%.
- Therefore, it was concluded that the charge consumed by HE within the pits might not be a critical factor in the underestimation of metastable r_{pit} determined from current transients recorded at anodic potentials below E_{pit}.

Chapter 6

The role of the spatiotemporal evolution of pit events on the estimated metastable pit sizes

6.1. Background

The charge accumulated by the current transients ($C_{transient}$), determined by integrating the area under the $I-t$ curve, provides a quantitative assessment of the mass loss incurred at the pitted site and therefore aids in the estimation of metastable pit sizes (i.e., pit radius (r_{pit}) calculated by assuming a hemispherical pit geometry) [Frankel 1998; Pistorius et al. 1992; Pride et al. 1994]. The estimated pit sizes were reported to be consistent with the distribution of the actual pit sizes in SS and pure aluminium [Williams et al. 1994; Pride et al. 1994]. The pit stability criterion, $I_{peak}/r_{pit,peak} > 10^{-2}$ A.cm^{-1} [Williams et al. 1994; Pride et al. 1994], developed based on Galvele's pioneering works [Galvele 1981; Galvele 1976], using the estimated r_{pit} values, enable the determination of the current transients associated with stable pit events. In an independent study using extreme value statistics, a critical $C_{transient}$ i.e., a critical V_{pit} with an equivalent r_{pit} of 6.75 µm, was found to be associated with the pits that transitioned from metastability to stability in AA2024-T3 [Trueman 2005]. Such prospects of estimating the actual r_{pit} or V_{pit}, parameters which directly relates to pit stability [Buzza et al. 1995] and critical in predicting the pit-to-crack transition [Kondo 1989], augments the relevance of $C_{transient}$ as a parameter of significance in understanding the pitting susceptibility of alloy systems.

‡ *G. Sridhar, N. Birbilis and V.S. Raja, Corrosion Science, Volume 182, 15 April 2021, 109276*

Despite its competence, the utilisation of $C_{transient}$ as a reliable parameter in determining the actual metastable r_{pit} has remained topical. In aluminium, the occurrence of copious hydrogen evolution within the pits is regarded to depreciate the $C_{transient}$ [Frankel 1998] by ~ 16% [Beck 1984]. Though Pride et al. showed that the difference in the distribution of the estimated versus actual metastable pit sizes was only marginal in pure aluminium and that the C_{HE} was minimal [Pride et al. 1994], severe discrepancies have been reported in aluminium alloys [Guan et al. 2015; Guan et al. 2014]. In particular, the discrepancy witnessed in the estimated r_{pit} in a binary Al-Mg alloy was attributed to the possibility of multiple pit reactivations as the number of actual pits was smaller than the total number of current transients recorded [Guan et al. 2020]. On the contrary, in an Al-Mg-Si alloy with cathodic second phase particles, the number of actual pits was found to be larger than the number of current transients, indicating the possibility of multiple co-occurring pit events, i.e., the presence of overlapped current transients [Guan et al. 2014]. Though such possibility of the occurrence of multiple overlapping current transients [Gupta et al. 2012; Guan et al. 2016b; Wang et al. 2016b] and pit reactivations [Burstein et al. 2001; Sasaki et al. 2004] is widely acknowledged, the error they introduce in the context of metastable r_{pit} estimation from $C_{transient}$ has often been overlooked. More specifically, a comparison between the magnitude of the error introduced by the spatiotemporal evolution of pit events and the conventionally held HE has remained unexplored. Such insights being critical in understanding the factors that limit the reliable assessment of metastable r_{pit} from current transients, forms the motive behind the present work. Accordingly, the work herein is an attempt to investigate if the conventional notion of treating each current transient as signals arising from single discrete pit events is valid in the context of metastable r_{pit} estimations from $C_{transient}$.

To understand the role of the (electrochemical) nature of the second phase particles, binary Al-Mg alloy with (so-called "anodic") Mg_2Al_3 (β) phase precipitates and commercially pure aluminium, which comprised a population of (so-called "cathodic") Al_3Fe constituent particles were studied herein.

6.2. Objective

The inconsistencies introduced in the r_{pit} estimated from $C_{transient}$ by treating each current transient as a signal arising from single discrete pit events were investigated as a

function of the electrochemical nature of the second phase particles by understanding the following: (a) is each current transient associated with a single discrete pit event or multiple co-occurring pit events, i.e., overlapped current transient? (b) does each subsequent transient arise from a recurring pit event or a new discrete pit event? and (c) do the answers to the questions (a) and (b) vary as a function of electrochemically distinct second phase particles.

6.3. Results

6.3.1. Electrochemical characterisation

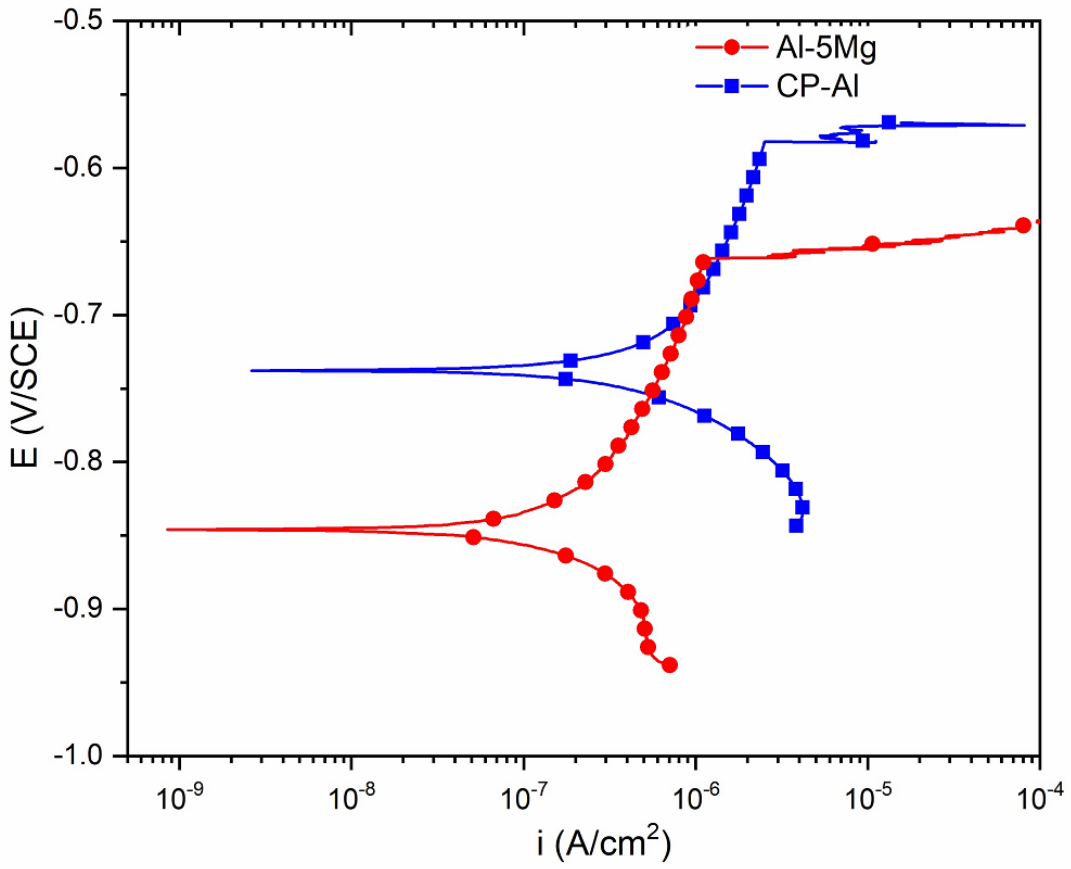

Figure 6.1. The potentiodynamic polarisation response of CP-Al and Al-5Mg recorded at a scan rate of 0.5 mV.s^{-1} in 0.01 M NaCl.

The typical potentiodynamic polarisation response of Al-5Mg and CP-Al in 0.01 M NaCl is presented in Figure 6.1. Based on the preliminary potentiostatic-imaging experiments, the potential for the potentiostatic studies was chosen as 25 mV below E_{pit}, which was - 0.605

V_{SCE} for CP-Al and - 0.710 V_{SCE} for Al-5Mg. The selected polarisation potential facilitated the generation of visually resolvable hydrogen bubbles at the pit locations, which permitted their mapping and association with the relevant current transients. The chosen potential also enabled the generation of an optimum number of current transients and minimised the probability of the formation of stable pits during the test duration.

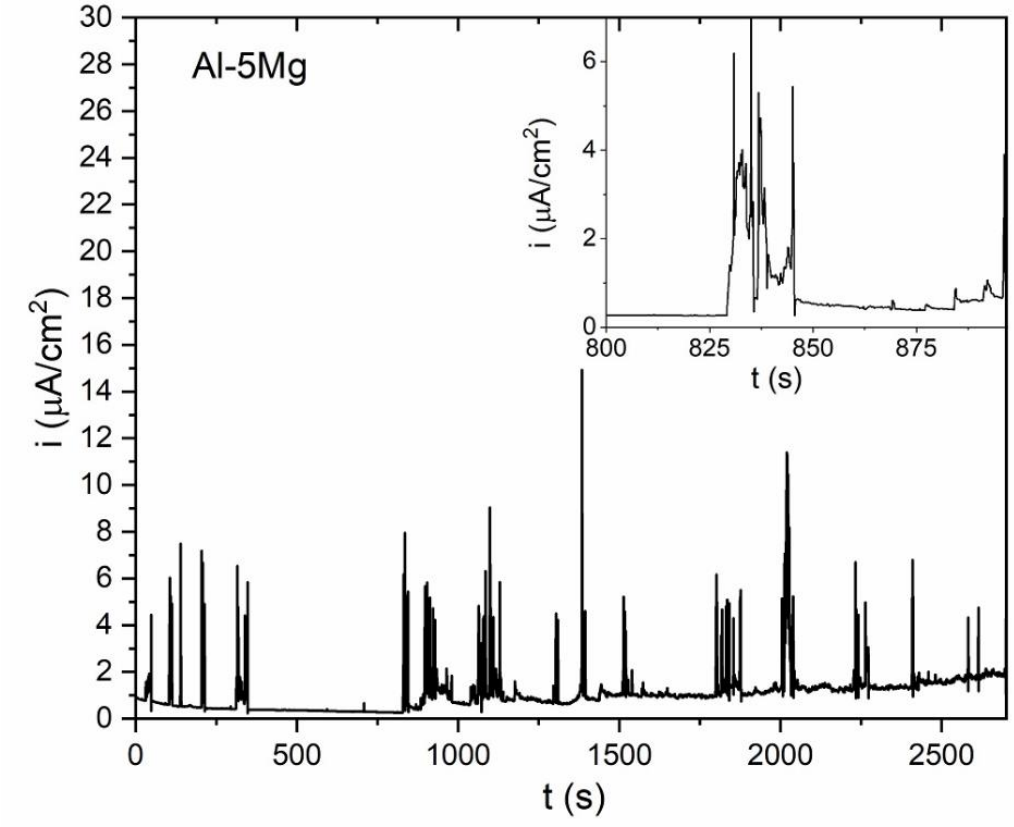

Figure 6.2. The potentiostatic polarisation trend of Al-5Mg tested at E_{pit} – 25 mV (- 0.710 V_{SCE}) in 0.01 M NaCl. The inset plot shows the onset of quasi-stable transients at 829 s.

The potentiostatic trend of Al-5Mg and CP-Al recorded at E_{pit} – 25 mV in 0.01 M NaCl is presented in Figure 6.2 and Figure 6.3, respectively. The CP-Al exhibited a higher cumulative number of current transients and charge accumulation (Figure 6.4 and Table 6.1) than Al-5Mg, demonstrating the higher metastable pitting propensity of CP-Al. The higher pitting rate and charge accumulation of current transients in CP-Al could be attributed to the cathodic Al_3Fe IMPs that stabilise the pit location by supporting cathodic reaction [Nisancioglu 1993]. However, it should be noted that this inference could be different had the comparison been made at iso-potentials. Both the potentiostatic trends in Figure 6.2 and Figure 6.3 exhibited all types of current transients, unlike SS, which predominantly exhibits transients of Type I [Pistorius et al. 1992; Frankel et al. 1987]. This observation suggests that the kinetic

factors governing the propagation of each pit event were distinct though the events evolved from the same type of second phase particles. The inset in Figure 6.2 and Figure 6.3 presents the instant of onset of quasi-stable transients in the potentiostatic trends, i.e., when an increment in the noise in $i_{passive}$ was witnessed after the first quasi-stable transient. From in situ imaging, these increments seem to arise from the unrecovered charge at the respective quasi-stable pit locations rather than representing an increase in the number of pit events. The presence of combined positive-negative transients was observed in the potentiostatic trend of CP-Al (Figure 6.11) that comprised cathodic Al_3Fe constituent particles is in agreement with the literature [Speckert et al. 2011].

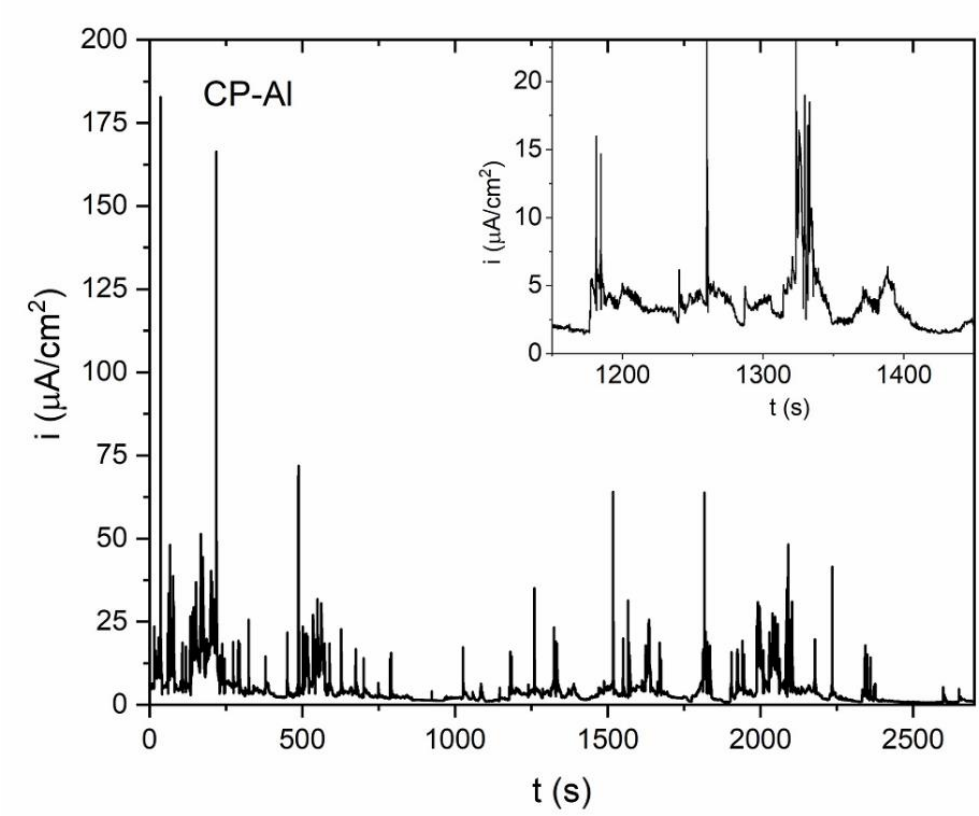

Figure 6.3. The potentiostatic polarisation trend of CP-Al tested at E_{pit} – 25 mV (- 0.605 V_{SCE}) in 0.01 M NaCl. The inset plot shows the onset of quasi-stable transients at 1176 s.

Table 6.1. The pitting rate and the charge accumulated by the pit events during the potentiostatic polarisation of Al-5Mg and CP-Al at E_{pit} - 25 mV in 0.01 M NaCl.

Material	Pitting rate ($cm^{-2}.s^{-1}$)	Charge accumulated by pit events (μC)
Al-5Mg	14 ± 2	17.04 ± 0.30
CP-Al	56 ± 6	51.36 ± 0.02

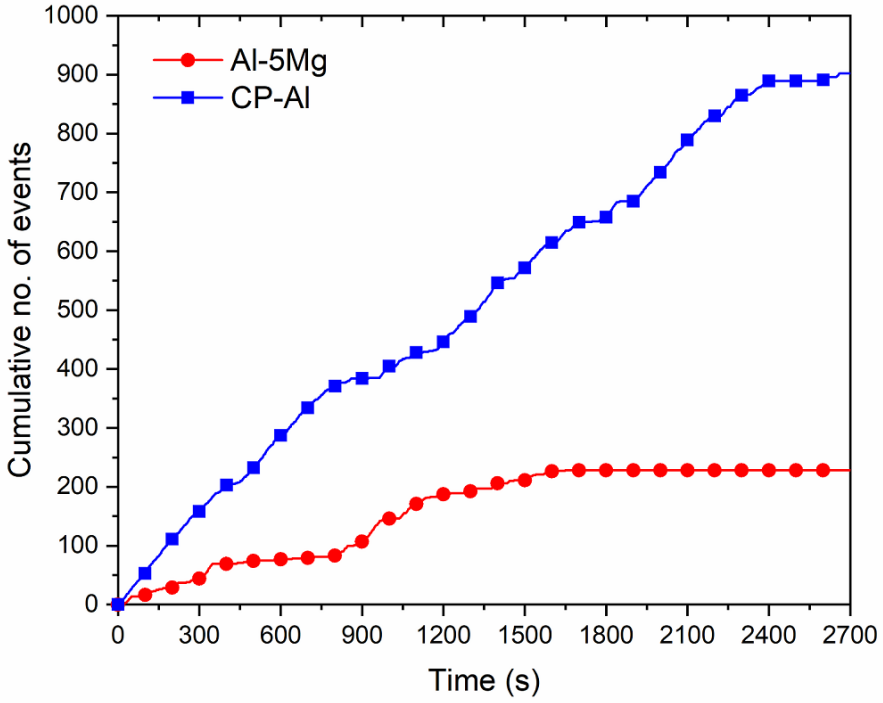

Figure 6.4. The plot of the cumulative no. of pit events witnessed in Al-5Mg and CP-Al when tested at E_{pit} – 25 mV in 0.01 M NaCl.

6.3.2. Spatio-temporal investigation of current transients associated with pit events:

Minuscule breakdown events:

In situ timelapse imaging revealed a ubiquitous occurrence of several short-lived minuscule pit events with diameters < 2 µm during the entire test duration. These events activated multiple times from the same location and co-occurred with numerous similar pit events. Figure 6.5 illustrates the in situ timelapse image of the minuscule breakdown events recorded upon Al-5Mg. The $I-t$ trend shown in the inset of Figure 6.5 indicates that the minuscule pit events were not associated with measurable current transients. This observation is not surprising since the co-occurrence of multiple pit events of similar magnitude would result in a collective increase in $i_{passive}$ rather than resulting in temporally resolved current transients.

The minuscule events witnessed may be ascribed to the breakdown and healing episodes of the passive film, termed as breakdown events, supporting the view that the $i_{passive}$ is composed of many such events rather than the passage of a constant charge [Frankel 1998,

Burstein et al. 2009]. Besides, a significant fraction of these events (~ 99 %) did not transition to propagating pit events, substantiating this inference. A detailed investigation of the pit sizes associated with these pit events was not possible due to the limitation posed by the magnitude of noise in $i_{passive}$ and the resolution of imaging. However, since the electrochemical signals arising from these events were insignificant, their influence on the pit sizes estimated for measurable current transients may be regarded as negligible.

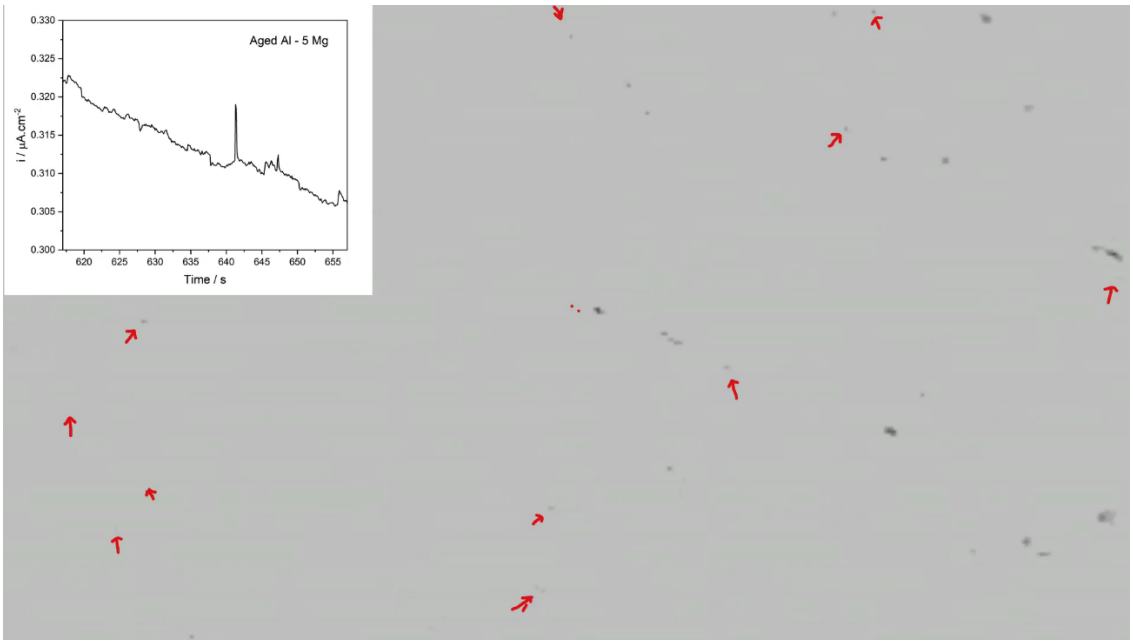

Table 6.5. The snapshot of minuscule breakdown events recorded during in situ imaging-potentiostatic testing of Al-5Mg at E_{pit} – 25 mV in 0.01 M NaCl.

Pit nucleation transients:

Pit nucleation transients, such as that presented in Figure 6.6, were associated with the rapid pit events that exhibited a lifetime lesser than 3 s. A detailed spatiotemporal investigation of these pit events was limited by the low frame rate of video recording. Figure 6.7 presents an in situ snapshot of the pit nucleation events recorded on Al-5Mg during potentiostatic testing at E_{pit} - 25 mV. Among the events that could be imaged, a significant fraction (~ 99%) of them underwent repassivation without propagation, which is in agreement with the works of Burstein [Burstein et al. 2001; Burstein et al. 1992]. This observation supports the notion that the investigation of pit propagation events is more critical than the pit nucleation events for understanding the phenomenon of pit stabilisation, as they represent the larger pits that develop the conditions necessary for stability [Laycock et al. 1997]. Therefore, the insights derived

from the following sections regarding the utilisation of metastable pitting data in investigating the stable pitting propensity of alloy systems are not altered by the inability to analyse the pit nucleation events. The evolution of pit propagation events was witnessed to be occasionally preceded by the occurrence of pit nucleation events in their vicinity which may be attributed to the local weakening of passive film induced by these events [Burstein et al. 1995b].

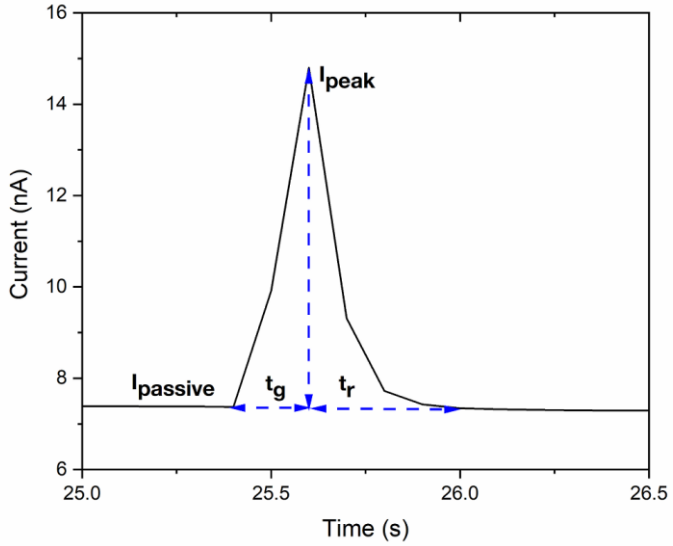

Figure 6.6. A pit nucleation transient recorded during the potentiostatic testing of Al-5Mg at E_{pit} – 25 mV in 0.01 M NaCl.

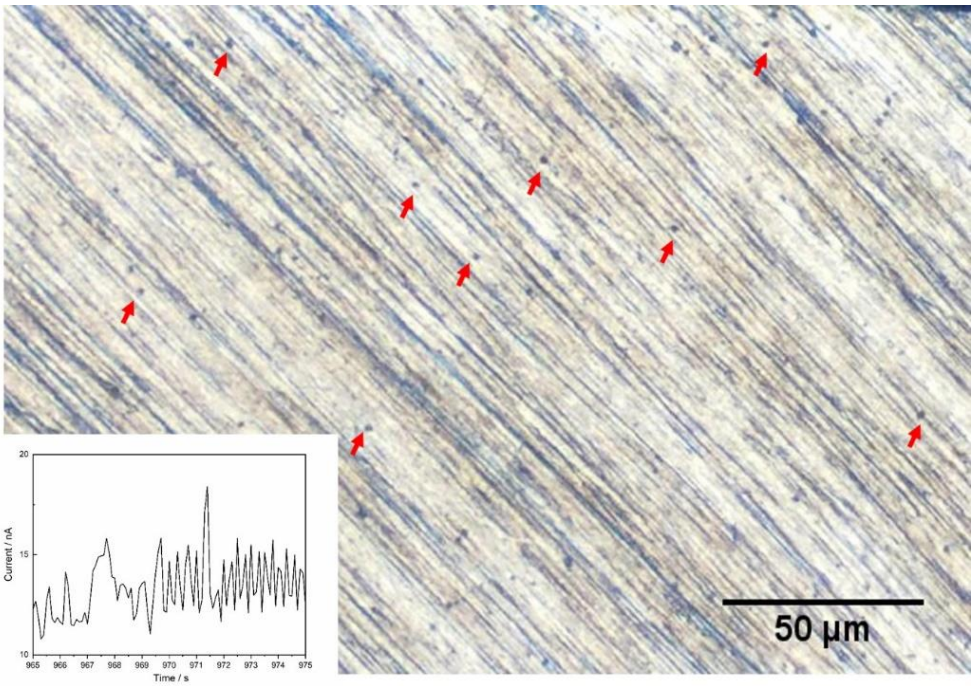

Figure 6.7. The snapshot of pit nucleation events recorded during the in situ imaging-potentiostatic testing of CP-Al at E_{pit} – 25 mV in 0.01 M NaCl. Inset shows the potentiostatic trend at the juncture of image capture.

Single peaked propagation transients: Type I and Type II

Single discrete pit events

Single peaked transients of Type I represent the pit events that underwent gradual propagation followed by rapid repassivation, i.e., $t_g > t_r$. Figure 6.8 presents the variation of d_{bubble} at the pit location (identified using in situ imaging) with I_{pit} during a single-peaked propagation transient of Type I.

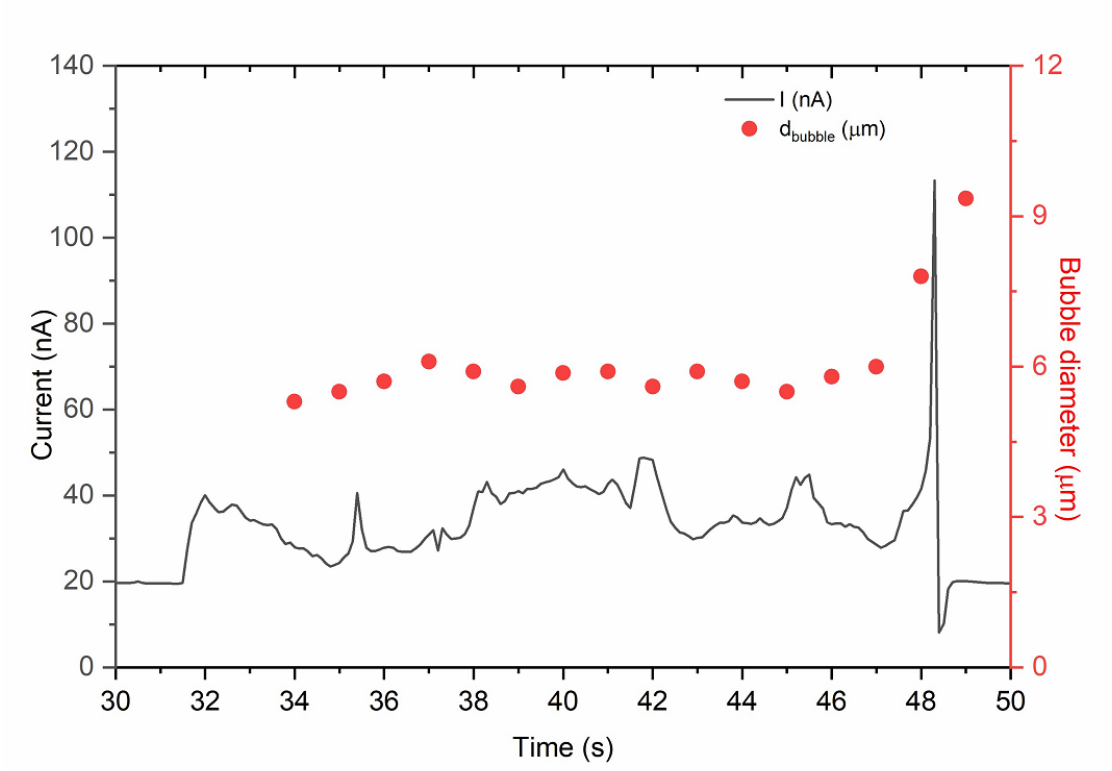

Figure 6.8 The variation of current with bubble diameter during a single-peaked pit propagation transient of Type I observed in the potentiostatic trend of Al-5Mg recorded at E_{pit} – 25 mV in 0.01 M NaCl.

The pit propagation during Type I transients is driven by the resistance of the porous pit covers that govern the diffusion of metal ions out of the pit [Frankel 1998]. During the repassivation phase (t_r) at the end of the transient, the bubble underwent rapid dissolution after reaching a maximum d_{bubble} of 10 µm, indicating the loss of pH necessary to sustain HE. This observation indicates that a rapid dilution of the pit anolyte has occurred, which could be induced by the rupturing of pit covers by the hydrogen bubble [Natishan et al. 1989]. The transient in Figure 6.8 was associated with the propagation of a single discrete pit event and therefore followed the conventional theory that each current transient represents single discrete

pit events [Frankel 1998, Pistorius et al. 1992]. The error in the estimated $r_{pit,\beta}$ for this transient arises from disregarding C_{HE}. The C_{HE} for a cumulative d_{bubble} of 10 µm witnessed during this transient is 4.5 nC. The total C_{pit} may be calculated from the sum of C_{HE} and $C_{transient}$ of 268.03 nC as 272.53 nC, which yields a $V_{pit,\beta}$ of 12.53 µm^3 and an equivalent $r_{pit,\beta}$ of 1.82 µm. The pit stability value for this transient is 0.496 mA.cm^{-1}. The pit growth rate of this event is 5.23 nA,s^{-1}. The percentage underestimation of the metastable pit size, in this case, is 0.55%.

Single peaked Type II transients were characterised by rapid growth followed by slow repassivation, wherein $t_g < t_r$ as shown in Figure 6.9.

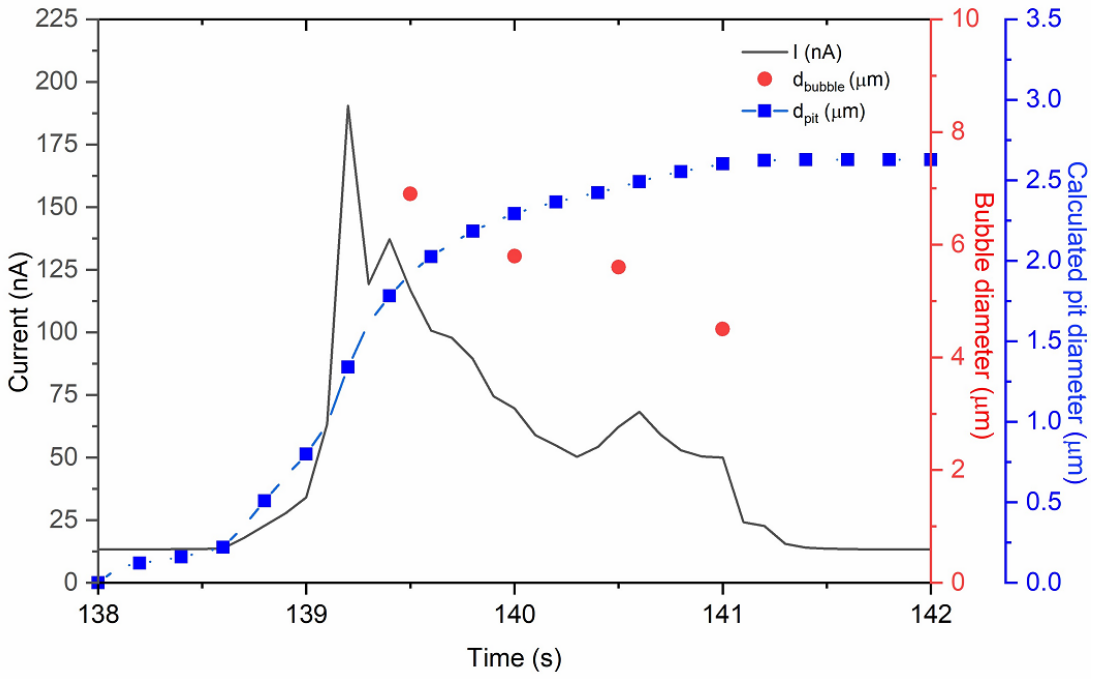

Figure 6.9 The variation of current with bubble diameter during a single-peaked pit propagation transient of Type II observed in the potentiostatic trend of Al-5Mg recorded at E_{pit} – 25 mV in 0.01 M NaCl.

The d_{bubble} at the pit location varied following a corresponding change in I_{pit} (identified using in situ imaging), similar to the Type I transients. Pride et al. attributed the higher t_r witnessed during these transients to the time required for the sluggish reformation of the oxide film in addition to the gradual dilution of the pit solution in aluminium [Pride et al. 1994]. In SS, Riley et al. explained that a phenomenon termed constructive dissolution resulted in a two-stage repassivation [Riley et al. 1991]. Kim and Buccheit observed a similar two-stage repassivation and attributed it to the influence of Cu in an Al-Cu alloy [Kim et al. 2007]. From

Figure 6.9, it is evident that the estimated pit diameter (d_{pit}) increased during t_r, i.e., after the I_{peak} at 139.2 s, indicating that the anodic dissolution prevailed at reduced rates in addition to gradual repassivation during t_r. This fact is supported by the observation of a gradually dissolving bubble during t_r after I_{peak} in contrast, to the rapidly dissolving hydrogen bubbles in the case of Type I transients. The transient in Figure 6.9 was associated with a single discrete pit event that did not undergo further activation. The C_{HE} for the cumulative d_{bubble} of 7.8 µm observed during this transient was 2.13 nC which when added to the $C_{transient}$ of 142.7 nC yields a C_{pit} of 144.83 nC, $V_{pit,\beta}$ of 6.66 µm^3 and an equivalent hemispherical $r_{pit,\beta}$ of 1.47 µm. The pit stability value for this transient is 2.46 mA.cm^{-1}. The growth rate of this pit event is 61.21 nA/s. By disregarding C_{HE}, a percentage underestimation of 0.54% is incurred in the hemispherical pit radius estimated from the $C_{transient}$.

Multiple recurring and co-occurring pit events

Single-peaked current transients are typically considered to be associated with single discrete pit events wherein extensive pit dissolution is anticipated at I_{peak}. However, with in situ imaging, it has been identified that the single-peaked current transients could also be associated with multiple co-occurring pit events, counterintuitive to the conventional theory. Figure 6.10 presents the transients associated with the co-occurrence of multiple discrete pit events (pit$_1$ and pit$_2$) during Transient B and the consecutive reactivation of the same pit location (pit$_1$) during the Transients A and B, in CP-Al. The metastable pitting parameters associated with the pit size estimation of these events are tabulated in Table 6.2. The charge relevant to pit$_1$ and pit$_2$ during their simultaneous occurrence in Transient B was resolved based on the relative ratio of their d_{bubble} (Table 6.2). With an estimated hemispherical $r_{pit,matrix}$ of 2.02 µm (i.e., $V_{pit,matrix}$ of 17.32 µm^3) at the end of Transient A, the event pit$_1$ led to consecutive reactivation of the same pit location during Transient B. The true hemispherical $r_{pit,matrix}$ equivalent to the total C_{pit} accrued by pit$_1$ from both the transients A and B is 2.48 µm (i.e., a $V_{pit,matrix}$ of 31.96 µm^3). In the absence of spatiotemporal insights, the pit size ($r_{pit,matrix}$) at this location would have been underestimated by 19% if the conventional approach had been adopted. The pit stability value and pit growth rate for pit$_1$ during Transient A are 2.57 mA.cm^{-1} and 600 nA.s^{-1}, respectively.

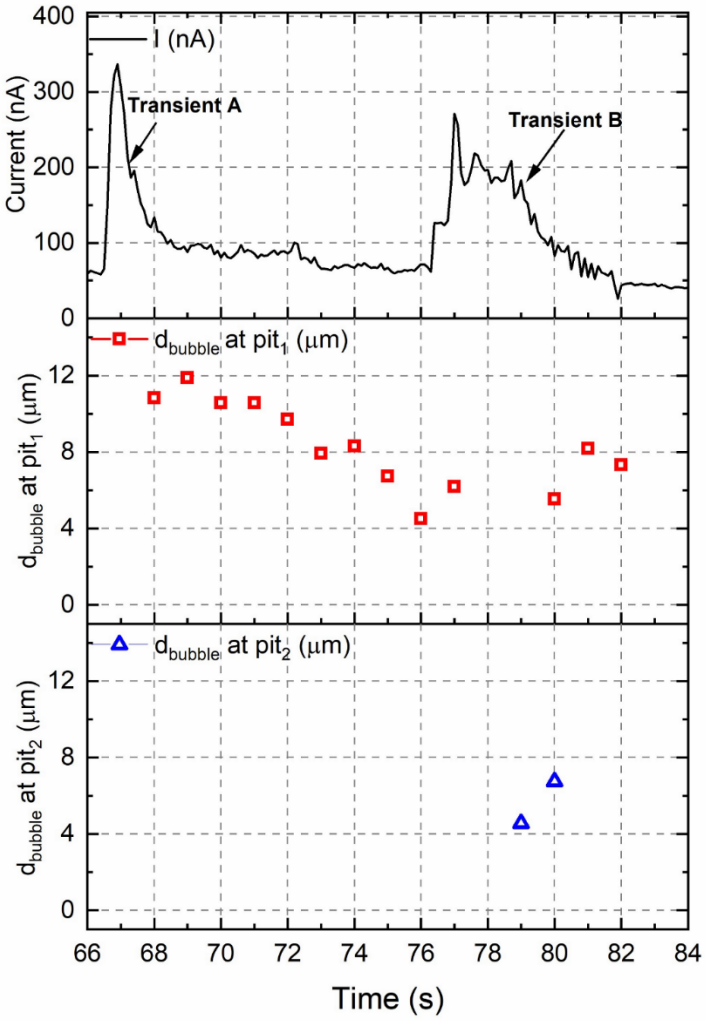

Figure 6.10. The consecutive current transients associated with the multiple activations of pit1 during Transient A and B and the simultaneous occurrence of pit_1 and pit_2 during Transient B, recorded during the potentiostatic testing of CP-Al at E_{pit} – 25 mV in 0.01 M NaCl.

Table 6.2. The metastable pitting parameters of the current transients associated with pit_1 and pit_2 presented in Figure 6.10.

Pit	**Transient**	**No. of pit activation**	**Cumulative bubble diameter, d_{bubble} (µm)**	**Charge consumed by the transient, $C_{transient}$ (nC)**	**Charge consumed by hydrogen evolution, C_{HE} (nC)**	**C_{pit} = $C_{transient}$ + C_{HE} (nC)**	**Total anodic charge consumed at the pit location, C_{total} = $C_{,pit_1}$ + C_{pit_2} (nC)**	**Final calculated hemispherical pit radius, $r_{pit,matrix}$ (µm)**
1	A	First	14.04	489.43	12.45	501.88	925.84	2.48
1	B	Second	8.32	421.37	2.59	423.96		
2	B	N/A	6.75	68.31	1.38	69.69	69.69	1.05

The multiple pit reactivations witnessed herein may be attributed to the presence of stable cathodic Al_3Fe constituent particles that promote localisation of pit dissolution due to their strong cathodic activity. In the case of pit_2, the true estimated $r_{pit,matrix}$ being 1.05 µm (i.e., $V_{pit.matrix}$ of 2.41 μm^3) would have been overestimated if the $C_{transient}$ of Transient B was entirely attributed to pit_2. The above discussions indicate that the pit sizes can be both underestimated and overestimated depending on the spatio-temporal evolution of pit events. Besides, it is evident that the single peaked transients may indeed comprise multiple overlapping current transients from co-occurring pit events without a precise transition point that marks the initiation of a co-occurring pit event. This observation signifies that the deconvolution of overlapped current transients is not straightforward and requires further computational analysis. The occurrence of multiple pit events during a single-peaked current transient contradicts the conventional notion of treating each current transient as signals arising from single discrete pit events.

The C_{HE}/C_{pit} for pit_1 and pit_2 during the Transients A and B were 0.016 and 0.020, respectively. These values do not introduce an error greater than 1.5% in the estimated pit sizes, emphasising that the error introduced by the spatiotemporal evolution of pit events was more significant than that introduced by HE.

Combined positive-negative current transients:

The appearance of combined positive-negative current transients in the potentiostatic trend of CP-Al (Figure 6.11) is in agreement with the work of Speckert and Burstein [Speckert et al. 2011]. A continuous liberation of hydrogen bubbles from the pit locations was witnessed during the occurrence of such transients. The charge of one negative spike between 1282 s and 1283 s was -1.370 nC. By considering this charge to be entirely responsible for HE, the evolution of a spherical bubble with a d_{bubble} of 3.38 µm is anticipated at the pit location. The average d_{bubble} witnessed during this timeframe was 3.26 µm. This observation indicates that the HE was the dominant reduction reaction during the occurrence of combined positive-negative current transients in CP-Al. During each consecutive combined positive-negative transient, the same location reactivated multiple times. The total $C_{transient}$ and C_{HE} for all the 5 transients being 82.13 nC and 3.1 nC, results in an accrued C_{pit} of 85.23 nC and calculated hemispherical r_{pit} of 1.12 µm (i.e., $V_{pit,matrix}$ of 2.94 μm^3). The $C_{transient}$ and $r_{pit,matrix}$

estimated for an individual positive-negative transient being 17.05 nC and 0.66 µm (i.e., $V_{pit,matrix}$ of 0.59 µm^3) respectively, indicates that the error in the estimated pit size is 41.07% if each subsequent combined positive-negative transient were to be treated as a discrete pit event. This observation indicates that the severe localisation of pit events in the presence of cathodic second phase particles could result in a series of combined positive-negative transients that result from recurring pit events. This phenomenon leads to a significant underestimation of the metastable pit sizes in aluminium alloys with cathodic second phase particles.

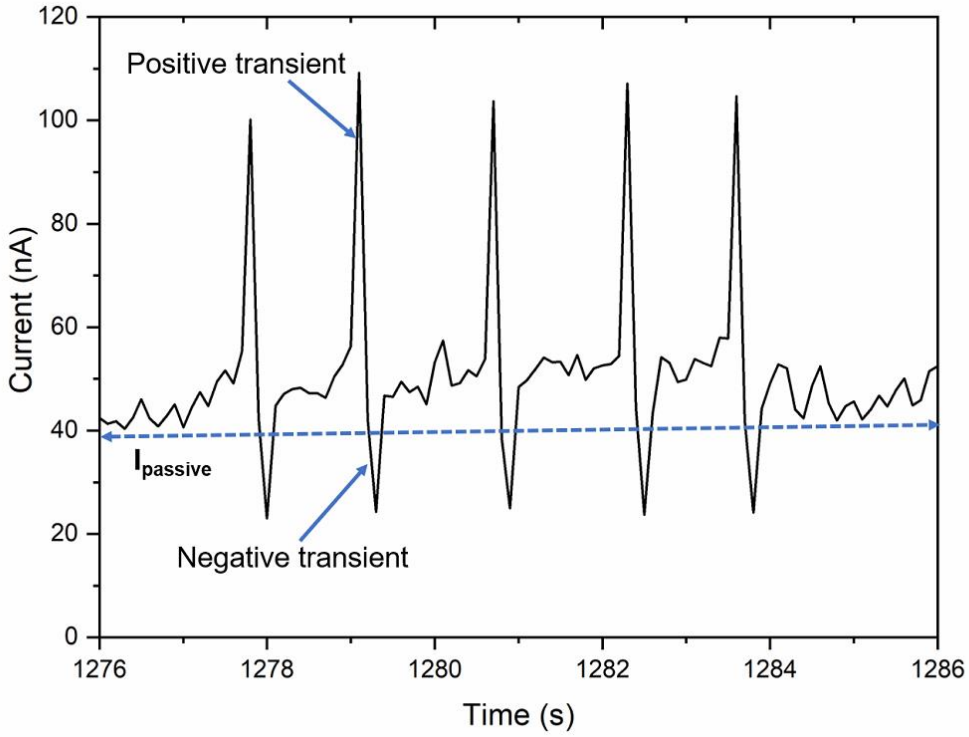

Figure 6.11. Combined positive-negative current transients observed in the potentiostatic trend of CP Al recorded at E_{pit} – 25 mV in 0.01 M NaCl.

Multi-peaked pit propagation transients: Type unclassified

Single discrete pit events

A significant fraction of the current transients in the potentiostatic trend of Figure 6.2 and Figure 6.3 exhibited multiple peaks and can be categorised as Type unclassified. Figure 6.12 illustrates a multi-peaked propagation transient associated with the occurrence of a single pit event in CP-Al. The multiple peaks within the transient were associated with the dynamic pit propagation processes occurring within the same pit location, as evident from the variation

of d_{bubble} following a corresponding change in I_{pit} in Figure 6.12. A similar inference was also reported by Sasaki et al. in a related study using pH-sensitive agar gels [Sasaki et al. 2004]. This observation indicates that the multiple peaks within a current transient may not necessarily arise from overlapping multiple pit events but from the multiple episodes of pit growth and repassivation occurring within the same pit location. For the transient in Figure 6.12, the $C_{transient}$ of 2499.79 nC and C_{HE} of 539.52 nC result in a C_{pit} of 2741.76 nC, $V_{pit,matrix}$ of 94.64 µm^3 and an equivalent hemispherical $r_{pit,matrix}$ of 3.56 µm. The percentage underestimation of pit size, in this case, is 2.53% which is introduced by not accounting C_{HE}. The relevant pit stability value and pit growth rate is 4.31 mA.cm^{-1} and 158.67 nA.s^{-1} respectively.

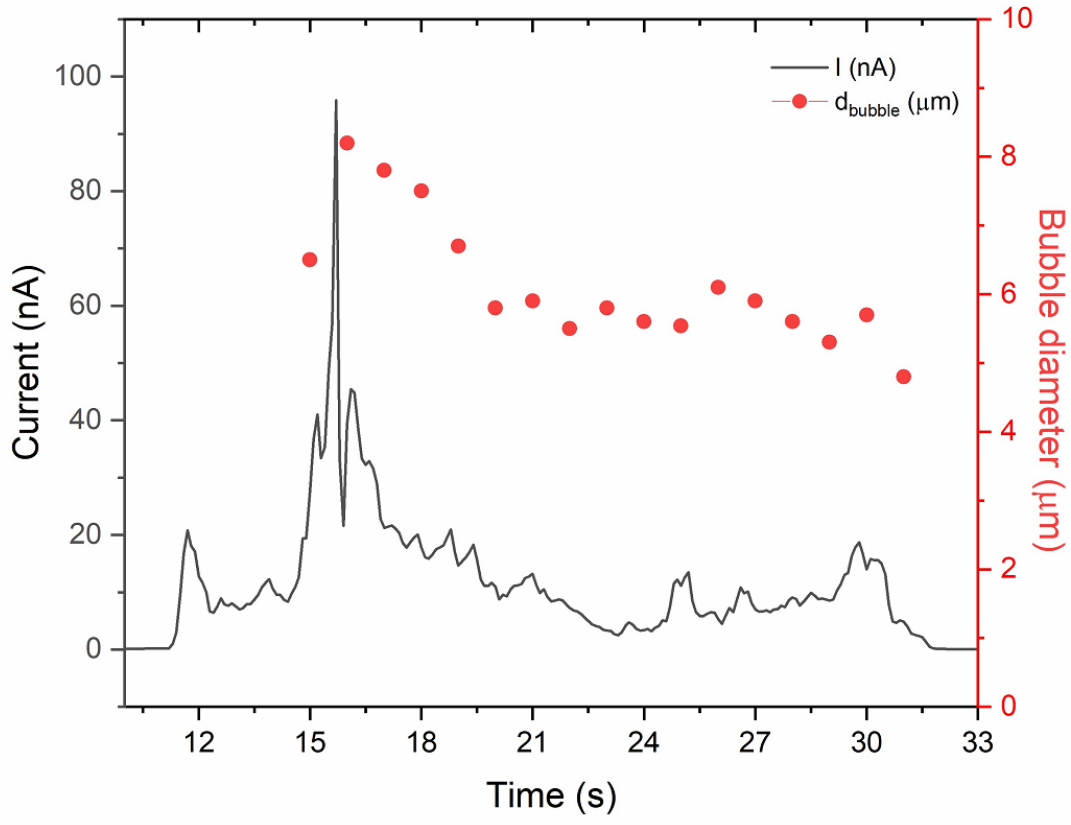

Figure 6.12. The variation of current with bubble diameter during a multi-peaked propagation transient of Type Unclassified observed in the potentiostatic trend of Al-5Mg recorded at E_{pit} – 25 mV in 0.01 M NaCl.

Multiple recursive pit events

Figure 6.13 presents the multi-peaked current transients associated with the reactivation of pit events from the same location during different timespans in Al-5Mg, as identified from in situ imaging. Table 6.3 presents the metastable pitting parameters associated with the pit events in Figure 6.13. This case demonstrates that the recursive pit events may not necessarily occur sequentially.

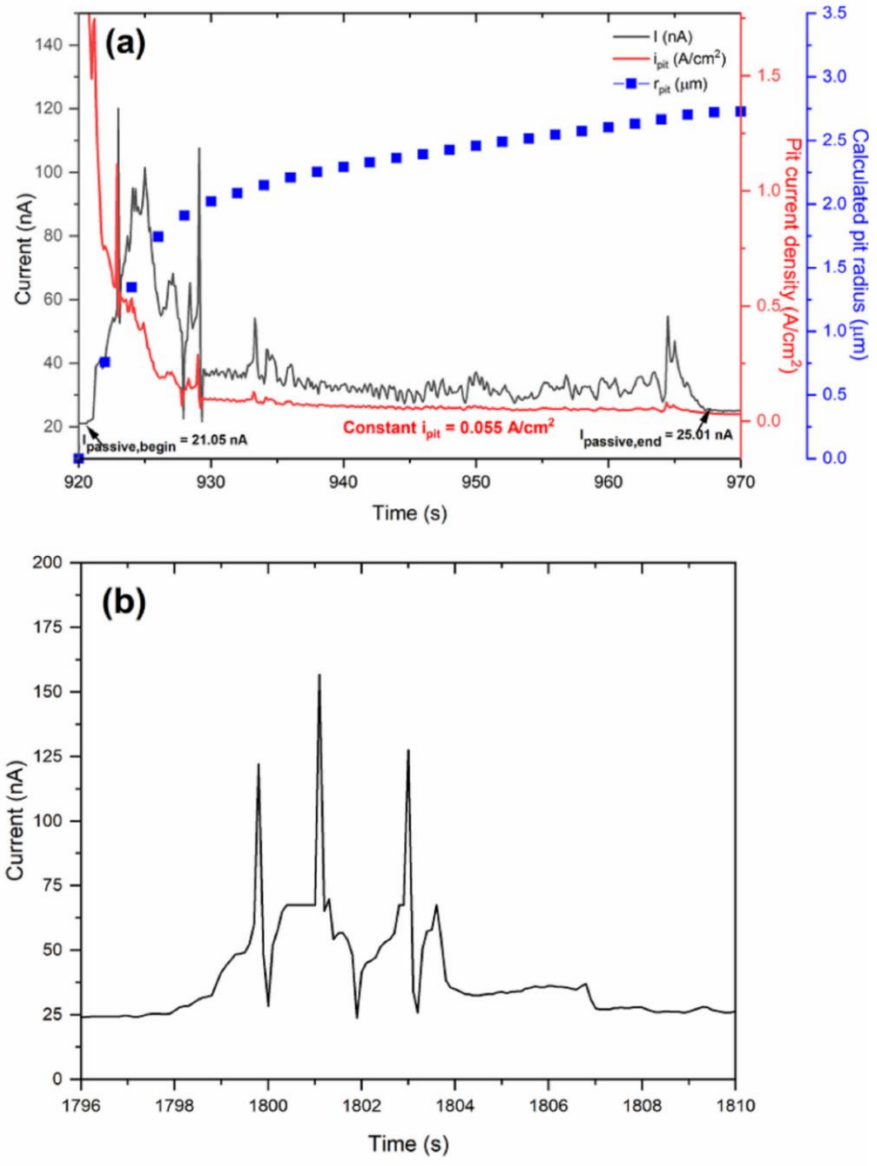

Figure 6.13. The multi-peaked current transients associated with the reactivation of the same pit location (a) first activation (b) second activation, recorded during the potentiostatic testing of Al-5Mg at E_{pit} – 25 mV in 0.01 M NaCl.

In Figure 6.13, the transient associated with the primary pit event that resulted in further activation of the pit location exhibited a t_{pit} of 48 s and a charge equivalent $r_{pit,\beta}$ of 2.99 µm (i.e., $V_{pit,\beta}$ of 55.87 µm^3). It is important to note that in order for this pit to reach a hemispherical $r_{pit,\beta}$ of 2.99 µm, an extensive propagation after the I_{peak} at 923 s was required. This observation indicates that the so-called "repassivation phase" of the transient [Pride et al. 1994; Kim et al. 2007] may not represent true pit re-passivation in reality. Instead, the pit seems to propagate under a constant current density of 55 mA.cm^{-2} during this period. The oscillatory noise in the region between 929 s and 964 s should arise from crystallographic tunnels propagating at the pit location [Kaesche 1990; Sasaki et al. 2002] since the current available for a hemispherical pit propagation is low [Newman 1995]. The final spike at 965 s marks the dissolution of the salt film that leads to the repassivation of the pit. Cook et al. discussed a similar jump in current due to the loss of salt film while investigating 1D pit electrodes of pure aluminium [Cook et al. 2012]. At the end of the so-called "repassivation", the transient did not recover to the $I_{passive,begin}$ (i.e., the event was quasi-stable), indicating that the location was active and prone to further activation. The pit stability value and the pit growth rate associated with this transient is 8.9 mA.cm^{-1} and 33.33 nA.s^{-1} respectively. The transient in Figure 6.13(b) was associated with the second activation of the same pit location wherein the presence of multiple peaks within this transient represents the complex and dynamic pit propagation processes involved. By disregarding the transient in Figure 6.13(b) associated with pit recurrence, pit size at the pit location is underestimated by 8.86%.

Table 6.3. The metastable pitting parameters of the current transients associated with the first and second activation of the same pit location for the transients presented in Figure 6.13.

No. of the pit activation	**Charge consumed by the transient, $C_{transient}$ (nC)**	**Calculated hemispherical pit radius from $C_{transient}$, $r_{pit,event,\beta}$ (µm)**	**Cumulative bubble diameter, d_{bubble} (µm)**	**Charge consumed by hydrogen evolution, C_{HE} (nC)**	**C_{pit} = $C_{transient}$ +C_{HE} (nC)**	**Total anodic charge consumed, C_{total} = C_{pit_1} + C_{pit_2} (nC)**	**Final calculated hemispherical pit radius, $r_{pit,\beta}$ (µm)**
First	921.86	2.73	22.24	49.47	971.33	1215.35	2.99
Second	222	1.7	16.98	22.02	244.02		

Multiple co-occurring pit events

Figure 6.14 illustrates the current transient associated with the simultaneous occurrence of pit events (pit_2 and pit_3) during the growth of pit_1 at 862 s and 886 s, respectively, as identified using in situ imaging, in CP-Al. The presence of an undissolved bubble at pit_1 (Figure 6.14) at the beginning of the transient indicates that this location has remained active from the previous pit propagation. The metastable pitting parameters associated with these pit events are tabulated in Table 6.4.

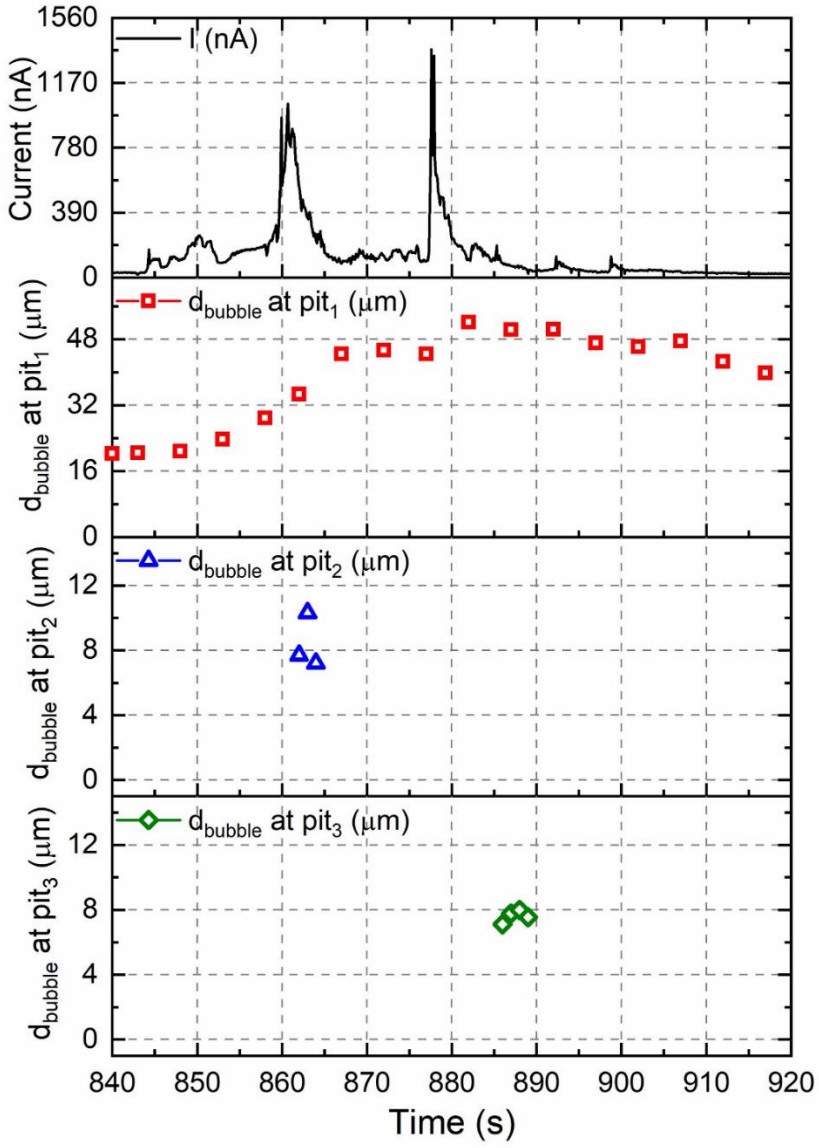

Figure 6.14. The simultaneous occurrence of multiple pit events (pit_1, pit_2 and pit_3) during an overlapped current transient recorded during the potentiostatic testing of CP-Al at E_{pit} – 25 mV in 0.01 M NaCl.

Table 6.4. The metastable pitting parameters of the co-occurring pit events during an overlapped current transient presented in Figure 6.14.

Charge of the transient, $C_{transient}$ (nC)	**Calculated hemispherical pit radius from $C_{transient}$, $r_{pit,matrix}$ (µm)**	**Pit event**	**C_{pit} from prior events (nC)**	**Cumulative bubble diameter, d_{bubble} (µm)**	**Charge consumed by hydrogen evolution, C_{HE} (nC)**	**Charge consumed by the individual current transients, $C_{transient}$ (nC)**	**C_{pit} = $C_{transient}$ + C_{HE} (nC)**	**Final calculated hemispherical pit radius, $r_{pit,matrix}$ (µm)**
8387.31	5.17	1	7525.55	54.39	723.6	7799.17	1.605×10^4	6.40
		2	N/A	10.3	4.91	451.98	456.89	1.96
		3	N/A	7.99	2.30	136.16	138.46	1.32

From Figure 6.14, it is evident that there was no precise transition point that marked the commencement of pit_2 or pit_3 within this transient, demonstrating the complexity involved in decoding the individual overlapped current transients. By treating each current transient as signals arising from single discrete pit events, the size of pit_1 would have been underestimated by 19.14 %. The size of the events pit_2 and pit_3 would have been either overestimated or disregarded from the calculation. This observation supports the findings of Guan et al., who reported that the number of pits observed on the pitted surface was larger than the number of current transients in an Al-Mg-Si alloy with cathodic second phase particles [Guan et al. 2014].

Irregular pit geometries

An assumption of hemispherical pit geometry is often adopted to estimate the metastable r_{pit} from current transients [Frankel 1998]. The present study demonstrates that the current transients may also originate from occluded geometries such as the pit propagation along abrasion lines and filiform-type propagations. Figure 6.15 presents the current transient associated with the propagation of a pit event along an abrasion line that led to the formation of multiple pit events in the vicinity of a primary pit location in Al-5Mg. As witnessed from the plot, the pit_1 underwent extensive pitting until it reached a $V_{pit,\beta}$ of 51.97 μm^3 at 210 s. Following this event, the pit events pit_2 and pit_3 initiated at locations to the left of pit_1. The duration between 215 s and 220 s was associated with pit propagation which was visible as black spots along the abrasion mark of pit_1 to generate pit_4 to the right of pit_1. Such preferential pit propagation along the abrasion lines that lead to progressive dissolution was also reported by Isaacs et al. in AA7075 [Isaacs et al. 2000]. They suspected such propagation to be induced by the diffusion of acidic pH from the high concentration of dissolved corrosion products at the pitted site along the abrasion marks. The type of second phase particles also influences the

pit geometry. The presence of Mg in Mg_2Al_3 (β phase) precipitates in aluminium is known to propagate with a filiform-like geometry [Lunder et al. 1994]. Ambat et al. 2006 showed similar morphologies on the surface and faceted pit interiors in aluminium alloys comprising Fe. Yasuda et al. 1990 reported that the presence of Cu in aluminium promoted irregular pitting in contrast to faceted pitting observed in pure aluminium. Therefore, the assumption of hemispherical pit geometry to determine r_{pit} from $C_{transient}$ in aluminium alloys could result in ambiguity.

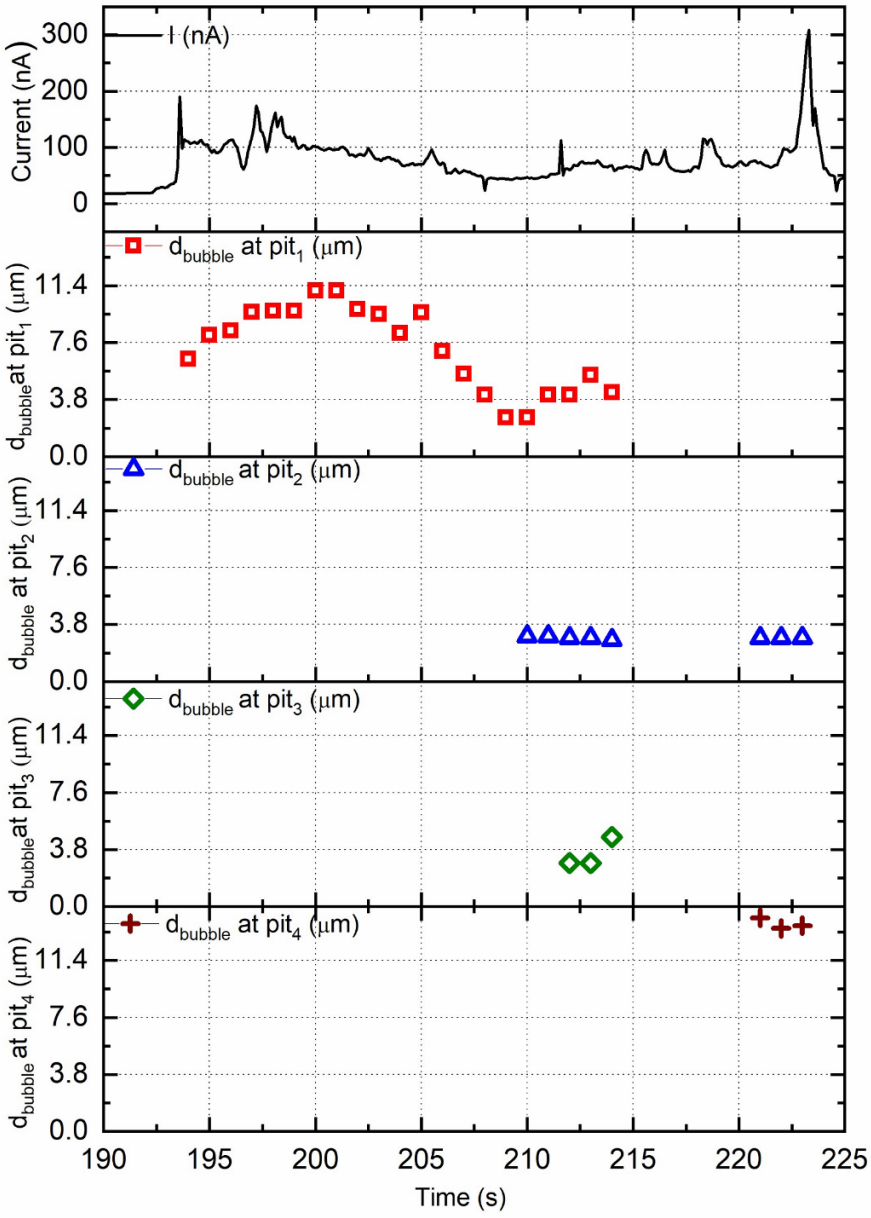

Figure 6.15. The multi-peaked pit propagation transient associated with the lateral propagation of pits along an abrasion line. The primary pit event (pit_1) induced pitting in its vicinity (pit_2, pit_3 and pit_4) during the potentiostatic testing of Al-5Mg at E_{pit} – 25 mV in 0.01 M NaCl.

Since the pit geometry of the location associated with the transient in Figure 6.15 was non-hemispherical, an estimation of hemispherical r_{pit} and other related metastable pitting parameters would be ambiguous. For instance, the estimated hemispherical r_{pit} of 3.5 µm equivalent to the C_{pit} for the transient in Figure 6.15 would be an extreme overestimation of the actual pit depth. Such overestimation of pit size by an inappropriate consideration of pit geometry has also been reported elsewhere [Hisamatsu et al. 1974]. The current transients in Al-5Mg were also observed to result in a filiform-type propagation, as shown in Figure 6.16.

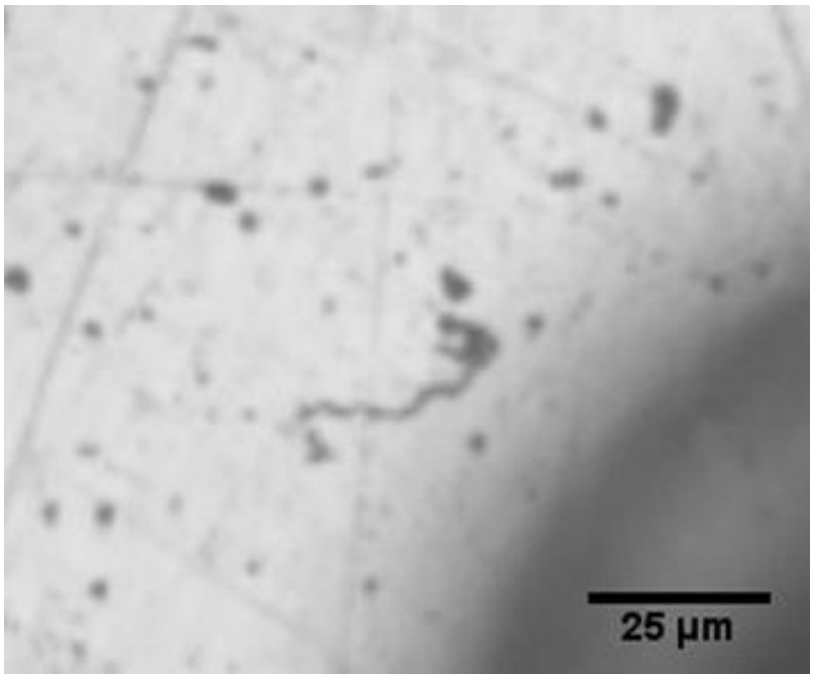

Figure 6.16. Filiform-like propagation of pitting recorded in situ during a metastable pit propagation transient generated during the potentiostatic testing of Al-5Mg (at the potential of E_{pit} – 25 mV) in 0.01 M NaCl.

The above discussions indicate that depending on the surface roughness and concentration of corrosion products resulting from extensive pit dissolution, the current transients may arise from the lateral propagation of pits or other occluded geometries rather than a uniform hemispherical pit dissolution. Therefore, the utilisation of an estimated hemispherical metastable pit radius/depth (r_{pit}) to determine the pit stability criterion could be misleading. Instead, a critical pit volume (V_{pit}), which does not involve a shape factor, could be a more suitable parameter in determining the pit stability.

Localised pit clusters

The temporal evolution of a cluster of pit events within a localised location in Al-5Mg is presented in the timelapse images shown in Figure 6.17. Figure 6.18, Table 6.5, and Table 6.6 present the current transients and metastable pitting parameters associated with these pit events.

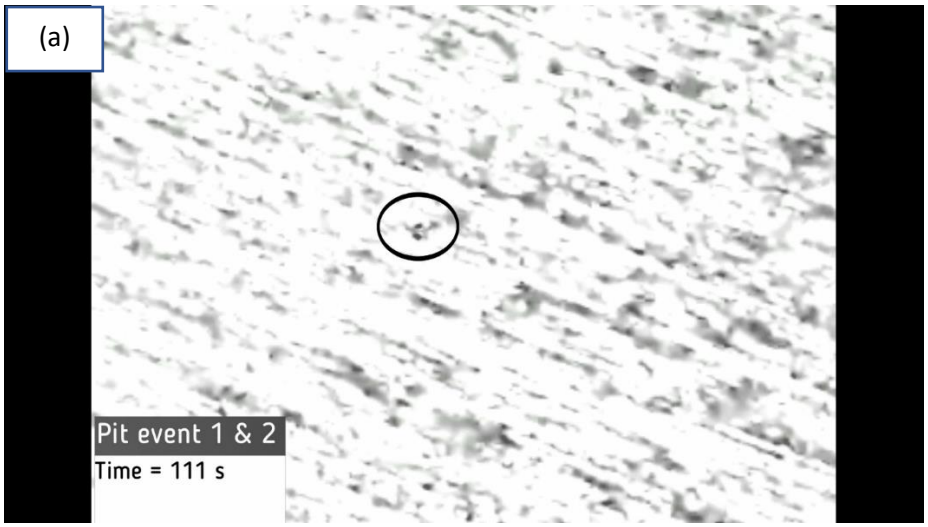

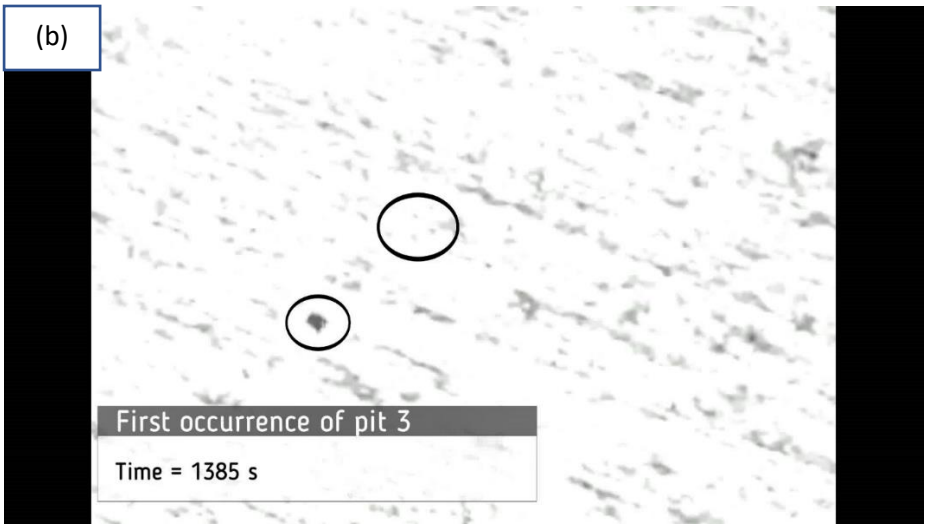

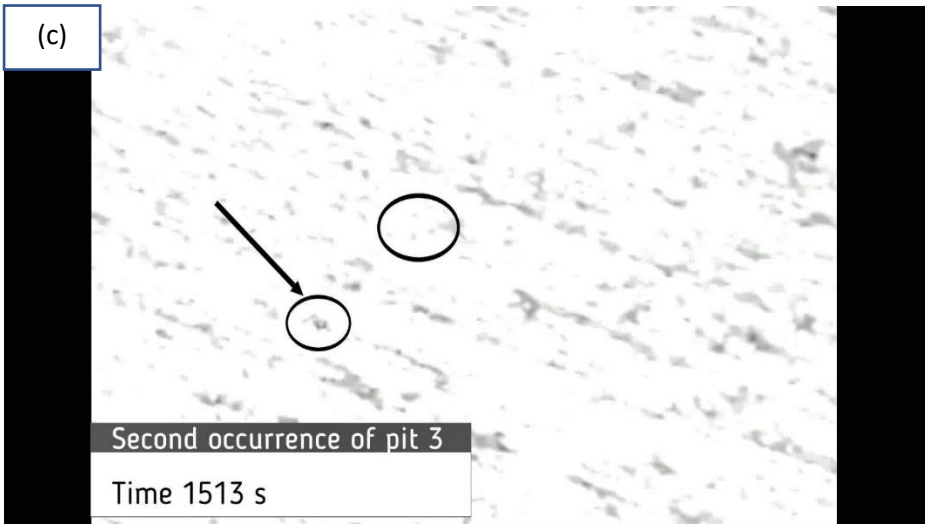
(c)
Second occurrence of pit 3
Time 1513 s

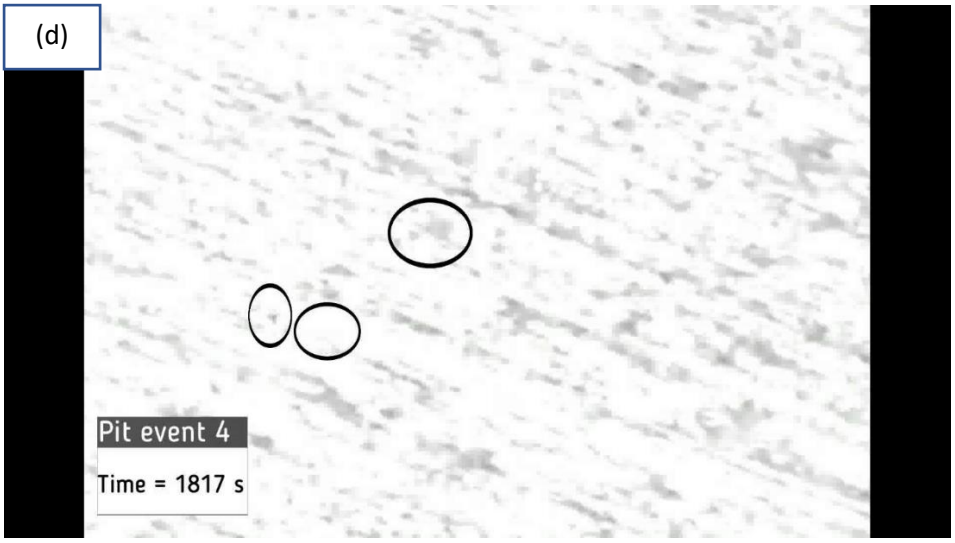
(d)
Pit event 4
Time = 1817 s


(e)
First occurrence of pit 5
Time 1856 s

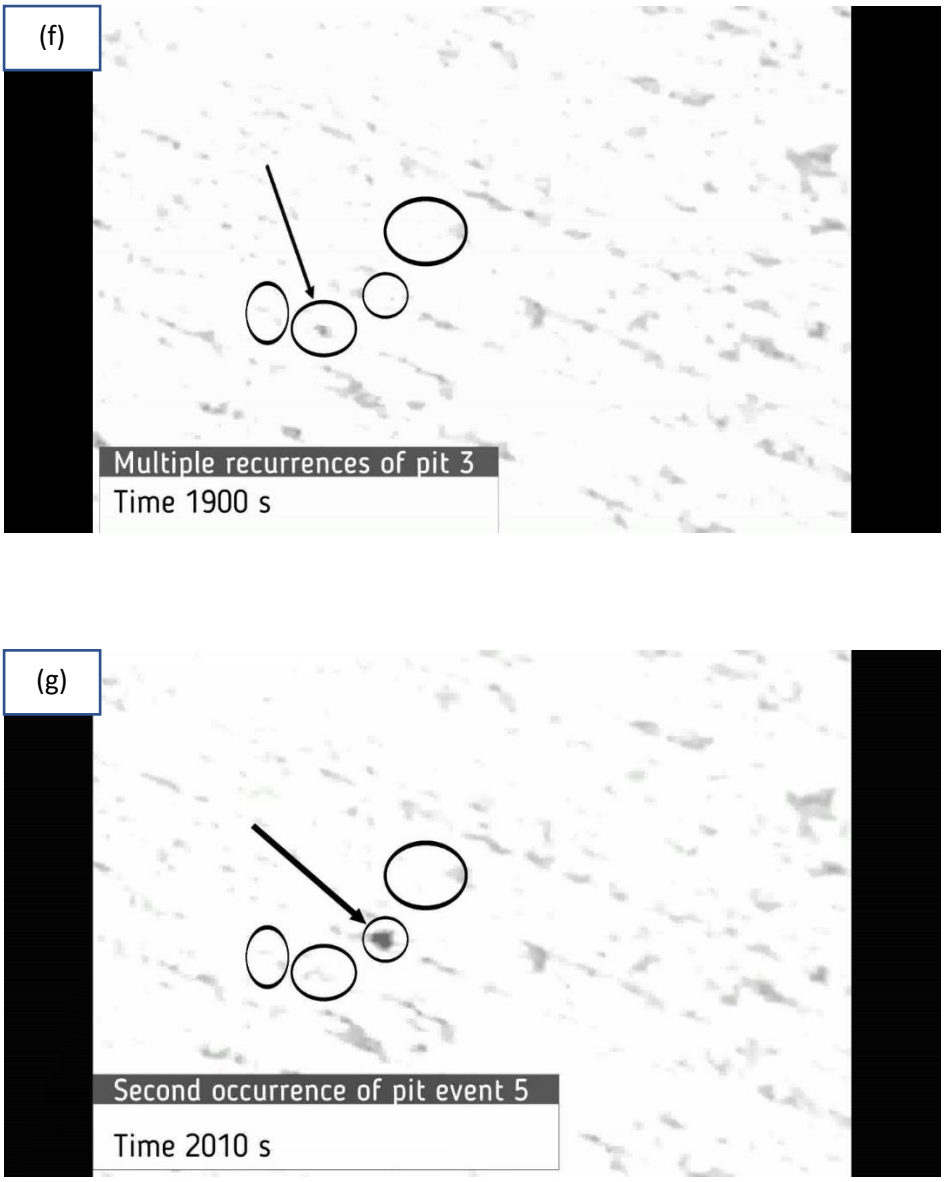

Figure 6.17. The timelapse images associated with the evolution of a cluster of pit events within a localised location during the potentiostatic testing of Al-5Mg at E_{pit} – 25 mV in 0.01 M NaCl.

The pit events, namely pit_1 and pit_2, co-occurred during the transient in Figure 6.18(a) while the events pit_3 and pit_5 reactivated multiple times from the same location. The shape of the current transients in Figure 6.18, being distinct, indicates that pit propagation kinetics in each case was different, though they were all influenced by the occurrence of pit events in their vicinity. Such localised clustering of pit events may be attributed to the lateral spreading of aggressive species from the prior pits that locally weaken the passive film [Punckt et al. 2004]. Seys et al. reported that the so-called "secondary pit initiation" occurred in the vicinity of a primary pit event when the dissolved hydrogen pinned the originally mobile dislocations and generated new pit initiation sites [Seys et al. 1974]. The localised clustering of pit locations

may also be attributed to the localised clustering of second phase particles in the microstructure [Hughes et al. 2006; Boag et al. 2010; Harlow 2011]. Localised clusters of IMPs in AA2024-T3 were observed to act as local cathode clusters resulting in localisation of pitting termed co-operative corrosion [Hughes et al. 2010]. Liao et al. 1998 observed that the sub-surface clustering of particles increased the severity of pitting.

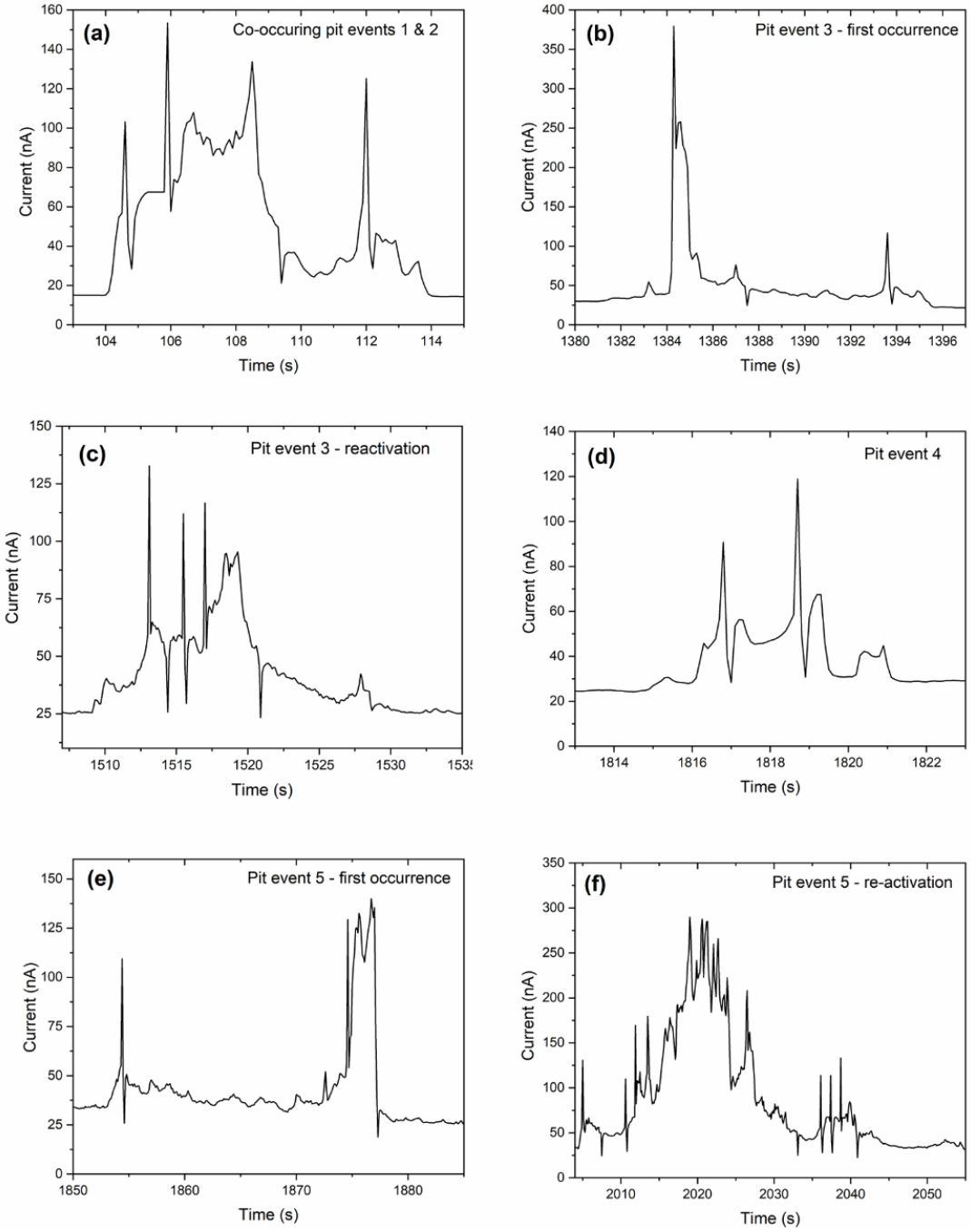

Figure 6.18. Multi-peaked propagation transients associated with the evolution of a cluster of pit events within a localised location shown in Figure 6.17 (a) co-occurrence of pit event 1 and 2 (b) pit event 3 (c) pit event 3 – reactivation (d) pit event 4 (e) pit event 5 (f) pit event 5 – reactivation.

Table 6.5. The metastable pitting parameters of the transients associated with the localised cluster of pit events presented in Figure 6.18.

Pit event	Charge consumed by the pit, C_{pit} = $C_{transient}$ + C_{HE} (nC)	Pit volume, $V_{pit,\beta}$ (μm^3)	Calculated hemispherical pit radius, $r_{pit,\beta}$ (μm)	Peak current, I_{peak} (nA)	Calculated pit radius at I_{peak}, $r_{pit,peak}$ (μm)	Pit stability value, $I_{peak}/r_{pit,peak}$ (mA/cm)	Pit growth rate, I_{peak}/t_g (nA/s)	Peak current density, i_{peak} (A/cm^2)
1	193.12*	8.88	1.62	62.58	0.94	0.67	31.29	1.13
2	246.42*	11.33	1.76	76.48	1.00	0.77	38.24	1.22
3	469.24**	21.57	2.18	356.71	1.18	3.02	82.96	4.08
4	153.41	7.05	1.50	94.24	1.19	0.63	20.94	1.06
5	561.4**	25.81	2.31	115.06	2.23	0.52	4.43	0.37

* The events pit$_1$ and pit$_2$ were simultaneously occurring.

**The events pit$_3$ and pit$_5$ were recursive events wherein the first transient associated with these events is shown in Table 6.6.

Table 6.6. The metastable pitting parameters associated with reactivating pit events pit$_3$ and pit$_5$ in Figure 6.18.

Pit event	C_{pit} of first activation (nC)	Calculated $r_{pit,\beta}$ from first activation (μm)	C_{pit} of the second activation (nC)	Total C_{pit} (nC)	Final calculated $r_{pit,\beta}$ (μm)	The percentage error in the pit size estimation (%)
3	469.24	2.18	480.73	949.87	2.75	21.45
5	561.4	2.31	2900.61	3462.01	4.24	46.23

From Table 6.5, it is evident that the first transient associated with the pit location that underwent multiple pit reactivations exhibited a $V_{pit,\beta}$ greater than 20 μm^3. This value concurs with the other estimated $V_{pit,\beta}$ values witnessed for recursive pit events in the present study. It should be noted that the other parameters, such as the pit growth rate (I_{peak}/t_g) or pit stability value ($I_{peak}/r_{pit,peak}$) were not successful in deciphering the recurring pit events, signifying the importance of V_{pit} in metastable pitting studies. For instance, though pit$_3$ exhibited a higher pit growth rate and pit stability value than pit$_5$ (Table 6.5), both the transients resulted in multiple recursive pit events as they transitioned to pit stability. This observation agrees with a critical pit dissolution volume being crucial in determining the pit stability [Trueman 2005]. From the transients studied herein, it is also evident that the pit stability value of the recursive pit events that eventually transitioned to stability could be in the order of ~ 10^{-4} A.cm$^{-1,}$ which is smaller than ~ 10^{-2} A.cm^{-1} proposed for the formation of stable pits [Pride et al. 1994]. This

inference indicates that the metastable pit propagation events with a pit stability value as low as a few mA.cm^{-1} could undergo multiple recurrences as they transition to stability.

6.3.3. Comparative study of the reliability of estimated metastable pit sizes in Al-5Mg and CP-Al

The inconsistencies witnessed in the metastable r_{pit} estimated from $C_{transient}$ were introduced by not accounting for the following factors: (a) charge lost to HE (C_{HE}), (b) the spatiotemporal evolution of pit events.

The fraction of total pit dissolution charge (C_{pit}) consumed by HE (C_{HE}), i.e., the ratio C_{HE}/C_{pit} maybe employed in investigating the error introduced by HE on the estimated metastable r_{pit}. The ratio C_{HE}/C_{pit} was observed to be dependent on the magnitude of $C_{transient}$ with its values ranging between 0.014 to 0.055 in Al-5Mg and 0.016 to 0.081 or CP-Al. The maximum error in the estimated metastable pit sizes (r_{pit}) introduced by HE, occurring within the pits, would not be greater than 1.51% in Al-5Mg and 2.47% in CP-Al.

The average rate of occurrence of the transients associated with recursive pit events for a set of 10 experiments performed under similar test conditions was 0.04 ± 0.01 cm^{-2}.s^{-1} in Al-5Mg and 0.35 ± 0.11 cm^{-2}.s^{-1} in CP-Al. The high scatter in this data is inevitable due to the stochastic nature of metastable pitting. Nevertheless, it can be observed that the average rate of occurrence of transients associated with recursive pit events was higher by an order of ~ 1 in CP-Al. This observation may be attributed to the presence of stable Al_3Fe constituent particles that enhance pitting in their vicinity. In contrast, anodic β phase-precipitates in Al-5Mg seem to dissolve away before the pits attained a critical pit depth to perpetuate pitting. This inference concurs with the severe underestimation of pit sizes in aluminium alloys [Guan et al. 2014]. In the present study, the maximum error introduced in the estimated hemispherical r_{pit} associated with the pit recurrences was 41.44 % in CP-Al during the occurrence of combined positive-negative current transients and 46.23% during the anodic current transients in Al-5Mg. The critical estimated hemispherical r_{pit} equivalent to the $C_{transient}$ of the primary pit events that resulted in multiple recurrences was 2.15 ± 0.16 µm (i.e., V_{pit} of 20.96 ± 0.01 µm^3) in Al-5Mg and 1.98 ± 0.05 µm (i.e., V_{pit} of 16.22 ± 0.003 µm^3) in CP-Al.

The average rate of transients associated with the co-occurring pit events in Al-5Mg and CP-Al was 0.01 ± 0.003 $cm^{-2}.s^{-1}$ and 0.94 ± 0.3 $cm^{-2}.s^{-1}$ respectively, indicating that this rate was higher by an order of ~ 2 for CP-Al. This observation supports the findings of Guan et al., who reported that the number of actual pits was higher than the MPR in an Al-Mg-Si alloy with cathodic second phase particles [Guan et al. 2014]. They attributed the inconsistency to the localised occurrence of both anodic and cathodic reactions to the extent that the $C_{transient}$ was almost nullified, making them indecipherable. However, the present study suggests that a significant reduction in MPR in CP-Al results from higher stochasticity of pit events that results in overlapping current transients. The highest error in the estimated pit sizes due to simultaneously occurring pit events reported in the present study was 19.14 %.

The above discussions signify that the percentage error in the estimated metastable r_{pit} introduced by the spatiotemporal evolution of pit events was higher than that introduced by HE occurring within the pits. Further, the discussions indicate that the error in the estimated pit sizes due to the spatiotemporal evolution of pit events was significantly higher in CP-Al than Al-5Mg. This inference maybe attributed to the presence of stable cathodic second phase particles that aggravate pitting in the case of CP-Al compared to Al-5Mg that has β phase-precipitates, which can dissolve away before attaining stability.

6.4. Discussion

The conventional notion of treating each current transient as a signal arising from a single discrete pit event could introduce error in the metastable r_{pit} estimated from $C_{transient}$ by assuming a hemispherical pit geometry. The results from the present study revealed that the larger pits that exceeded a critical V_{pit}, underwent multiple reactivations in the process of developing and sustaining the pit chemistry required for stability. The calculated r_{pit} for the larger pits would be underestimated by disregarding the transients associated with the subsequent pit reactivations. On the contrary, the smaller pit events may co-occur with multiple pit events, resulting in overlapped current transients. The existence of recurring and co-occurring pit events may explain why the pit size of larger pits was underestimated, while that of the smaller pits were overestimated in the investigation of metastable pitting in SS by Pistorius and Burstein [Pistorius et al. 1992]. With such spatiotemporal insights, the present study identifies the factors associated with the pit recurrences in relevance to improving the

reliability of the current transient data analysis to enable a better interpretation of the stable pitting susceptibility.

The factors that resulted in recursive pit events, as observed from the present study, were as follows: (a) propagation of pits to a critical pit volume, V_{pit} (b) presence of 'cathodic' sites and (c) incomplete repassivation of the pit events (quasi-stable pits). A critical V_{pit} was found to be associated with the primary pit events that resulted in the reactivation of the same pit location, as reported by Trueman [Trueman 2005]. This observation indicates that a critical concentration of dissolved metal ions is necessary to develop and maintain acidification for the pits to recur as they transition to stability. The second factor being the influence of cathodic second phase particles is witnessed from the multiple pit reactivations observed during the series of combined anodic-cathodic current transients. The V_{pit} of the primary pit event in the series of combined positive-negative transients that resulted in multiple pit reactivations was 0.59 μm^3. This value is much smaller than the critical V_{pit} (~ 16 μm^3) witnessed for the enunciation of pit reactivations during anodic current transients, demonstrating the strong influence of cathodic second phase particles [Curioni et al. 2015]. The third factor that promoted pit recurrences was the incomplete repassivation of pit events that resulted in quasi-stable transients. The most likely explanation for the pit reactivations following such transients could be the retention of aggressive species within the microscopic crystallographic tunnels [Kaesche 1990] within the pits that propagate at low rates [Newman 1995]. In fact, the duration after I_{peak} which is termed conventionally as the repassivation phase [Pride et al. 1994; Kim et al. 2007] may not necessarily represent true repassivation. During this duration, the propagation of pits could be related to the preferential dissolution at the crystallographic micro-tunnels within the pit that preferentially dissolve at low currents [Newman 1995].

The rate of overlapped transients was higher in CP-Al in concert with an increase in the number of pit events. This observation demonstrates how the reliability of the metastable pit sizes, determined using the conventional theory, depreciates depending on the extent of microstructural heterogeneity. Analysis of individual current transients from overlapped current transients could be challenging due to the absence of precise transition points to identify the evolution of co-occurring pit events. Guan et al. employed a wavelet analysis to investigate overlapping current transients by assuming that all the multi-peaked transients were overlapped [Guan et al. 2016b]. However, in the present study, it was found that not all multi-peaked

transients represent overlapping current transients, indicating that such assumptions could lead to ambiguity. Several other analytical methods have been proposed to analyse such transients whilst in the absence of spatiotemporal insights [Cheng et al. 2000; Bertocci et al. 1995; Wang et al. 2016a]. With the methodology adopted in the present study, the current understanding of the analysis of overlapped current transients can be improved in conjunction with the noise analytical techniques.

The results from the investigation herein demonstrate that a critical pit volume (V_{pit}) can be employed as a deterministic parameter in distinguishing and quantitatively evaluating the transients associated with recurring pit events that would eventually transition to stability. This fact is also evident from the quasi-stable nature of the transients that exceed a critical $C_{transient}$ and therefore a critical V_{pit}. The grading based on V_{pit} could also eliminate the ambiguities introduced from the assumption of a hemispherical pit geometry during the estimation of r_{pit} . However, the present study could not provide insights regarding the decoding of individual transients from overlapped current transients as they required further computational analysis. Therefore, the issue of underestimating and overestimating V_{pit} may exist when the transients are graded exclusively based on the $C_{transient}$ in the absence of spatiotemporal insights and requires further work. The critical V_{pit} could vary depending on the (electrochemical and metallurgical) nature of the second phase particles of the alloy systems under consideration.

The findings from the present study emphasise that a significant fraction of the error in the estimated metastable r_{pit} was introduced by disregarding the spatiotemporal evolution of pit events and an inappropriate consideration of pit geometry. In contrast, the contribution of hydrogen evolution within the pits to such error was observed to be minimal.

6.5. Conclusions:

The novel approach adopted to visualise the metastable pit events in situ during potentiostatic testing in the present study enabled an investigation of the role of the recurring and co-occurring pit events on the reliability of the metastable pitting data analysis. Following are the key conclusions:

- The inconsistencies introduced in the metastable pit sizes estimated from the (dissolution) charge was dependent on the nature of the second phase particles and increased with the rate of pit recurrences and co-occurrences. However, the influence of hydrogen evolution within the pits on this inconsistency was comparatively minimal.
- Current transients were observed to arise from pit geometries other than hemispherical pit geometries, such as the propagation of pits along abrasion lines or irregular geometries (such as filiform-like patterns). The pit sizes estimated from such transients by assuming hemispherical pit geometries resulted in an overestimated pit depth.
- A critical pit volume (V_{pit}) equivalent to a critical pit dissolution charge was found to be associated with the transients that resulted in multiple pit recurrences. Accordingly, it was found that the pits/transients which propagated to a critical V_{pit} as low as 20.96 μm^3 in aged Al – 5 wt.% Mg binary alloy and 16.22 μm^3 in commercially pure aluminium could recur multiple times and eventually transition to stability.
- Both the single-peaked and multi-peaked current transients were associated with overlapped current transients with no precise transition points that marked the beginning of individual pit events.
- A significant proportion of the breakdown and pit nucleation events did not transition to pit propagating events despite several instances of metastable pit reactivation from the same location. This fact reinforces that the investigation of the propagation pit events is more critical in understanding the stable pitting susceptibility of alloy systems.

Chapter 7

Conclusion

7.1. Summary

Metastable pitting studies, in their remarkable capacity, provide significant insights that are not limited to quantitatively determining the stable pitting susceptibility of alloy systems but also in understanding the mechanistic and kinetic aspects of pitting, a feature that other contending techniques fail to offer. Therefore, the topic of this thesis is important in light of deploying metastable pitting studies as a potential tool to investigate the pitting characteristics of aluminium alloys in relevance to predicting their pit-to-crack transition behaviour and engineering life.

The dissertation has provided critical insights on the reliability of estimating metastable pit sizes (r_{pit}) and pit volume (V_{pit}) from the metastable pitting data. A detailed investigation of the various factors, namely, hydrogen evolution within the pits, the spatiotemporal evolution of pit events, pit geometry and the (electrochemical and metallurgical) nature of the second phase particles, on the reliability of the metastable r_{pit} and V_{pit} determined from $C_{transient}$ has been presented.

The outcome of this work is given below:

- A novel approach was devised for visualising and mapping the dynamic metastable pit locations in situ based on the hydrogen evolution occurring at the pit sites. The method allowed a direct correlation of the current transients to their associated metastable pit events/locations in situ. When coupled with post-mortem SEM and 3D profilometry

investigations, this technique provided a comprehensive understanding of the metastable pitting characteristics. The in situ imaging technique, however, could not aid in the detailed investigation of the pit nucleation events and an instantaneous correlation of i_{H_2} with i_{anodic}. These limitations, nevertheless, did not compromise the findings of the present work towards addressing the objective of the dissertation.

- The fraction of the pit dissolution charge (C_{pit}) consumed by hydrogen evolution (C_{HE}) within the pits was investigated to understand the error it introduces in the r_{pit} and V_{pit} estimated from current transients. From the C_{HE} estimated from the bubble diameter (d_{bubble}) (after accounting for the volume of dissolved hydrogen), the C_{HE}/C_{pit} during metastable pitting regime was determined to range between 0.019 and 0.052 depending on the $C_{transient}$. By incorporating this ratio, the error in the estimated r_{pit} was observed to be less than 2%, indicating that the hydrogen evolution does not introduce significant error in the metastable r_{pit} estimated from the current transients. The reason behind the lower C_{HE}/C_{pit} during metastable pit growth compared to the stable pit growth may be attributed to the reduced catalytic activity of the pit surface for hydrogen evolution during metastable pitting.

- The role of the spatiotemporal evolution of pit events on the metastable r_{pit} estimated from $C_{transient}$ was investigated. This study questioned the conventional notion of treating each current transient as a signal arising from a single discrete pit event. Irrespective of the shape and number of peaks of the current transient, single current transients were observed to be associated with multiple co-occurring pit events or reactivating pit events. The findings signify that the number of peaks does not represent the number of actual pit events. Accordingly, the estimated r_{pit} was found to be either overestimated or underestimated, respectively.

- A critical charge was observed to be associated with the pit events that underwent multiple reactivations as they transitioned to pit stability. It was found that neither the pit stability criterion nor the pit growth rate could effectively predict the pit stability, as much as the critical $C_{transient}$ and V_{pit}, from the current transient data. The spatiotemporal evolution of the minuscule pit nucleation and breakdown events was observed to have little relevance as they did not transition to stability even after multiple pit nucleation. This aspect re-

instates that the pit propagation events are more vital in understanding the stable pitting susceptibility of alloy systems.

- The factors that induced multiple pit reactivations at the same pit location were identified as follows: (a) the current transient of the pit event exceeded a critical $C_{transient}$ i.e., V_{pit}, (b) presence of cathodic second phase particles and (c) incomplete repassivation of the pit events as identified from the quasi-stable nature of the current transients (i.e., $I_{passive,end} > I_{passive,begin}$).

- Some current transients were found to be associated with irregular pit geometries such as filiform-like propagation rather than the conventional hemispherical pit geometry. Owing to the comparatively smaller depth of these pits, the hemispherical r_{pit} calculated from $C_{transient}$ and the other relevant parameters such as pit current density, pit stability value were ambiguous. Hence, V_{pit} was proposed as a reliable parameter over r_{pit} in predicting the pit stability, as the estimation of V_{pit} does not require a shape factor.

- Localised pit clusters were found to evolve during metastable pitting in aluminium. It was observed that though not all the current transients associated with the pits in the cluster exceeded the critical charge, the localised clustering of pitting resulted in the eventual transition of the location to a stable corrosion site.

- The error in the estimated metastable r_{pit} imparted by the electrochemical nature of the second phase particles was investigated using an aged Al-Mg binary alloy and commercially pure aluminium. It was observed that the rate of recurring and co-occurring pit events was significantly higher in the commercially pure aluminium owing to the presence of cathodic Al_3Fe constituent particles and relatively higher heterogeneity in the microstructure.

- The findings from the dissertation emphasise that the error introduced by the spatiotemporal evolution of pit events to the r_{pit} and V_{pit} estimated from $C_{transient}$ was significant as compared to that introduced by the hydrogen evolution occurring within the pits.

7.2. Scope for future work

The combined potentiostatic polarisation – in situ imaging technique provided considerable insights regarding the reliability of the metastable r_{pit} deduced from the current transients. While this dissertation could provide insights regarding the contribution of various factors to the error introduced in the r_{pit} estimation from $C_{transient}$, it does not provide the mitigation strategies to improve the overall reliability of the metastable pitting data analysis. A significant part of such work would involve the application of electrochemical noise analytical techniques and advanced computational/statistical methods. The following would be the scope for future work:

(a) Develop a computational/statistical method to deconvolute the overlapped current transients associated with multiple recurring pit events based on the insights derived from potentiostatic polarisation – in situ imaging techniques.

(b) As a part of this study, it was proposed that a critical charge was associated with recurring pit events. However, a method to identify the subsequent current transients associated with recurring pit events was not proposed and could form the scope for future work.

(c) The rate of pit co-occurrences and recurrences scale with potential and compromise the reliability of the metastable pitting data. Hence, the possibility of investigating the metastable pitting characteristics at potentials closer to the repassivation potential needs to be explored as a way to improve the reliability of metastable pitting data analysis.

(d) Investigation of C_{HE}/C_{pit} in commercially pure aluminium since the pitting characteristics would be different due to the presence of Al_3Fe IMPs.

(e) Understand the evolution of metastable pit morphology using simulated in situ X-ray tomography studies on 1D/2D electrodes."

References

Alkire, R. C., and Wong, K. P. 1988. 'The corrosion of single pits on stainless steel in acidic chloride solution', *Corrosion Science*, 28: 411-21.

Alwitt, R. S. 1974. 'The growth of hydrous oxide films on aluminum', *Journal of The Electrochemical Society*, 121: 1322.

Alwitt, R. S., Beck, T. R, and Herbert, K. R. 1990. Isaacs, H. S., Bertocci, U., Kruger, J. and Smialowska, S. (eds.), *Advances in Localised corrosion* (NACE International).

Balasubramaniam, R. 2000. 'On the corrosion resistance of the Delhi iron pillar', *Corrosion Science*, 42: 2103-29.

Balkwill, P. H., Westcott, C., and Williams, D. E. 1991. 'Stochastic approach to the initiation of pitting corrosion', *Materials Science Forum*, 44-45: 299-312.

Bargeron, C. B., and Benson, R. C. 1980a. 'Analysis of the gases evolved during the pitting corrosion of aluminum in various electrolytes', *Journal of The Electrochemical Society*, 127: 2528-30.

Bargeron, C. B., and Givens, R. B. 1977. 'Localized corrosion of aluminum: blister formation as a precursor of pitting', *Journal of The Electrochemical Society*, 124: 1845-48.

Bargeron, C. B., and Givens, R.B. 1980b. 'Precursive blistering in the localized corrosion of aluminum', *CORROSION*, 36: 618-25.

Baumgärtner, M., and Kaesche, H. 1988. 'The nature of crevice corrosion of aluminum in chloride solutions', *Materials and Corrosion*, 39: 129-35.

Beck, T. R. 1990. Isaacs, H. S., Bertocci, U., Kruger, J. and Smialowska, S. (eds.), *Advances in Localised Corrosion* (NACE International: Houston).

Beck, T. R. 1984. 'Salt film formation during corrosion of aluminum', *Electrochimica Acta*, 29: 485-91.

Beck, T. R., and Alkire, R. C. 1979. 'Occurrence of salt films during initiation and growth of corrosion pits', *Journal of The Electrochemical Society*, 126: 1662.

Bertocci, U., and Huet, F. 1995. 'Noise analysis applied to electrochemical systems', *CORROSION*, 51: 131-44.

Bianchi, G., Cerqumi, A., Mazza, F., and Torchio, S. 1970. 'Chemical etching and pitting of stainless steel', *Corrosion Science*, 10: 19-27.

Birbilis, N., and Buchheit, R. G. 2005. 'Electrochemical characteristics of intermetallic phases in aluminum alloys: an experimental survey and discussion', *Journal of The Electrochemical Society*, 152: B140-B51.

Birbilis, N., and Buchheit. R. G. 2008. 'Investigation and discussion of characteristics for intermetallic phases common to aluminum alloys as a function of solution pH'. Journal of The Electrochemical Society, 155, 3, C117-C126.

Birbilis, N., Meyer, K., Muddle, B. C., and Lynch, S. P. 2009. 'In situ measurement of corrosion on the nanoscale', *Corrosion Science*, 51: 1569-72.

Boag, A., Taylor, R. J., Muster, T. H., Goodman, N., McCulloch, D., Ryan, C., Rout, B., Jamieson, D., and Hughes, A. E. 2010. 'Stable pit formation on AA2024-T3 in a NaCl environment', *Corrosion Science*, 52: 90-103.

Bobby Kannan, M., Bala, S. P., and Raja, V. S. 2011. '8 - Stress corrosion cracking (SCC) of aluminium alloys.' in Raja, V. S. and Shoji, Tetsuo (eds.), *Stress Corrosion Cracking* (Woodhead Publishing).

Boer, J. H. de, and Linsen, B. G. 1970. 'Physical and chemical aspects of adsorbents and catalysts : dedicated to J. H. de Boer on the occasion of his retirement from the Technological University, Delft, The Netherlands'.

Bohni, H. 1987. 'Breakdown of passivity and localized corrosion processes', *Langmuir*, 3: 924-30.

Böhni, H., Suter, T., and Schreyer, A. 1995. 'Micro- and nanotechniques to study localized corrosion', *Electrochimica Acta*, 40: 1361-68.

Bonzom, R., and Oltra, R. 2016. 'Intergranular corrosion propagation rate of 2024 alloy investigated via the "one-dimensional artificial pit" technique', *Corrosion Science*, 111: 850-55.

Brennert, J. 1936. *Journal of the Iron and Steel Institute*: 101 - 11.

Brigham, R. J, and Tozer, E. W. 1973. 'Temperature as a pitting criterion', *CORROSION*, 29: 33-36.

Büchler, M., Watari, T., and Smyrl, W. H. 2000. 'Investigation of the initiation of localized corrosion on aluminum alloys by using fluorescence microscopy', *Corrosion Science*, 42: 1661-68.

Buchheit, R. G. 1995. 'A compilation of corrosion potentials reported for intermetallic phases in aluminum alloys', *Journal of The Electrochemical Society*, 142, 11: 3994-3996.

Burstein, G. T. 1994. '1.5 - Passivity and localised corrosion.' in Shreir, L. L., Jarman, R. A. and Burstein, G. T. (eds.), *Corrosion (Third Edition)* (Butterworth-Heinemann: Oxford).

Burstein, G. T., Liu, C., Moloney, J. J., and Vines, S. P. 2009. 'The remarkable passivity of metals and the origins of its breakdown', *Corrosion and Materials*, 34: 26-35.

Burstein, G. T., and Mattin, S. P. 1992. 'Nucleation of corrosion pits on stainless steel', *Philosophical Magazine Letters*, 66: 127-31.

Burstein, G. T., and Mattin, S. P. 1996a. 'The nucleation and early stages of growth of corrosion pits.' in Natishan, P. M., Kelly, R. G., Frankel, G. S. and Newman, R. C. (eds.), *Critical Factors in Localised Corrosion II* (The Electrochemical Society: Pennington).

Burstein, G. T., and Moloney, J. J. 2004. 'Cyclic thermammetry', *Electrochemistry Communications*, 6: 1037-41.

Burstein, G. T., and Pistorius, P. C. 1995a. 'Surface roughness and the metastable pitting of stainless steel in chloride solutions', *CORROSION*, 51: 380-85.

Burstein, G. T., Salter, V. C., Ball, J., and Sharman, J. D. B. 1996b. 'The growth of pits during the electrograining of aluminium.' in Datta, M., MacDougall and Fenton, J. M. (eds.), *High Rate Metal Dissolution Processes* (The Electrochemical Society: Pennington).

Burstein, G. T., and Souto, R. M. 1995b. 'Observations of localised instability of passive titanium in chloride solution', *Electrochimica Acta*, 40: 1881-88.

Burstein, G. T., and Vines, S. P. 2001. 'Repetitive nucleation of corrosion pits on stainless steel and the effects of surface roughness', *Journal of The Electrochemical Society*, 148: B504-B16.

Buzza, D. W., and Alkire, R. C. 1995. 'Growth of corrosion pits on pure aluminum in 1M NaCl', *Journal of The Electrochemical Society*, 142: 1104-11.

Casillas, N., Charlebois, S. J., Smyrl, W. H., and White, H. S. 1993. 'Scanning electrochemical microscopy of precursor sites for pitting corrosion on titanium', *Journal of The Electrochemical Society*, 140: L142-L45.

Cavanaugh, M. K. 2009. 'Modeling the environmental dependence of localized corrosion evolution in AA7075-T651', The Ohio State University.

Cavanaugh, M. K., Birbilis, N., and Buchheit, R. 2009. 'A quantitative study on the effects of environment and microstructure on pit initiation in Al-alloys', *ECS Transactions*, 16: 1-11.

Cheng, Y. F., Luo, J. L., and Wilmott, M. 2000. 'Spectral analysis of electrochemical noise with different transient shapes', *Electrochimica Acta*, 45: 1763-71.

Chiba, A., Muto, I., Sugawara, Y., and Hara, N. 2012. 'A microelectrochemical system for in situ high-resolution optical microscopy: morphological characteristics of pitting at MnS inclusion in stainless steel', *Journal of The Electrochemical Society*, 159: C341-C50.

Cole, G. S., and Sherman, A. M. 1995. 'Light weight materials for automotive applications', *Materials Characterization*, 35: 3-9.

Comotti, I. M., Trueba, M., and Trasatti, S. P. 2013. 'The pit transition potential in the repassivation of aluminium alloys', *Surface and Interface Analysis*, 45: 1575-84.

Connolly, B. J., Horner, D. A., Fox, S. J., Davenport, A. J., Padovani, C., Zhou, S., Turnbull, A., Preuss, M., Stevens, N. P., Marrow, T. J., Buffiere, J. Y., Boller, E., Groso, A., and Stampanoni, M. 2006. 'X-ray microtomography studies of localised corrosion and transitions to stress corrosion cracking', *Materials Science and Technology*, 22: 1076-85.

Cook, A. B., Engelberg, D. L., Stevens, N. P., Laycock, N. J., White, S., Ghahari, M., Monir, M., Holroyd, H. J., and Newman, R. C. 2012. 'Pit propagation in pure aluminum investigated via the 1D artificial pit technique: growth regimes, surface morphology and implications for stability criteria', *ECS Transactions*, 41: 121-32.

Cook, A. B., and Newman, R. C. 2002. 'Critical conditions for stability of pits in aluminium: a contribution to the mechanism of tunneling corrosion.' in Virtanen, S., Schmuki, P. and Frankel, G. S. (eds.), *Critical Factors in Localized Corrosion IV - A Symposium in Honour of the 65th Birthday of Hans Boehni* (Pennington: NJ).

Curioni, M., and Scenini, F. 2015. 'The mechanism of hydrogen evolution during anodic polarization of aluminium', *Electrochimica Acta*, 180: 712 - 21.

Czaban, M. 2018. 'Aircraft corrosion – review of corrosion processes and its effects in selected cases', *Fatigue of Aircraft Structures*, 2018: 5.

Davis, G. D., Moshier, W. C., Fritz, T. L., Cote, G. 1990, 'Evolution of the chemistry of passive films of sputter-deposited, supersaturated Al alloys', *Journal of The Electrochemical Society*, 137, 422-427

de Wit, J. H. W., and Lenderink, H. J. W. 1996. 'Electrochemical impedance spectroscopy as a tool to obtain mechanistic information on the passive behaviour of aluminium', *Electrochimica Acta*, 41: 1111-19.

Di Quarto, F., and Santamaria, M. 2004. 'Semiconductor electrochemistry approach to passivity and passivity breakdown of metals and metallic alloys', *Corrosion Engineering, Science and Technology*, 39: 71-81.

Ding, H., Hawthorn, G. A., and Hihara, L. H. 2009. 'Inhibitive effect of seawater on the corrosion of particulate-reinforced aluminum-matrix composites and monolithic aluminum alloy', *Journal of The Electrochemical Society*, 156: C352.

Dražić, D. M., and Popić, J. P. 1999. 'Corrosion rates and negative difference effects for Al and some Al alloys', *Journal of Applied Electrochemistry*, 29: 43-50.

Ebrahimi, N., Momeni, M., Kosari, A., Zakeri, M., and Moayed, M. H. 2012. 'A comparative study of critical pitting temperature (CPT) of stainless steels by electrochemical impedance spectroscopy (EIS), potentiodynamic and potentiostatic techniques', *Corrosion Science*, 59: 96-102.

Edeleanu, C. 1960. 'The propagation of corrosion pits in metals', *Journal of Institute of Metals*, 89: 90-94.

Epstein, P. S., and Plesset, M. S. 1950. 'On the stability of gas bubbles in liquid-gas solutions', *The Journal of Chemical Physics*, 18: 1505-09.

Evans, U. R. 1927. 'CXL.—The passivity of metals. Part I. The isolation of the protective film', *Journal of the Chemical Society*: 1020-40.

Evans, U. R. 1960. Arnold, Edwards (ed.), *The corrosion and oxidation of metals: scientific principles and practical applications* (London).

Foroulis, Z. A., and Thubrikar, M. J. 1975. 'On the kinetics of the breakdown of passivity of preanodized aluminum by chloride ions', *Journal of The Electrochemical Society*, 122: 1296-301.

Frankel, G. S. 1990. 'The growth of 2-D pits in thin film aluminum', *Corrosion Science*, 30: 1203 - 18.

Frankel, G. S. 1998. 'Pitting corrosion of metals: a review of the critical factors', *Journal of The Electrochemical Society*, 145: 2186-98.

Frankel, G. S., Fajardo, S., and Lynch, B. M. 2015. 'Introductory lecture on corrosion chemistry: a focus on anodic hydrogen evolution on Al and Mg', *Faraday Discussions*, 180: 11-33.

Frankel, G. S., Newman, R. C., Jahnes, C. V., and Russak, M. A. 1993. 'On the pitting resistance of sputter-deposited aluminum alloys', *Journal of The Electrochemical Society*, 140: 2192-97.

Frankel, G. S., Samaniego, A., and Birbilis, N. 2013. 'Evolution of hydrogen at dissolving magnesium surfaces', *Corrosion Science*, 70: 104-11.

Frankel, G. S., Scully, J. R., and Jahnes, C. V. 1996. 'Repassivation of pits in aluminum thin films', *Journal of The Electrochemical Society*, 143: 1834-40.

Frankel, G. S., Stockert, L., Hunkeler, F., and Boehni, H. 1987. 'Metastable pitting of stainless steel', *CORROSION*, 43: 429-36.

Frankenthal, R. P., and Pickering, H. W. 1972. 'On the mechanism of localized corrosion of iron and stainless steel', *Journal of The Electrochemical Society*, 119: 1304.

Galvele, J. R. 1976. 'Transport processes and the mechanism of pitting of metals', *Journal of The Electrochemical Society*, 123: 464-74.

Galvele, J.R. 1981. 'Transport processes in passivity breakdown—II. Full hydrolysis of the metal ions', *Corrosion Science*, 21: 551 - 79.

Ghahari, S. M., Davenport, A. J., Rayment, T., Suter, T., Tinnes, J. P., Padovani, C., Hammons, J. A., Stampanoni, M., Marone, F., and Mokso, R. 2011. 'In situ synchrotron X-ray micro-tomography study of pitting corrosion in stainless steel', *Corrosion Science*, 53: 2684-87.

Gharbi, O., Birbilis, N., and Ogle, K. 2016. 'In-situ monitoring of alloy dissolution and residual film formation during the pretreatment of Al-alloy AA2024-T3', *Journal of The Electrochemical Society*, 163: C240-C51.

Gharbi, O., Jiang, D., Feenstra, D. R., Kairy, S. K., Wu, Y., Hutchinson, C. R., and Birbilis, N. 2018. 'On the corrosion of additively manufactured aluminium alloy AA2024 prepared by selective laser melting', *Corrosion Science*, 143: 93-106.

Glas, J. P., and Westwater, J. W. 1964. 'Measurements of the growth of electrolytic bubbles', *International Journal of Heat and Mass Transfer*, 7: 1427 - 43.

Goad, D. 1996. 'A new hypothesis for D.C. tunnel etching of aluminum.' in Natishan, P. M., Kelly, R. G., Frankel, G. S. and Newman, R. C. (eds.), *Critical Factors in Localised Corrosion II* (The Electrochemical Society: Pennington).

Guan, L., Cai, J., and Li, Y. 2020. 'Characteristics of the random transients caused by clustered pitting corrosion for Al–Mg microelectrode', *Materials and Corrosion*, 71: 86-92.

Guan, L., Zhang, B., Wang, J. Q., Han, E.-H., and Ke, W. 2014. 'The reliability of electrochemical noise and current transients characterizing metastable pitting of Al–Mg–Si microelectrodes', *Corrosion Science*, 80: 1 - 6.

Guan, L., Zhou, S., Lin, H.Q., Zhang, B., Wang, J. Q., Han, E.-H., and Ke, W. 2015. 'Detection and analysis of anodic current transients associated with nanoscale β-phase precipitates on an Al–Mg microelectrode', *Corrosion Science*, 95: 6 - 10.

Guan, L., Zhou, Y., Zhang, B., Wang, J. Q., Han, E.-H., and Ke, W. 2016a. 'The electrochemical and morphological characteristics of single metastable pit for 304 stainless steel under potentiostatic polarization', *International Journal of Electrochemical Science*: 2326-34.

Guan, L., Zhou, Y., Zhang, B., Wang, J. Q., Han, E.-H., and Ke, W. 2016b. 'Influence of aging treatment on the pitting behavior associated with the dissolution of active nanoscale β-phase precipitates for an Al–Mg alloy', *Corrosion Science*, 103: 255 - 67.

Gupta, R. K., Hinton, B. R. W., and Birbilis, N. 2014. 'The effect of chromate on the pitting susceptibility of AA7075-T651 studied using potentiostatic transients', *Corrosion Science*, 82: 197 - 207.

Gupta, R. K., Sukiman, N. L., Cavanaugh, M. K., Hinton, B. R. W., Hutchinson, C. R., and Birbilis, N. 2012. 'Metastable pitting characteristics of aluminium alloys measured using current transients during potentiostatic polarisation', *Electrochimica Acta*, 66: 245 - 54.

Harlow, D. G. 2012. 'Constituent particle clustering and pitting corrosion', *Metallurgical and Materials Transactions A: Physical Metallurgy and Materials Science*, 43, 8, 2832-2838.

Hart, R. K. 1957. 'The formation of films on aluminium immersed in water', *Transactions of the Faraday Society*, 53: 1020-27.

Hashimoto, T., Zhang, X., Zhou, X., Skeldon, P., Haigh, S.J. and Thompson, G.E. 2016, 'Investigation of dealloying of S phase (Al2CuMg) in AA2024-T3 aluminium alloy using high resolution 2D and 3D electron imaging, *Corrosion Science*, 103, 157-164.

Hebert, K., and Alkire, R. 1988. 'Growth rates of aluminum etch tunnels', *Journal of The Electrochemical Society*, 135: 2447-52.

Hisamatsu, Y., T., Yoshii, and Y., Matsumura. 1974. 'Electrochemical and microscopical study of pitting corrosion of austenitic stainless steel.' in Staehle, R. W., Brown, B. F., Kruger, J. and Agarwal, A. (eds.), *Localized Corrosion* (National Association of Corrosion Engineers: Houston, Texas 77084).

Hoar, T. P. 1937. 'The corrosion of tin in nearly neutral solutions', *Transactions of the Faraday Society*, 33: 1152-67.

Hoar, T. P., and Jacob, W. R. 1967. 'Breakdown of passivity of stainless steel by halide ions', *Nature*, 216: 1299-301.

Hoar, T. P., Mears, D. C., and Rothwell, G. P. 1965. 'The relationships between anodic passivity, brightening and pitting', *Corrosion Science*, 5: 279-89.

Houghton, G., Ritchie, P. D., and Thomson, J. A. 1962. 'The rate of solution of small stationary bubbles and the diffusion coefficients of gases in liquids', *Chemical Engineering Science*, 17: 221-27.

Huang, R., Hebert, K. R., and Chumbley, L. S. 2004a. 'Microscopic observations of voids in anodic oxide films on aluminum', *Journal of The Electrochemical Society*, 151: B379-B86.

Huang, R., Hebert, K. R., Gessmann, T., and Lynn, K. G. 2004b. 'Effect of impurities on interfacial void formation in aluminum', *Journal of The Electrochemical Society*, 151: B227-B32.

Hughes, A., Muster, T. H., Boag, A., Glenn, A. M., Luo, C., Zhou, X., Thompson, G. E., and McCulloch, D. 2010, *Corrosion Science*, 52, 665-668.

Hunkeler, F., and Bohni, H. 1981. 'Determination of pit growth rates on aluminum using a metal foil technique', *CORROSION*, 37: 645-50.

Hunkeler, F., and Bohni, H. 1984. 'Mechanism of pit growth on aluminum under open circuit conditions', *CORROSION*, 40: 534-40.

Hunkeler, F., Krolikowski, A., and Böhni, H. 1987. 'A study of the solid salt film on nickel and stainless steel', *Electrochimica Acta*, 32: 615-20.

Ilevbare, G. O., Schneider, O., Kelly, R. G., and Scully, J. R. 2004. 'In situ confocal laser scanning microscopy of AA 2024-T3 corrosion metrology: I. localized corrosion of particles', *Journal of The Electrochemical Society*, 151: B453-B64.

Inturi, R. B., and Szklarska-Smialowska, Z. 1993. 'Dependence of the pitting potential of Al alloys on solubility of alloying element oxides', *Corrosion Science*, 34: 705-10.

Isaacs, H. S. 1973. 'The behavior of resistive layers in the localized corrosion of stainless steel', *Journal of The Electrochemical Society*, 120: 1456.

Isaacs, H. S. 1989. 'The localized breakdown and repair of passive surfaces during pitting', *Corrosion Science*, 29: 313-23.

Isaacs, H. S., Adzic, G., and Jeffcoate, C. S. 2000. '2000 W.R. Whitney Award Lecture: Visualizing corrosion', *CORROSION*, 56: 8.

Isaacs, H. S., and Kissel, G. 1972. 'Surface preparation and pit propagation in stainless steels', *Journal of The Electrochemical Society*, 119: 1628.

Kaesche, H. 1962. 'Untersuchungen über die gleichmä§ige Auflösung und den Lochfra§ von Aluminiumelektroden*', *Zeitschrift für Physikalische Chemie*, 34: 87-108.

Kaesche, H. 1990. Isaacs, H. S., Bertocci, U., Kruger, J. and Smialowska, S. (eds.), *Advances in Localised Corrosion* (NACE International: Houston).

Kairy, S. K., Rometsch, P. A., Diao, K., Nie, J. F., Davies, C. H. J. and Birbilis, N. 2016. 'Exploring the electrochemistry of 6xxx series aluminium alloys as a function of Si to Mg ratio, Cu content, ageing conditions and microstructure', *Electrochimica Acta*, 190, 92-103.

Kim, Y., and Buchheit, R. G. 2007. 'A characterization of the inhibiting effect of Cu on metastable pitting in dilute Al–Cu solid solution alloys', *Electrochimica Acta*, 52: 2437-46.

Koch, G. H., Brongers, M. P. H., Thompson, N. G., Virmani, Y. Paul, and Payer, J. H. 2002. 'Corrosion cost and preventive strategies in the United States [Final report]'.

Kolotyrkin, Y. M. 1963. 'Pitting corrosion of metals', *CORROSION*, 19: 261 - 68.

Kondo, Y. 1989. 'Prediction of fatigue crack initiation life based on pit growth', *CORROSION*, 45: 7-11.

Krieger, I. M., Mulholland, G. W., and Dickey, C. S. 1967. 'Diffusion coefficients for gases in liquids from the rates of solution of small gas bubbles', *The Journal of Physical Chemistry*, 71: 1123-29.

Kruger, J., and Ambrose, J. R. 1976. 'Qualitative use of ellipsometry to study localized corrosion processes', *Surface Science*, 56: 394-412.

Laycock, N. J., Moayed, M. H., and Newman, R. C. 1998a. 'Metastable pitting and the critical pitting temperature', *Journal of The Electrochemical Society*, 145: 2622-28.

Laycock, N. J., and Newman, R. C. 1997. 'Localised dissolution kinetics, salt films and pitting potentials', *Corrosion Science*, 39: 1771-90.

Laycock, N. J., and Newman, R. C. 1998b. 'Temperature dependence of pitting potentials for austenitic stainless steels above their critical pitting temperature', *Corrosion Science*, 40: 887-902.

Laycock, N. J., and Newman, R. C. 2001a. 'Localised corrosion of austenitic stainless steels.' in Frankel, G. S. and Scully, J. C. (eds.), *NACE International* (Houston).

Laycock, N. J., and White, S. P. 2001b. 'Computer simulation of single pit propagation in stainless steel under potentiostatic control', *Journal of The Electrochemical Society*, 148: B264.

Lebouil, S., Duboin, A., Monti, F., Tabeling, P., Volovitch, P., and Ogle, K. 2014. 'A novel approach to on-line measurement of gas evolution kinetics: Application to the negative difference effect of Mg in chloride solution', *Electrochimica Acta*, 124: 176-82.

Li, T., Scully, J. R., and Frankel, G. S. 2018. 'Localized corrosion: passive film breakdown vs pit growth stability: Part II. A model for critical pitting temperature', *Journal of The Electrochemical Society*, 165: C484-C91.

Li, Y., Cai, J. M., Guan, L., and Wang, G. 2019. 'pH-dependent electrochemical behaviour of Al_3Mg_2 in NaCl solution', *Applied Surface Science*, 467-468: 619 - 33.

Liao, C. M., Olive, J. M., Gao, M., and Wei, R. P. 1998. 'In-situ monitoring of pitting corrosion in aluminum alloy 2024', *CORROSION* 54, 6, 451-458.

Lim, M. C., Kelly, R. G., and Scully, J. R. 2016. 'Overview of intergranular corrosion mechanisms, phenomenological observations, and modeling of AA5083', *CORROSION*, 72: 198-220.

Lin, C.-J., Du, R.-G., and Nguyen, T. 2000. 'In-situ imaging of chloride ions at the metal/solution interface by scanning combination microelectrodes', *CORROSION*, 56: 41-47.

Liu, M., Schmutz, P, Zanna, S., Seyeux, A., Ardelean, H., Song, G., Atrens, A., and Marcus, P. 2010. 'Electrochemical reactivity, surface composition and corrosion mechanisms of the complex metallic alloy Al_3Mg_2', *Corrosion Science*, 52: 562 - 78.

Liu, M., Zanna, S., Ardelean, H., Frateur, I., Schmutz, P, Song, G., Atrens, A., and Marcus, P. 2009. 'A first quantitative XPS study of the surface films formed, by exposure to water, on Mg and on the Mg–Al intermetallics: Al_3Mg_2 and $Mg_{17}Al_{12}$', *Corrosion Science*, 51: 1115 - 27.

Lyndon, J. A., Gupta, R. K., Gibson, M. A., and Birbilis, N. 2013. 'Electrochemical behaviour of the β-phase intermetallic (Mg_2Al_3) as a function of pH as relevant to corrosion of aluminium–magnesium alloys', *Corrosion Science*, 70: 290 - 93.

Mansfeld, F., Lin, S., and Shih, H. 1992. 'Detection and monitoring of localized corrosion of aluminum alloys with electrochemical impedance spectroscopy.' in Agarwala, V. S. and Ugiansky, G. M. (eds.) (ASTM International: West Conshohocken, PA).

Mansfeld, F., and Shih, H. 1988. 'Detection of pitting with electrochemical impedance spectroscopy', *Journal of The Electrochemical Society*, 135: 1171-72.

Marcus, P., Maurice, V., and Strehblow, H. H. 2008. 'Localized corrosion (pitting): A model of passivity breakdown including the role of the oxide layer nanostructure', *Corrosion Science*, 50: 2698-704.

Martin, F. J., Cheek, G. T., O'Grady, W. E., and Natishan, P. M. 2005. 'Impedance studies of the passive film on aluminium', *Corrosion Science*, 47: 3187-201.

McCafferty, E. 2003. 'Sequence of steps in the pitting of aluminum by chloride ions', *Corrosion Science*, 45: 1421 - 38.

McCafferty, E., and Wightman, J. P. 1997. 'Determination of the surface isoelectric point of oxide films on metals by contact angle titration', *Journal of Colloid and Interface Science*, 194: 344-55.

Menezes, S., Haak, R., Hagen, G., and Kendig, M. 1989. 'Photoelectrochemical characterization of corrosion inhibiting oxide films on aluminum and Its alloys', *Journal of The Electrochemical Society*, 136: 1884-86.

Mishra, P., and Mahapatra, B. K. 2020. 'Aluminium industry - challenges and opportunities'. https://aluminiumandalloys.com/aluminium-industry-challenges-and-opportunities/.

Moayed, M. H., and Newman, R. C. 2006. 'Evolution of current transients and morphology of metastable and stable pitting on stainless steel near the critical pitting temperature', *Corrosion Science*, 48: 1004-18.

Moore, K. L., Sykes, J. M., and Grant, P. S. 2008. 'An electrochemical study of repassivation of aluminium alloys with SEM examination of the pit interiors using resin replicas', *Corrosion Science*, 50: 3233-40.

Muster, T. H., and Hughes, A. E. 2006. 'Applications and limitations of scanning kelvin probe force microscopy for the surface analysis of aluminum alloys', *Journal of The Electrochemical Society*, 153: B474.

Natishan, P. M., and McCafferty, E. . 1989. 'The mechanism of blister formation and rupture in the pitting of ion-implanted aluminum', *Journal of The Electrochemical Society*, 136: 53.

Natishan, P. M., McCafferty, E., and Hubler, G. K. 1988. 'Surface charge considerations in the pitting of ion-implanted aluminum', *Journal of The Electrochemical Society*, 135: 321-27.

Natishan, P. M., and O'Grady, W. E. 2014. 'Chloride ion interactions with oxide-covered aluminum leading to pitting corrosion: a review', *Journal of The Electrochemical Society*, 161: C421-C32.

Newman, R. C. 1995. 'Local chemistry considerations in the tunnelling corrosion of aluminium', *Corrosion Science*, 37: 527-33.

Newton, C. J., and H., Holroyd N. J. 1992. *Time-lapse video techniques in the corrosion testing of aluminum alloys new methods for corrosion testing of aluminum alloys* (ASTM International: West Conshohocken, PA).

Nguyen, T. H., and Foley, R. T. 1979. 'On the mechanism of pitting of aluminum', *Journal of The Electrochemical Society*, 126: 1855-60.

Nisancioglu, K. 1993. 'Electrochemical behavior of Al_3Fe intermetallic compound', *Journal of Japan Institute of Light Metals*, 43, 6, 319-327.

Nisancioglu, K., and Holtan, H. 1978. 'The protection potential of aluminium', *Corrosion Science*, 18: 1011-23.

Niu, L., Yin, Y., Guo, W., Lu, M., Qin, R., and Chen, S. 2009. 'Application of scanning electrochemical microscope in the study of corrosion of metals', *Journal of Materials Science*, 44: 4511-21.

Novakovski, V. M., and Sorokina, A. N. 1966. 'Model study of chloride pitting in 18-8 stainless steel', *Corrosion Science*, 6: 227-33.

Ogle, K. 2019. 'Atomic emission spectroelectrochemistry: real-time rate measurements of dissolution, corrosion, and passivation', *CORROSION*, 75: 1398-419.

Oltra, R., Malki, B., and Rechou, F. 2010. 'Influence of aeration on the localized trenching on aluminium alloys', *Electrochimica Acta*, 55: 4536-42.

Ovarfort, R. 1989. 'Critical pitting temperature measurements of stainless steels with an improved electrochemical method', *Corrosion Science*, 29: 987-93.

Paik, C. H., White, H. S., and Alkire, R. C. 2000. 'Scanning electrochemical microscopy detection of dissolved sulfur species from inclusions in stainless steel', *Journal of The Electrochemical Society*, 147: 4120.

Park, J. O., Paik, C. H., Huang, Y. H., and Alkire, R. C. 1999. 'Influence of Fe-Rich intermetallic inclusions on pit initiation on aluminum alloys in aerated NaCl', *Journal of The Electrochemical Society*, 146: 517-23.

Pickering, H. W., and Frankenthal, R. P. 1972. 'On the mechanism of localized corrosion of iron and stainless steel', *Journal of The Electrochemical Society*, 119: 1297.

Pistorius, P. C., and Burstein, G. T. 1992. 'Metastable pitting corrosion of stainless steel and the transition to stability', *Philosophical Transactions of the Royal Society of London. Series A: Physical and Engineering Sciences*, 341: 531-59.

Pourbaix, M. 1966. *Atlas of electrochemical equilibria in aqueous solutions* (Pergamon Press: Oxford; New York).

Pourbaix, M., Klimzack-Mathieiu, L., Mertens, Ch, Meunier, J., Vanleugenhaghe, Cl, de Munck, L., Laureys, J., Neelemans, L., and Warzee, M. 1963. 'Potentiokinetic and corrosimetric investigations of the corrosion behaviour of alloy steels', *Corrosion Science*, 3: 239-59.

Pride, S. T., Scully, J. R., and Hudson, J. L. 1994. 'Metastable pitting of aluminum and criteria for the transition to stable pit growth', *Journal of The Electrochemical Society*, 141: 3028-40.

Punckt, C., Bölscher, M., Rotermund, H. H., Mikhailov, A. S., Organ, L., Budiansky, N., Scully, J. R., and Hudson, J. L. 2004. 'Sudden onset of pitting corrosion on stainless steel as a critical phenomenon', *Science*, 305: 1133-36.

Ralston, K.D., Birbilis, N., Cavanaugh, M. K., Weyland, M., Muddle, B.C., and Marceau, R.K.W. 2010. 'Role of nanostructure in pitting of Al–Cu–Mg alloys', *Electrochimica Acta*, 55: 7834 - 42.

Riley, A. M., Wells, D. B., and Williams, D. E. 1991. 'Initiation events for pitting corrosion of stainless steel?', *Corrosion Science*, 32: 1307 - 13.

Romhanji, E., and Popovj , M. 2006. 'Problems and prospect of Al-Mg alloys application in marine constructions', *Metalurgija*, 12: 297-307.

Rosenfeld, I. L., and Danilov, I. S. 1967. 'Electrochemical aspects of pitting corrosion', *Corrosion Science*, 7: 129-42.

Rousar, I., and Cezner, V. 1975. 'Transfer of mass or heat to an electrode in the region of hydrogen evolution—I theory', *Electrochimica Acta*, 20: 289 - 93.

Rudd, W. J., and Scully, J. C. 1980. 'The function of the repassivation process in the inhibition of pitting corrosion on aluminium', *Corrosion Science*, 20: 611-31.

Sander, G., Cruz, V., Bhat, N., and Birbilis, N. 2020. 'On the in-situ characterisation of metastable pitting using 316L stainless steel as a case study', *Corrosion Science*, 177: 109004.

Sasaki, K., and Burstein, G. T. 1996. 'The generation of surface roughness during slurry erosion-corrosion and its effect on the pitting potential', *Corrosion Science*, 38: 2111-20.

Sasaki, K., and Isaacs, H. S. 2004. 'Origins of electrochemical noise during pitting corrosion of aluminum', *Journal of The Electrochemical Society*, 151: B124-B33.

Sasaki, K., Levy, P. W., and Isaacs, H. S. 2002. 'Electrochemical noise during pitting corrosion of aluminum in chloride environments', *Electrochemical and Solid-State Letters*, 5: B25.

Sato, F., and Newman, R.C. 1998 a, 'Mechanism of activation of aluminum by low melting point elements: part 1 effect of zinc on activation of aluminum in metastable pitting', *CORROSION* 54:12

Sato, F., and Newman, R. C. 1998 b. 'Mechanism of activation of aluminum by low melting point elements: part 1 effect of zinc on activation of aluminum in metastable pitting', *CORROSION*, 54: 9.

Sato, N. 1971. 'A theory for breakdown of anodic oxide films on metals', *Electrochimica Acta*, 16: 1683-92.

Sato, N. 1978. Frankenthal, R. P and Kruger, J. (eds.), *Passivity of Metals* (Electrochemical Society: Princeton).

Sato, N. 1982. 'Anodic breakdown of passive films on metals', *Journal of The Electrochemical Society*, 129: 255-60.

Scamans, G. M., Birbilis, N., and Buchheit, R. G. 2010. '3.08 - Corrosion of aluminum and its alloys.' in Cottis, B., Graham, M., Lindsay, R., Lyon, S., Richardson, T., Scantlebury, D. and Stott, H. (eds.), *Shreir's Corrosion* (Elsevier: Oxford).

Scheiner, S., and Hellmich, C. 2007. 'Stable pitting corrosion of stainless steel as diffusion-controlled dissolution process with a sharp moving electrode boundary', *Corrosion Science*, 49: 319-46.

Scheiner, S., and Hellmich, C. 2009. 'Finite Volume model for diffusion- and activation-controlled pitting corrosion of stainless steel', *Computer Methods in Applied Mechanics and Engineering*, 198: 2898-910.

Schneider, O., Ilevbare, G. O., Scully, J. R., and Kelly, R. G. 2004. 'In situ confocal laser scanning microscopy of AA2024-T3 corrosion metrology: II. Trench formation around particles', *Journal of The Electrochemical Society*, 151, 8, B465-B472.

Schönbein, C. F. 1836. 'Ueber das Verhalten des Zinns und des Eisens gegen die Salpetersäure', *Annalen der Physik*, 113: 390-99.

Schwenk, W. 1964. 'Theory of stainless steel pitting', *CORROSION*, 20: 129t-37t.

Schwenk, W. 1965. 'Diskussion der eigenschaften des lochfrasspotentials nichtrostender Stähle in zusammenhang mit seinen bestimmungsmethoden', *Corrosion Science*, 5: 245-54.

Scully, J. R., Budiansky, N. D., Tiwary, Y., Mikhailov, A. S., and Hudson, J. L. 2008. 'An alternate explanation for the abrupt current increase at the pitting potential', *Corrosion Science*, 50: 316-24.

Serebrennikova, I., Lee, S., and White, H. S. 2002. 'Visualization and characterization of electroactive defects in the native oxide film on aluminium', *Faraday Discussions*, 121: 199-210.

Serebrennikova, I., and White, H. S. 2001. 'Scanning electrochemical microscopy of electroactive defect sites in the native oxide film on aluminum', *Electrochemical and Solid-State Letters*, 4: B4.

Seys, A. A., Brabers, M. J., and Van Haute, A. A. 1974. 'Analysis of the influence of hydrogen on pitting corrosion and stress corrosion of austenitic stainless steel in chloride environment', *CORROSION*, 30: 47-52.

Sheng, W., Zhuang, Z., Gao, M., Zheng, J., Chen, J. G., and Yan, Y. 2015. 'Correlating hydrogen oxidation and evolution activity on platinum at different pH with measured hydrogen binding energy', *Nature Communications*, 6: 5848.

Shibata, S. 1963. 'The concentration of molecular hydrogen on the platinum cathode', *Bulletin of the Chemical Society of Japan*, 36: 53-57.

Siitari, D. W., and Alkire, R. C. 1982. 'Initiation of crevice corrosion: I . experimental investigations on aluminum and iron', *Journal of The Electrochemical Society*, 129: 481-87.

Soltis, J. 2015. 'Passivity breakdown, pit initiation and propagation of pits in metallic materials – Review', *Corrosion Science*, 90: 5 - 22.

Speckert, L., and Burstein, G. T. 2011. 'Combined anodic/cathodic transient currents within nucleating pits on Al–Fe alloy surfaces', *Corrosion Science*, 53: 534 - 39.

Sridhar, G., Birbilis, N., and Raja, V. S. 2021. 'The reliability of metastable pit sizes estimated from dissolution current in aluminium alloys', *Corrosion Science*, 182: 109276.

Still, J. W., and Wipf, D. O. 1997. 'Breakdown of the iron passive layer by use of the scanning electrochemical microscope', *Journal of The Electrochemical Society*, 144: 2657-65.

Strehblow, H. 1984. *Ninth International Congress on Metallic Corrosion*, edited by Canada, National Research Council of, 99 - 106. Ottawa.

Strehblow, H. -H., and Wenners, J. 2002. 'Mechanisms of pitting.' in Marcus, P. (ed.), *Corrosion mechanism in theory and practice* (Marcel Dekker Inc: New York).

Szklarska-Smialowska, Z. 1971. 'Review of literature on pitting corrosion published since 1960', *CORROSION*, 27: 223-33.

Szlarska-Smialowska. 1999. 'Pitting corrosion of aluminum', *Corrosion Science*, 41: 1743-67.

Tang, Y., Zuo, Y., Wang, J., Zhao, X., Niu, B., and Lin, B. 2014. 'The metastable pitting potential and its relation to the pitting potential for four materials in chloride solutions', *Corrosion Science*, 80: 111-19.

Tester, J. W., and Isaacs, H. S. 1975. 'Diffusional effects in simulated localized corrosion', *Journal of The Electrochemical Society*, 122: 1438-45.

Tian, W., Chao, B., Xiong, X., and Li, Z. 2018. 'Effect of surface roughness on pitting corrosion of 2A12 aluminum alloy', *International Journal of Electrochemical Science*, 13, 3107-3123.

Trueman, A. R. 2005. 'Determining the probability of stable pit initiation on aluminium alloys using potentiostatic electrochemical measurements', *Corrosion Science*, 47: 2240-56.

Uhlig, H. H. 1979. 'Passivity in metals and alloys', *Corrosion Science*, 19: 777-91.

United, States, Federal Aviation, Administration, Battelle Memorial, Institute, and Columbus, Laboratories. 2008. 'MMPDS-04 : Metallic materials properties development and standardization (MMPDS)'.

Urquidi, M., and Macdonald, D. D. 1985. 'Solute-vacancy interaction model and the effect of minor alloying elements on the initiation of pitting corrosion', *Journal of The Electrochemical Society*, 132: 555-58.

Vargel, C. 2004. 'Chapter A.1 - The advantages of aluminium.' in Vargel, Christian (ed.), *Corrosion of Aluminium* (Elsevier: Amsterdam).

Vedder, W., and Vermilyea, D. A. 1969. 'Aluminum + water reaction', *Transactions of the Faraday Society*, 65: 561-84.

Vetter, K. J., and Strehblow, H. H. 1974. Staehle, R. W., Brown, B. F., Kruger, J. and Agarwal, A. (eds.), *Localised Corrosion* (NACE International: Houston).

Vogt, H. 2011. 'On the gas-evolution efficiency of electrodes I – Theoretical', *Electrochimica Acta*, 56: 1409 - 16.

Wang, Y., and Cheng, G. 2016a. 'Quantitative evaluation of pit sizes for high strength steel: Electrochemical noise, 3-D measurement, and image-recognition-based statistical analysis', *Materials & Design*, 94: 176-85.

Wang, Y., Wu, G., He, L., and Singh, P. M. 2016b. 'Effect of thiosulfate on metastable pitting of 304L and S32101 in chloride- and thiosulfate-containing environment', *CORROSION*, 72: 628-35.

Wilde, B. E., and Williams, E. 1971. 'The relevance of accelerated electrochemical pitting tests to the long-term pitting and crevice corrosion behavior of stainless steels in marine environments', *Journal of The Electrochemical Society*, 118: 1057.

Williams, D. E., Mohiuddin, T. F., and Zhu, Y. Y. 1998. 'Elucidation of a trigger mechanism for pitting corrosion of stainless steels using submicron resolution scanning electrochemical and photoelectrochemical microscopy', *Journal of The Electrochemical Society*, 145: 2664-72.

Williams, D. E., Stewart, J., and Balkwill, P. H. 1994. 'The nucleation, growth and stability of micropits in stainless steel', *Corrosion Science*, 36: 1213 - 35.

Williams, D. E., Westcott, C., and Fleischmann, M. 1985a. 'Stochastic models of pitting corrosion of stainless steels: I . modeling of the initiation and growth of pits at constant potential', *Journal of The Electrochemical Society*, 132: 1796-804.

Williams, D. E., Westcott, C., and Fleischmann. 1985b. 'Stochastic models of pitting corrosion of stainless steels: II . measurement and interpretation of data at constant potential', *Journal of The Electrochemical Society*, 132: 1804-11.

Winkler, L. W. 1891. 'Die Löslichkeit der Gase in Wasser', *Berichte der deutschen chemischen Gesellschaft*, 24: 3602-10.

Yang, X., Karnbach, F., Uhlemann, M., Odenbach, S., and Eckert, K. 2015. 'Dynamics of single hydrogen bubbles at a platinum microelectrode', *Langmuir*, 31: 8184-93.

Yang, Y-K., and Allen, T. 2013. 'Direct visualization of β phase causing intergranular forms of corrosion in Al–Mg alloys', *Materials Characterization*, 80: 76 - 85.

Yasuda, M., Weinberg, F., and Tromans, D. 1990. 'Pitting corrosion of Al and Al-Cu single crystals', *Journal of The Electrochemical Society*, 137: 3708-15.

Yu, Y., and Li, Y. 2020. 'New insight into the negative difference effect in aluminium corrosion using in-situ electrochemical ICP-OES', *Corrosion Science*, 168: 108568.

Zavadil, K. R., Ohlhausen, J. A., and Kotula, P. G. 2003. "Nanoscale morphology development in the passive oxide on aluminum and the relationship to pitting." In *Proceedings - Electrochemical Society*, 283-93.

Zavadil, K. R., Ohlhausen, J. A., and Kotula, P. G. 2006. 'Nanoscale void nucleation and growth in the passive oxide on aluminum as a prepitting process', *Journal of The Electrochemical Society*, 153: B296.

Zhang, T., Wang, D., Shao, Y., Meng, G., and Wang, F. 2012. 'A new criterion to determine the critical pitting temperature (CPT) based on electrochemical noise measurement', *Corrosion Science*, 58: 202-10.

Zheng, J., Sheng, W., Zhuang, Z., Xu, B., and Yan, Y. 2016. 'Universal dependence of hydrogen oxidation and evolution reaction activity of platinum-group metals on pH and hydrogen binding energy', *Science advances*, 2: e1501602-e02.

Zhu, Y. , and Williams, D. E. 1997. 'Scanning electrochemical microscopic observation of a precursor state to pitting corrosion of stainless steel', *Journal of The Electrochemical Society*, 144: L43-L45.

Publications

1. G. Sridhar, N. Birbilis and V.S. Raja, “In situ investigation on the role of hydrogen evolution on the estimated metastable pit sizes in an Al-Mg alloy”, CORROSION 2021; 3688.
2. G. Sridhar, N. Birbilis and V.S. Raja, “The reliability of metastable pit sizes estimated from dissolution current in aluminium alloys”, Corrosion Science, Volume 182, 15 April 2021, 109276.

Conferences & Symposiums

1. G. Sridhar, V.S. Raja and N. Birbilis, “Understanding metastable pitting in Al – 5 wt.% Mg alloy”, GRC Aqueous Corrosion – 2018 (New London, USA). *(Poster presentation).*
2. G. Sridhar, N. Birbilis and V.S. Raja, “The reliability of metastable pitting data in aluminium alloys”, MEMS Department Symposium – 2020 (IITB Mumbai, India - Virtual). *(Paper presentation).*
3. G. Sridhar, N. Birbilis and V.S. Raja, “A novel approach for the in-situ investigation of metastable pitting in aluminium alloys”, NSEST 2020 – 2021 (IISC Bengaluru, India - Virtual). *(Paper presentation).*
4. G. Sridhar, N. Birbilis and V.S. Raja, “Employing metastable pitting tests to determine the engineering life of aluminium alloys”, STIN 2021 (ARCI Hyderabad, India - Virtual) *(3-minute presentation).*
5. G. Sridhar, N. Birbilis and V. S. Raja, “Metastable pitting characteristics in aluminium alloys investigated from the in situ mapping of hydrogen evolution at metastable pit locations”, ICC 2021 *(Paper presentation).*
6. G. Sridhar, N. Birbilis and V.S. Raja, “Role of hydrogen evolution on the metastable pit sizes estimated from current transients”, Eurocorr 2021 *(Accepted-Paper presentation).*

Awards & Scholarships

1. Best paper for the paper titled “A novel approach for the in-situ investigation of metastable pitting in aluminium alloys” at NSEST 2020 by the Electrochemical Society of India and sponsored by Springer Nature.
2. NACE Foundation India Scholarship 2021.